Metastable State of Ultracold and Quantum Degenerate Ytterbium Atoms:

High-Resolution Spectroscopy and Cold Collisions

by

Atsushi Yamaguchi

A dissertation in the Physics department of the Kyoto University

March, 2008

Abstract

The study of laser-cooled two-electron atoms is one of the most interesting research fields in atomic physics. In particular, the unique characteristics of the metastable $^3P_2$ state of two-electron atoms have recently attracted attention both for their applications and study of their intrinsic characteristics.

In this thesis, I present experiments for studying new aspects of the metastable states in two-electron atoms. First, unique collisional properties of metastable Yb[$^3P_2$] atoms at ultralow temperatures are revealed in detail. In previous studies, evaporative cooling of metastable atoms in a magnetic trap was unsuccessful in forming a Bose-Einstein condensate (BEC) due to trap loss caused by strong spin-flip collision processes. We overcame this difficulty by employing, instead, an optical trap in which atoms in every magnetic sublevel of the $^3P_2$ state can be trapped. We successfully achieved a number density of 2×10^{13} cm^{-3}, which is larger than that achieved in a previous study by an order of three [1], at a temperature of 2 μK with a phase space density of 0.01. We also measured a large two-body inelastic collision rate in a far-off-resonance trap, which we interpret as fine-structure changing collisions in this ultracold temperature regime. Although a recent experiment with magnetically trapped Ca atoms studied multichannel collisions between $^3P_2$ atoms and discussed the possibility of the fine-structure changing process [2], we believe that our study is the first definite experimental measurement of this process between $^3P_2$ atoms.

The other important achievement in this study is the successful observation of the ultranarrow magnetic quadrupole $^1S_0 \leftrightarrow {}^3P_2$ transition. We first developed a novel 507-nm laser source. By tightly locking the laser frequency to a high-finesse external optical cavity, we stabilized the laser frequency and reduced the linewidth to less than 1 kHz. Using this laser source, we observed the $^1S_0 \leftrightarrow {}^3P_2$ transition in Yb bosonic (^{174}Yb) and fermionic (^{171}Yb, ^{173}Yb) isotopes. High-resolution spectroscopy of ultracold atoms and BECs was performed using this ultranarrow transition. The frequency shift and broadening due to the mean field energy of a BEC was observed. Furthermore, we determined the polarizabilities of all the magnetic sublevels of the $^3P_2$ state. Using an optical frequency comb, we also measured the optical frequency of the magnetic-field-insensitive $^1S_0 \leftrightarrow {}^3P_2$ ($m = 0$) transition in ^{174}Yb, which is one of the candidates for next-generation time and frequency standards [3].

Contents

Chapter 1

Introduction

The technique of laser cooling and trapping of neutral atoms has progressed rapidly in recent years. One of the major breakthroughs in this field is the achievement of the Bose-Einstein condensate (BEC) in dilute gasses of alkali metals in 1995 [4, 5, 6]. BEC has enabled us to study fundamental quantum mechanics experimentally in a macroscopic system, and thus numerous fascinating experiments have been performed worldwide using BEC.

At the same time, laser cooled two-electron atoms, including alkaline-earth metals (e.g., Ca and Sr) and Ytterbium (Yb), have attracted increasing interest in various fields of atomic physics due to their unique features, which alkali metal atoms do not possess [7, 8]. In particular, the unique characteristics of metastable $^3P_2$ atoms have recently attracted attention, both for their applications and for the study of their collisional properties [9]. These atoms are different from the more commonly studied alkali metal atoms because collisions between $^3P_2$ atoms are intrinsically anisotropic. Recent theories have investigated the effects of this anisotropy, including its interplay with magnetic field effects, which enable novel control of the scattering length [10], and multichannel collisions due to strong coupling among the partial waves of relative motion [11]. Also, the magnetic dipole dipole interaction between $^3P_2$ atoms is nine times larger than that between alkali metal atoms. This has led to theoretical predictions such as novel quantum phases and use in quantum information systems [12, 13].

On the other hand, studies on extremely narrow optical transitions in two-electron atoms between the metastable state and the ground state have also progressed rapidly. For example, in metrology, studies on an ultraprecise atomic clock using such ultranarrow transitions have been pursued to achieve an uncertainty of 10^{-16} and beyond with the aim of producing an optical lattice clock [8]. In quantum information science, an optical two-level system with large coherence times of the metastable state in two-electron atoms is useful as a well-defined quantum bit (qubit), which can be easily converted to a flying qubit of a photon. Sideband cooling using narrow transitions to cool a neutral atom down to the vibrational ground state of a trap is also possible [14, 15]. In addition, the combination of the ultranarrow $^1S_0 \leftrightarrow {}^3P_2(m = \pm 2)$ transition and its Zeeman shift enables ultraprecise measurement of a magnetic field and high-resolution spatial addressing of atoms, for example, atoms confined in optical lattice potentials in a magnetic field gradient.

In this study, I present experiments for studying new aspects of the metastable $^3P_2$ state in two-electron atoms. To study the fascinating possibilities of $^3P_2$ atoms, several groups have performed laser cooling and trapping of two-electron atoms in the $^3P_2$ state. For example, in order to investigate unique collisional properties, laser cooling of metastable Ca[$^3P_2$] and Sr[$^3P_2$] atoms has previously been performed; however, the atomic temperature was relatively high ($\sim$ a few millikelvin). In this study, we developed a new method to obtain ultracold and dense $^3P_2$ atoms in a trap. Using such atoms, we investigated unique collisional properties in the ultracold temperature regime. As for the ultranarrow transitions, while previous studies mainly focused on its application to the next-generation frequency standards, we demonstrated high-resolution spectroscopy of ultracold atoms and BECs using an ultranarrow optical transition in Yb. In the following text, I will briefly introduce the experiments performed in this work.

Unique collisional properties of metastable Yb[$^3P_2$] atoms at ultracold temperatures

First, unique collisional properties of metastable Yb[$^3P_2$] atoms at ultralow temperatures are revealed in detail. Previously, several laboratories have realized laser cooling and trapping of metastable two-electron atoms. Ca and Sr atoms decaying to the $^3P_2$ state from the $^1P_1$ state, which is the upper state in the $^1S_0 \leftrightarrow {}^1P_1$ magneto-optical trap (MOT) transition, have been successfully trapped in a magnetic trap [16, 17, 1]. Also, a MOT operating on the $^3P_2 \leftrightarrow {}^3D_3$ transition has been used to load a magnetic trap [18]. In spite of the success of these approaches, evaporative cooling of $^3P_2$ atoms in a magnetic trap to realize a BEC was unsuccessful due to trap loss caused by strong multichannel collisional processes. More recently, a similar large inelastic collision rate in Ca[$^3P_2$, m_J=2] was observed at temperatures of a few millikelvin [2].

The loss induced by multichannel collisions in a magnetic trap can be overcome by employing an optical far-off-resonance trap (FORT) instead of a magnetic trap. The FORT wavelength can be chosen so that atoms in every magnetic sublevel of the $^3P_2$ state can be trapped with the same strength. As a result, although multichannel collisions can still occur, they will not lead to trap loss. In this study, we developed a new method to prepare ultracold and dense $^3P_2$ atoms in a FORT. Unlike previous methods, we first trapped Yb[$^1S_0$] atoms in a FORT and performed evaporative cooling. Then, we optically excited Yb[$^1S_0$] to the $^3P_2$ state to obtain ultracold trapped Yb[$^3P_2$] atoms. Using this method, we achieved a number density of 2×10^{13} cm^{-3} at a temperature of 2 μK with a phase space density (PSD) of 0.01. Our newly achieved number density is larger than that achieved in a previous study by an order of three [1].

While the trap loss due to the multichannel collisions must be suppressed in our FORT, we still observed a large two-body inelastic collision rate. Thus, we deduce the existence of a different inelastic collisional process, which we interpret as fine-structure changing collisions in this ultracold temperature regime. Although fine-structure changing inelastic collisional properties have previously been investigated for Mg[^3P_j], O[^3P_j], Sc[^2D_j], and Ti[^3F_j] colliding with closed-shell atoms [19, 20, 21, 22, 23], they had not been seen in collisions between $^3P_2$ atoms. While a recent experiment on magnetically trapped Ca

atoms studied multichannel collisions between $^3P_2$ atoms and discussed the possibility of the fine-structure changing process [2], we believe that our study is the first definite experimental measurement of this process between $^3P_2$ atoms.

High-resolution spectroscopy of ultracold atoms and BECs using the ultranarrow $^1S_0 \leftrightarrow {}^3P_2$ transition

The other important achievement in this study is the successful observation of the ultranarrow magnetic quadrupole $^1S_0 \leftrightarrow {}^3P_2$ transition (507 nm) in Yb bosonic (^{174}Yb) and fermionic (^{171}Yb, ^{173}Yb) isotopes.

We first developed a 507-nm ultranarrow-linewidth laser system, which consists of an extended cavity laser diode, a tapered amplifier, and a periodically poled lithium niobate nonlinear crystal. In order to observe the ultranarrow transition, the laser linewidth was reduced below 1 kHz by tightly locking it to a high-finesse optical cavity. Due to its ultranarrow linewidth, this transition had never been observed prior to this study. Hence, we also estimated the transition frequency using an optical frequency comb. Using the developed laser system and the estimated transition frequency, we observed the $^1S_0 \leftrightarrow {}^3P_2$ transition for the first time.

High-resolution spectroscopy of ultracold atoms and BECs was demonstrated using this transition. The polarizabilities of all magnetic sublevels of the $^3P_2$ state were determined with high precision. Using an optical frequency comb, we also measured the frequency of the magnetic-field-insensitive $^1S_0 \leftrightarrow {}^3P_2$ ($m = 0$) transition in ^{174}Yb, which is one of the candidates for next-generation atomic frequency standards [3]. However, the highlight of this study is the detection of the mean field shift of a BEC using this ultranarrow optical transition. We observed, not only the large mean field shift in a BEC, but also the change in the lineshape, which reflects the density distribution of a BEC in a trap. As a result, we successfully determined a_{12} (the scattering length between atoms in the $^1S_0$ state and the $^3P_2$ state) from the observed spectrum. Furthermore, we also performed spectroscopy of condensates in 1D optical lattice potentials and observed the mean field shift due to on-site interaction at each site.

Thesis outline

- Chapter 2: We will introduce all important aspects of laser cooling and trapping of Yb atoms in this study. Details about laser systems will be also presented.

- Chapter 3: This chapter deals with the ultranarrow laser system developed in this study in order to observe the ultranarrow $^1S_0 \leftrightarrow {}^3P_2$ transition.

- Chapter 4: Overview of the excitation of atoms by a laser field such as E1, E2, and M2 transitions. All of these transitions play a key role in this study. The calculation of the light shift is also presented.

- Chapter 5: The spectral shifts and broadenings that we have to consider when analyzing the data obtained in this study are discussed.

- Chapter 6: Optical trapping of $^3P_2$ atoms and investigation of unique collisional properties are presented. A new method involving the trapping of atoms in a FORT and estimation of elastic and inelastic collision rate constants are discussed.
- Chapter 7: Details about our first observation of the $^1S_0 \leftrightarrow {}^3P_2$ transition are described. Estimation of the resonance frequency and measurement and control of the polarizability of the $^3P_2$ state are also included.
- Chapter 8: Spectroscopy of a BEC using the ultranarrow $^1S_0 \leftrightarrow {}^3P_2$ transition is reported. The detected mean field shift will be shown and analyzed in detail. In addition, the spectroscopy of condensates in 1D optical lattice potentials is reported.
- Chapter 9: This chapter presents the frequency measurement of the $^1S_0 \leftrightarrow {}^3P_2(m = 0)$ "clock" transition. Some basic properties of our frequency comb are described.
- Chapter 10: A summary of this study and some future prospects are presented.
- Appendices: Short but important topics related to this study are briefly summarized, including the estimation of the magic wavelength of the $^3P_2$ state, a novel laser system based on narrow iodine spectra, and a new stable laser system to obtain the MOT beam.

Chapter 2

Laser cooling and trapping of neutral Yb atoms

In this Chapter, I will present details of laser cooling and trapping of Yb atoms. First, general properties of Yb atoms will be introduced. Then, basic characteristics of our Zeeman slower system, MOT, FORT, and imaging system will be presented. Finally, details about laser systems will be described.

2.1 General properties of neutral Yb atoms

Laser cooling and trapping of Yb atoms have been yielding a fundamental progress in atomic physics. After the first realization of a BEC of ^{174}Yb in 2003, BECs of ^{176}Yb and ^{170}Yb and Fermi degeneracies of ^{173}Yb and ^{171}Yb have been successfully realized in our laboratory [24, 25, 26, 27]. As shown in Table 2.1, rich kind of stable isotopes of Yb (five bosons and two fermions) enables a variety of mixtures such as Bose-Bose, Bose-Fermi and Fermi-Fermi gasses and even mixtures of three species. Seven other unstable isotopes are also known. The scattering length which governs atomic collisions at ultracold temperatures has been precisely measured via photoassociation spectroscopy [28, 29, 30] and estimated for all pairs of isotopes using the mass scaling law [31]. The other significant feature of Yb is the existence of ultranarrow optical transitions. The so-called "clock transition" ($^1S_0 \leftrightarrow {}^3P_0$) is one of the primary candidates of next-generation frequency standards and ultraprecise atomic clocks whose stability has already reached 3×10^{-16} [32]. The clock transition has been observed in fermionic isotopes (^{171}Yb and ^{173}Yb) and a bosonic isotope (^{174}Yb) [33, 34, 35]. Novel sideband cooling technique using the clock transition in fermionic isotopes has been also proposed [15]. In addition, Yb is regarded as one of the good candidates for the test of time-reversal symmetry violation [36] and the study of atomic parity nonconservation [37].

Yb is a rare earth metal. The ground state electronic configuration[1] is [Xe]$4f^{14}6s^2$. Its atomic mass is 173.04. The melting point and the boiling point are 1097 K (824 °C) and 1700 K (1427 °C), respectively. At room temperature, Yb is very stable. Because of two

[1] $1s^2 2s^2 2p^6 3s^2 3p^6 3d^{10} 4s^2 4p^6 4d^{10} 5s^2 5p^6 4f^{14} 6s^2$

valence electrons, the structure of energy levels are similar to that of alkaline-earth metals, that is to say, Yb has singlet and triplet series in energy levels as shown in Fig.2.1 and 2.2. Isotope shifts in the ${}^1S_0 \leftrightarrow {}^1P_1$ and ${}^1S_0 \leftrightarrow {}^3P_1$ transitions are listed in Table 2.2. According to the calculation in [38], the saturated vapor pressure of Yb is 3×10^{-21} Torr at room temperature, which means that there exists no Yb atoms in air at room temperature. We heat the Yb oven up to 375°C in the experiment.

Table 2.1: Natural abundance and nuclear spin of Yb [39].

Atomic Mass	Natural Abundance (%)	Nuclear Spin
174	31.8	0
172	21.9	0
173	16.12	5/2
171	14.3	1/2
176	12.7	0
170	3.05	0
168	0.13	0

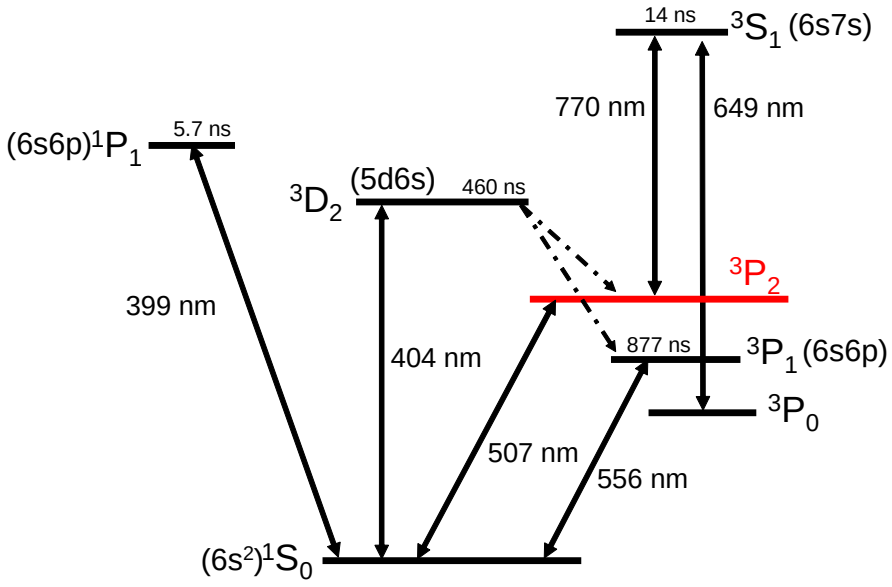

Figure 2.1: Low lying energy levels of Yb

Table 2.2: Yb isotope shifts of the $^1S_0 \leftrightarrow {}^1P_1$ transition at 399 nm [41] and $^1S_0 \leftrightarrow {}^3P_1$ transition at 556 nm [42] relative to the resonance frequency of ^{174}Yb.

$^1S_0 \leftrightarrow {}^1P_1$		$^1S_0 \leftrightarrow {}^3P_1$	
Atomic Mass	Isotope Shift (MHz)	Atomic Mass	Isotope Shift (MHz)
176	−509.3	173(5/2−7/2)	−2386
173(5/2−5/2)	−253.4	171(1/2→1/2)	−2132
174	0	176	−955
173(5/2−3/2)	516.0	174	0
172	533.3	172	1000
173(5/2−7/2)	588.0	170	2287
171(1/2−3/2)	832.4	173(5/2−5/2)	2312
171(1/2−1/2)	1153.7	168	3655
170	1192.4	171(1/2−3/2)	3805
168	1887.4	173(5/2−3/2)	3806

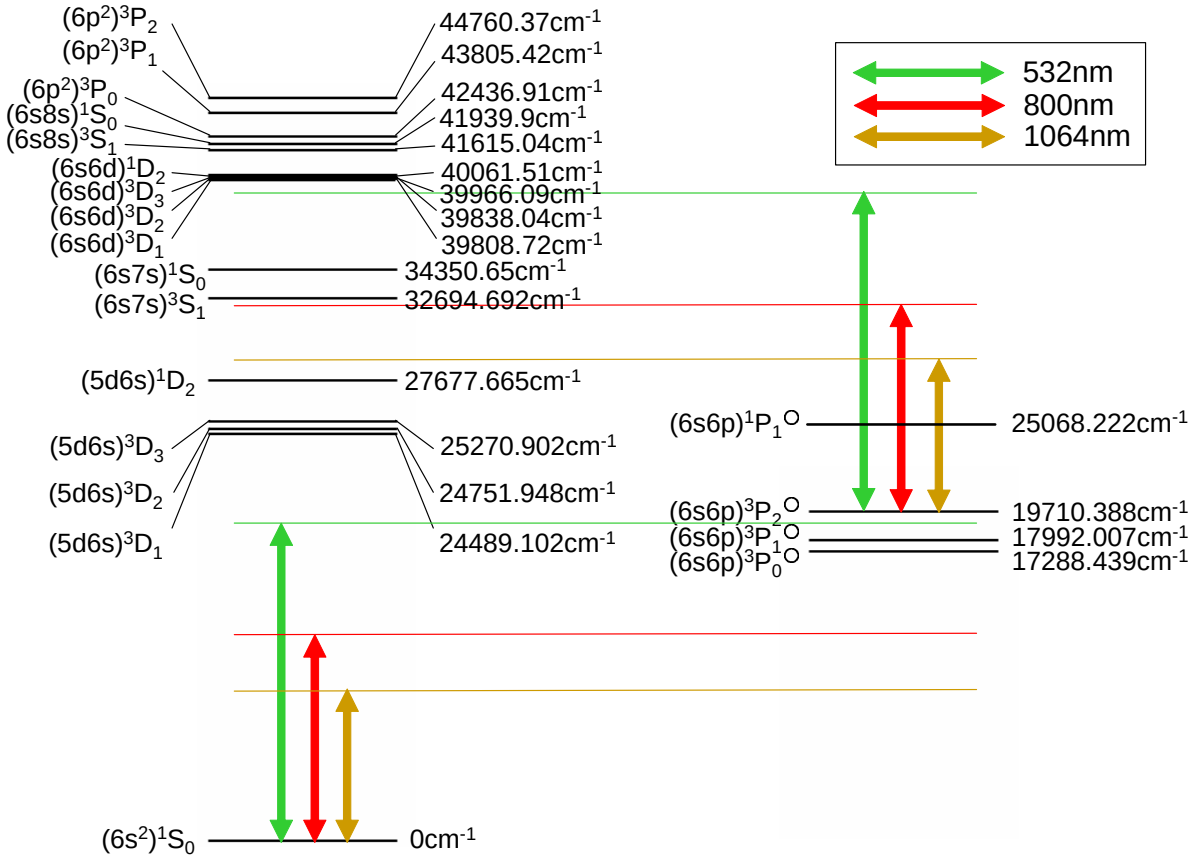

Figure 2.2: Energy levels in Yb in the unit of cm^{-1} [40]. Energy between each levels and the $(6s^2)^1S_0$ ground state is reflected as an amplitude of the interval in the vertical direction. The positions of typical wavelength for a FORT (532nm, 800nm and 1064 nm) are also shown for the $(6s^2)^1S_0$ and $(6s6p)^3P_2$ states.

2.2 Laser cooling and imaging of Yb atoms

In this section, each cooling stage from an atomic oven to a BEC will be presented in detail [43, 44, 7]. We use the ${}^1S_0 \leftrightarrow {}^1P_1$ and the ${}^1S_0 \leftrightarrow {}^3P_1$ transitions for the Zeeman slower and MOT transitions, respectively. Important values of these two transitions are summarized in Table 2.3.

Table 2.3: Important values of cooling transition ${}^1S_0 \leftrightarrow {}^1P_1$ and ${}^1S_0 \leftrightarrow {}^3P_1$ [40].

		${}^1S_0 \leftrightarrow {}^1P_1$	${}^1S_0 \leftrightarrow {}^3P_1$	Unit
Wavelength (in air)	λ	398.8	555.6	nm
Lifetime	τ	5.7	877	nsec
Natural linewidth	$\frac{\Gamma}{2\pi} = \frac{1}{2\pi\tau}$	27.9	0.181	MHz
Saturation Intensity	$I_{\mathrm{sat}} = \frac{\pi hc}{3\lambda^3\tau}$	57	0.14	mW/cm^2
Doppler limit temperature	$T_{\mathrm{D}} = \frac{\hbar\Gamma}{2k_{\mathrm{B}}}$	670	4.35	μK
Doppler limit velocity	$v_{\mathrm{D}} = \sqrt{\frac{k_{\mathrm{B}}T_{\mathrm{D}}}{m}}$	18	1.4	cm/sec
g-factor	g	1.04	1.49	
Absorption cross section	$\sigma_{\mathrm{ab}} = \frac{3\lambda^2}{2\pi}$	76	147	10^{-15}m^2
Recoil frequency	$\nu_{\mathrm{R}} = \frac{\hbar k^2}{4\pi m}$	7.2	3.7	kHz

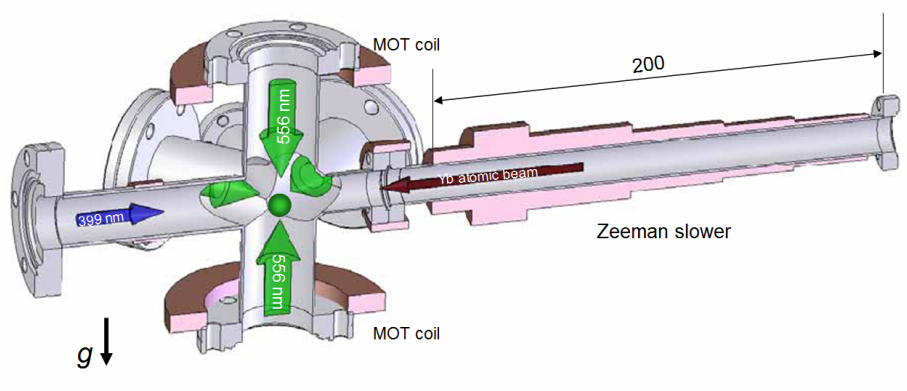

Figure 2.3: Schematics of Zeeman slower and MOT laser beams in vacuum chamber.

2.2.1 Zeeman slower

To slow down atoms emitted from a Yb oven at 375 °C, a Zeeman slower system is used. Basically, the resonance frequency of atoms in an atomic beam is shifted due to the Doppler effect depending on the atomic velocity. In a Zeeman slower system, such frequency shifts are compensated by the gradually varied external magnetic field.

There exist two kinds of Zeeman slower configurations which are referred to as the $\sigma+$ and $\sigma-$ configurations. In the $\sigma+(-)$ configuration, amplitude of the magnetic field decreases (increases) from the oven to the MOT region. The important difference between these two configurations is that the frequency of the slower beam. It is far red-detuned in case of the $\sigma+$ configuration while it is almost resonant in the $\sigma-$ configuration. The $\sigma+$ configuration has an advantage of small leak of the magnetic field into the MOT region. However, in this work, the MOT transition ($^1S_0 \leftrightarrow {}^3P_1$) is different from the transition used for the Zeeman slower ($^1S_0 \leftrightarrow {}^1P_1$). In such a case, atoms in a MOT may be blew out by the slower beam in the $\sigma+$ configuration. Thus the $\sigma-$ configuration is better than the $\sigma+$ one[2]. The 399 nm slowing laser are detuned by about 500MHz from the resonance and applied to the atomic beam from the opposite direction as shown in Fig.2.3.

Cleaning of coated windows

Since we irradiate a slowing laser from the opposite direction of the Yb atomic beam, the input window is gradually coated with Yb atoms. As this coating becomes thick, the slowing laser is scattered at the window, which leads to decrease of the efficiency of the Zeeman slower system. To clean up the Yb coating, we have blew away Yb atoms into the vacuum chamber by irradiating the focused green (532 nm) CW laser[3]. The intensity of $I\sim$ 2.5 kW/cm^2(P=1 W, ω = 5 μm) is strong enough. This method enables us to recover the efficiency of the Zeeman slower system without opening the vacuum chamber.

[2]To overcome this problem, the so-called zero-crossing configuration is available.
[3]We can also use the green (532 nm) pulsed laser.

2.2.2 MOT

Atoms slowed by the Zeeman slower system are trapped in a magneto-optical trap (MOT). A MOT consists with three pairs of two circularly polarized couterpropagating lasers and the quadrupole magnetic field. We use the narrow ${}^1S_0 \leftrightarrow {}^3P_1$ transition for a MOT (λ = 556 nm, $\Gamma/2\pi$ = 181 kHz) whose saturation intensity $I_{\rm sat}$ = 0.14 mW/cm^2 and the Doppler limit temperature T_D =4.4 μK (see Table 2.3).

When we load ^{174}Yb atoms in a MOT, detuning and intensity of MOT beams are -1.3 MHz ($-7 \times \Gamma/2\pi$) and 45 $I_{\rm sat}$ ($\simeq$ 6 mW/cm^2, P=10 mW and ω_0 = 1 cm), respectively. The MOT magnetic field gradient is 1.3 G/cm for x and y direction (2.6 G/cm for z direction). After about 10 s loading, we can typically collect 2×10^7 atoms in a MOT.

In order to increase atomic density, to realize better mode matching with a FORT potential and to carry out the additional cooling, a compressed MOT scheme is used. After the loading, the magnetic field gradient is increased to 14 G/cm in 200 ms for x and y direction (28 G/cm for z direction). Then, the intensity of the MOT beam is decreased to 4 $I_{\rm sat}$ for 100 ms to cool atoms. Detuning of the MOT beam is not changed before and after the compressed MOT. As a result, just after the transfer of atoms from a MOT to a FORT, typical number and temperature of atoms are 1×10^6 and 50 μK, respectively.

2.2.3 Evaporative cooling in a FORT

Since Yb atoms in the ground state do not possess electric spins, the magnetic trap can not be used as successfully used in typical BEC experiment of alkali metal atoms. Instead, the optical trap, which is also called a Far Off-Resonance Trap (FORT), is used.

We chose 532 nm as the FORT wavelength for two reasons. One is that, at this wavelength (532 nm), very high power ($\sim$10 W) and stable lasers are now commercially available. The second reason is that the theoretical estimation shows that the trap potential made by tightly focused 532 nm laser is deep enough ($\sim$1 mK) to trap cold Yb atoms in the ground state.

Plain evaporation

Figure 2.4 shows how atoms in a FORT reach thermal equilibrium after the transfer of atoms from a MOT to a FORT. $\eta = U_0/k_{\rm B}T$ is the ratio of the trap depth U_0 and the temperature of atoms in a trap. $k_{\rm B}$ is the Boltzmann constant.

After the cooling due to plain evaporation in a FORT for about 1.5 s, the system reaches thermal equilibrium where cooling due to elastic collisions equilibrate with heating due to inelastic collisions (three body collisions). Under thermal equilibrium, we found $\eta_{\rm eql}$ = 14 for Yb[$^1S_0$] which corresponds to $\gamma = \sigma_{\rm el}/\sigma_{\rm in}$ = 2200 (see section 6.2). Here, $\sigma_{\rm el}$ and $\sigma_{\rm in}$ are the scattering cross section of elastic and inelastic (three body) collisions. In general, the condensation by evaporative cooling is thought to be straightforward if $\gamma > 10^4$ and impossible if $\gamma < 10$ [22]. Thus, γ = 2200 of Yb is not bad for us to realize a BEC by evaporative cooling [7].

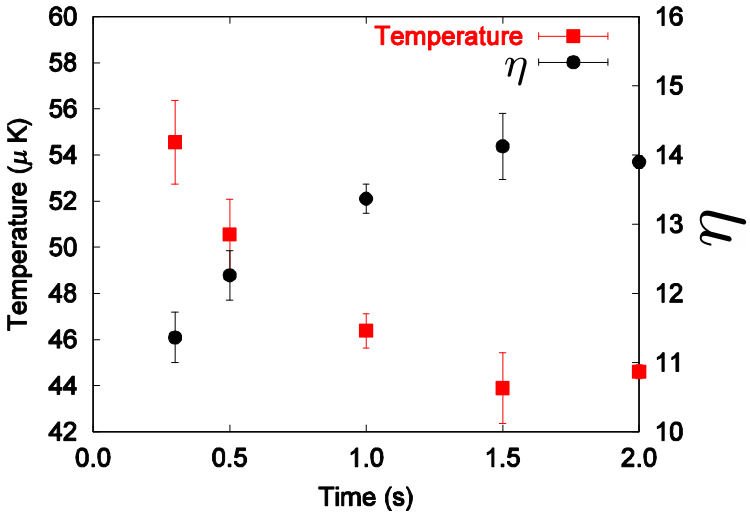

Figure 2.4: Plain evaporation. Temperature of Yb[$^1S_0$] atoms and η in a FORT are plotted as a function of holding time. After the transfer of atoms from a MOT to a FORT, atoms are cooled by plain evaporation in 1.5 s and then the system reaches thermal equilibrium.

Trap lifetime of atoms in a FORT

Figure 2.5 shows the typical trap lifetime of atoms in a single FORT. Trap depth is about 700 μK and the temperature of atoms is about 50 μK. Non-exponential trap loss up to 1 s is the three body inelastic trap loss due to the high atomic density just after the transfer of atoms. The solid line is a fit of the data after 1 s by an exponential function. A trap lifetime determined by one body collisions (collisions between Yb and a background gas) is 15 s.

Forced evaporation in a crossed FORT

In order to realize a BEC, increasing an atomic number density is crucial. To this end, we use a crossed FORT configuration. One of two FORT beams enters the MOT region along the horizontal direction (perpendicular to the gravity) and the other along the vertical direction (parallel to the gravity).

First, trap depth of the horizontal and vertical FORT is about 700 μK and 10 μK, respectively. Thus atoms are trapped mainly in the horizontal FORT at the beginning. As we decrease the trap depth of the horizontal FORT in order to induce forced evaporative cooling, atoms gather in the crossed region through elastic collisions. At the same time, their phase space density increases. Finally, a BEC is achieved. During forced evaporative cooling for 6 s, trap depth of the vertical FORT is kept constant at 10 μK.

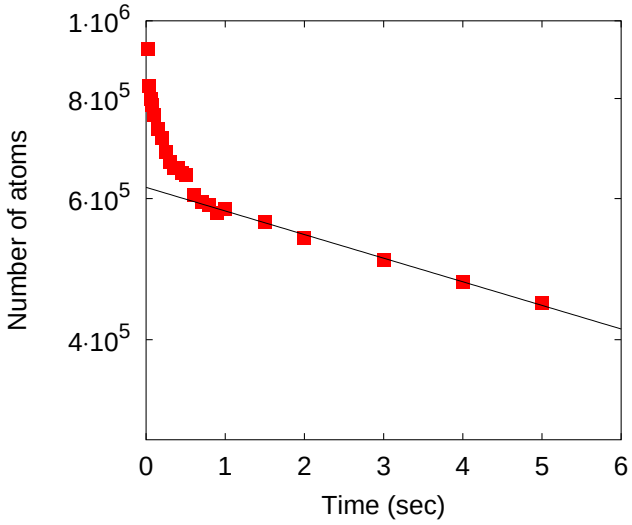

Figure 2.5: Trap lifetime of atoms in a single FORT. Trap potential is about 700 μK and the temperature of atoms is about 50 μK. After the inelastic loss due to the three body collisions up to 1 s, one body collisions govern the trap lifetime. The solid line is a result of a fit by an exponential function. One body decay time is measured to be 15 s.

Technical issues

In a crossed FORT configuration, two tightly focused FORT beams must be perfectly crossed at the trap region. However, there is instability of pointing of the FORT beam due to a heating effect by RF power at an AOM. AOMs are used to control the FORT power. In order to get rid of this instability, we put a copper plate under the AOM and flow water inside it. Temperature of the water is stabilized at 15°C by a chiller. In addition, we wait for about an hour after starting the time sequence of evaporative cooling to make everything thermally equilibrium.

In addition, since the FORT beam is tightly focused, it is rather difficult to correctly guide in a MOT region. Thus when we first find the FORT beam in a MOT region, we sometimes use the resonant light (399 nm or 556 nm) instead of 532 nm. If the resonant beam hits the MOT, we can easily recognized it in a CCD image on a TV monitor. Then, we put the FORT beam in the same optical path. In addition, since the trap depth of the vertical FORT is shallow, we should use cold atoms (< 10 μK) to align the vertical FORT.

2.2.4 Absorption imaging

Ultracold atoms and a BEC in a vacuum chamber are observed by absorption imaging. The imaging laser which is resonant to the strong transition ${}^1S_0 \leftrightarrow {}^1P_1$ is irradiated to an atomic cloud and then detected by a CCD camera after some imaging optics. The magnification is designed to be 2.25 [45] by using proper achromatizing lenses. Since

atoms absorb the imaging laser, they can be detected as a shadow on a CCD image whose intensity and size have information about the number of atoms and their spatial distribution, respectively.

Number of atoms

The number of atoms N can be derived from a CCD image by using the equation,

$$N = -\frac{tS}{\sigma_{\mathrm{ab}}} \sum_{i,j} \ln \frac{P_{i,j} - D_{i,j}}{F_{i,j} - D_{i,j}}, \tag{2.1}$$

where S is the area of each pixel, t is the magnification ratio of the imaging system, σ_{ab} is the photon scattering cross section. $P_{i,j}$, $F_{i,j}$ and $D_{i,j}$ are the signal intensity on a CCD camera at a pixel (i, j) with atoms (Probe), without atoms (Flat) and without both atoms and probe beam (Dark), respectively. For the closed two-level system, σ_{ab} is given by

$$\sigma_{\mathrm{ab}}(\delta, s) = \frac{3\lambda^2}{2\pi} \left(\frac{1}{1 + (2\delta\tau)^2} \right) \left(\frac{1}{1+s} \right), \tag{2.2}$$

where λ is the wavelength of the transition, δ is the detuning of the probe laser and τ is the lifetime of the excited state[4]. s is the saturation parameter which is defined by

$$s = \frac{I}{I_{\mathrm{sat}}}, \quad I_{\mathrm{sat}} = \frac{h\pi c}{3\tau\lambda^3}, \tag{2.4}$$

where I is the laser intensity, I_{sat} is the saturation intensity and c is the speed of light.

In our experiment, the laser intensity of a probe beam is much lower than the saturation intensity of the ${}^1S_0 \leftrightarrow {}^1P_1$ transition ($I < 0.1\ I_{\mathrm{sat}}$ for $P = 100\ \mu$W and $\omega_0 = 1$ mm) and the detuning is zero due to the frequency locking ($\delta = 0$). As a result, the photon scattering cross section becomes

$$\sigma_{\mathrm{ab}}(0, 0) = \frac{3\lambda^2}{2\pi}. \tag{2.5}$$

Temperature - Time of flight (TOF) technique

Temperature T of atoms can be determined by measuring how fast atomic cloud expands after turning off the trap potential. Assuming that the initial density distribution and the velocity distribution of atoms in a trap can be approximated by the Gaussian function and

[4]Full Width of the Half Maximum (FWHM) of the natural linewidth is given by

$$\delta\omega_{\mathrm{nat}} = \gamma, \quad \delta\nu_{\mathrm{nat}} = \frac{\gamma}{2\pi}, \quad \left(\gamma = \frac{1}{\tau} \right). \tag{2.3}$$

the Maxwell-Boltzmann distribution, respectively, the density distribution after turning off the trap potential is given by

$$n(\mathbf{r},t) = \frac{N}{(2\pi)^{3/2}(\sigma_0^2+\sigma_v^2t^2)^{3/2}} \exp\left[-\frac{r^2}{2(\sigma_0^2+\sigma_v^2t^2)}\right], \quad \sigma_v(T) = \sqrt{\frac{k_{\rm B}T}{m}}, \tag{2.6}$$

where N the number of atoms, σ_0 the initial width of density distribution, $k_{\rm B}$ the Boltzmann constant, and m the atomic mass. In the experiment, we obtain the optical density (OD) which corresponds to the integration of $n(\mathbf{r},t)$ along the propagation direction (z) of the probe laser, that is,

$$\mathrm{OD}(T,t) = \mathrm{OD}_0 \exp\left[-\frac{x^2+y^2}{2\sigma^2(T,t)}\right], \quad \sigma(T,t) = \sqrt{\sigma_0^2+\sigma_v(T)^2t^2}. \tag{2.7}$$

As a result, taking the density distribution at two (or more) different times, t_1 and t_2, σ_v can be determined, i.e., T is given by

$$T = \left(\frac{m}{k_{\rm B}}\right)\frac{\sigma^2(T,t_1)-\sigma^2(T,t_2)}{t_1^2-t_2^2}. \tag{2.8}$$

Typical absorption images for thermal atoms and a BEC are shown in Fig. 2.6.

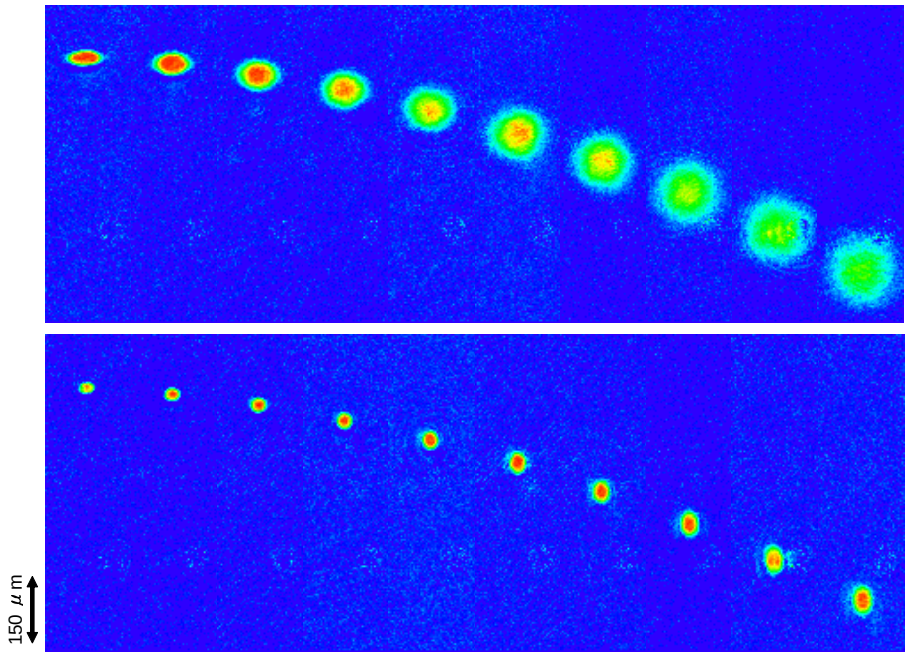

Figure 2.6: Typical TOF images. (Top): Thermal atoms. (Bottom): BEC. TOF time is 1 msec to 10 msec (from left to right) with the interval of 1 msec.

2.3 Vacuum system

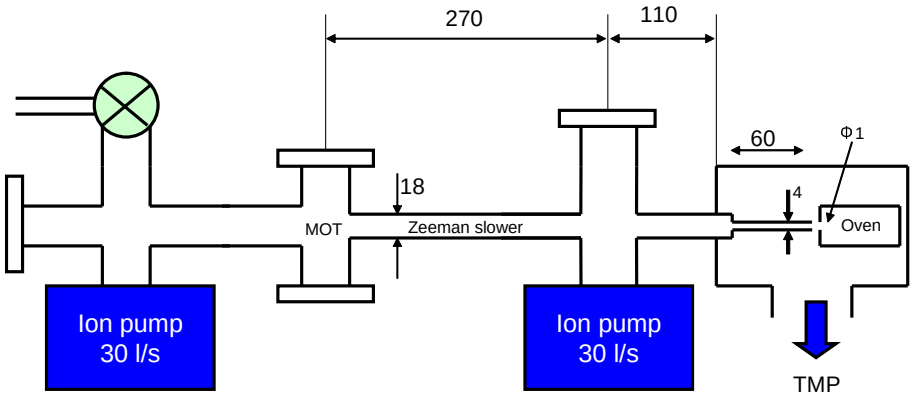

Figure 2.7: Schematics of vacuum systems. Unit: mm.

Our vacuum chamber is schematically shown in Fig. 2.7. Two ion pumps (PST030, ULVAC, 30 l/s) are installed at the beginning of the Zeeman slower and behind the MOT region. In order to keep good vacuum at the MOT region, the differential pumping technique is used. The MOT region is well separated from an atomic oven by a thin pipe (ϕ = 4 mm, l = 6 mm). In addition, vacuum of the oven region is kept by a turbo-molecular pump (TMP).

2.4 Lasers

2.4.1 399 nm ($^1S_0 \leftrightarrow {}^1P_1$)

Zeeman slower laser

The slower beam at 399 nm is obtained by a frequency doubling unit (WAVE TRAIN, Laser Analytical Systems Inc.) which has an LBO crystal (CRYSTECH, CPM, Type-I)[5] inside a bow-tie ring cavity with oxygen flow. Oxygen extends the lifetime of the LBO crystal. The fundamental light is generated by a Ti:sapphire laser (∼1 W at 800 nm, MBR-110, Microlase Optical Systems) which is excited by a green laser (Millennia Xs, Coherent Inc., 532 nm, 10 W). The output power is typically ∼50 mW at 399 nm. About the frequency locking, details will be discussed later in this chapter.

Instead of this SHG system, we also have succeeded in slowing atoms by using a blue laser diode (Nichia Corporation) which is stabilized by the injection locking method. But in this work, we did not use the injection lock system at all.

[5]Crystal parameters: $\theta = 90°$, $\phi = 31.9°$ and Brewster angle θ_B=58.17°, dimension 4×4×12 mm. Details about the SHG cavity are discussed in Appendix B.

Imaging laser

For absorption imaging, we do not need much laser power since the ${}^1S_0 \leftrightarrow {}^1P_1$ transition is strong ($I_{\rm sat} = 57$ mW/cm^2). The frequency of the imaging laser, however, should be stable both in a short term and in a long term. Details about the frequency stabilization are discussed here.

We use a GaN blue laser diode (NLHV500E, Nichia Corporation). By using an external cavity laser diode (ECLD) system [46] with the Littrow configuration, the laser linewidth is narrowed to about 10 MHz. Details about the Littrow configuration will be discussed in the next chapter. For the purpose of absorption imaging of Yb atoms, frequency of the imaging laser is required to be scanned for $\sim$2 GHz without any mode hops to cover all Yb isotopes (see Table 2.2). Figure 2.8 shows fluorescence spectra observed by our imaging laser. Except for ^{168}Yb (natural abundance: 0.13 %), we can clearly identify signals corresponding to all stable isotopes. These spectra are obtained by irradiating the imaging laser with a narrow Yb atomic beam in a reference oven from the orthogonal direction in order to eliminate a Doppler width as much as possible. This atomic beam is used for frequency locking for a long term.

The natural linewidth of the ${}^1S_0 \leftrightarrow {}^1P_1$ transition is $\gamma/2\pi = 29$ MHz. Hence, 10 MHz may be narrow enough. For the stable imaging, however, the narrower linewidth is desirable. In addition, since the imaging laser is also used to stabilize the other external cavity (transfer cavity), further frequency narrowing has been carried out.

To this end, we have constructed the optical feedback system [47, 48, 49] which is schematically shown in Fig. 2.9. We pick up about 10 % of the ECLD output and put it into the additional confocal cavity (Mirrors: LASEROPTIK GmbH, Curvature = 10 cm, $R = 99.5$ %, PZT: NEC Tokin, AER 13.6$\times$10$\times$20$-$D15). Only when the laser frequency is resonant to the confocal cavity, the reflection light can return to the LD and the laser frequency is narrowed due to the additional optical feedback. In such a case, since the laser frequency is drawn to the cavity frequency, the square shape of the transmission spectrum of the confocal cavity is observed when we scan the laser frequency as shown in Fig. 2.10.

In order to lock the laser frequency to the confocal cavity, the length between the ECLD and the confocal cavity is modulated by a PZT-ϕ attached to a mirror in front of the confocal cavity by $f = 40$ kHz. The error signal is obtained by putting the modulated transmission signal of the confocal cavity into a lock-in amplifier and applied to the PZT-ϕ. The PZT-ϕ is also used to adjust the phase of optical feedback. In addition, the distortion of the cavity transmission signal is detected by taking its third-order derivative. This is experimentally realized by taking error signal by a lock-in amplifier with $3f$(= 120 kHz) reference frequency. The $3f$ error signal is applied to the PZT-G inside the ECLD. By simultaneously applying the $1f$ and $3f$ electric feedback, the optical feedback is kept for more than one hour as shown in Fig. 2.12.

Moreover, we stabilize laser frequency to the Yb atomic spectrum for the long term stability. The laser frequency of the present optical feedback system is modulated at 40 kHz. Thus the fluorescence signal which is obtained by irradiating a Yb atomic beam with this modulated light is also modulated at 40 kHz. Since the lifetime of the ${}^1P_1$ state

(5.5 ns) is much shorter than the modulation frequency, we can obtain the error signal by putting the modulated fluorescence signal into a lock-in amplifier as shown in Fig. 2.11. This error signal is applied to the PZT-C at the confocal cavity.

Other candidates

We also construct some laser systems for a more stable and powerful blue laser source. One of the candidates is a waveguide PPLN crystal (NGK Insulators, Ltd.) instead of the present LBO system. Since we do not need the optical cavity, the waveguide PPLN is easy to handle. So far, the larger blue output power than that of the present LBO system has not been stably obtained.

The other candidate is using the MOPA system. We construct an ECLD at 800 nm (Eagleyard) and the output about 20 mW is amplified to about 1 W by a tapered amplifier (Eagleyard). Then it is put into a bow-tie cavity in which the PPKTP nonlinear crystal is installed. This system is now under development in our group and preliminary about 50 mW blue light is obtained.

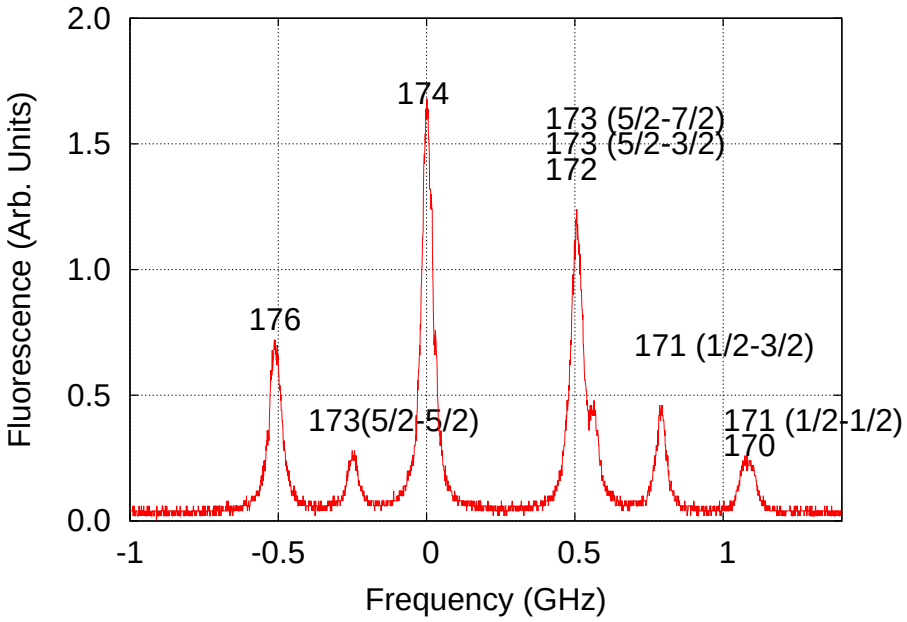

Figure 2.8: Fluorescence signal ($^1S_0 \leftrightarrow {}^1P_1$) obtained by the present imaging laser. Signals corresponding to all isotopes except for ^{168}Yb (natural abundance: 0.13 %) are observed without a mode hopping.

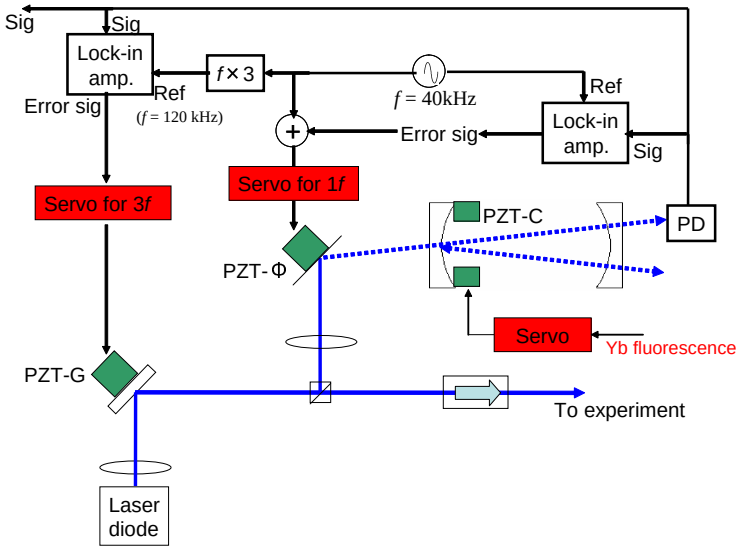

Figure 2.9: Optical feedback system for absorption imaging.

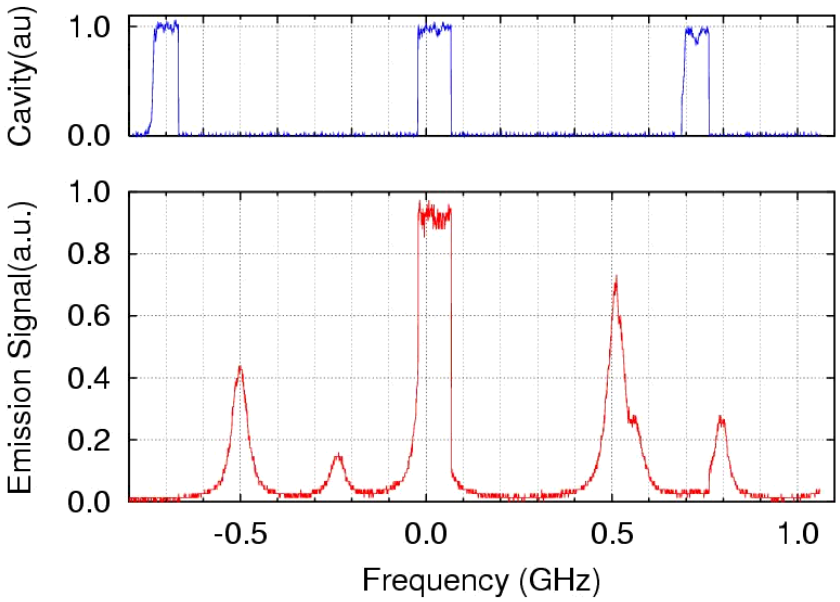

Figure 2.10: Typical transmission signal of the cavity in a optical feedback system. The laser frequency is drawn to the reference cavity because of the optical feedback system which results in a square shape.

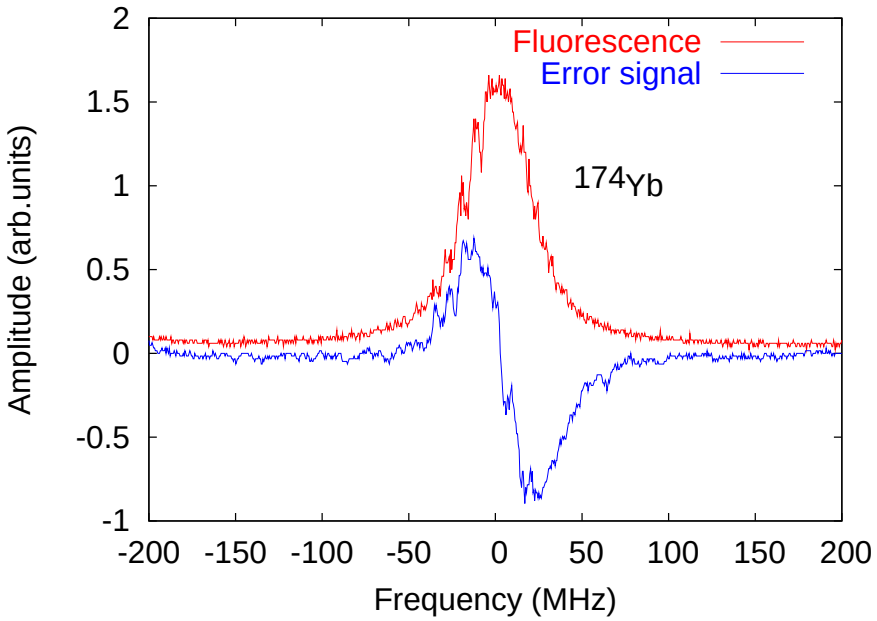

Figure 2.11: Error signal of the atomic spectrum. Since the lifetime of $^1P_1$ state (5.5 ns) is much shorter than the modulation frequency (40 kHz), we can obtain the error signal by using a fluorescence signal.

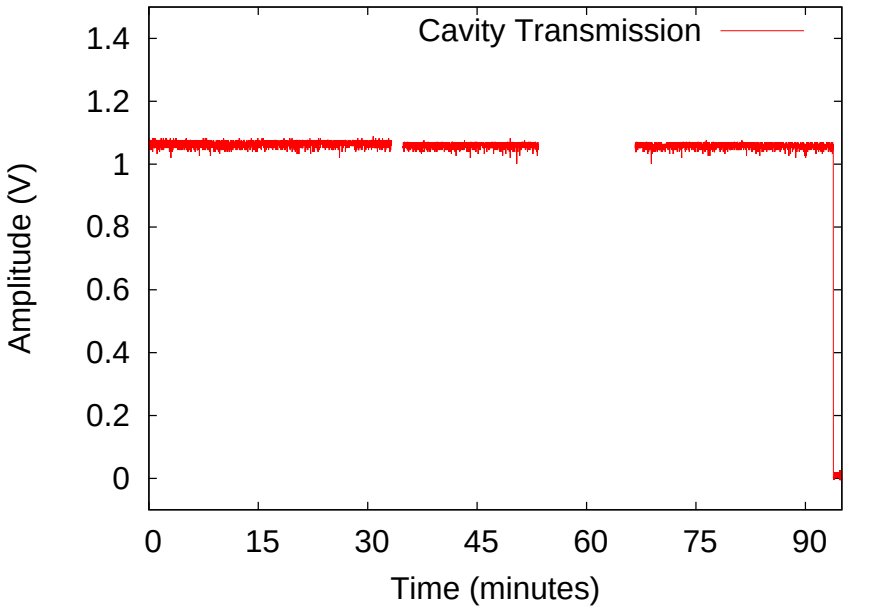

Figure 2.12: Due to simultaneous feedback of $1f$ and $3f$ error signal, the frequency locking survives for more than 90 minutes. Lack of some data is due to a trivial technical problem of data logging.

2.4.2 556 nm ($^1S_0 - ^3P_1$) - MOT

Dye laser

A MOT beam at 556 nm is obtained by a ring dye laser (Coherent 899) excited by Ar ion laser (∼5 W). Rhodamin 560 (Exciton) is used and it is circulated by a circulator (RD1000, Radiant Dyes Laser & Accessories GmbH). This circulator is made of stainless steel (brass free). We found that brass in the circulator system decreases the lifetime of a circulated dye.

Laser frequency should be narrowed below the natural linewidth of the MOT transition ($\gamma/2\pi = 182$ kHz). Frequency of the dye laser is locked to a high finesse ULE (Corning) cavity. The error signal obtained by the Pound-Drever-Hall method [50] is applied both to an EOM inside the ring cavity and to an AOM out side the cavity. The EOM suppresses the fast varying component of the frequency fluctuation [52] and the AOM suppressed the slowly varying part. As a result, the linewidth is suppressed below 100 kHz. The ULE cavity is placed in a vacuum chamber whose temperature is stabilized to reduce the long term drift of the resonance frequency. So far, the frequency drift is suppressed to 70 kHz/s.

Transfer cavity - 556 nm and 800 nm

To stabilize the laser frequency of the Zeeman slower laser for a long term, we use the transfer cavity. First, we stabilize the transfer cavity (RG-91T, Burleigh) to the 556 nm laser which is stabilized to the ULE cavity. Then, the fundamental light of the slower beam at 800 nm is locked to the transfer cavity. As a result, the long term frequency stability of the ULE cavity is transferred to the frequency of the slower beam via the transfer cavity.

Zeeman modulation

At the beginning of this work when we did not have a ULE cavity, we stabilized the frequency to the Yb atomic spectrum by a Zeeman modulation technique. Though the system is now totally replaced by the ULE cavity, the Zeeman modulation technique is briefly introduced here since I developed the system.

For the purpose of the frequency stability of the MOT beam for a long term, we lock the frequency to the atomic spectrum of the $^1S_0 \leftrightarrow ^3P_1$ transition. To make the error signal, the Zeeman modulation method is used. We apply both static B_0 and modulated magnetic field $B_1 \sin \omega_{\mathrm{mod}} t$ (3 kHz) to the Yb atomic beam. These magnetic fields induce the modulated Zeeman shift ΔE on the $|m_J| = 1$ magnetic sublevels of the $^3P_1$ state. Here ΔE is given by

$$\Delta E = m_J \mu_B g (B_0 + B_1 \sin \omega_{\mathrm{mod}} t). \tag{2.9}$$

where g is a g-factor (1.49 for the $^3P_1$ state). As a result, the intensity of the fluorescence detected by a PMT from the atomic beam is also modulated. By putting this signal into a lock-in amplifier, a steep error signal is obtained as shown in Fig. 2.13. The static

magnetic field is used to tune the locking point and to adjust the detuning of the MOT laser.

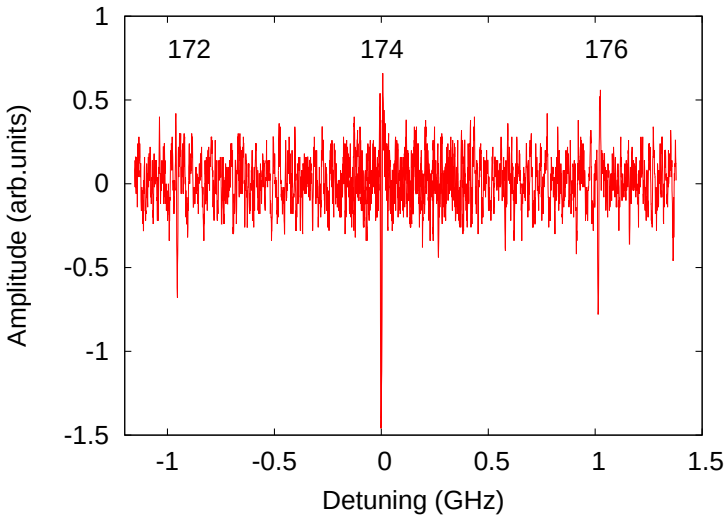

Figure 2.13: Error signals of the ${}^1S_0 \leftrightarrow {}^3P_1$ spectra obtained by the Zeeman modulation method. Three peaks corresponds to isotopes ^{172}Yb, ^{174}Yb and ^{176}Yb.

Fiber laser system

The MOT laser at 556 nm is obtained by a dye laser. In order to use a dye laser, we (students) have to work very hard; we must change dye and clean up the cavity almost every week, use Ar ion laser and so on. Thus, the new laser source at 556 nm which is stable and maintenance-free is strongly desired.

The double wavelength of the MOT laser is 1111.3 nm. This wavelength is close to the wavelength 1.3 μm which is known as zero-dispersion wavelength of the optical fiber. Since the 1.3 μm laser is recently well used in the field of optical broadband communications, many stable commercial lasers around 1 μm are now available. Additionally, we find that a nonlinear crystal LBO can convert 1111.3 nm to 555.6 nm efficiently by a proper ring cavity. Then, we decided to construct a new SHG system.

We use a commercial fiber laser (Koheras or Keopsys) at 1111.3 nm whose linewidth is below 100 kHz. Using this new system, we can obtain more than 400 mW green laser and its frequency locking survives for more than ten hours! In Appendix B, details about this SHG system are described.

2.4.3 404 nm (${}^1S_0 \leftrightarrow {}^3D_2$)

A 404-nm laser is used to excite atoms to the ${}^3P_2$ state via the intermediate ${}^3D_2$ state (see section 6.1). The laser system is completely same as that used in the imaging system

stabilized by the optical feedback technique. The linewidth is narrowed to about 1 MHz for 0.5 s.

For the long term stability, we use the transfer cavity as shown in Fig. 2.14. First, we stabilized the transfer cavity to the imaging laser which is stabilized to the Yb atomic spectrum. Then, the 404 nm laser is stabilized to the transfer cavity. The double passed AOM between the transfer cavity and the optical feedback system is used to tune the laser frequency. In the experiment, we first find the resonance signals using the atomic beam in a reference oven as shown in Fig. 2.15 and then irradiate it with atoms in a trap.

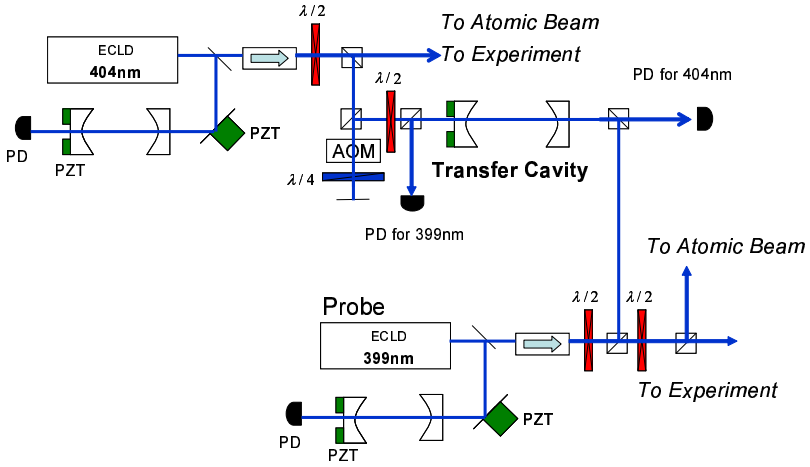

Figure 2.14: Transfer cavity system to stabilize the 404 nm laser for a long term.

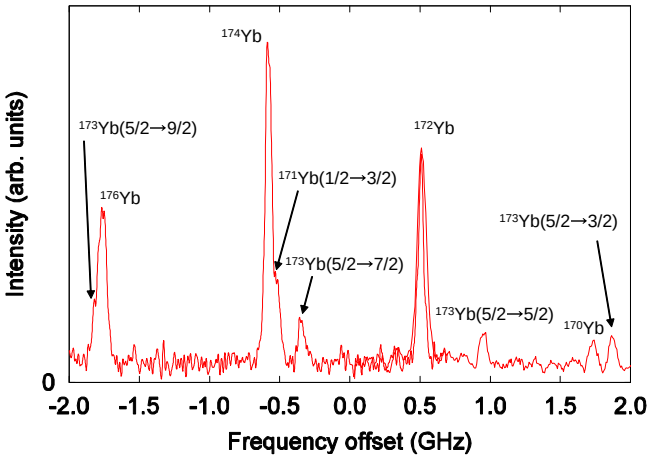

Figure 2.15: The ${}^1S_0 \leftrightarrow {}^3D_2$ spectra obtained by our laser system.

Beam profiler

When we excite atoms in a FORT by the 404 nm laser, its focal point should be coincide with that of the FORT laser (trap region) whose beam waist is 15 μm. To this end, the beam profiler (BP, DataRay Inc., Beam R) is used. We put a glass plate (no coat) in front of the input window of the vacuum chamber and let the partially reflected FORT light go into the BP. BP shows us a radius of the input light. Thus by moving the stage of BP, we can set the BP at the focal point of the FORT laser. Then, at the focal point of the FORT laser, we put the 404 nm laser into the BP and adjust the focal point of 404 nm laser.

2.4.4 770 nm ($^3P_2 - ^3S_1$) and 649 nm ($^3P_0 - ^3S_1$) - Repumping

In this work, repumping lasers at 770 nm ($^3P_2 - ^3S_1$) and 649 nm ($^3P_0 - ^3S_1$) are used to return atoms in the $^3P_2$ state to the ground state where we can apply the absorption imaging.

Both wavelengths are obtained by laser diodes. As for 770 nm, we use the commercial product (6200, New Focus Inc). As for 649 nm (Toptica), we construct the ECLD system in the Littrow configuration.

A laser galvatron of Yb (L2783-70NE-Yb, Hamamatsu Co.) is used for spectroscopy of these two wavelength. In the laser galvatron, the metastable $^3P_2$ and $^3P_0$ states have some population due to strong collisions between hot Yb atoms or recombination of Yb ions. In order to avoid the Doppler broadening, we carry out the saturation spectroscopy. Typical spectra are shown in Fig. 7.5 and Fig. 7.6.

At the beginning of this work, we stabilized both lasers to Yb atomic spectra. But the system was not so stable. We then have constructed a new system as schematically shown in Fig. 2.16. First, the transfer cavity is stabilized to the MOT laser (556 nm) which is stabilized to the ULE cavity. Then, both the 649 nm and the 770 nm lasers are stabilized to the transfer cavity. In order to spatially well separate the 556 nm and 649 nm, a prism is used. Since we lock three colors 556 nm, 649 nm and 770 nm to the same cavity, the mirror reflectivity is reduced to 95 % but is constant from 500 nm to 800 nm (Lattice Electro Optics). The cavity transmissions for all lasers before and after the locking are also shown in Fig. 2.16.

2.4.5 532 nm - FORT

As the FORT lasers, we use two diode-pumped solid state lasers (Verdi-V10, Coherent Inc.). High power fundamental laser at 1064 nm obtained at Nd:YVO_4 crystal is converted to 532 nm by the LBO crystal. The maximum power is 10W.

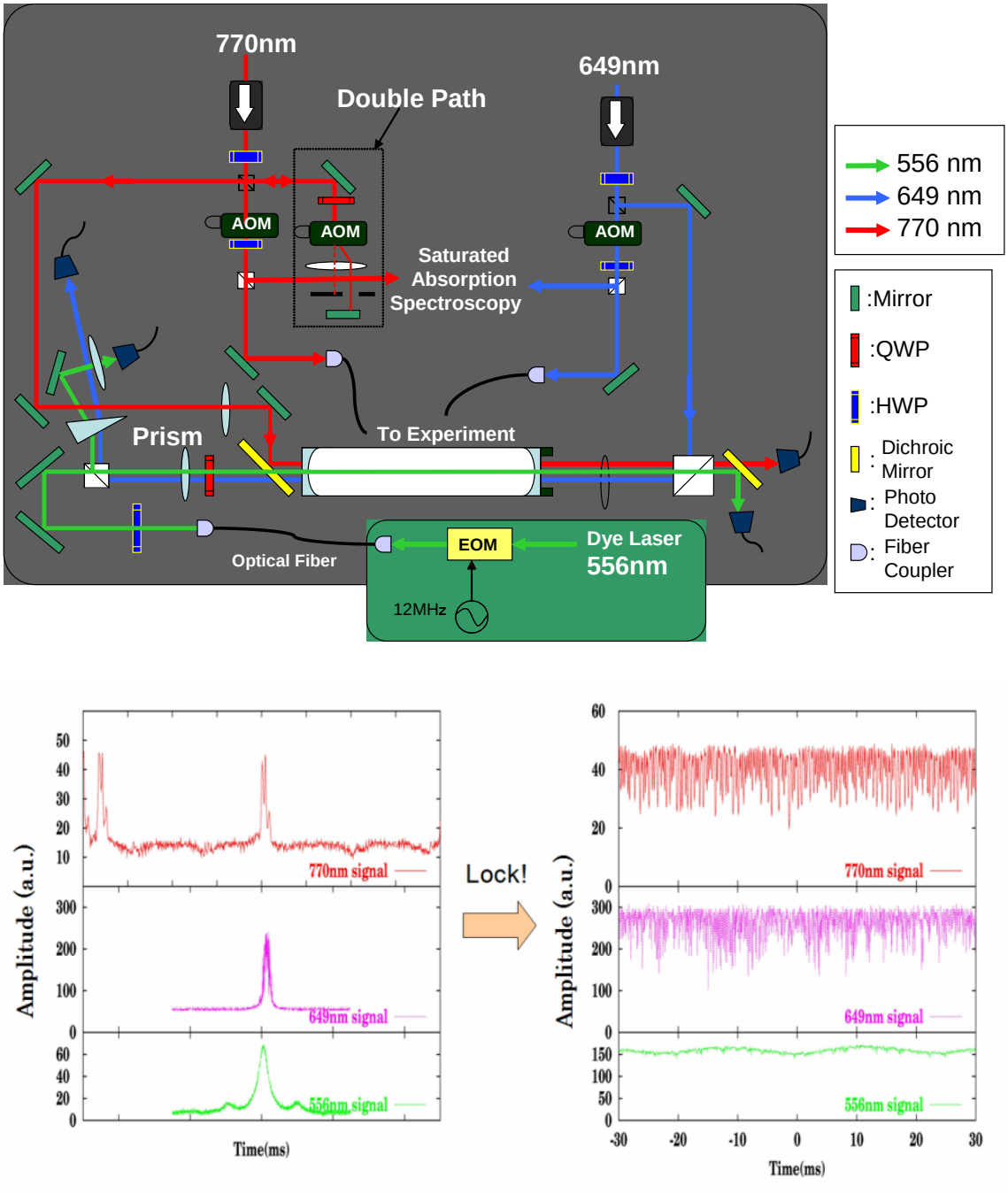

Figure 2.16: Three color lock. The transfer cavity is stabilized to the MOT laser which is stabilized to the ULE. Then, the 649 nm and 770 nm lasers are stabilized to the transfer cavity.

Chapter 3

A diode laser system for spectroscopy of the ultranarrow magnetic quadrupole transition in ytterbium atoms

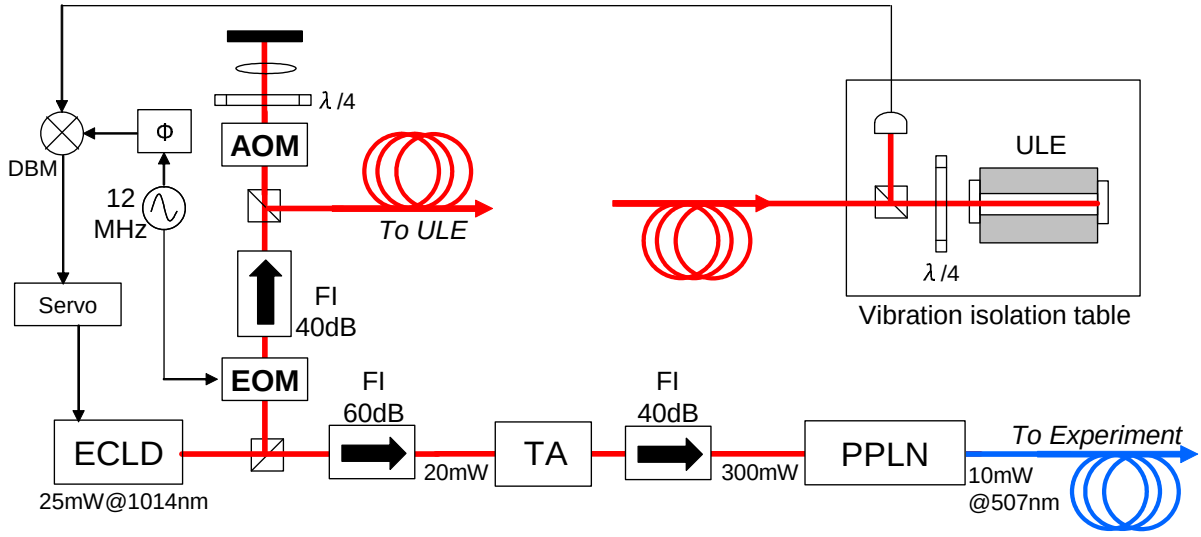

Figure 3.1: Apparatus used for generating the 507-nm narrow-line laser. FI, Faraday isolator; AOM, Acousto-optic modulator; DBM, Double-balanced mixer; ϕ, phase shifter.

In this chapter, we describe the development of a compact diode-laser based system to generate 507-nm laser for the purpose of a spectroscopy of the ${}^1S_0 \leftrightarrow {}^3P_2$ transition in Yb atoms. In previous studies, lasers around 507 nm is produced by, e.g., a frequency doubled Yb:YAG disk laser [53] and frequency doubled single-frequency diode laser [54, 55]. The narrowest linewidth is about 100 kHz [55]. In this study, in order to observe the ultranarrow transition, the laser linewidth has been reduced to less than 1 kHz by tightly

locking it to a high finesse optical cavity. We developed an ultranarrow-linewidth laser system which consists of an extended cavity laser diode (ECLD), a tapered amplifier, and a MgO-doped periodically poled lithium niobate nonlinear crystal (PPLN). In addition, since the transition linewidth of iodine molecules becomes narrowest around 507 nm, our simple and compact system could be a high performance and transportable frequency reference. Toward this application, we also demonstrate laser spectroscopy of iodine molecules over the range of 50 GHz at 507 nm, which is presented in Appendix C.

3.1 External cavity with diffraction grating

Gain-width of recent solitary laser diodes reaches about 100 nm. It is sure that the laser linewidth can be narrowed by putting an external cavity around such laser medium. However, the additional external cavity also produces many longitudinal modes. Thus, if we just put two mirrors in front of and behind the medium, the laser operates with multi-modes. This problem can be overcome by using a dispersive external cavity. The diffraction grating is used to this purpose.

Diffraction grating diffracts incident lights to some discrete directions determined by the so-called grating equation. The direction which satisfies the reflection law to the incident angle is defined as the 0th order diffracted direction. From this angle to outer angle, 1st, 2nd... orders are defined. Usually, we let the first order diffracted light go back to the laser medium, so that the backward facet of an LD and a grating surface construct the external cavity. The direction of the 1st order light strongly depends on the laser wavelength. As a result, many longitudinal modes caused by the external cavity could be suppressed to the desired one (sometimes a few modes). This results in the single-mode operation of the LD. In such a configuration, the 0th order diffraction is used as an output coupler.

For now, as for the external cavity which consists of mirrors and diffraction gratings, two configurations are well used, that is, Littman and Littrow configurations. Both methods have advantages and disadvantages. In the next section, I will discuss them.

3.1.1 Littman vs Littrow

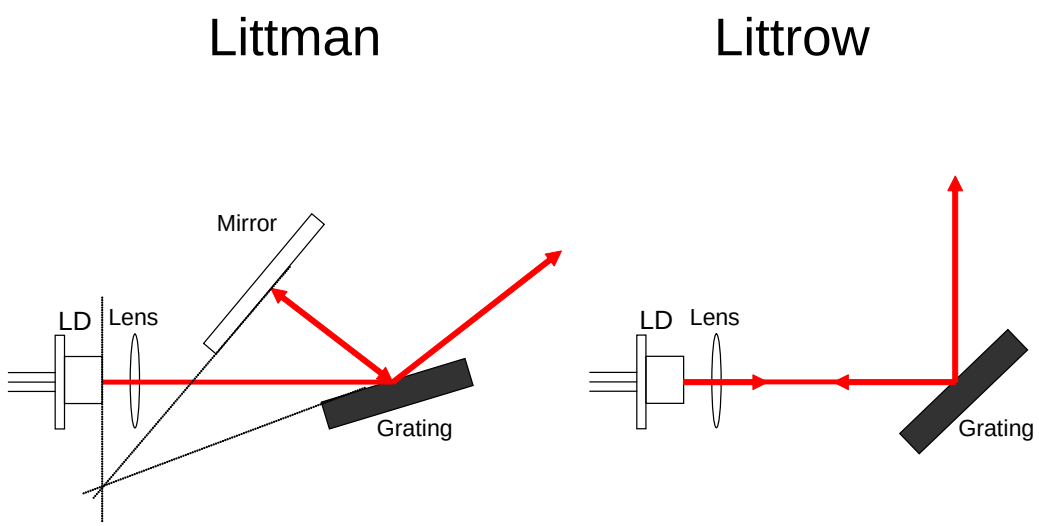

Figure 3.2: Littman and Littrow configurations

Littrow configuration

In the Littrow configuration, the 1st order diffracted light returns to the LD and 0th order direction is used as an output coupler. In this configuration, the backside facet of an LD and the diffraction grating surface make the external cavity (I assume that the front facet of an LD is AR coated). In order to change the laser wavelength, we should move the grating back and forth by a PZT element attached to the grating.

The advantage of this method is that we can expect a strong feedback because we use the diffraction grating once whereas Littman configuration uses twice. Strong feedback may contribute to the frequency narrowing. Sometimes this feedback is too strong. Since strong feedback may damage the LD chip, we have to be careful when we choose the grating [56]. The other advantage is that we can easily make this system and make it compact. Thermal stability is one of the key point of the stable LD oscillation. If the system is compact, controlling the temperature becomes easier.

On the other hand, disadvantages also exist in the Littrow configuration. One of them is the change of the output direction which results from tuning of the laser wavelength. When we rotate the grating to change the wavelength, the 0th order direction is also rotated together. This change is negligibly small for usual experiments. However, it may be a big problem for long optical path without an optical fiber, position-sensitive experiment and so on. The other disadvantage is that sometimes the selectivity of longitudinal modes by grating is not good enough for a stable and widely tunable single-mode operation. To avoid this problem, you can put a thin etalon between an LD and a grating to suppress residual longitudinal modes. This is, however, not common because additional optics are

not desirable. Instead the common method is to use a non-AR coated LD. In this case, the front facet and back facet of the LD play a same role as a thin etalon.

Littman configuration

Unlike the Littrow configuration, 1st order diffracted light goes to the additional tuning mirror in the Littman configuration. It returns to the grating and the 1st order diffracted light goes back to the LD. Hence, the LD back facet and an additional mirror construct the external cavity.

One of the advantages of the Littman configuration is its small frequency passband. In this configuration, we can select an arbitrary incident angle to the grating. Hence, we can choose a grazing incidence to use as many grooves on the grating as possible. Since the optical passband of grating is determined by how many grooves are interacted with the incident light, using a wide area of the grating surface is desirable. In addition, the grating surface is used twice in one round trip. Thus, this effect becomes doubled. Usually, in the Littman configuration, the frequency passband is small enough for an LD to operate in a single-mode and be tuned for a wide area of wavelength without any other additional optics. The other advantage is that output direction does not change at all when we tune its wavelength. In the Littman configuration, the cavity length can be changed by moving not the grating but the tuning mirror. Hence the 0th order direction doesn't change at all.

Additionally, Littman found the special configuration which enables us to simultaneously change the cavity length and the angle of the tuning mirror without breaking the grating equation [57]. The principle is as follows.

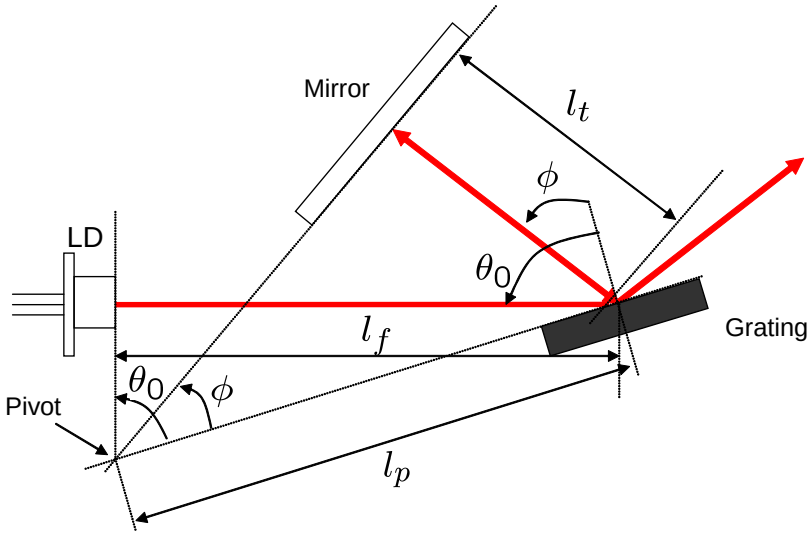

Figure 3.3: Littman configuration

Figure 3.3 is the Littman configuration. The point at which three lines – grating surface, tuning mirror surface and back facet of LD – are crossed is called a pivot point.

In this configuration, as long as you rotate the tuning mirror around the pivot point, laser frequency never experiences the mode hops, so that extremely wide tuning range could be realized in principle. The reason can be explained as the following.

Two equations must be satisfied in this configuration.

$$L = \frac{\lambda}{2}N \tag{3.1}$$

$$\lambda = \frac{d}{m}(\sin\theta_0 + \sin\phi), \tag{3.2}$$

where L is the cavity length, N is a positive integer, λ is the laser wavelength, d is groove spacing, m is the diffraction order, and θ_0 and ϕ are incident and diffracted angle, respectively. (3.1) is the ordinary equation which determines the longitudinal modes. (3.2) is known as the grating equation. As illustrated in Fig. 3.3,

$$L = l_f + l_p \sin\phi. \tag{3.3}$$

By substituting (3.3) to (3.1), the following equations are obtained.

$$\lambda = \frac{2}{N}(l_f + l_p \sin\phi) \tag{3.4}$$

$$\lambda = \frac{d}{m}(\sin\theta_0 + \sin\phi). \tag{3.5}$$

Here, when we scan the wavelength, variables are only λ and ϕ and all of the other parameters (l_f, l_p, θ_0, d, N, and m) are constant. If these constants satisfy the following two equations

$$l_p = \frac{Nd}{2m}, \tag{3.6}$$

$$l_f = \frac{Nd}{2m}\sin\theta_0, \tag{3.7}$$

then both (3.4) and (3.5) are always satisfied for arbitrary λ and ϕ. Hence, we can tune the laser wavelength continuously by changing ϕ without any mode hops.

The disadvantage of the Littman configuration is the complexity of the system. We have to put an additional tuning mirror and properly arrange every element which can define the correct pivot point.

We chose the Littman configuration for two reasons. First, we planned to use a tapered amplifier which is very sensitive to the input direction of the seed laser. We considered that change of the output direction in the Littrow configuration may be crucial. In our different work, however, we have succeeded in using a TA with ECLD in the Littrow configuration. Thus, in practice, both configurations can be used. Second, we want to narrow the laser linewidth as much as possible by the ECLD. Then the Littman configuration is better as discussed above.

3.1.2 ECLD at 1014 nm - Littman configuration

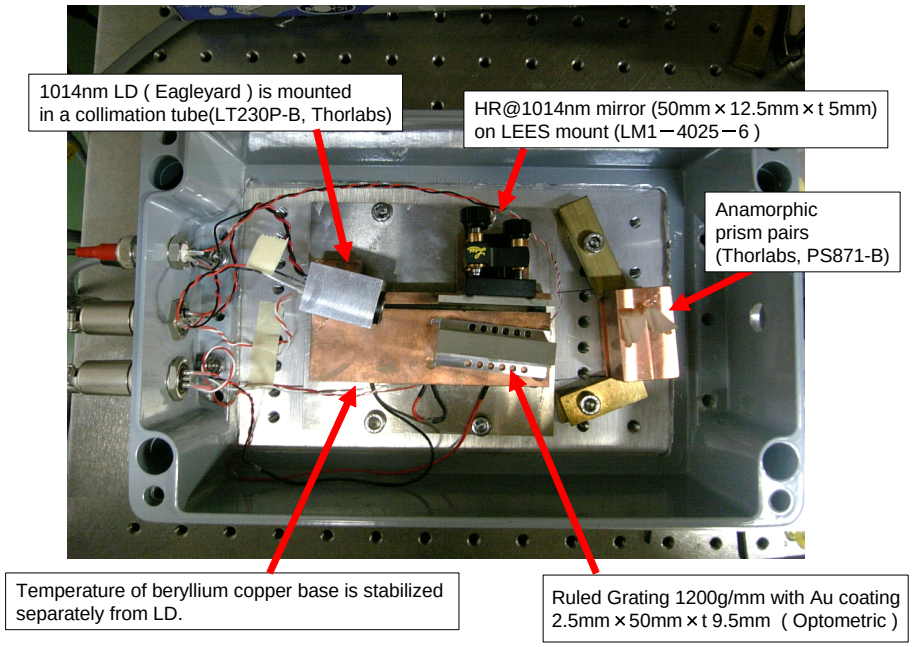

Figure 3.4: Picture of the developed ECLD system in the Littman configuration. Laser diode is stabilized by the external cavity which consists of a diffraction grating and a mirror.

Figure 3.4 is a picture of our ECLD system. We first constructed an ECLD system at 1014 nm in the Littman configuration. The laser source is a ridge waveguide GaAs semiconductor laser diode (Eagleyard Photonics, EYP-RWE-1060-10020-0750-SOT01-0000). Due to the anti-reflection coating, the tuning range expands from 960 nm to 1080 nm. The laser diode is installed in a aluminum mount. The polarization is TE mode. The output beam is collimated by an aspheric lens ($f = 4.5$ mm, Thorlabs, C230TM-B) which is also installed in an aluminum mount with a Teflon tape so that the screw of the lens mount can be stably installed.

About 15 % of the diode output is diffracted by a grating with Au coating (Optometrics, 1200 grooves/mm) and retroreflected by a mirror (LASEROPTIK GmbH, □50 mm×12.5 mm×t5 mm). A laser (linear) polarization is parallel to the graves of the diffraction grating. The mirror is glued to a stable "LEES" mirror mount (LINOS Photonics, LM1-4025-6). As a result, a 12 cm-long extended cavity is constructed. A total feedback to the laser diode is only 2 %, which is smaller than the typical feedback rate ($\sim 60\%$) in a usual ECLD system. The reason is that the AR-coated Eagleyard LD chip seems to be easily damaged by the optical feedback [56]. The position of the mirror determines the laser frequency. It can be tuned by a PZT actuator placed in a leaf spring on which the mirror is mounted. The supporting point of the leaf spring corresponds in position to the pivot point of the Littman configuration. The distorted beam shape of the laser

diode is shaped by a pair of anamorphic prisms (Thorlabs, PS871-B). Thus, we can scan the frequency over more than 30 GHz without mode hopping. The linewidth is reduced to a few hundred kilohertz.

Since the cavity length is relatively long in the Littman configuration, temperature stability of all components is crucial. The temperature of a laser diode and a base of the ECLD system is separately stabilized at the same temperature by Peltier elements (Melcor) and temperature controller (Thorlabs, TED200) [58]. In addition, beryllium copper (CuBe) alloy was chosen for the material of the base because CuBe has a good thermal conductivity, good elastic modulus (for a leaf spring), and a small rate of thermal expansion. In Fig. 3.5, the main properties of CuBe are compared to those of phosphor bronze and aluminum. We can make the elastic modulus of CuBe better by annealing, though we did not carry out. Note that since the powder of CuBe may be harmful to our health, we have to pay careful attention when we fabricate it. After fabrication, metallic plating of CuBe may be desirable to safely handle it in the experiment.

Material	Longitudinal elastic modulus (縦弾性係数)	Thermal conductivity (熱伝導率)	Rate of thermal expansion (熱膨張率)
Beryllium copper (ベリリウム銅)	127.5	0.56	18
Phosphor bronze (リン青銅)	98.1	0.13	16.8
Aluminum (アルミニウム)	70	0.57	23.5
	kN/mm^2	cal/cm・sec・℃	10^{-6}/℃

Figure 3.5: Basic parameters of CuBe are compared to those of Cu and Al which are commonly used as a base of the ECLD system.

3.2 Tapered amplifier

Adaptor and mount

Since the 20 mW diode output is too weak to generate enough power at 507 nm by using the PPLN nonlinear crystal, we use a tapered amplifier (m2k-laser GmbH, TA_1030_1000). Its polarization is TE mode. Thus the polarization of the seed light should be parallel to the epi-layer (the wing of the TA chip) as shown in Fig. 3.6(Left). We use a half wave plate to precisely tune the polarization. We put a 60 dB optical isolator (Isowave,

I−98−SD−5) between the ECLD and the TA to protect the ECLD from the backward emission of the TA.

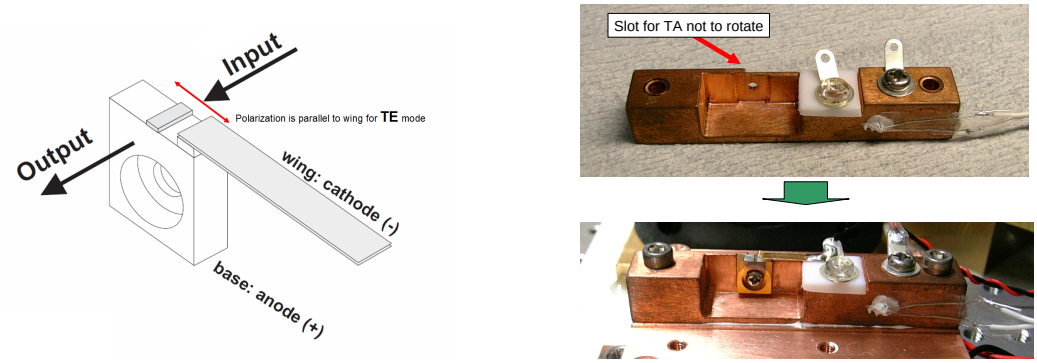

Figure 3.6: (Left): Input and output direction of the C-mount type tapered amplifier. (Right): The adaptor for a TA chip developed in this work.

We first developed a TA adaptor as shown in Fig. 3.6(Right). Our TA adaptor is made of Cu and its temperature is detected by a thermistor. The anode and cathode parts are separated by an insulator (Teflon).

Next we constructed a mount for the TA adaptor, an input coupler and an output coupler. One of the important points to operate a TA chip is the stability of the position of the lens mount of the input coupler. Since the aperture size of a TA chip is 2 μm in height and 4 μm in width, small position shift of the input lens due to, for example, the thermal expansion of the mount is sometimes crucial. We found that this problem can be overcome by putting all elements on a same plate as shown in Fig. 3.7. To make the system stable, we got rid of adjustment parts as much as possible and we fixed all movable parts by epoxy after adjustment. Thus, finally, all components are completely fixed to the mount.

The seed light and output amplified light are collimated by aspheric lenses whose effective focal length are f=4.5 mm (Thorlabs, C230TM-B) and f = 2.8 mm (Thorlabs, C390TM-B), respectively. We use two LEES stable mirror mounts to adjust the input. As a result of these efforts, the seed laser has been coupled to the TA chip for more than one month without any adjustment.

We also constructed a current controller for the TA based on [56]. The current driver module whose maximum current is 2.5 A (Thorlabs, LD3000) is controlled by the additional circuit. With the operating current of 2.5 A and the seed power of 20 mW, the tapered amplifier provides 600 mW at 1014 nm (Fig. 3.8).

Alignment of the seed light

When a large current is applied to a TA chip, breaking the input coupling of the seed light may damage the TA chip. We should carry out the alignment with low operating current (500 mA $\sim$ 1 A). Also note that the output beam shape of the TA chip strongly

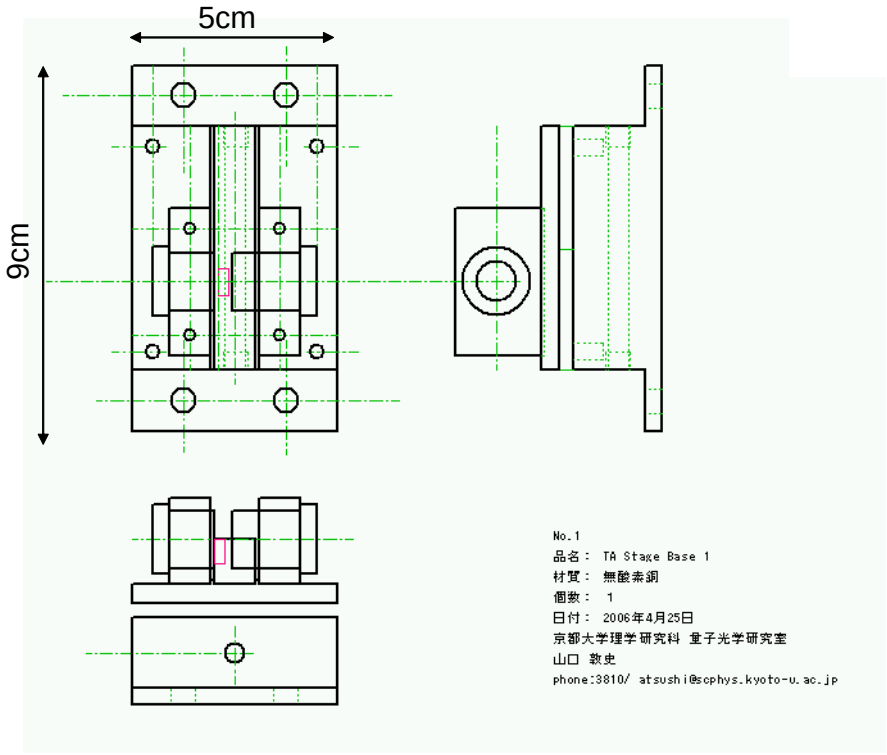

Figure 3.7: Design of the TA mount. The key point is putting all elements on one plane.

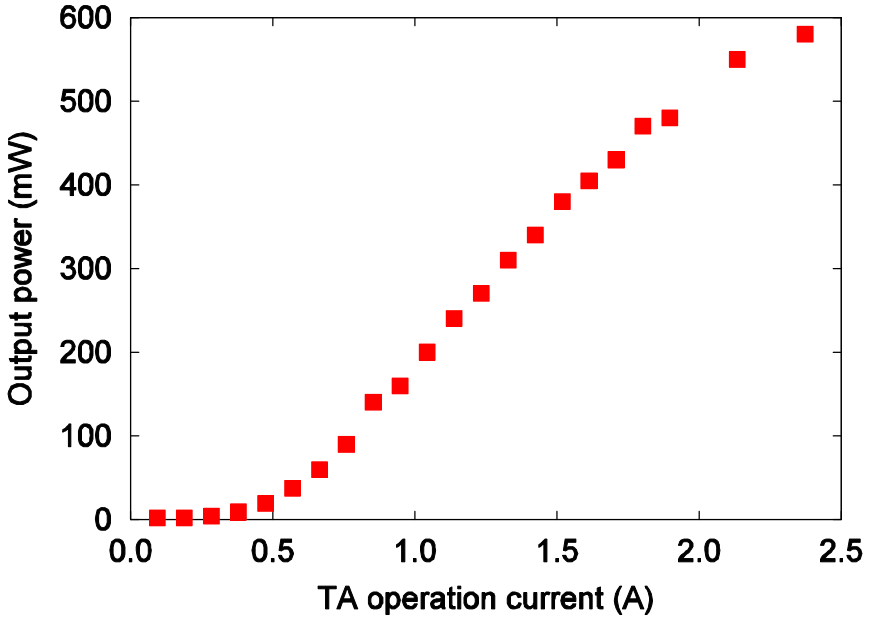

Figure 3.8: Amplified power at a tapered amplifier with 20 mW seed light as a function of the TA operating current.

depends on the operating current. As a result, when one makes an optical path using a TA output, one should operate the TA current at the value you want to use (not the low current).

The followings are the method to align a seed light to a TA chip obtained from our trial and error.

1. Tune the xy (normal plane to the input laser) position of the input coupler lens for a TA backward emission to locate at the center of the input coupler.

2. Tune the input coupler focus by seeing a far side image of TA backward emission.

3. Tune two coupling mirrors to make the optical path of the seed laser to correspond to the TA backward emission.

4. Tune coupling mirrors by seeing the amplified laser power.

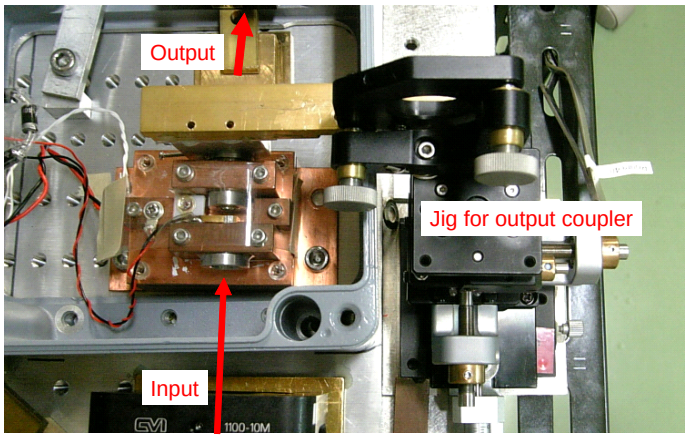

Figure 3.9: By using a handmade jig, the output coupler of the TA system was carefully adjusted by observing the amplified beam shape.

Beam shaping

A beam divergence of TA output along the horizontal axis is different from that along the vertical axis. Basically, we first collimate the horizontal axis by the output coupler and then collimate the vertical axis by using cylindrical lenses. However, we observed a interference pattern in the collimated beam. As a result, in order to obtain the proper beam radius and good beam shape, we needed several optics as shown in Fig. 3.10. More investigations will be required to understand the mechanism of this interference pattern.

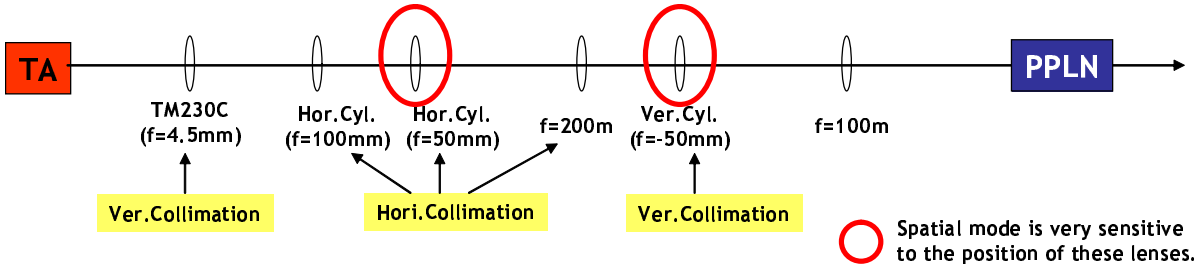

Figure 3.10: Several convex lenses and cylindrical lenses were required to make the beam shape of amplified light clean.

3.3 PPLN crystal

By using the SHG (Second Harmonic Generation) technique, we obtained 507-nm laser light. We use a bulk PPLN – Periodically Poled (MgO doped Congruent) Lithium Niobate – crystal (HC Photonics) which converts the wavelength of 1014 nm to 507 nm. The quasi phase matching (QPM) period of our PPLN crystal is 5.97 μm and QPM temperature is about 40 °C. The dimension is 50×3×0.5 mm (see Fig. 3.11) and both input and output facets are AR coated both for 1014 nm and 507 nm.

We developed a crystal oven as shown in Fig. 3.11. Since the conversion efficiency strongly depends on the crystal temperature, we have to uniformly heat the crystal. Hence, the oven is made by Cu and covers whole crystal (top cover is not shown in Fig. 3.11). Additionally, the oven is covered by thermal insulators (foamed polypropylene) and its temperature is controlled by Peltier elements.

After the 40 dB optical isolator (Isowave, I−98T−5−H) which protects the TA chip from the back scattering at the PPLN input surface, we put the fundamental light (1014 nm) into the crystal. Since the polarization must be vertical, we adjust the polarization by using a half wave plate in front of the PPLN crystal. In addition, we have to make the Rayleigh length[1] long enough to cover the crystal length 5 cm. Present parameters in our system are the followings: beam waist w_0 = 86 μm, the Rayleigh length z_R=2.3 cm, and the beam radius at the surface of PPLN = 86 μm. According to the data sheet provided by the company, the average conversion efficiency is expected to be 2.6 % W^{-1} cm^{-1}, i.e., 13 % W^{-1} for our 5 cm crystal. However, so far, we have realized only 3 %. The reason of such a bad conversion efficiency has not been clear yet. Bad spatial mode of TA output may be one of the reasons. Investigations are in progress.

[1]Rayleigh length z_R is given by

$$z_R = \frac{\pi w_0^2}{\lambda}, \tag{3.8}$$

where w_0 is the beam waist, λ is the wavelength.

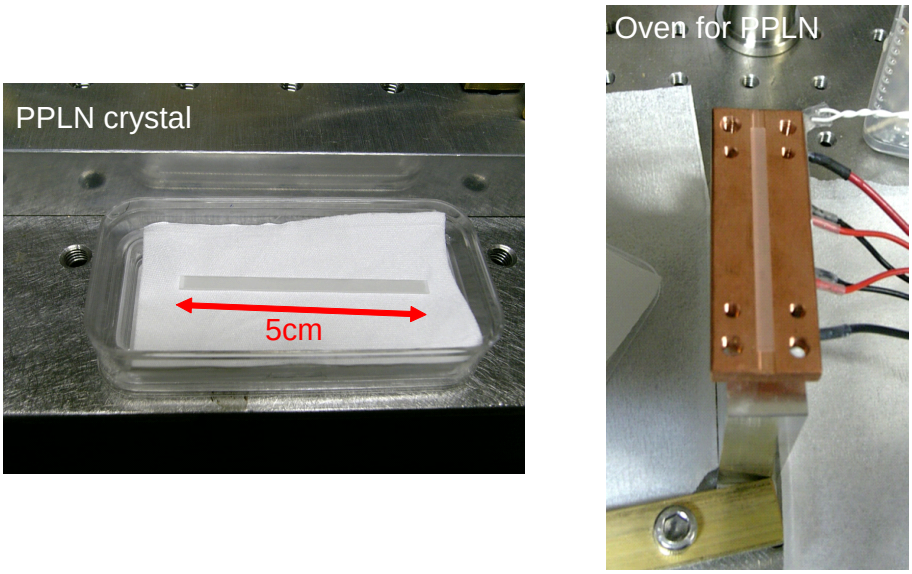

Figure 3.11: (Left) PPLN crystal used in the developed system. (Right): Developed oven to stabilize the temperature of the PPLN crystal at phase matching temperature.

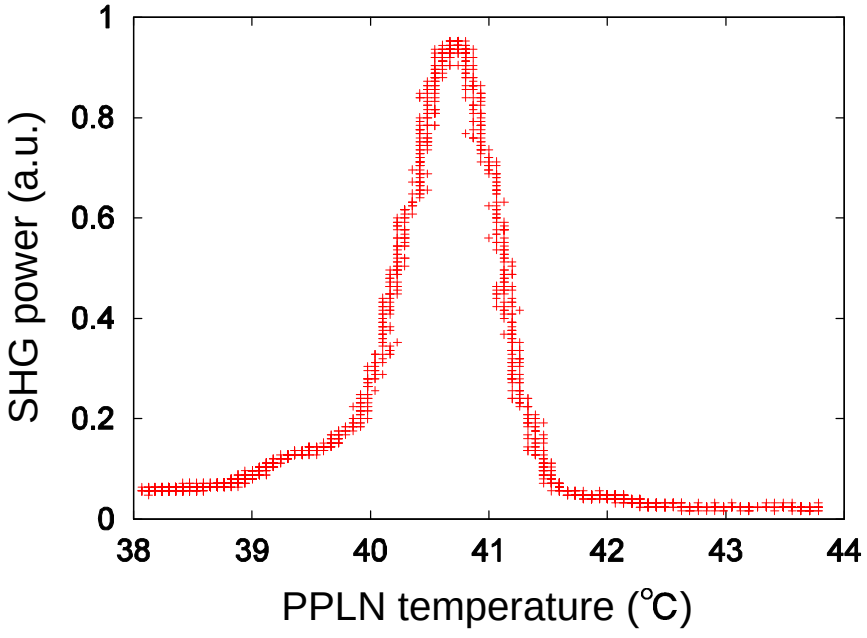

Figure 3.12: Dependence of output power of SHG on the PPLN temperature.

3.4 ULE cavity

To achieve further reduction of the laser linewidth, we lock the laser to a high-finesse Fabry-Pérot cavity by the Pound-Drever-Hall technique [50]. To this end, a small part of the diode output (< 1 mW) is phase modulated by an electro-optic modulator (EOM) driven at 12 MHz and sent to the cavity. The finesse and the free spectral range (FSR) is 50 000 and 1.5 GHz, respectively, at 1014 nm. The electric feedback is applied to the laser current through a servo circuit whose gain bandwidth expands over 3 MHz. As a result, the laser linewidth is reduced to less than 1 kHz which is estimated by the residual width of the error signal after the frequency locking.

In order to isolate the cavity from the environmental noise such as thermal and acoustic fluctuations, the cavity spacer is made of an ultra-low expansion (ULE) glass (Corning) and placed in a vacuum chamber whose vacuum is kept below 10^{-8} Torr by an ion pump (Varian, StarCell, 20 l/s). Figure 3.14 shows how to enclose the high-finesse cavity in a vacuum chamber. The cavity is supported by two viton O-rings at Airy points (see Fig. 3.14) at which we can support the cavity so that the both input side and output side can be maximally parallel to each other. Moreover, in the vacuum chamber, the cavity is doubly covered with copper plates coated with Au in order to achieve a uniform heating by black body radiation. The temperature of the vacuum chamber is also stabilized by Peltier units almost at the zero-expansion temperature of the ULE glass through the copper plate placed at the bottom of the chamber. The vacuum chamber is covered with thermal insulators (foamed polypropylene) in order to thermally isolate it from the environment. As a result, the long-term drift is reduced to 0.4 Hz/s at 507 nm measured by the ${}^1S_0 \leftrightarrow {}^3P_2(m = 0)$ transition in ^{174}Yb (see Fig. 3.13). Furthermore, by placing the cavity on a bench top vibration isolation platform (Minus K Technology, 350BM-1), we isolate the cavity from the floor vibration at frequencies above 0.5 Hz. The double-passed acousto-optic modulator (AOM) between the EOM and the cavity is used to tune the laser frequency. In order to cover all of the FSR (=1.5 GHz) of the cavity, we use a combination of 350 MHz and 190 MHz modulators. After the frequency locking, the laser frequency is scanned by changing the RF frequency applied to AOMs.

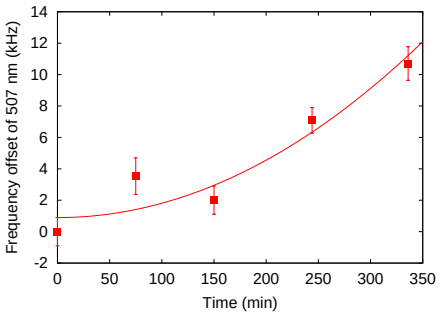

Figure 3.13: Stability of the ULE cavity was measured as the shift of the resonance frequency of the ${}^1S_0 \leftrightarrow {}^3P_2(m = 0)$ transition in Yb.

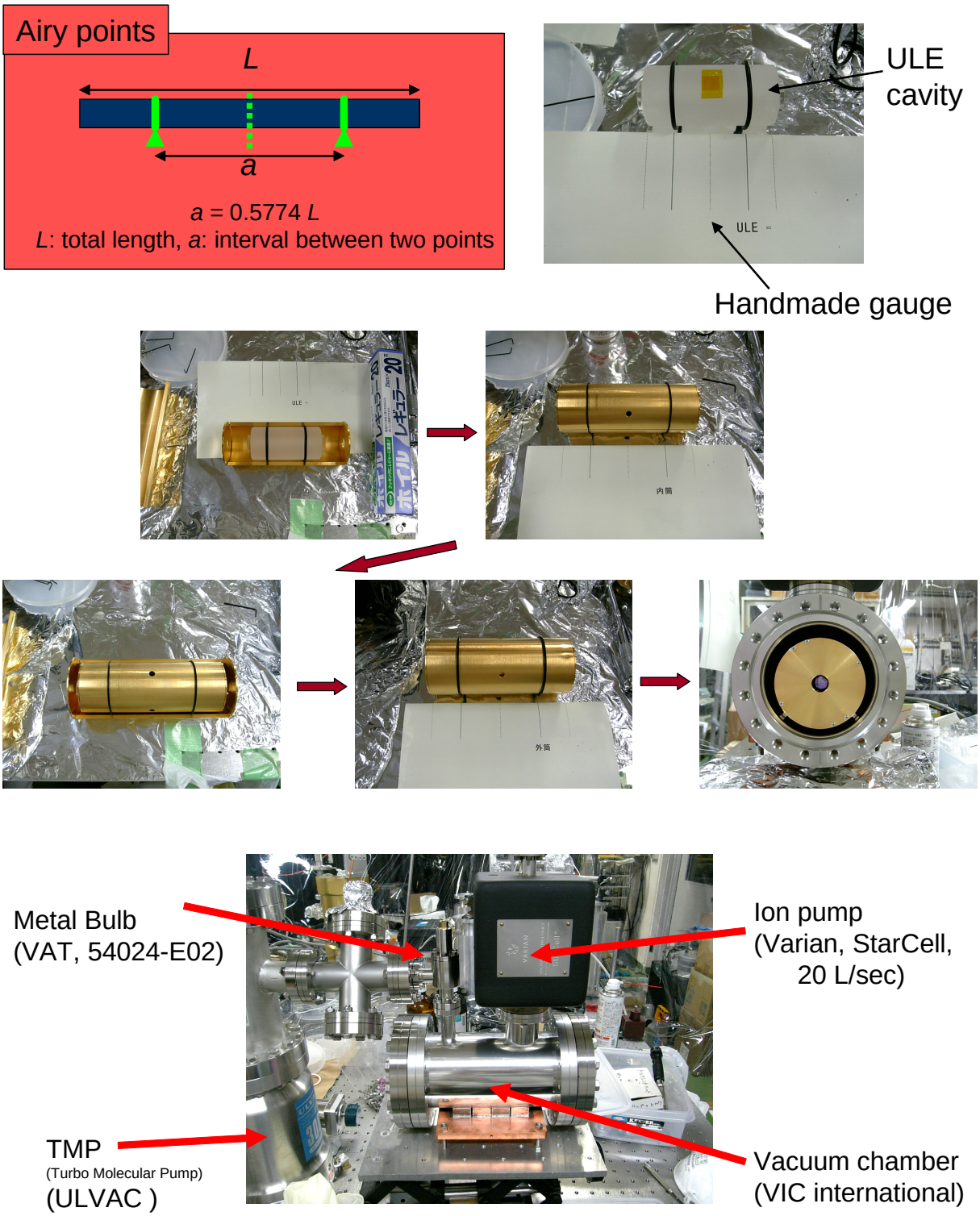

Figure 3.14: How to install a ULE cavity in a vacuum chamber.

Chapter 4

Optical excitations

In this chapter, theories of optical excitations are described. First, we introduce the multipole expansion of an electromagnetic field and then see how each terms induce multipole transitions in atoms. Calculations of transition matrix elements of atoms interacting with a laser field yield selection rules. We derive the selection rules of the electric dipole (E1), electric quadrupole (E2), magnetic dipole (M1) and magnetic quadrupole (M2) transitions, all of which play a key role in this work except for the M1 transition [51].

4.1 Multipole expansion of an electromagnetic field

Basic algebras

We first introduce some basic algebras required in the following discussions. When we carry out a multipole expansion, vector spherical harmonics $\mathbf{Y}_{J,L,M}(\theta,\phi)$ are used as a basis which are defined by

$$\mathbf{Y}_{J,L,M}(\theta,\phi) = (-1)^{1-L-M}\sqrt{2J+1}\sum_{q=-1}^{+1}\begin{pmatrix} L & 1 & J \\ M-q & q & -M \end{pmatrix} Y_{L,M-q}(\theta,\phi)\hat{\mathbf{e}}_q, \tag{4.1}$$

where $Y_{L,M}$ is the spherical harmonics and $\hat{\mathbf{e}}_q$ $(q = -1, 0, +1)$ are the unit vectors in spherical basis which are related to the three Cartesian unit vectors[1] by

$$\hat{\mathbf{e}}_{+1} = -\frac{1}{\sqrt{2}}(\hat{\mathbf{e}}_x + i\hat{\mathbf{e}}_y), \quad \hat{\mathbf{e}}_0 = \hat{\mathbf{e}}_z, \quad \hat{\mathbf{e}}_{-1} = \frac{1}{\sqrt{2}}(\hat{\mathbf{e}}_x - i\hat{\mathbf{e}}_y). \tag{4.3}$$

In (4.1),

$$\begin{pmatrix} J & k & J' \\ -M & q & M' \end{pmatrix} \tag{4.4}$$

[1]The inverse relations are

$$\hat{\mathbf{e}}_x = -\frac{1}{\sqrt{2}}(\hat{\mathbf{e}}_{+1} - \hat{\mathbf{e}}_{-1}), \quad \hat{\mathbf{e}}_y = \frac{i}{\sqrt{2}}(\hat{\mathbf{e}}_{+1} + \hat{\mathbf{e}}_{-1}), \quad \hat{\mathbf{e}}_z = \hat{\mathbf{e}}_0 \tag{4.2}$$

is a Wigner 3j-Symbol which vanishes unless it satisfies the following three conditions.

$$\begin{pmatrix} j_1 & j_2 & J \\ m_1 & m_2 & -M \end{pmatrix}$$

$$\begin{aligned} &1. \quad -|j_1| \le m_1 \le |j_1|,\ -|j_2| \le m_2 \le |j_2| \text{ and} - |J| \le M \le |J| \\ &2. \quad m_1 + m_2 = M \\ &3. \quad |j_1 - j_2| \le J \le j_1 + j_2 \quad \text{(triangular inequalities).} \end{aligned} \tag{4.5}$$

As we can see later, these restrictions determine the selection rules of atomic transitions. As a consequence of the orthogonality relation of the spherical harmonics[2], vector spherical harmonics satisfy the following orthogonality relation

$$\int \mathbf{Y}_{J,L,M} \cdot \mathbf{Y}_{J',L',M'} \mathrm{d}\Omega = \delta_{J,J'}\delta_{L,L'}\delta_{M,M'}, \tag{4.7}$$

where $\mathrm{d}\Omega = \sin\theta \mathrm{d}\theta\mathrm{d}\phi$ is an element of solid angle.
Relations between Cartesian and spherical coordinates[3], inner product and cross product of two vectors in spherical basis are given by

$$\begin{aligned} \mathbf{A} &= A_x\hat{\mathbf{e}_x} + A_y\hat{\mathbf{e}_y} + A_z\hat{\mathbf{e}_z} \\ &= -A_{+1}\hat{\mathbf{e}_{-1}} + A_0\hat{\mathbf{e}_0} - A_{-1}\hat{\mathbf{e}}_{+1} \end{aligned} \tag{4.9}$$

$$\begin{aligned} \mathbf{A}\cdot\mathbf{B} &= \sum_{q=-1}^{+1}(-1)^q A_q B_{-q} \\ &= -A_{+1}B_{-1} + A_0 B_0 - A_{-1}B_{+1} \end{aligned} \tag{4.10}$$

$$\begin{aligned} &\mathbf{A}\times\mathbf{B} \\ &= i(A_0B_{-1} - A_{-1}B_0)\hat{\mathbf{e}}_{+1} + i(A_{-1}B_{+1} - A_{+1}B_{-1})\hat{\mathbf{e}}_0 + i(A_{+1}B_0 - A_0B_{+1})\hat{\mathbf{e}}_{-1}. \end{aligned} \tag{4.11}$$

Bessel functions $j_n(x)$ also play an important role in the discussion of selection rules which satisfy the following identities,

$$j_{n-1}(x) = \frac{n+1}{x}j_n(x) + \frac{\mathrm{d}}{\mathrm{d}z}j_n(x) \tag{4.12}$$

$$j_{n+1}(x) = \frac{n}{x}j_n(x) - \frac{\mathrm{d}}{\mathrm{d}z}j_n(x), \tag{4.13}$$

[2]
$$\int Y^*_{L,M}(\theta,\phi)Y_{L',M'}(\theta,\phi)\sin\theta\mathrm{d}\theta\mathrm{d}\phi \equiv \int Y^*_{L,M}(\theta,\phi)Y_{L',M'}(\theta,\phi)\sin\theta\mathrm{d}\Omega = \delta_{L,L'}\delta_{M,M'} \tag{4.6}$$

[3]The relations between $A_{x,y,z}$ and $A_{-1,0,+1}$ are

$$A_{\pm1} = \mp\frac{1}{\sqrt{2}}(A_x \pm iA_y), \quad A_0 = A_z \tag{4.8}$$

and

$$j_n(x) \simeq \frac{x^n}{(2n+1)!!} \qquad (x \ll 1) \tag{4.14}$$

For the convenience in later calculations, some spherical harmonics and vector spherical harmonics are listed in Appendix D.

Multipole expansion

Let us consider a plane electromagnetic wave whose vector potential $\mathbf{A}$ is given by[4]

$$\mathbf{A}^{\pm}(\mathbf{r}, t) = \hat{\mathbf{e}}_{k\lambda} e^{\pm i(\mathbf{k}\cdot\mathbf{r} - \omega t)}, \tag{4.15}$$

where $\mathbf{k}$ is the wave number vector which is parallel to the wave propagating direction, $\hat{\mathbf{e}}_{k\lambda}$ is the polarization (unit) vector, $\omega = ck$ and c is the speed of light. In the following discussion, the time dependent factor in (4.15) is not important and thus it is eliminated.

First, we expand (4.15) in a series of vector spherical harmonics

$$\mathbf{A}^{\pm}(\mathbf{r}) = \sum_{J,L,M} A^{\pm}_{J,L,M} \mathbf{Y}_{J,L,M}(\theta_r, \phi_r), \tag{4.16}$$

where θ_r and ϕ_r are the angular coordinates of $\mathbf{r}$. $A^{\pm}_{J,L,M}$ can be calculated from (4.15), (4.16) and (4.7),

$$\begin{aligned} \int (\mathbf{Y}_{J,L,M}(\theta_r, \phi_r) \cdot \hat{\mathbf{e}}_{k\lambda}) e^{\pm i\mathbf{k}\cdot\mathbf{r}} \mathrm{d}\Omega &= \sum_{J',L',M'} A^{\pm}_{J',L',M'} \int \mathbf{Y}_{J',L',M'}(\theta_r, \phi_r) \cdot \mathbf{Y}_{J,L,M}(\theta_r, \phi_r) \mathrm{d}\Omega \\ \therefore A^{\pm}_{J,L,M} &= \int (\mathbf{Y}_{J,L,M}(\theta_r, \phi_r) \cdot \hat{\mathbf{e}}_{k\lambda}) e^{\pm i\mathbf{k}\cdot\mathbf{r}} \mathrm{d}\Omega. \end{aligned} \tag{4.17}$$

The plane wave can be expanded in a series of spherical Bessel functions,

$$e^{\pm i\mathbf{k}\cdot\mathbf{r}} = 4\pi \sum_{l=0}^{\infty} \sum_{m=-l}^{l} (\pm i)^l j_l(kr) Y^*_{l,m}(\theta_k, \phi_k) Y_{l,m}(\theta_r, \phi_r) \tag{4.18}$$

where θ_k and ϕ_k are the angular coordinates of $\mathbf{k}$.

By substituting (4.18) into (4.17) and performing integration, we can describe $\mathbf{A}^{\pm}$ as

$$\mathbf{A}^{\pm}(\mathbf{r}) = 4\pi \sum_{J,L,M} (\pm i)^L (\mathbf{Y}_{J,L,M}(\theta_k, \phi_k) \cdot \hat{\mathbf{e}}_{k\lambda}) (j_L(kr) \mathbf{Y}_{J,L,M}(\theta_r, \phi_r)). \tag{4.19}$$

Here, due to the restrictions (4.5) of a Wigner-3j symbol, possible values of L are $J-1, J, J+1$ and possible values of M are $J, J-1, \cdots -J$. In other words, only three independent unit vectors $\mathbf{Y}_{J,J-1,M}$, $\mathbf{Y}_{J,J,M}$, and $\mathbf{Y}_{J,J+1,M}$ are possible. When we consider the interaction between atoms and a laser field, it is more convenient to form mutually

[4]The amplitude of the vector potential is not considered (assumed to be 1) since it doesn't play any role here. It will be introduced in the next section.

orthogonal unit vectors $\mathbf{Y}^{(-1)}_{J,M}$, $\mathbf{Y}^{(0)}_{J,M}$, and $\mathbf{Y}^{(+1)}_{J,M}$ which correspond to longitudinal (-1) and transverse $(0, +1)$ polarizations of a laser field. Relations between these two bases in spherical coordinates were given by Akhiezer and Berestetsky [59] in the form[5]

$$\begin{aligned}
\mathbf{Y}_{J,J-1,M}(\theta,\phi) &= \sqrt{\frac{J}{2J+1}}\mathbf{J}^{(-1)}_{J,M}(\theta,\phi) + \sqrt{\frac{J+1}{2J+1}}\mathbf{Y}^{(+1)}_{J,M}(\theta,\phi) \\
\mathbf{Y}_{J,J,M}(\theta,\phi) &= \mathbf{Y}^{0}_{J,M}(\theta,\phi) \\
\mathbf{Y}_{J,J+1,M}(\theta,\phi) &= -\sqrt{\frac{J+1}{2J+1}}\mathbf{Y}^{(-1)}_{J,M}(\theta,\phi) + \sqrt{\frac{J}{2J+1}}\mathbf{Y}^{(+1)}_{J,M}(\theta,\phi).
\end{aligned}$$

Thus, we can rewrite (4.19) in the multipole expansion

$$\mathbf{A}^{\pm}(\mathbf{r}) = 4\pi\sum_{J=1}^{\infty}\sum_{M=-J}^{J}\sum_{\mu=0}^{+1}(\pm i)^{J-\mu}(\mathbf{Y}^{(\mu)}_{J,M}(\theta_k,\phi_k)\cdot\hat{\mathbf{e}}_{k\lambda})\mathbf{a}^{(\mu)}_{J,M}(\mathbf{r}), \tag{4.20}$$

where[6]

$$\begin{aligned}
&\text{TE mode} && (\text{M}J \text{ transition}) \\
&\mathbf{a}^{(0)}_{J,M}(\mathbf{r}) &&= j_J(kr)\mathbf{Y}^{(0)}_{J,M}(\theta_r,\phi_r) \\
&\text{TM mode} && (\text{E}J \text{ transition}) \\
&\mathbf{a}^{(+1)}_{J,M}(\mathbf{r}) &&= \left(\frac{\mathrm{d}}{\mathrm{d}(kr)}j_J(kr) + \frac{j_J(kr)}{kr}\right)\mathbf{Y}^{(1)}_{J,M}(\theta_r,\phi_r) + \sqrt{J(J+1)}\frac{j_J(kr)}{kr}\mathbf{Y}^{(-1)}_{J,M}(\theta_r,\phi_r).
\end{aligned} \tag{4.21}$$

The longitudinal term $\mathbf{a}^{(-1)}_{J,M}$ is not included in (4.20) since it is parallel to the $\mathbf{k}$ and always $\mathbf{k}\cdot\hat{\mathbf{e}}_{k\lambda} = 0$. Note that, in (4.20), the polarization ($\mathbf{e}_{k\lambda}$) and propagation direction of the laser field (θ_k and ϕ_k) are included in the expansion coefficient.

[5]Inverse relations are

Longitudinal mode($\parallel \mathbf{k}$) :

$$\mathbf{Y}^{(-1)}_{J,M}(\theta,\phi) = \sqrt{\frac{J}{2J+1}}\mathbf{Y}_{J,J-1,M}(\theta,\phi) - \sqrt{\frac{J+1}{2J+1}}\mathbf{Y}_{J,J+1,M}(\theta,\phi)$$

Transverse (TM and TE) mode :

$$\mathbf{Y}^{0}_{J,M}(\theta,\phi) = \mathbf{Y}_{J,J,M}(\theta,\phi)$$

$$\mathbf{Y}^{(+1)}_{J,M}(\theta,\phi) = \sqrt{\frac{J+1}{2J+1}}\mathbf{Y}_{J,J-1,M}(\theta,\phi) + \sqrt{\frac{J}{2J+1}}\mathbf{Y}_{J,J+1,M}(\theta,\phi).$$

[6]Here we use following relations between spherical Bessel functions.

$$\begin{aligned}
j_{n-1}(x) &= \frac{n+1}{x}j_n(x) + \frac{\mathrm{d}}{\mathrm{d}x}j_n(x) \\
j_{n+1}(x) &= \frac{n}{x}j_n(x) - \frac{\mathrm{d}}{\mathrm{d}x}j_n(x)
\end{aligned}$$

We should also remember that $\mathbf{a}^{(\mu)}_{J,M}$ satisfies the transversality condition

$$\begin{aligned} \boldsymbol{\nabla} \cdot \mathbf{a}^{\mu}_{J,M}(\mathbf{r}) &= 0 \\ \therefore \quad \mathbf{a}^{\mu}_{J,M}(\mathbf{r}) \cdot \mathbf{p} &= \mathbf{p} \cdot \mathbf{a}^{\mu}_{J,M}(\mathbf{r}). \end{aligned} \tag{4.22}$$

In addition, the wave vector $\mathbf{k}$ must be always orthogonal to the polarization vector $\hat{\mathbf{e}}_{k\lambda}(= -\lambda_{+1}\hat{\mathbf{e}}_{-1} + \lambda_0\hat{\mathbf{e}}_0 - \lambda_{-1}\hat{\mathbf{e}}_{+1})$, i.e., $\mathbf{k} \cdot \hat{\mathbf{e}}_{k\lambda} = 0$. Thus, the following equation must be always satisfied.

$$(\lambda_{-1} - \lambda_{+1}) \sin\theta_k \cos\phi_k - i(\lambda_{-1} + \lambda_{+1}) \sin\theta_k \sin\phi_k + \lambda_0 \cos\theta_k = 0. \tag{4.23}$$

4.2 Matrix elements and selection rules for E1, E2, M1, and M2 transitions

4.2.1 Interaction between atoms and a laser field

First of all, we derive matrix elements for the E1, E2, M1, and M2 transitions which determine their selection rules.

A Hamiltonian describing the system of atoms and an electromagnetic field interacting with them is given by

$$H = (H_{\text{rad}} + H_{\text{atom}}) + H_{\text{int}} \tag{4.24}$$

where

$$H_{\text{rad}} = \sum_{k\lambda} \hbar\omega_k (\hat{a}^{\dagger}_{k\lambda}\hat{a}_{k\lambda} + \frac{1}{2}) \tag{4.25}$$

is the Hamiltonian for a free field. $k\lambda$ represents the mode of the field, k and λ are the wave vector and the polarization ($\lambda = 1, 2$) respectively and $\omega_k = ck$. $\hat{a}_{k\lambda}$ and $\hat{a}^{\dagger}_{k\lambda}$ are annihilation and creation operators, respectively, for a photon with wave vector $\mathbf{k}$ and polarization vector $\hat{\mathbf{e}}_{\lambda}$.

$$H_{\text{atom}} = \sum_i \Big(\frac{p_i^2}{2m}\Big) + V' \tag{4.26}$$

is the atomic Hamiltonian for every electron i. V' contains all terms which is necessary to define the atomic state (interaction between nucleus and electrons, repulsion among electrons, and so on...).

If we take the most dominant term in the interaction Hamiltonian H_{int}, it can be given by

$$H_{\text{int}} \cong \Big(\frac{e}{mc}\Big)\mathbf{p} \cdot \mathbf{A} \tag{4.27}$$

where $\mathbf{p}$ and $\mathbf{A}$ represent electron momentum and vector potential of external electromagnetic field, respectively [51].

In our calculations, the Hamiltonian H may be written as

$$H = H_0 + H_{\text{int}} \tag{4.28}$$

where $H_0 = H_{\rm rad} + H_{\rm atom}$. We regard the second term $H_{\rm int}$ as a perturbation. Thus what we have to do first is to examine details of $H_{\rm int}$.

In the Schrödinger representation and in SI unit, the vector potential for plane wave $\mathbf{A}$ is described as,

$$\mathbf{A}(\mathbf{r}) = \sum_{k\lambda} \sqrt{\frac{\hbar c^2}{2V\epsilon_0\omega_k}} \hat{\mathbf{e}}_{k\lambda}[\hat{a}_{k\lambda} e^{i\mathbf{k}\cdot\mathbf{r}} + \hat{a}^\dagger_{k\lambda} e^{-i\mathbf{k}\cdot\mathbf{r}}] \tag{4.29}$$

where V is the volume of the considered system. With (4.27) and (4.29), $H_{\rm int}$ can be written as

$$\begin{aligned} H_{\rm int} &= \sum_{k\lambda} \Big(\frac{e}{m}\Big) \sqrt{\frac{\hbar}{2V\epsilon_0\omega_k}} (\hat{\mathbf{e}}_{k\lambda}\cdot\mathbf{p})[\hat{a}_{k\lambda} e^{i\mathbf{k}\cdot\mathbf{r}} + \hat{a}^\dagger_{k\lambda} e^{-i\mathbf{k}\cdot\mathbf{r}}] &(4.30)\\ &\equiv H^{(+)}_{\rm int} + H^{(-)}_{\rm int} &(4.31)\end{aligned}$$

where

$$\begin{aligned} H^{(-)}_{\rm int} &= \sum_{k\lambda} \Big(\frac{e}{m}\Big) \sqrt{\frac{\hbar}{2V\epsilon_0\omega_k}} (\hat{\mathbf{e}}_{k\lambda}\cdot\mathbf{p}) \hat{a}_{k\lambda} e^{i\mathbf{k}\cdot\mathbf{r}} &(4.32)\\ H^{(+)}_{\rm int} &= \sum_{k\lambda} \Big(\frac{e}{m}\Big) \sqrt{\frac{\hbar}{2V\epsilon_0\omega_k}} (\hat{\mathbf{e}}_{k\lambda}\cdot\mathbf{p}) \hat{a}^\dagger_{k\lambda} e^{-i\mathbf{k}\cdot\mathbf{r}}. &(4.33)\end{aligned}$$

In the following calculations of the excitation rate or the trap depth of a FORT, matrix elements of these Hamiltonians $|\langle b, n'_{k\lambda}|H_{\rm int}|a, n_{k\lambda}\rangle|^2$ play a major role. Here $|a\rangle$ and $|b\rangle$ are the atomic state vectors and $n'_{k\lambda}$ and $n_{k\lambda}$ represent the occupation number of $k\lambda$ mode of the external field.

By using $\hat{a}_{k\lambda}|n_{k\lambda}\rangle = \sqrt{n_{k\lambda}}\,|n_{k\lambda}-1\rangle$ and $\hat{a}^\dagger_{k\lambda}|n_{k\lambda}\rangle = \sqrt{n_{k\lambda}+1}\,|n_{k\lambda}+1\rangle$, the square of matrix elements can be modified as

$$\begin{aligned} |\langle b, n_{k'\lambda'}|H_{\rm int}|a, n_{k\lambda}\rangle|^2 &= |\langle b, n_{k'\lambda'}|H^{(-)}_{\rm int}|a, n_{k\lambda}\rangle \delta(n_{k'\lambda'}-1, n_{k\lambda}) \\ &\qquad + \langle b, n_{k'\lambda'}|H^{(+)}_{\rm int}|a, n_{k\lambda}\rangle \delta(n_{k'\lambda'}+1, n_{k\lambda})|^2 \\ &= |\langle b; n_{k\lambda}-1|H^{(-)}_{\rm int}|a; n_{k\lambda}\rangle|^2 + |\langle b; n_{k\lambda}+1|H^{(+)}_{\rm int}|a; n_{k\lambda}\rangle|^2. \end{aligned} \tag{4.34}$$

Two terms in the last equation can be easily calculated by (4.32) and (4.33).

Substituting (4.20) to (4.32), (4.33), and (4.34), we have

$$\begin{aligned} \langle b; n_{k\lambda}-1|H^{(-)}_{\rm int}|a; n_{k\lambda}\rangle &= \Big(\frac{e}{m}\Big)\sqrt{\frac{\hbar n_{k\lambda}}{2V\epsilon_0\omega_k}} 4\pi \sum_{J,M}\sum_{\mu=0}^{+1} i^{J-\mu} (\mathbf{Y}^{(\mu)}_{J,M}(\theta_k,\phi_k)\cdot\hat{\mathbf{e}}_{k\lambda}) \langle b|\mathbf{a}^{(\mu)}_{J,M}\cdot\mathbf{p}|a\rangle, \\ \langle b; n_{k\lambda}+1|H^{(+)}_{\rm int}|a; n_{k\lambda}\rangle &= \Big(\frac{e}{m}\Big)\sqrt{\frac{\hbar(n_{k\lambda}+1)}{2V\epsilon_0\omega_k}} 4\pi \sum_{J,M}\sum_{\mu=0}^{+1} (-i)^{J-\mu} (\mathbf{Y}^{(\mu)}_{J,M}(\theta_k,\phi_k)\cdot\hat{\mathbf{e}}_{k\lambda}) \langle b|\mathbf{a}^{(\mu)}_{J,M}\cdot\mathbf{p}|a\rangle. \end{aligned} \tag{4.35}$$

The transition induced by the TM (transverse magnetic) field is called "EJ transition". It corresponds to the case where $\mu = +1$ in (4.20). In a similar manner, when $\mu = 0$, i.e., the TE (transverse electric) field induces the transition, it is called "MJ transition". In the following, we will see the E1, E2, M1, and M2 transitions (J=1, 2 and μ = 0, 1) in detail. All of these transitions (except for the M1 transition) play an important role in this work.

Here, we introduce a useful equation. By using a commutation law between the position r and the momentum p ($[x, p^2] = 2i\hbar p_x$ and so on), we find

$$[\mathbf{r}, H_{\rm atom}] = \left(\frac{i\hbar}{m}\right)\mathbf{p}, \tag{4.36}$$

which leads to

$$\begin{aligned}\langle b|\mathbf{p}|a\rangle &= \left(\frac{m}{i\hbar}\right)\langle b|[\mathbf{r}, H_{\rm atom}]|a\rangle \\ &= \left(\frac{m}{i\hbar}\right)(E_b - E_a)\langle b|\mathbf{r}|a\rangle \\ &= im\omega_k\langle b|\mathbf{r}|a\rangle, \end{aligned}\tag{4.37}$$

where $\hbar\omega_k = E_b - E_a$. For an N-electron system, we consider $\mathbf{r} = \Sigma_{j=1}^{N}\mathbf{r}_j$, where $\mathbf{r}_j$ is the position of the electron j.

4.2.2 E1 transition

The E1 transition is induced by the term in (4.35) with $\mu = +1$ and J=1. With the aid of (4.21), (4.37) and $j_1(kr) \simeq kr/3$ (when $kr \ll 1$),

$$4\pi\sum_{M=-1}^{+1}(\mathbf{e}_{k\lambda}\cdot\mathbf{Y}_{1,M}^{(+1)}(\theta_k,\phi_k))\langle b|\mathbf{a}_{1,M}^{(+1)}\cdot\mathbf{p}|a\rangle \tag{4.38}$$

$$\simeq 4\pi\sum_{M=-1}^{+1}(\mathbf{e}_{k\lambda}\cdot\mathbf{Y}_{1,M}^{(+1)}(\theta_k,\phi_k))\langle b|\left(\frac{2}{3}\mathbf{Y}_{1,M}^{(1)} + \frac{\sqrt{2}}{3}\mathbf{Y}_{1,M}^{(-1)}\right)\cdot\mathbf{p}|a\rangle$$

$$= 4\pi\frac{im\omega_k}{\sqrt{6\pi}}\sum_{M=-1}^{+1}(\mathbf{e}_{k\lambda}\cdot\mathbf{Y}_{1,M}^{(+1)}(\theta_k,\phi_k))\hat{\mathbf{e}}_M\cdot\langle b|\mathbf{r}|a\rangle. \tag{4.39}$$

The matrix element is given by

$$\langle b; n_{k\lambda}-1|H_{\rm int}^{(-)}|a; n_{k\lambda}\rangle_{\rm E1} = ie\sqrt{\frac{\hbar n_{k\lambda}\omega_k}{2V\epsilon_0}}\sqrt{\frac{8\pi}{3}}\sum_{M=-1}^{+1}(\mathbf{e}_{k\lambda}\cdot\mathbf{Y}_{1,M}^{(+1)}(\theta_k,\phi_k))\hat{\mathbf{e}}_M\cdot\langle b|\mathbf{r}|a\rangle, \tag{4.40}$$

$$\langle b; n_{k\lambda}\pm 1|H_{\rm int}^{(\pm)}|a; n_{k\lambda}\rangle_{\rm E1} = ie\sqrt{\frac{\hbar(n_{k\lambda}+1)\omega_k}{2V\epsilon_0}}\sqrt{\frac{8\pi}{3}}\sum_{M=-1}^{+1}(\mathbf{e}_{k\lambda}\cdot\mathbf{Y}_{1,M}^{(+1)}(\theta_k,\phi_k))\hat{\mathbf{e}}_M\cdot\langle b|\mathbf{r}|a\rangle. \tag{4.41}$$

Since $\mathbf{r}$ is the first rank irreducible tensor, the Wigner-Eckart theorem[7] gives

$$\langle \alpha, J, M | r_q^{(1)} | \alpha', J', M' \rangle = (-1)^{J-M} \begin{pmatrix} J & 1 & J' \\ -M & q & M' \end{pmatrix} \langle \alpha, J || r^{(1)} || \alpha', J' \rangle. \tag{4.45}$$

Due to the restriction (4.5) of a Wigner-3J symbol, the selection rule is given by

$$\Delta J = 0, \pm 1 \qquad \Delta M = 0, \pm 1, \qquad J_a + J_b \geq 1, \qquad \pi_a = -\pi_b, \tag{4.46}$$

The conservation of parity requires $\pi_a \pi_{\rm em} \pi_b = +1$ where $\pi_a, \pi_b, \pi_{\rm em}$ are parity of the initial and final states and the multipole electromagnetic field, respectively. Parity of an electromagnetic field is defined as the parity of the magnetic field $\mathbf{B} = \nabla \times \mathbf{A}$. From (4.20), parity of the TM and TE fields is determined by $\mathbf{Y}_{J,L,M}$ and given by $(-1)^L$. In the case of the E1 transition, parity of the TE field $\mathbf{Y}^{\pm 1}_{1,M}$ with $J = 1$ is given by $\pi_{\rm E1} = (-1)^J = -1$ which leads to (4.46).

For the E1 transition, $\mathbf{Y}^{(1)}_{1,M}$ are given by

$$\mathbf{Y}^{(1)}_{1,\pm 1} = \frac{1}{\sqrt{4\pi}} \frac{1}{12} \left\{ 3\sqrt{6}(1 + \cos^2\theta_k) \hat{\mathbf{e}}_{\pm 1} \pm 6\sqrt{3} \cos\theta_k \sin\theta_k e^{\pm i\phi_k} \hat{\mathbf{e}}_0 + 18\sqrt{5} \sin^2\theta_k e^{\pm 2i\phi_k} \hat{\mathbf{e}}_{\mp 1} \right\} \tag{4.47}$$

$$\mathbf{Y}^{(1)}_{1,0} = \frac{3}{2} \frac{1}{\sqrt{6\pi}} \sin^2\theta_k \hat{\mathbf{e}}_0 + \sqrt{\frac{3}{16\pi}} \cos\theta_k \sin\theta_k (e^{-i\phi_k} \hat{\mathbf{e}}_{+1} + e^{i\phi_k} \hat{\mathbf{e}}_{-1}). \tag{4.48}$$

As an example, let us consider the case where $\mathbf{k} \parallel \mathbf{e}_z$ ($\theta_k = 0$) and $\mathbf{e}_{k\lambda} = \mathbf{e}_{+1}$. This corresponds to the situation where a laser field propagates along the z direction and it is circularly polarized. Since

$$\begin{aligned} \mathbf{Y}^{(+1)}_{1,\pm 1}(0, \phi_k) &= \sqrt{\frac{3}{8\pi}} \hat{\mathbf{e}}_{\pm} \\ \mathbf{Y}^{(+1)}_{1,0}(0, \phi_k) &= 0, \end{aligned}$$

[7] Wigner-Eckart Theorem:

$$\langle \alpha, J, M | T_q^{(k)} | \alpha', J', M' \rangle = (-1)^{J-M} \begin{pmatrix} J & k & J' \\ -M & q & M' \end{pmatrix} \langle \alpha, J || T^{(k)} || \alpha', J' \rangle \tag{4.42}$$

where $T_q^{(k)}$ is an irreducible tensor operator and J,M and J', M' are angular momentum quantum numbers. α and α' are additional quantum numbers required to completely identify the states. $\langle \alpha, J || T^{(k)} || \alpha', J' \rangle$ is called "reduced matrix element" and

$$\begin{pmatrix} J & k & J' \\ -M & q & M' \end{pmatrix} \tag{4.43}$$

is called "Wigner 3j-Symbol". It can be described by using a Clebsch-Gordon coefficient $(j_1, j_2, m_1, m_2 | j_1, j_2, j, m)$.

$$\begin{pmatrix} J & k & J' \\ -M & q & M' \end{pmatrix} = \frac{(-1)^{k-J+M'}}{\sqrt{2J'+1}} (J, k, -M, 1 | J, k, J', -M') \tag{4.44}$$

when $\mathbf{k} \parallel z$, only the $\Delta M = \pm 1$ transitions (σ_+ and σ_- transitions) are possible and the $\Delta M = 0$ transition (π transition) is impossible for any laser polarization. In addition, due to the circular polarization $\hat{\mathbf{e}}_{+1}$ only $M = +1$ term survives and the matrix element is given by

$$\langle b; n_{k\lambda} - 1 | H_{\rm int}^{(-)} | a; n_{k\lambda} \rangle_{\rm E1} = ie \sqrt{\frac{\hbar n_{k\lambda} \omega_k}{2V\epsilon_0}} \langle b | r_{+1}^{(1)} | a \rangle, \tag{4.49}$$

$$\langle b; n_{k\lambda} + 1 | H_{\rm int}^{(+)} | a; n_{k\lambda} \rangle_{\rm E1} = ie \sqrt{\frac{\hbar (n_{k\lambda} + 1) \omega_k}{2V\epsilon_0}} \langle b | r_{+1}^{(1)} | a \rangle, \tag{4.50}$$

which means that the transition which satisfies $\Delta M = 1$ occurs.

4.2.3 M1 transition

The M1 transition is induced by the term in (4.35) with $\mu = 0$ and J=1. With the aid of (4.21), (4.37) and $j_1(kr) \simeq kr/3$ (when $kr \ll 1$)[8],

$$\begin{aligned} \mathbf{a}_{1,M}^{(0)}(\mathbf{r}) \cdot \mathbf{p} &\simeq \frac{1}{3} kr \mathbf{Y}_{1,1,M}(\theta_r, \phi_r) \cdot \mathbf{p} \\ &= -i \frac{k}{\sqrt{24\pi}} (\mathbf{r} \times \hat{\mathbf{e}}_M) \cdot \mathbf{p} \\ &= i \frac{k}{\sqrt{24\pi}} \hat{\mathbf{e}}_M \cdot (\mathbf{r} \times \mathbf{p}) \\ &= i \frac{k}{\sqrt{6\pi}} \hat{\mathbf{e}_M} \cdot \left(\frac{\hbar}{2} \mathbf{L} \right). \end{aligned} \tag{4.52}$$

Since $\mathbf{L}$ is related to the magnetic momentum operator by

$$\left(\frac{\hbar}{2} \right) \mathbf{L} = - \left(\frac{mc}{e} \right) \boldsymbol{\mu}_L, \tag{4.53}$$

the matrix element is given by

$$\langle b; n_{k\lambda} - 1 | H_{\rm int}^{(-)} | a; n_{k\lambda} \rangle_{\rm M1} = -i \sqrt{\frac{\hbar n_{k\lambda} \omega_k}{2V\epsilon_0}} \sqrt{\frac{8\pi}{3}} \sum_{M=-1}^{+1} (\mathbf{e}_{k\lambda} \cdot \mathbf{Y}_{1,M}^{(0)}(\theta_k, \phi_k)) \hat{\mathbf{e}}_M \cdot \langle b | \boldsymbol{\mu}_L | a \rangle, \tag{4.54}$$

$$\langle b; n_{k\lambda} + 1 | H_{\rm int}^{(+)} | a; n_{k\lambda} \rangle_{\rm M1} = i \sqrt{\frac{\hbar (n_{k\lambda} + 1) \omega_k}{2V\epsilon_0}} \sqrt{\frac{8\pi}{3}} \sum_{M=-1}^{+1} (\mathbf{e}_{k\lambda} \cdot \mathbf{Y}_{1,M}^{(0)}(\theta_k, \phi_k)) \hat{\mathbf{e}}_M \cdot \langle b | \boldsymbol{\mu}_L | a \rangle. \tag{4.55}$$

[8] In addition, next property of the scalar triple product is used.

$$\mathbf{a} \cdot (\mathbf{b} \times \mathbf{c}) = \mathbf{b} \cdot (\mathbf{c} \times \mathbf{a}) = \mathbf{c} \cdot (\mathbf{a} \times \mathbf{b}). \tag{4.51}$$

Since $\boldsymbol{\mu}_L$ is the first rank irreducible tensor, the selection rule is given by

$$\Delta J = 0, \pm 1 \qquad \Delta M = 0, \pm 1, \qquad J_a + J_b \geq 1, \qquad \pi_a = \pi_b, \tag{4.56}$$

where $\pi_{\mathrm{M1}} = 1$ is used. The M1 transition is allowed between states which has same parity. It is, then, sometimes used to induce the RF transition between the magnetic sublevels in a same J state.

4.2.4 E2 transition

The E2 transition is induced by the term in (4.35) with $\mu = +1$ and J=2. With the aid of (4.21), (4.37) and $j_2(kr) \simeq (kr)^2/15$ (when $kr \ll 1$),

$$\begin{aligned}
\mathbf{a}^{(+1)}_{2,M}(\mathbf{r}) \cdot \mathbf{p} &\simeq \left(\frac{1}{5}(kr)\mathbf{Y}^{(1)}_{2,M}(\theta_r, \phi_r) + \frac{\sqrt{6}}{15}(kr)\mathbf{Y}^{(-1)}_{2,M}(\theta_r, \phi_r) \right) \cdot \mathbf{p} \\
&= \sqrt{\frac{1}{15}}(kr)\mathbf{Y}_{2,1,M}(\theta_r, \phi_r) \cdot \mathbf{p} \\
&= \sqrt{\frac{1}{20\pi}} \begin{cases} r^{(1)}_{\pm 1} p^{(1)}_{\pm 1} & (M = \pm 2) \\ \dfrac{1}{\sqrt{2}} \left(r^{(1)}_{\pm 1} p^{(1)}_0 + r^{(1)}_0 p^{(1)}_{\pm 1} \right) & (M = \pm 1) \\ \dfrac{1}{\sqrt{6}} \left(r^{(1)}_{-1} p^{(1)}_{+1} + 2 r^{(1)}_0 p^{(1)}_0 + r^{(1)}_{+1} p^{(1)}_{-1} \right), & (M = 0) \end{cases}
\end{aligned} \tag{4.57}$$

where $r^{(1)}$ and $p^{(1)}$ are the first rank irreducible tensor. Due to the transversality (4.22), $p^{(1)}_{q'} r^{(1)}_q + p^{(1)}_q r^{(1)}_{q'} = r^{(1)}_q p^{(1)}_{q'} + r^{(1)}_{q'} p^{(1)}_q$. Thus we find

$$\begin{aligned}
& \langle b | r^{(1)}_q p^{(1)}_{q'} + r^{(1)}_{q'} p^{(1)}_q | a \rangle \\
= \; & \left(\frac{m}{i\hbar} \right) \left\{ \langle b | r^{(1)}_q [r^{(1)}_{q'}, H_{\mathrm{atom}}] | a \rangle + \langle b | r^{(1)}_{q'} [r^{(1)}_q, H_{\mathrm{atom}}] | a \rangle \right\} \\
= \; & 2E_a \left(\frac{m}{i\hbar} \right) \langle b | r^{(1)}_q r^{(1)}_{q'} | a \rangle - \left(\frac{m}{i\hbar} \right) \left\{ \langle b | r^{(1)}_q H_{\mathrm{atom}} r^{(1)}_{q'} | a \rangle + \langle b | r^{(1)}_{q'} H_{\mathrm{atom}} r^{(1)}_q | a \rangle \right\}
\end{aligned} \tag{4.58}$$

$$\begin{aligned}
& \langle b | p^{(1)}_{q'} r^{(1)}_q + p^{(1)}_q r^{(1)}_{q'} | a \rangle \\
= \; & \left(\frac{m}{i\hbar} \right) \left\{ \langle b | [r^{(1)}_{q'}, H_{\mathrm{atom}}] r^{(1)}_q | a \rangle + \langle b | [r^{(1)}_q, H_{\mathrm{atom}}] r^{(1)}_{q'} | a \rangle \right\} \\
= \; & -2E_b \left(\frac{m}{i\hbar} \right) \langle b | r^{(1)}_q r^{(1)}_{q'} | a \rangle + \left(\frac{m}{i\hbar} \right) \left\{ \langle b | r^{(1)}_q H_{\mathrm{atom}} r^{(1)}_{q'} | a \rangle + \langle b | r^{(1)}_{q'} H_{\mathrm{atom}} r^{(1)}_q | a \rangle \right\}.
\end{aligned} \tag{4.59}$$

From the summation of (4.58) and (4.59) and the transversality condition (4.22) is

$$\langle b | r^{(1)}_q p^{(1)}_{q'} + r^{(1)}_{q'} p^{(1)}_q | a \rangle = im\omega_k \langle b | r^{(1)}_q r^{(1)}_{q'} | a \rangle. \tag{4.60}$$

In addition, according to the definition of a tensor product of two irreducible tensor operators [9],

$$\begin{aligned} Q^{(2)}_{\pm 2} &= (r^{(1)}_{\pm 1})^2 \\ Q^{(2)}_{\pm 1} &= \sqrt{2} r^{(1)}_{\pm 1} r^{(1)}_0 \\ Q^{(2)}_{\pm 0} &= \frac{2}{\sqrt{6}} \left\{ r^{(1)}_{+1} r^{(1)}_{-1} + (r^{(1)}_0)^2 \right\}. \end{aligned} \tag{4.61}$$

Using (4.57), (4.60) and (4.61), the matrix element of the E2 transition is

$$\langle b; n_{k\lambda} - 1 | H^{(-)}_{\rm int} | a; n_{k\lambda} \rangle_{\rm E2} = -\frac{e}{c} \sqrt{\frac{\hbar n_{k\lambda} \omega_k^3}{8 V \epsilon_0}} \sqrt{\frac{4\pi}{5}} \sum_{M=-2}^{+2} (\mathbf{e}_{k\lambda} \cdot \mathbf{Y}^{(+1)}_{1,M}(\theta_k, \phi_k)) \langle b | Q^{(2)}_M | a \rangle, \tag{4.62}$$

$$\langle b; n_{k\lambda} + 1 | H^{(+)}_{\rm int} | a; n_{k\lambda} \rangle_{\rm E2} = \frac{e}{c} \sqrt{\frac{\hbar (n_{k\lambda} + 1) \omega_k^3}{8 V \epsilon_0}} \sqrt{\frac{4\pi}{5}} \sum_{M=-2}^{+2} (\mathbf{e}_{k\lambda} \cdot \mathbf{Y}^{(+1)}_{1,M}(\theta_k, \phi_k)) \langle b | Q^{(2)}_M | a \rangle. \tag{4.63}$$

Since $Q^{(2)}_M$ is the second rank irreducible tensor, the selection rule is given by

$$\Delta J = 0, \pm 1, \pm 2, \qquad \Delta M = 0, \pm 1, \pm 2, \qquad J_a + J_b \geq 2, \qquad \pi_a = \pi_b. \tag{4.64}$$

When we desire to carry out the $\Delta M = m$ transition, we should choose proper $\mathbf{k}$ (incident direction) and $\mathbf{e}_{k\lambda}$ (polarization) which does not eliminate $\mathbf{Y}^{(1)}_{2,m} \cdot \mathbf{e}_{k\lambda}$. For the E2 transition, $\mathbf{Y}^{(1)}_{2,M}$ are given by the following equations.

$$\begin{aligned} \mathbf{Y}^{(1)}_{2,\pm 2}(\theta_k, \phi_k) &= \mp \frac{e^{\pm i\phi_k}}{\sqrt{40\pi}} \sin\theta_k (7 - 5\sin^2\theta_k) \hat{\mathbf{e}}_{\pm 1} - \sqrt{\frac{5}{16\pi}} e^{\pm 2i\phi_k} \cos\theta_k \sin^2\theta_k \hat{\mathbf{e}}_0 \\ &\qquad \mp \sqrt{\frac{5}{96}} e^{\pm 3i\phi_k} \sin^3\theta_k \hat{\mathbf{e}}_{\mp 1} \\ \mathbf{Y}^{(1)}_{2,\pm 1}(\theta_k, \phi_k) &= \frac{5\cos^3\theta_k}{\sqrt{40\pi}} \hat{\mathbf{e}}_{\pm 1} \mp \frac{e^{\pm i\phi_k}}{\sqrt{20\pi}} \sin\theta_k \left\{ 3 - 2\sin\theta_k (5\sin^2\theta_k - 4) \right\} \hat{\mathbf{e}}_0 \\ &\qquad + \sqrt{\frac{5}{8\pi}} e^{\pm 2i\phi_k} \cos\theta_k \sin^2\theta_k \hat{\mathbf{e}}_{\mp 1} \\ \mathbf{Y}^{(1)}_{2,0}(\theta_k, \phi_k) &= \sqrt{\frac{3}{80\pi}} e^{-i\phi_k} (5\sin\theta_k \cos^2\theta_k) \hat{\mathbf{e}}_{+1} + \sqrt{\frac{3}{40\pi}} \cos\theta_k (1 + 4\sin^2\theta_k) \hat{\mathbf{e}}_0 \\ &\qquad - \sqrt{\frac{3}{80\pi}} e^{\pm i\phi_k} (5\sin\theta_k \cos^2\theta) \hat{\mathbf{e}}_{-1}. \end{aligned} \tag{4.65}$$

[9]

$$\begin{aligned} V^{(K)}_Q &= [\mathbf{A}^{(k)} \mathbf{B}^{(k')}]^{(K)}_Q \\ &= \sqrt{2K+1} \sum_{q,q'} (-1)^{-k+k'-Q} \begin{pmatrix} k & k' & K \\ q & q' & -Q \end{pmatrix} A^{(k)}_q B^{(k)}_{q'} \end{aligned}$$

For example, when the incident direction of the excitation laser is parallel to the z axis, i.e., $\theta_k = 0$,

$$\mathbf{Y}^{(1)}_{2,\pm2}(0,\phi_k) = 0 \tag{4.66}$$

$$\mathbf{Y}^{(1)}_{2,\pm1}(0,\phi_k) = \frac{5}{\sqrt{40\pi}}\hat{\mathbf{e}}_{\pm1} \tag{4.67}$$

$$\mathbf{Y}^{(1)}_{2,0}(0,\phi_k) = \sqrt{\frac{3}{40\pi}}\hat{\mathbf{e}}_0. \tag{4.68}$$

Since the linear polarization along the z direction is impossible when $\mathbf{k} \parallel z$, $\mathbf{Y}^{(1)}_{2,0}(0,\phi_k) \cdot \mathbf{e}_{k\lambda} \equiv 0$. As a result, only the $\Delta M = \pm1$ transition is possible in this case.

4.2.5 M2 transition

The M2 transition is induced by the term in (4.35) with $\mu = 0$ and J=2. In the following, we carry out calculations in case of $M = \pm2$, which can be easily applied to the case of $M = \pm1$ and 0. With the aid of (4.21), (4.37) and $j_2(kr) \simeq (kr)^2/15$ (when $kr \ll 1$),

$$\begin{aligned}
\mathbf{a}^{(0)}_{2,\pm2}(\mathbf{r}) \cdot \mathbf{p} &\simeq \left(\frac{k^2}{15}\right) r^2 \mathbf{Y}_{2,2,\pm2}(\theta_r,\phi_r) \cdot \mathbf{p} \\
&= \pm\frac{k^2}{15}\sqrt{\frac{5}{4\pi}} r^{(1)}_{\pm} \left\{ r^{(1)}_{\pm1}\hat{\mathbf{e}}^{(1)}_0 - r^{(1)}_0 \hat{\mathbf{e}}_{\pm} \right\} \cdot \mathbf{p} \\
&= -i\frac{k^2}{15}\sqrt{\frac{5}{4\pi}} r^{(1)}_{\pm1} (\mathbf{r} \times \hat{\mathbf{e}}^{(1)}_{\pm1}) \cdot \mathbf{p} \\
&= -i\left(\frac{2mc}{e}\right)\left(\frac{k^2}{15}\right)\sqrt{\frac{5}{4\pi}} r^{(1)}_{\pm1}\mu^{(1)}_{\pm1},
\end{aligned} \tag{4.69}$$

where (4.53) is used. Here, we define a second rank irreducible tensor $T^{(2)}_q$ which is a tensor product of two irreducible first rank tensor $r^{(1)}_q$ (position) and $\mu^{(1)}_q$ (magnetic moment) operators and described by

$$\begin{aligned}
T^{(2)}_{\pm2} &= r^{(1)}_{\pm1}\mu^{(1)}_{\pm1} \\
T^{(2)}_{\pm1} &= \frac{1}{\sqrt{2}}(r^{(1)}_{\pm1}\mu^{(1)}_0 + r^{(1)}_0\mu^{(1)}_{\pm1}) \\
T^{(2)}_0 &= \frac{1}{\sqrt{6}}(r^{(1)}_{+1}\mu^{(1)}_{-1} + 2r^{(1)}_0\mu^{(1)}_0 + r^{(1)}_{-1}\mu^{(1)}_{+1}).
\end{aligned}$$

By carrying out same calculations for $M = \pm1$ and 0, the matrix elements of the M2 transition are given by

$$\langle b; n_{k\lambda} - 1|H^{(-)}_{\rm int}|a; n_{k\lambda}\rangle_{\rm M2} = -\frac{i}{c}\sqrt{\frac{\hbar n_{k\lambda}\omega_k^3}{2V\epsilon_0}}\left(\frac{4}{15}\right)\sqrt{5\pi}\sum_{M=-2}^{+2}(\mathbf{e}_{k\lambda}\cdot\mathbf{Y}^{(0)}_{1,M}(\theta_k,\phi_k))\langle b|T^{(2)}_M|a\rangle, \tag{4.70}$$

$$\langle b; n_{k\lambda}+1|H_{\rm int}^{(+)}|a; n_{k\lambda}\rangle_{\rm M2} = -\frac{i}{c}\sqrt{\frac{\hbar(n_{k\lambda}+1)\omega_k^3}{2V\epsilon_0}}\left(\frac{4}{15}\right)\sqrt{5\pi}\sum_{M=-2}^{+2}(\mathbf{e}_{k\lambda}\cdot\mathbf{Y}_{1,M}^{(0)}(\theta_k,\phi_k))\langle b|T_M^{(2)}|a\rangle. \tag{4.71}$$

As in the case of E2 transition, since $T_M^{(2)}$ is a second rank irreducible tensor, the selection rule is given by

$$\Delta J = 0,\pm1,\pm2, \qquad \Delta M = 0,\pm1,\pm2, \qquad J_a + J_b \geq 2, \qquad \pi_a = -\pi_b. \tag{4.72}$$

For the M2 transition, $\mathbf{Y}_{2,M}^{(0)}$ are given by the following equations.

$$\mathbf{Y}_{2,\pm2}^{(0)} = \sqrt{\frac{5}{16\pi}}e^{\pm i\phi_k}\sin\theta_k\left(\sqrt{2}\cos\theta_k\hat{\mathbf{e}}_{\pm1}\pm\sin\theta_k e^{\pm i\phi_k}\hat{\mathbf{e}}_0\right) \tag{4.73}$$

$$\mathbf{Y}_{2,\pm1}^{(0)} = \mp\frac{1}{4}\sqrt{\frac{5}{6\pi}}\left\{(3\cos^2\theta_k-1)\hat{\mathbf{e}}_{\pm1}\pm\sqrt{6}\cos\theta_k\sin\theta_k e^{\pm i\phi_k}\hat{\mathbf{e}}_0-\sqrt{3}\sin^2\theta_k e^{\pm2i\phi_k}\hat{\mathbf{e}}_{\mp}\right\} \tag{4.74}$$

$$\mathbf{Y}_{2,0}^{(0)} = -\frac{1}{4}\sqrt{\frac{15}{\pi}}\cos\theta_k\sin\theta_k(e^{-i\phi_k}\hat{\mathbf{e}}_{+1}+e^{i\phi_k}\hat{\mathbf{e}}_{-1}) \tag{4.75}$$

One of the important points in these equations is that in order to observe the $\Delta M = 0$ transition we should let $\theta_k \neq 0$ and $\pi/2$.

Let us consider, as an example, the case where $\theta_k = \pi/4$ and $\phi_k = 0$ and the polarization is parallel to the y axis, i.e., $\hat{\mathbf{e}}_{k\lambda} \parallel \hat{\mathbf{e}}_y$ which satisfies the condition $\mathbf{k}\cdot\hat{\mathbf{e}}_{k\lambda} = 0$. Then,

$$\hat{\mathbf{e}}_{k\lambda}\cdot\mathbf{Y}_{2,\pm2}^{(0)}(0,\phi_k) = i\sqrt{\frac{5}{16\pi}} \tag{4.76}$$

$$\hat{\mathbf{e}}_{k\lambda}\cdot\mathbf{Y}_{2,\pm1}^{(0)}(0,\phi_k) = \pm\frac{1}{8}\sqrt{\frac{5}{6\pi}}(\sqrt{3}-1) \tag{4.77}$$

$$\hat{\mathbf{e}}_{k\lambda}\cdot\mathbf{Y}_{2,0}^{(0)}(0,\phi_k) = -\frac{i}{8}\sqrt{\frac{15}{\pi}}. \tag{4.78}$$

Thus all of the $\Delta M = 0,\pm1,\pm2$ can be observed while the relative transition strengths are different.

4.3 Light shift – Far Off Resonance Trap (FORT)

The evaluation of transition matrix elements also enables the estimation of light shift, i.e. the trap depth of a FORT.

When atoms are in a laser field, according to the perturbation theory, the laser field causes a shift of an atomic energy level (ΔE). This is called "light shift" and can be described as

$$\Delta E = \sum_{b(\neq a)}\frac{|\langle b|H_{\rm int}|a\rangle|^2}{E_a - E_b}. \tag{4.79}$$

Here we assume that $H_{\rm int}$ describes a dipole interaction between atoms and a laser field, $|a\rangle$ is the level considered and $|b\rangle$ is the energy levels which connect to a through the interaction $H_{\rm int}$. E_a and E_b are the energies of $|a\rangle$ and $|b\rangle$, respectively.

We can utilize this property for trapping atoms in space because ΔE in (4.79) can be written by the intensity of the laser field $I(\mathbf{r})$,

$$U(\mathbf{r}) \equiv \Delta E(\mathbf{r}) = \frac{e^2 I(\mathbf{r})}{\epsilon_0 \hbar c}\Big[\sum_{b(\neq a)} |\langle b|r|a\rangle|^2 \frac{\omega_{ab}}{\omega_{ab}^2 - \omega^2}\Big]. \tag{4.80}$$

This equation shows that we can trap atoms because a position-dependent potential $U(\mathbf{r})$ makes the force $\mathbf{F}(\mathbf{r})$ to atoms,

$$\mathbf{F}(\mathbf{r}) = -\nabla U(\mathbf{r}). \tag{4.81}$$

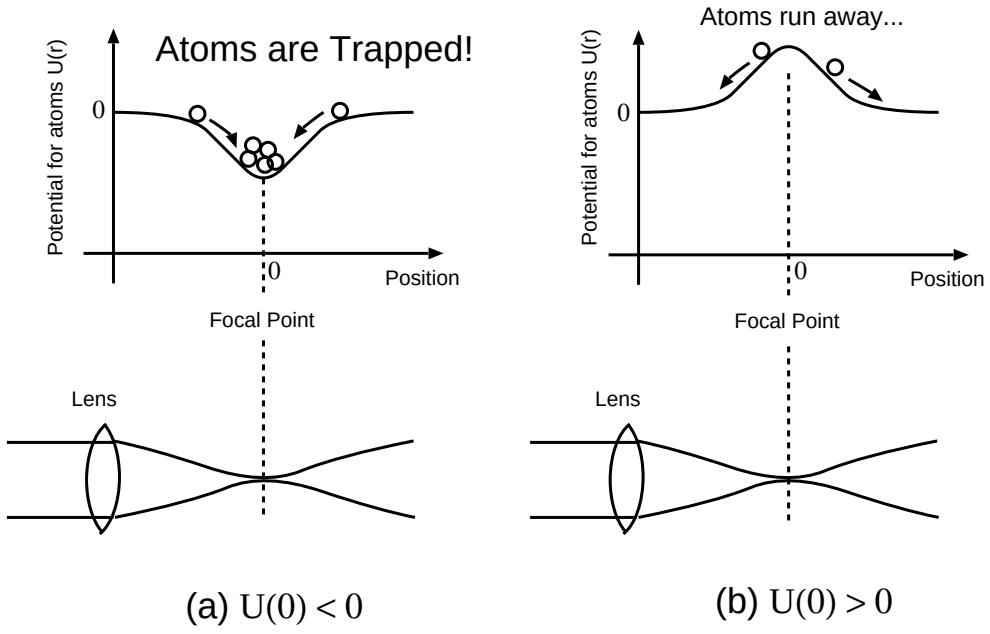

Figure 4.1: Whether we can trap atoms or not depends on the sign of the light shift.

Note that the sign of this potential could be both positive and negative, depending on the sign of parentheses [] in (4.80). If it is negative (−), the potential depth is lowest at a focal point and we can trap atoms. But if it is positive (+), we can not trap them because the focal point is the most unstable point for atoms (Fig.4.1). Hence, before trying to trap $^3P_2$ atoms in a FORT, it is better to calculate the trap depth or its sign at least. In the following discussion, the approximate calculation will be carried out.

4.3.1 Numerical estimation

From (4.79) and (4.31)

$$\Delta E = \sum_{b(\neq a)} \frac{|\langle b|H_{\rm int}|a\rangle|^2}{E_a - E_b} = \sum_{b(\neq a)} \frac{|\langle b|H_{\rm int}^{(+)} + H_{\rm int}^{(-)}|a\rangle|^2}{E_a - E_b}. \tag{4.82}$$

By using (4.40), light shift can be calculated as

$$\begin{aligned}
\Delta E(\mathbf{r}) &= \sum_{b(\neq a)} \Big[\frac{|\langle b; n-1|H_{\rm int}^{(-)}|a; n\rangle|^2}{(E_a + n\hbar\omega) - \{E_b + (n-1)\hbar\omega\}} + \frac{|\langle b; n+1|H_{\rm int}^{(+)}|a; n\rangle|^2}{(E_a + n\hbar\omega) - \{E_b + (n+1)\hbar\omega\}} \Big] \\
&= \sum_{b(\neq a)} \Big[\frac{|\langle b; n-1|H_{\rm int}^{(-)}|a; n\rangle|^2}{E_a - E_b + \hbar\omega} + \frac{|\langle b; n+1|H_{\rm int}^{(+)}|a; n\rangle|^2}{E_a - E_b - \hbar\omega} \Big] \\
&\simeq \sum_{b(\neq a)} \Big[\frac{e^2\hbar\omega n}{2\epsilon_0 V} |\hat{\mathbf{e}} \cdot \langle b|\mathbf{r}|a\rangle|^2 \Big\{ \frac{1}{E_a - E_b + \hbar\omega} + \frac{1}{E_a - E_b - \hbar\omega} \Big\} \Big] \\
&= \sum_{b(\neq a)} \Big[\frac{n\hbar\omega c}{V} \frac{e^2}{2\epsilon_0\hbar c} |\hat{\mathbf{e}} \cdot \langle b|\mathbf{r}|a\rangle|^2 \frac{2\omega_{ab}}{\omega_{ab}^2 - \omega^2} \Big] \\
&= \sum_{b(\neq a)} \Big[\frac{e^2 I(\mathbf{r})}{\epsilon_0\hbar c} |\hat{\mathbf{e}} \cdot \langle b|\mathbf{r}|a\rangle|^2 \frac{\omega_{ab}}{\omega_{ab}^2 - \omega^2} \Big],
\end{aligned} \tag{4.83}$$

where $I(\mathbf{r}) = n\hbar\omega c/V$ and $n + 1 \simeq n$ because the photon number n is very large in the present system. $\hat{\mathbf{e}}$ is a polarization vector (unit vector) of the FORT beam and $\mathbf{r}$ is parallel to the direction of an induced dipole moment. We use a linearly polarized laser beam. Thus, if we let the polarizing direction be z-axis[10],

$$\hat{\mathbf{e}} \cdot \langle b|\mathbf{r}|a\rangle = \langle b|r_0^{(1)}|a\rangle. \tag{4.84}$$

The light shift is given by

$$\Delta E(\mathbf{r}) = \frac{e^2 I(\mathbf{r})}{\epsilon_0\hbar c} \sum_{b(\neq a)} \Big[|\langle b|r_0^{(1)}|a\rangle|^2 \frac{\omega_{ab}}{\omega_{ab}^2 - \omega^2} \Big]. \tag{4.85}$$

It is very difficult to numerically calculate this equation because we have to consider all levels ($\sum_{b(\neq a)}$) which connect with the $^3P_2$ state through the interaction $H_{\rm int}$.

Here, instead, we will carry out the calculation by using the information about a few levels given in [60]. Of course, this is not good enough to determine whether we can trap $^3P_2$ atoms in a FORT or not. However in order to estimate the higher limit of the potential depth, it is worth carrying out.

By using the Wigner-Eckart theorem,

$$\begin{aligned}
\langle b|r|^3P_2\rangle &= \langle b, J, M|r_0^{(1)}|^3P_2, 2, M' = (0, \pm 1, \pm 2)\rangle \\
&= (-1)^{J-M} \begin{pmatrix} J & 1 & 2 \\ -M & 0 & M' \end{pmatrix} \langle b, J||r^{(1)}||^3P_2, 2\rangle.
\end{aligned} \tag{4.86}$$

[10]Details of tensor analysis for E1 transition will be discussed in 2.3.5.

In our experiment, only the case of $M - M' = \Delta M = 0$ has to be considered because a Wigner 3j-symbol doesn't vanish only when $M - M' = \Delta M = 0$. In this case, (4.85) becomes

$$\Delta E = \frac{e^2 I_0}{\epsilon_0 \hbar c} \begin{pmatrix} J & 1 & 2 \\ -M & 0 & M' \end{pmatrix}^2 |\langle a, J||r^{(1)}||^3P_2, 2\rangle|^2 \frac{\omega_{ab}}{\omega_{ab}^2 - \omega^2} \tag{4.87}$$

where I_0 is the intensity at the focal point.

The theoretical values of reduced matrix elements are listed in Table 4.1 [60]. Our experimental parameters are $I_0 = 2.1 \times 10^{10}$ W/m^2(532 nm, 6.4 W, beam waist=14 μm).

Table 4.1: Reduced matrix elements of Yb [60][atomic unit:a_0]

	^{3}D$_1$(5d6s)	^{3}D$_2$(5d6s)	^{3}D$_3$(5d6s)	^{1}D$_2$5d6s)	^{3}S$_1$(6s7s)
^{3}P$_2$(6s6p)	0.60	2.39	6.12	0.38	5.05

Table 4.2: Light shift [MHz]

	$^3D_1(5d6s)$	$^3D_2(5d6s)$	$^3D_3(5d6s)$	$^1D_2(5d6s)$	$^3S_1(6s7s)$	Total
$^3P_2(6s6p)(M{=}\pm2)$	–	0.50	1.31	0.0226	–	1.84
$^3P_2(6s6p)(M{=}\pm1)$	0.0222	0.125	2.10	0.00565	7.65	9.90
$^3P_2(6s6p)(M{=}0)$	0.0296	0	2.36	0	10.2	12.6

According to this estimation, light shifts are positive for all magnetic sublevels (1.84, 9.90 and 12.6 MHz). This means that we can not trap any atoms in the $^3P_2$ state. However, in this study, we succeeded in trapping $^3P_2$ atoms in a FORT at 532 nm. This means that the light shift for the $^3P_2$ state is negative and that the influence from upper levels we did not include in above calculations is very large.

Chapter 5

Line shift and broadening

Laser spectroscopy is one of the strongest techniques to understand the microscopic systems such as atoms, molecules and ions. Absorption and emission spectra include rich information about the atomic internal structure and interaction between atoms and an external field. Usually, such effects appear as line shifts and broadenings of spectra. Thus, in order to extract information as much as possible from the spectrum, we have to understand the mechanism of the line shift and broadening, which is the main purpose of this chapter.

5.1 Doppler shift and recoil shift

Let us consider the relativistic description of energy

$$E = \sqrt{(pc)^2 + (m_0c^2)^2}, \tag{5.1}$$

where p and m_0 are the atomic momentum and rest mass and c is the speed of light. Considering the case where an atom in the initial state (momentum p_i) is excited to the final state (momentum p_f) by absorbing a photon ($\hbar\mathbf{k}$), the conservation of energy and momentum are

$$h\nu_\mathrm{L} + \sqrt{(p_\mathrm{i}c)^2 + (m_0c^2)^2} = \sqrt{(p_\mathrm{f}c)^2 + (m_0c^2 + h\nu_0)^2} \tag{5.2}$$

$$\mathbf{p}_\mathrm{i} + \hbar\mathbf{k} = \mathbf{p}_\mathrm{f}, \tag{5.3}$$

where ν_L and $\mathbf{k}$ denote the frequency and wavenumber vector of the excitation laser and ν_0 is the resonance frequency between states i and f. Substituting (5.3) into (5.2) and taking some leading terms,

$$h\nu_\mathrm{L} = h\nu_0 + \mathbf{v}_\mathrm{i} \cdot (\hbar\mathbf{k}) + \frac{(\hbar k)^2}{2m_0} - \left(\frac{v_\mathrm{i}^2}{2c^2}\right) h\nu_0 + \cdots, \tag{5.4}$$

where $\mathbf{v}_\mathrm{i}$ is a velocity vector of atoms in the initial state. Due to the second, third and forth terms, the resonance frequency is shifted from ν_0 and broadened. In the following, details of these terms will be discussed.

First-order Doppler shift - Doppler broadening

Let us consider that the laser (frequency $\nu_{\rm L}$) is irradiated to an atom which moves with the velocity $v_{\rm i}$. Due to the Doppler effect, atoms absorb the photon whose frequency is, in the rest frame,

$$\nu_{\rm L} = \nu_0 + \frac{\nu_{\rm L}}{c}(\mathbf{e}_k \cdot \mathbf{v}_{\rm i}), \tag{5.5}$$

where $\mathbf{e}_k$ denotes the unit vector of $\mathbf{k}$. This is the second therm in (5.4), which is known as the first-order Doppler shift. However, due to the linear dependence on $\mathbf{v}$, the first-order Doppler shift are observed not as a frequency shift but as a broadening. Under thermal equilibrium conditions, the velocity of atoms is governed by the Maxwell velocity distribution,

$$p(v_k)\mathrm{d}v_k = \frac{1}{v_{\rm p}\sqrt{\pi}} \exp\left[-\left(\frac{v_k}{v_p}\right)^2\right] \mathrm{d}v_k, \qquad v_p = \sqrt{\frac{2k_{\rm B}T}{m}}, \tag{5.6}$$

where v_p is the most probable velocity and $v_k = \mathbf{e}_k \cdot \mathbf{v}_{\rm i}$. Thus substituting (5.5) into (5.6) and integrating it by v_k, the lineshape $I(\nu)$ is described as

$$I(\nu_{\rm L}) = I_0 \exp\left[\left(\frac{c}{v_{\rm p}}\frac{\nu_{\rm L}-\nu_0}{\nu_0}\right)^2\right], \tag{5.7}$$

and its full width at half maximum is

$$\delta\nu_{\rm FWHM} = 2\nu_0\sqrt{\left(\frac{2k_{\rm B}T}{mc^2}\right)\ln 2}. \tag{5.8}$$

For the ${}^1S_0 \leftrightarrow {}^3P_2$ transition (507 nm) in ^{174}Yb, the Doppler width (FWHM) is given by

$$\delta\nu_{\rm FWHM}[\mathrm{kHz}] = 32.0 \times \sqrt{T[\mu\mathrm{K}]}. \tag{5.9}$$

Second-order Doppler shift

The next frequency shift in (5.4) related to the atomic velocity $v_{\rm i}$ is the fourth term, which is known as the second-order Doppler shift (SODS). Due to its quadratic dependence on $v_{\rm i}$, the SODS leads to a frequency shift. For the ${}^1S_0 \leftrightarrow {}^3P_2$ transition (507 nm) in ^{174}Yb at 1 μK ($v_{\rm i} = v_{\rm p} = 1$ cm/sec), it is

$$\begin{aligned} \delta\nu_{\rm SODS} &= \left(\frac{v_{\rm i}^2}{2c^2}\right)\nu_0 \\ &= 3.1 \times 10^{-7}\ \mathrm{Hz}. \end{aligned} \tag{5.10}$$

Thus, the SODS can be safely neglected in this work. In general, the SODS yield a large influence to the high-energy transition in light atoms such as the UV transition in hydrogen [61].

Recoil shift

The third term in (5.4) corresponds to the frequency shift caused by the momentum of a photon $\hbar k$ received by an atom. It is called a recoil shift. For the ${}^1S_0 \leftrightarrow {}^3P_2$ transition (507 nm) in ^{174}Yb, it is given by

$$\begin{aligned} \delta\nu_{\text{recoil}} &= \frac{\hbar k^2}{4\pi m} \\ &= 4.423 \text{ kHz}. \end{aligned} \tag{5.11}$$

5.2 Temperature shift

When atoms are confined in a trap, vibrational energy levels of the trap are occupied, depending on the Maxwell-Boltzmann distribution at an atomic temperature T. In such a case, the peak position of the spectrum does not correspond to the bottom of the trap but to the peak position of the Maxwell-Boltzmann distribution in a trap [62]. As a result, the resonance frequency slightly shifts except for the case of the magic wavelength. Such a spectral shift which is referred to as a temperature shift was introduced in [63] and is briefly summarized here.

According to the Fermi's golden rule, the absorption spectrum is given by

$$I(\omega) = \sum_{i,f} \rho_i |\langle f|V|i\rangle|^2 \delta(\omega - \omega_{f,i}), \tag{5.12}$$

where ρ_i is the distribution function for the trapped atoms, $|i\rangle = |g\rangle |\mathbf{n}\rangle$ and $|f\rangle = |ex\rangle |\mathbf{m}\rangle$ are the initial and final states of an atom. $|\mathbf{n}\rangle_{\text{g}} = |n_x, n_y, n_z\rangle_{\text{g}}$ and $|\mathbf{m}\rangle_{\text{ex}} = |m_x, m_y, m_z\rangle_{\text{ex}}$ describes the vibrational levels of an atom in a harmonic trap. Let the incident direction of the excitation laser be x. Then the interaction V between an atom and an excitation laser can be given by

$$V = \sum_{\text{ex}} \left(|\text{ex}\rangle T_{\text{ex}} \exp\left(i\kappa x\right) \langle \text{g}| + \text{H.c.} \right), \tag{5.13}$$

where T_{ex} describes the transition operator (rank 2 irreducible tensor in case of the M2 transition) and κ describes the wave number of the excitation laser.

Atoms in the ground state is in a certain vibrational level of a harmonic trap. Such atoms can be excited to one of the vibrational levels in a harmonic trap. Then, strictly speaking, the spectral shape $I(\omega)$ is obtained by summing the overlap integral over possible vibrational levels in (5.12). However, when the number of atoms N is large as in this experiment $N \sim 10^5$, such calculations are not realistic.

We think of the semiclassical approximation which is valid when the temperature of atoms is so high that the semiclassical approximation is valid. In this approximation, we can label atoms by the radius vector $\mathbf{r}$ and momentum vector $\mathbf{p}$ and the density of states in the six-dimensional phase space is h^{-3}. Then, the number density of atoms $\rho(\mathbf{r}, \mathbf{p}, T)$ in the phase space is

$$\rho(\mathbf{r}, \mathbf{p}, T) = \frac{1}{h^3} \frac{1}{e^{\beta(H_{\text{g}} - \mu)} \pm 1}, \tag{5.14}$$

where + and − correspond to the Fermi-Dirac distribution and the Bose-Einstein distribution, respectively. For the present purpose, it is true that we have to consider only the Maxwell-Boltzmann distribution. However, for the future convenience, we derive the spectral shape for all distributions. $H_{\rm g}$ describes the energy of an atom in a harmonic trap and given by

$$H_{\rm g,ex}(\mathbf{r},\mathbf{p}) = \frac{p^2}{2M} + \frac{M\Omega_{\rm g,ex}^2(x^2+\lambda_y y^2+\lambda_z z^2)}{2}, \tag{5.15}$$

where M is the atomic mass, $\Omega_{\rm g,ex}$ is the trap frequency for the ground state and the excited state, respectively. The dimensionless parameters λ_y and λ_z describe the anisotropy of the trap. Substituting (5.13), (5.14) and (5.15) into (5.12) and considering the energy conservation gives

$$I(\omega) = A\int \rho(\mathbf{r},\mathbf{p},T)\delta(\omega-\omega_{\mathbf{r},\mathbf{p}})\mathrm{d}^3\mathbf{r}\mathrm{d}^3\mathbf{p}, \tag{5.16}$$

$$\omega_{\mathbf{r},\mathbf{p}} = \frac{M(\Omega_{\rm ex}^2-\Omega_{\rm g}^2)(x^2+\lambda_y y^2+\lambda_z z^2)}{2\hbar} + \frac{p_x\kappa}{M} + \omega_{\rm rec} + \omega_0 \tag{5.17}$$

where $A=|T_{\rm ex}|^2$ and $\omega_{\rm rec}=\hbar\kappa^2/M$ is the recoil energy of the excitation laser.

The delta function in (5.16) can be described as

$$\delta(\omega-\omega_{\mathbf{r},\mathbf{p}}) = \left(\frac{M}{\kappa}\right)\delta\left[p_x - \left(\frac{M}{\kappa}\right)\left\{\omega-\omega_{\max}+\frac{M\Omega_{\rm g}^2}{2\hbar}m_{\rm ex}r^2\right\}\right], \tag{5.18}$$

where $\omega_{\max}=\omega_0+\omega_{\rm rec}$ and $m_{\rm ex}=1-\Omega_{\rm ex}^2/\Omega_{\rm g}$. Thus we can perform the integration of p_x and let $\mathrm{d}p_y\mathrm{d}p_z = p\cos\phi\mathrm{d}p\mathrm{d}\phi$, we find

$$I(\omega) = \left(\frac{2\pi M}{h^3\kappa}\right)\int \mathrm{d}^3\mathbf{r}\int_0^\infty \frac{p\mathrm{d}p}{e^{\left(\frac{\beta}{2M}\right)p^2-\left[-\left(\frac{\beta M}{2\kappa^2}\right)\left\{\omega-\omega_{\max}+\frac{M\Omega_{\rm g}^2}{2\hbar}m_{\rm ex}r^2\right\}^2-\frac{\beta M\Omega_{\rm g}^2}{2}r^2+\beta\mu\right]}\pm 1}, \tag{5.19}$$

where the integration of p is known as a polylogarithm $\mathrm{Li}_n(x)$ which satisfies

$$\int_0^\infty \frac{k^s\mathrm{d}k}{e^{k-\mu}\pm 1} = \mp\Gamma(s+1)\mathrm{Li}_{1+s}(\mp e^\mu), \tag{5.20}$$

where $\Gamma(x)$ is the gamma function. When s=0, $\Gamma(1)=1$ and $\mathrm{Li}_1(x) = -\ln(1-x)$. Thus the lineshape is given by

$$I(\omega) = \frac{A'(\lambda_y,\lambda_z)}{16\pi\alpha^6\Omega_{\rm g}^6 p^{5/2}} \times \begin{cases} \displaystyle\int_0^\infty \pm\ln\left[1\pm\exp\left[\beta\mu - y^2 - p\left(\omega-\omega_{\max}+\frac{m_{\rm ex}y^2}{\beta\hbar}\right)^2\right]\right]y^2\mathrm{d}y \\ \qquad (+\text{: Fermi}, -\text{ : Bose}) \\ \displaystyle\int_0^\infty \exp\left[\beta\mu - y^2 - p\left(\omega-\omega_{\max}+\frac{m_{\rm ex}y^2}{\beta\hbar}\right)^2\right]y^2\mathrm{d}y \\ \qquad (\text{Maxwell}) \end{cases} \tag{5.21}$$

5.3 Collision shift and broadening

Interactions between atoms leads to the line shifts and broadenings, which is known as the collision shift and broadening. Studies of such shift and broadening have been considerably improved [64, 65, 66, 67, 68] because the collisional line shift is a major part in the inaccuracy of the present time and frequency clocks such as Cs or Rb fountains [69, 70].

For bosons at very low temperatures, only s-wave scattering occurs which can be characterized by the scattering length a. For a nondegenerate gas of bosons, the mean-field energy due to elastic collisions between atoms shift the energy level of the atom, which is given by

$$\Delta E = h\left(\frac{4\hbar n}{m}\right) a_{11}, \tag{5.22}$$

where n is the density and a_{11} is the s-wave scattering length of the collision between state 1 atoms. When atoms are excited to the state 2, the energy level of the 2 state is also shifted due to the atomic interaction between atoms in the 1 state and 2 state. This interaction can be characterized by the scattering length a_{12} and the shift of the energy level of the 2 state is given by replacing a_{11} with a_{12}in (5.22). As a result of shifts of energy levels both of the 1 state and 2 state, the resonance frequency between these state also shifts, which is give by the difference between them,

$$\Delta\nu_{12} = (a_{12} - a_{11})\frac{4\hbar n_1}{m}, \tag{5.23}$$

where n_1 is the density of atoms in the 1 state. Since we do not consider the interaction between atoms in the 2 state, (5.23) is valid for the weak excitation in which the 2 state atoms interact only with the 1 state atoms. More rigorous and general description has been traditionally given using the quantum Boltzmann equation, in which the collision shift $\Delta\nu_{\rm col}$ and the broadening $\Delta\gamma_{\rm col}$ are described by

$$\Delta\nu_{\rm col} = \frac{2\hbar}{m}\sum_j n_j(1+\delta_{1j})(1+\delta_{2j})(a_{2j}-a_{1j}), \tag{5.24}$$

$$\Delta\gamma_{\rm col} = \frac{2\hbar}{m}\sum_j n_j(1+\delta_{1j})(1+\delta_{2j})(a_{1j}^2+a_{2j}^2)k, \tag{5.25}$$

where δ_{ab} is the Kronecker delta and $\hbar k$ is the relative momentum of the colliding atoms. $\hbar k = mv_{\rm rel}/2$ where $v_{\rm rel} = 4\sqrt{(k_{\rm B}T)/(\pi m)}$ is the mean relative velocity. Note that we neglect the inelastic contributions between atoms in the state 1. As for Yb in a FORT, only possible inelastic process is the three body recombination, which is negligibly small [24]. In this study, we have to consider only the case in $j = 1$ in (5.24) and (5.25). Thus, the collisional shift and broadening for Yb atoms at 1 μK is given by

$$\begin{aligned}\Delta\nu[\mathrm{kHz}] &= \frac{4\hbar}{m}(a_{12}-a_{11})n_1 \\ &= 1.4494\times10^{-15}\ (a_{12}-a_{11})[\mathrm{nm}]\times n_1\ [\mathrm{cm}^{-3}]\end{aligned} \tag{5.26}$$

$$\begin{aligned}\Delta\gamma[\mathrm{kHz}] &= \frac{4\hbar}{m}(a_{11}^2 + a_{12}^2)k \\ &= 1.554 \times 10^{-17}\ (a_{11}^2 + a_{12}^2)[\mathrm{nm}^2] \times n_1\ [\mathrm{cm}^{-3}] \times \sqrt{T[\mu\mathrm{K}]}. \end{aligned} \tag{5.27}$$

For the typical parameters $n_1 = 5{\times}10^{13}$ cm^{-3}, $a_{11} = 5.53$ nm, $a_{12} = -33$ nm and $T = 1$ μK, the collision shift and broadening become 2.8 kHz and 0.87 kHz, respectively. Thus both are relatively small if we compare them to other shifts and broadening. However, collisional shift and broadening plays a significant role in a BEC spectrum.

5.4 Other shifts and broadenings

Interaction time broadening

Since the interaction time between atoms and an excitation pulse is finite, it also yields a spectral broadening. Let us consider the square excitation pulse given by

$$f(t) = \begin{cases} E_0 \cos\omega_0 t & (-\tau/2 < t < \tau/2) \\ 0 & (\text{otherwise}) \end{cases}, \tag{5.28}$$

where E_0 is the amplitude, ω_0 is the laser frequency and τ is the interaction time. From the inverse Fourier transformation of $f(t)$, the power spectrum (of the positive frequency component) is given by

$$|F(\omega - \omega_0)|^2 = \left(\frac{E_0\tau}{2}\right)^2 \frac{\sin^2[(\omega-\omega_0)\tau/2]}{[(\omega-\omega_0)\tau/2]^2}. \tag{5.29}$$

The full width of half maximum (FWHM) of this spectrum is given by

$$\Delta\nu_{\mathrm{int}}^{\mathrm{FWHM}} = \frac{0.8859}{\tau}. \tag{5.30}$$

Thus the laser frequency is broadened due to the finite interaction time τ. This is the interaction time broadening. For example, a square excitation pulse for 1 ms has the interaction time broadening of 886 Hz. In this work, the pulse width of the excitation laser is at least 10 ms ($\Delta\nu_{\mathrm{int}}^{\mathrm{FWHM}} = 89$ Hz). Hence, it is negligible.

Saturation broadening

Let us consider N two-level atoms. By using the Einstein coefficients A and B, the stationary state including the spontaneous emission and stimulated emission and absorption of the radiation field $\rho(\nu)$ is given by

$$(B\rho(\nu) + A)N_2 = B\rho(\nu)N_1, \tag{5.31}$$

where N_1 and N_2 are the number of atoms in the ground and excited state, respectively. Here we introduce the saturation parameter S defined by

$$S = \frac{2B}{A}\rho(\nu). \tag{5.32}$$

From (5.31), the population N_2 is written as

$$N_2 = \frac{S}{2(1+S)}N. \tag{5.33}$$

When we consider the atomic transition, the frequency dependence of absorption B is given by the Lorentzian function. Hence,

$$S = \frac{I}{I_{\text{sat}}}\frac{(\frac{1}{4\pi\tau})^2}{(\frac{1}{4\pi\tau})^2 + (\nu-\nu_0)^2}, \quad I_{\text{sat}} = \frac{\pi hc}{3\lambda^3\tau} \tag{5.34}$$

where τ is the lifetime of the excited state, I and ν are the intensity and frequency of the excitation laser. Substituting (5.34) into (5.33), we have

$$N_2 = \frac{I/I_{\text{sat}}}{2(1+I/I_{\text{sat}})}\frac{(\frac{\gamma}{2}\sqrt{1+I/I_{\text{sat}}})^2}{(\frac{\gamma}{2}\sqrt{1+I/I_{\text{sat}}})^2 + (\nu-\nu_0)^2}, \tag{5.35}$$

where $\gamma = 1/(2\pi\tau)$. This is a Lorentzian function with the broadened linewidth

$$\gamma' = \gamma\sqrt{1+I/I_{\text{sat}}}. \tag{5.36}$$

Thus the observed linewidth γ' becomes broader than the original linewidth by a factor of $\sqrt{1+I/I_{\text{sat}}}$ which is known as saturation broadening (or power broadening).

Chapter 6

Inelastic collisions in optically trapped ultracold metastable ytterbium

Optical trapping of dense and ultracold metastable $^3P_2$ atoms has been successfully demonstrated and their collisional properties in a FORT have been investigated.

Previously, several laboratories have realized laser cooling and trapping of $^3P_2$ atoms in a magnetic trap. In spite of successes of trapping of $^3P_1$ atoms, evaporative cooling of $^3P_2$ atoms in a magnetic trap turned out to be unsuccessful due to trap loss caused by strong multichannel collision processes. The loss induced by multichannel collisions in a magnetic trap can be overcome by employing a FORT. Thus we have first demonstrated the optical trapping of Yb[$^3P_2$] atoms in every magnetic sublevel. Also, the trap frequency for the atoms in the $^3P_2$ state in a FORT was measured by using a parametric resonance technique. Whether or not we can trap Yb[$^3P_2$] in a FORT at 532 nm was unknown before this study because the precise calculation of transition strength between the $^3P_2$ state and a lot of upper levels which include relativistic effects is difficult for heavy atoms such as Yb. Moreover, during the course of the experiment, the light shift of magnetic sublevels $M = \pm 1, \pm 2$ of the $^3D_2$ state was also determined. These experimental results must be valuable for the precise theoretical calculations of Yb which is important, for example, to understand the ultraprecise atomic clock using the clock transition between the ground state and the metastable state in Yb.

By exciting pre-cooled Yb[$^1S_0$] atoms in a crossed FORT, we have successfully obtained high density ultracold metastable Yb[$^3P_2$] atoms . These atoms are prepared at a density of 2×10^{13} cm^{-3} and at a temperature of less than 2 μK. Although in principle a PSD could be increased by further evaporative cooling of the Yb[$^3P_2$] atoms to achieve a BEC, we found this impossible due to the large trap loss.

We, then, next measured the trap lifetime of atoms in the $^3P_2$ state trapped in a FORT and quantitatively measured the inelastic collision rate constant. Considering the suppression of multichannel collisional loss in a FORT which can trap atoms in every magnetic sublevel of the $^3P_2$ state with zero magnetic field, the observed inelastic collision rate is anomalously large. As a result, a different inelastic collision process – fine-structure

changing collisions – is strongly suggested. The previous theoretical works revealed details of fine-structure changing transitions in collisions of Mg[^3P_j], O[^3P_j], Sc[^2D_j], and Ti[^3F_j] atoms with closed-shell atoms at a high temperature. However, there has not been no theoretical work on the fine-structure changing collisions between atoms in the $^3P_2$ state at ultralow temperature achieved in the present work. As our experimental results suggest, further theoretical investigation is warranted.

6.1 Optical trapping of Yb atoms in the $^3P_2$ state

6.1.1 Preparation and detection of atoms in the $^3P_2$ state in the FORT

Basic procedure

Our typical procedure to prepare and detect atoms in the $^3P_2$ state is summarized in Fig. 6.1. At the first stage A, we prepare cold ^{174}Yb atoms in the ground state in a FORT by the method described in Chap. 2 and briefly summarized here. With about 10 s loading, we typically collect 10^7 Yb atoms in the ground state at a temperature below 50 μK by the MOT using the narrow intercombination transition $^1S_0 \leftrightarrow {}^3P_1$. These atoms are then transferred to a single or crossed FORT created by focused diode-pumped solid state 10 W-lasers at 532 nm. After carrying out evaporative cooling by gradually reducing the trap depth, we typically have 10^6 atoms at a temperature of 30 μK in a single FORT. When we use a crossed FORT configuration and perform evaporative cooling, a temperature of atoms reaches below 1 μK.

At the next stage B, we optically excite atoms to the $^3P_2$ state in a FORT. We use the intermediate $^3D_2$ state for the excitation (transition linewidth: 346 kHz [71]) and the subsequent spontaneous decay to the $^3P_2$ state with the lifetime 460 ns of the $^3D_2$ state. From the $^3D_2$ state, about 10% of atoms can decay to the $^3P_2$ state by the spontaneous emission. Although other atoms decay to the $^3P_1$ state, they immediately decay to the ground state with the lifetime 875 ns of the $^3P_1$ state and are re-excited to the $^3D_2$ state. Thus, after iterating this excitation cycle for several times, we can transfer all atoms to the $^3P_2$ state typically within 5 ms. In order to efficiently excite atoms, we stabilize a blue GaN laser diode (404 nm) by an external cavity laser diode system combined with an optical feedback technique (see section 2.4.3). The resulting linewidth is narrowed to 1 MHz for 0.5 s. The excitation laser is superposed with the FORT laser (see Fig. 6.2) and the peak intensity at atoms reaches 140 W/cm^2. Just after the excitation, we irradiate a short blast pulse which blows remaining atoms in the ground state by using the strong $^1S_0 \leftrightarrow {}^1P_1$ transition.

The $^1S_0 \leftrightarrow {}^3D_2$ transition (404 nm) is the electric quadrupole (E2) transition whose properties are summarized in Table.6.1. In this experiment, as shown in Fig. 6.2(top), we set $\vec{\mathbf{e}}_{404} \parallel z$ (or $\vec{\mathbf{e}}_{404} \perp z$) and $\vec{\mathbf{e}}_k \parallel x$, where $\vec{\mathbf{e}}_{404}$ and $\vec{\mathbf{e}}_k = \vec{\mathbf{k}}/|\vec{\mathbf{k}}|$ are the polarization and the wavenumber vectors of the 404 nm excitation laser. Thus atoms are excited to the $^3D_2$, $m = \pm 1$ and $m = \pm 2$ in case of $\vec{\mathbf{e}}_{404} \parallel z$ and $\vec{\mathbf{e}}_{404} \perp z$, respectively due to the

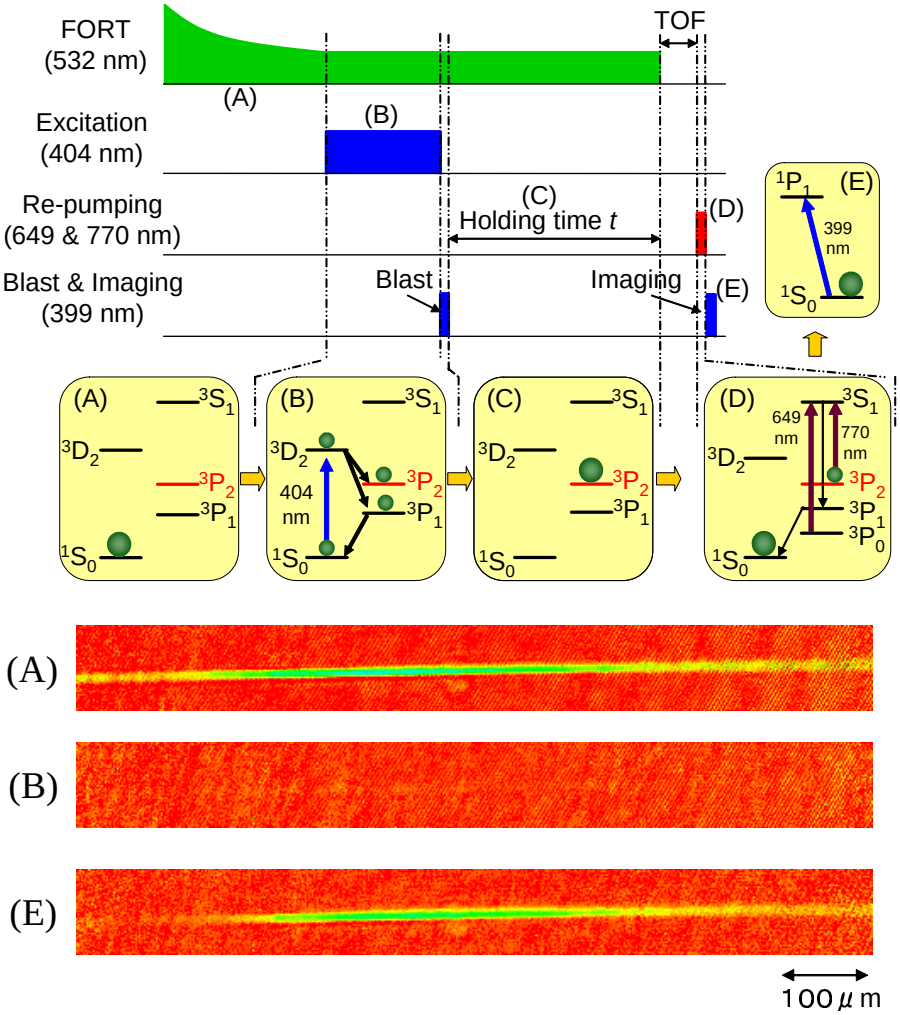

Figure 6.1: Experimental procedures to excite atoms in the $^3P_2$ state. Absorption images of atoms in the ground state at stages (A), (B) and (E) are also shown. (A): Yb atoms trapped in a MOT are transferred to the FORT and then are excited to the $^3P_2$ state in the FORT via the intermediate $^3D_2$ state and subsequent spontaneous decay ($^3D_2 \rightarrow ^3P_2$) (B). Since all atoms are now in the $^3P_2$ state, no atoms are observed in the absorption image (B) of atoms in the ground state. (C): After the excitation, metastable atoms are left in the FORT during the holding time t. (D): In order to measure temperature and the number of atoms by using an absorption imaging, metastable atoms are repumped to the ground state by 770 nm ($^3P_2 \leftrightarrow ^3 S_1$) and 649 nm ($^3P_0 \leftrightarrow ^3 S_1$) laser pulses of 100 μs and then atoms are detected (E).

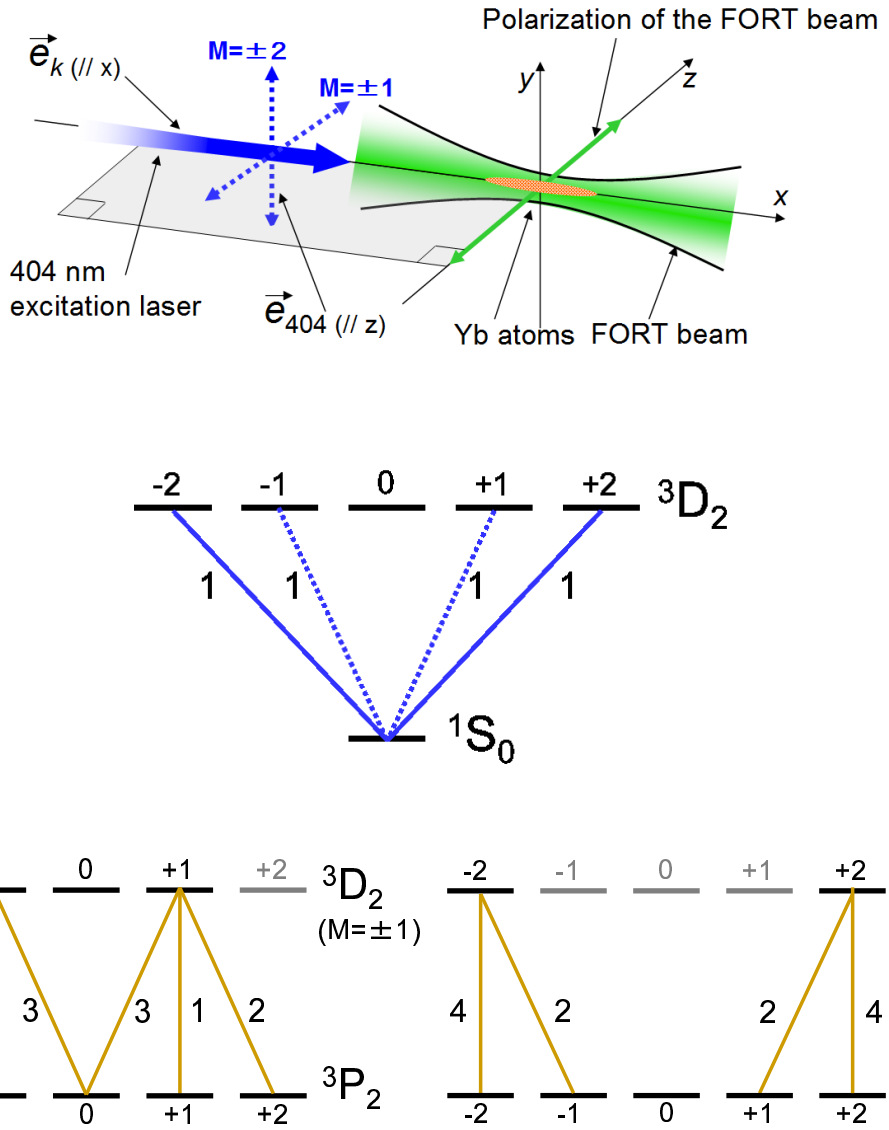

Figure 6.2: (Top) Polarizations of the excitation laser (404 nm) and FORT laser are shown for two cases used in this experiment. (Bottom) Relative ratio of transition probability via spontaneous emission from the $^3D_2$ state to the $^3P_2$ state are shown for two configurations indicated above.

selection rule (see Chapter 4). Subsequently, atoms decay to the magnetic sublevels of the $^3P_2$ state $|m|$=0, 1, and 2 with the transition ratio shown in Fig. 6.2(bottom).

At the stage C, we hold metastable atoms in a FORT for a time t. Then, at the stage D, in order to measure the temperature and the number of atoms in the $^3P_2$ state with a time-of-flight (TOF) technique, we rapidly repump all the metastable $^3P_2$ atoms to the ground state after a TOF time. A 770 nm ($^3P_2 \leftrightarrow {}^3S_1$) resonant pulse excites atoms from the $^3P_2$ state to the $^3S_1$ state, from which all the $^3P_2$, $^3P_1$, and $^3P_0$ states are populated through spontaneous decay. By simultaneous application of a 649 nm ($^3P_0 \leftrightarrow {}^3S_1$) resonant pulse, all atoms return through the $^3P_1$ state to the ground state where we can use an absorption imaging technique using the strong cyclic $^1S_0 \leftrightarrow {}^1P_1$ transition at the stage E. Since 100 μs duration for the repumping procedure is short enough compared with a typical TOF time, we can safely regard that the observed atomic distribution precisely reflects that of atoms in the $^3P_2$ state.

Table 6.1: Important values of the $^1S_0 \leftrightarrow {}^3D_2$ transition [71].

		$^1S_0 \leftrightarrow {}^3D_2$	
Wavelength	λ	404	nm
Lifetime	τ	460	ns
Natural linewidth	$\dfrac{\Gamma}{2\pi} = \dfrac{1}{2\pi\tau}$	346	kHz
Saturation Intensity	$I_{\rm sat} = \dfrac{\pi hc}{3\lambda^3\tau}$	0.69	mW/cm^2
Doppler Broadening at 1 μK (FWHM)	$\delta\nu_{\rm D}$	40	kHz

Excitation rate ($^1S_0 \leftrightarrow {}^3D_2$)

Let us calculate the excitation rate of the $^1S_0 \leftrightarrow {}^3D_2$ (E2) transition. From the Fermi's golden rule, the average transition rate $R_{\rm ab}$ from one state $|a\rangle$ to the other state $|b\rangle$ is given by

$$R_{\rm ab} = \frac{2\pi}{\hbar^2}|\langle {}^3D_2|H_{\rm int}|{}^1S_0\rangle|^2 \int_0^\infty \delta(\omega - \omega_{\rm ab}) g(\omega) {\rm d}\omega \tag{6.1}$$

where $g(\omega)$ is the normalized Lorentzian lineshape

$$g(\omega) = \frac{\gamma/2\pi}{(\omega - \omega_{\rm ab})^2 + \gamma^2/4}. \tag{6.2}$$

Here $\gamma/2\pi$ is the linewidth of the (laser or atomic) spectrum. Substituting a squared matrix element in (4.62) for this equation and using the relation $I = n(\hbar\omega)c/V$ where I is a laser intensity, we have

$$|\langle {}^3D_2|H_{\rm int}|{}^1S_0\rangle|^2 = \frac{\omega^2 e^2}{16\epsilon_0 c^3} I |\langle {}^3D_2|Q^{(2)}|{}^1S_0\rangle|^2. \tag{6.3}$$

As for the matrix element $\langle {}^3D_2|Q^{(2)}|{}^1S_0\rangle$, we have to consider the magnetic sublevels of the $^3D_2$ state. In other words, we should calculate

$$\langle {}^3D_2, J=2, M|Q^{(2)}|{}^1S_0, J'=0, M'=0\rangle. \tag{6.4}$$

We can use the Wigner-Eckart theorem to factor (6.4) because $Q^{(2)}$ is an irreducible tensor. For any possible transitions from the $^1S_0$ state to the $^3D_2$ state, the matrix element takes the same value because

$$\begin{pmatrix} 2 & 2 & 0 \\ -M & q(=M) & 0 \end{pmatrix}^2 = \frac{1}{5}. \qquad (M=-2,-1,0,1,2). \tag{6.5}$$

Thus the matrix element can be calculated as

$$|\langle {}^3D_2, J=2, M|Q^{(2)}|{}^1S_0, J'=0, M'=0\rangle|^2 = \Big(\frac{1}{\sqrt{5}}\langle {}^3D_2, 2||Q^{(2)}||{}^1S_0, 0\rangle\Big)^2. \tag{6.6}$$

The transition rate $R_{\rm ab}$ is obtained by (6.1) and (6.6),

$$R_{\rm ab}(\omega) = I\frac{2\pi}{\hbar^2}\frac{\omega^2 e^2}{8\epsilon_0 c^3}\Big(\frac{1}{\pi\gamma}\Big)\Big(\frac{1}{\sqrt{5}}\langle {}^3D_2, 2||Q^{(2)}||{}^1S_0, 0\rangle\Big)^2. \tag{6.7}$$

For numerical computations of the transition rate $R_{\rm ab}$, a reduced matrix element is the only unknown parameter. It is theoretically calculated in [71] for the $^1S_0 \rightarrow {}^3D_2$ transition.

$$\frac{1}{\sqrt{5}}\langle {}^3D_2, 2||Q^{(2)}||{}^1S_0, 0\rangle \simeq 0.5(4)a_0^2 \qquad \text{(theory)} \tag{6.8}$$

In this study, the peak intensity of the 404 nm excitation laser $I(=2P/(\pi w_0^2))$ is 140 W/cm^2(P = 2 mW, w_0 = 30 μm) and the linewidth of the $^1S_0 \leftrightarrow {}^3D_2$ transition is $1/\gamma$ = 460 ns. Therefore the excitation rate at the resonant frequency can be computed as $R_{\rm ab}$ = 66 kHz.

By using this result, let us simulate the excitation process. The rate equations are

$$\frac{{\rm dN_S(t)}}{{\rm dt}} = -R_{\rm ex}N_{\rm S}(t) + R_{\rm P_1}N_{\rm P_1}(t) \tag{6.9}$$

$$\frac{{\rm dN_D(t)}}{{\rm dt}} = R_{\rm ex}N_{\rm S}(t) - R_{\rm D}N_{\rm D}(t) \tag{6.10}$$

$$\frac{{\rm dN_{P_1}(t)}}{{\rm dt}} = 0.88R_{\rm D}N_{\rm D}(t) - R_{\rm P_1}N_{\rm P_1}(t) \tag{6.11}$$

$$\frac{{\rm dN_{P_2}(t)}}{{\rm dt}} = 0.12R_{\rm D}N_{\rm D}(t) \tag{6.12}$$

where $N_{\rm S}(t)$, $N_{\rm D}(t)$, $N_{\rm P_1}(t)$ and $N_{\rm P_2}(t)$ are the number of atoms of the $^1S_0$, $^3D_2$, $^3P_1$ and $^3P_2$ states, respectively. Constant $R_{\rm P_1}$, $R_{\rm D}$ and $R_{\rm ex}$ are $1/R_{\rm P_1} = 875$ ns, $1/R_{\rm D} = 460$ ns and $R_{\rm ex}$= 55 Hz[1]. 0.88 and 0.12 are the branching ratio of the $^3D_2 \rightarrow ^3{\rm P}_1(0.88)$ and $^3D_2 \rightarrow ^3 P_2(0.12)$ transitions.

The results of numerical computations are shown in Fig. 6.3 as a function of excitation time. According to this result, we can excite all atoms in the ground state to the $^3P_2$ state in $3 \sim 4$ ms, which is almost consistent with an experimental result.

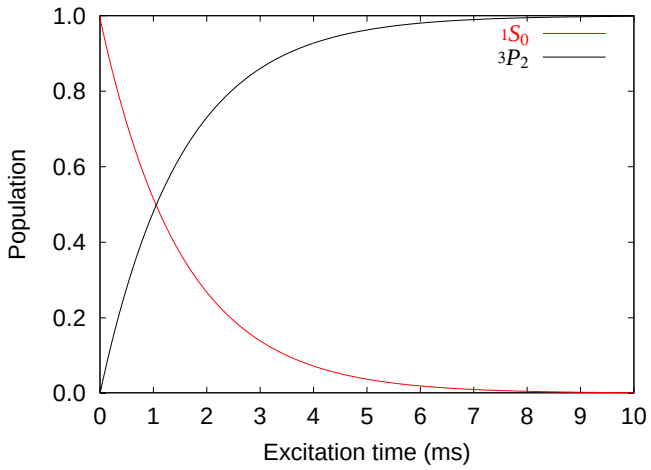

Figure 6.3: Numerical simulations of the excitation $^1S_0 \leftrightarrow ^3P_2$ through the $^3D_2$ state. $3 \sim 4$ ms is required to excite all atoms, which is consistent in an experimental result.

[1]The effect of saturation broadening is included.

6.1.2 Polarizabilities of the $^3D_2$ state

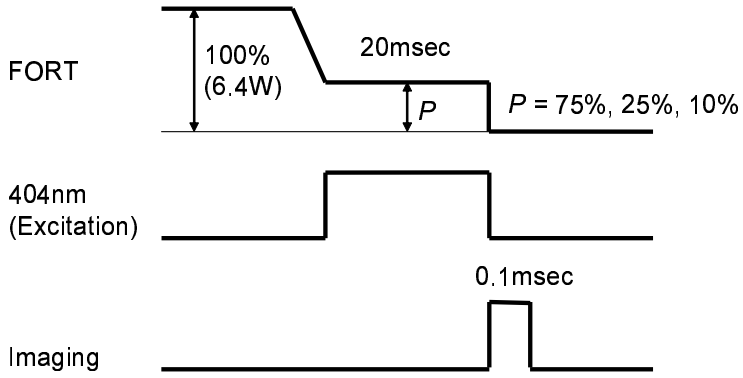

Figure 6.4: Time sequence for the measurement of polarizabilities of the $^3D_2$ state.

In a strong laser field, the energy levels of atoms shift (see section 4.3). Due to this light shift, the resonance frequency of atoms in a FORT is shifted from the unperturbed one. This is because the light shifts induced to atoms in the ground state and in the excited state are, in general, different from each other [2]. The coefficient $\alpha_{|a\rangle}$ of the light shift to laser intensity I for the state $|a\rangle$ which is defined by

$$\Delta E_{|a\rangle} = \frac{\alpha_{|a\rangle}}{4} I, \tag{6.13}$$

is called polarizability.

We determined the polarizability of the $^3D_2$ state. The resonance frequency $h\nu$ of the $^1S_0 \leftrightarrow {}^3D_2$ transition in a FORT is given by

$$h\nu = h\nu_0 - \frac{I}{4}(\alpha_{|^3D_2\rangle} - \alpha_{|^1S_0\rangle}), \tag{6.14}$$

where ν_0 is the unperturbed resonance frequency. We measured dependence of shift of the resonance frequency on the FORT-laser intensity, which corresponds to the measurement of $\alpha_{|^3D_2\rangle} - \alpha_{|^1S_0\rangle}$ in (6.14). Since the polarizability of the ground state $\alpha_{|^1S_0\rangle}$ can be precisely estimated, we can determine $\alpha_{|^3D_2\rangle}$.

The time sequence of the measurement is schematically shown in Fig. 6.4. After loading atoms in a single FORT, excitation spectra were taken for various FORT powers. Frequency of the 404 nm excitation laser was scanned by changing the radio frequency (RF) applied to the AOM which compensates the frequency difference between the transfer cavity and the excitation laser (see section 2.4.3). Polarizabilities of two different magnetic sublevels ($M = \pm 1, \pm 2$) of the $^3D_2$ state were measured by choosing the proper polarization of the 404 nm excitation laser (see Fig. 6.2).

[2] By choosing a so-called "Magic wavelength", we can cancel the difference of the light shift between the ground state and the excited state. Such technique is crucially important in the frequency standard and atomic clock experiment using neutral atoms in a FORT.

Experimental results

The experimental results are shown in Fig. 6.5 for magnetic sublevels $M = \pm 1$ and ± 2 of the $^3D_2$ state. The excitation spectrum for different FORT powers are shown and frequency shifts are clearly observed. By fitting Gaussian functions (solid lines) to the data, we determined the resonance frequency of each peak. The shift of the resonance frequency are summarized in Fig. 6.6. According to (6.14), both lines should coincide at zero FORT power in zero magnetic field. In Fig. 6.6, two independently fitted lines are shown. One can find that two lines coincide at zero FORT power, which proves that the experimental results are consistent with (6.14). Using the polarizability of the ground state, the polarizability of the $^3D_2$ state are determined as listed in Table 6.2.

Table 6.2: Polarizabilities of the $^3D_2$ state. FORT laser is linearly polarized at 532 nm (ω_0 = 15 μm). The listed value for the $^1S_0$ state is calculated by the information of $^1S_0 \leftrightarrow {}^1P_1$ and $^1S_0 \leftrightarrow {}^3P_1$ transitions and contributions of other upper levels are neglected.

State	Polarizability (Hz$\cdot$ cm^2/W)
$^3D_2(M = \pm 2)$	+18
$^3D_2(M = \pm 1)$	-23
$^1S_0$	-24

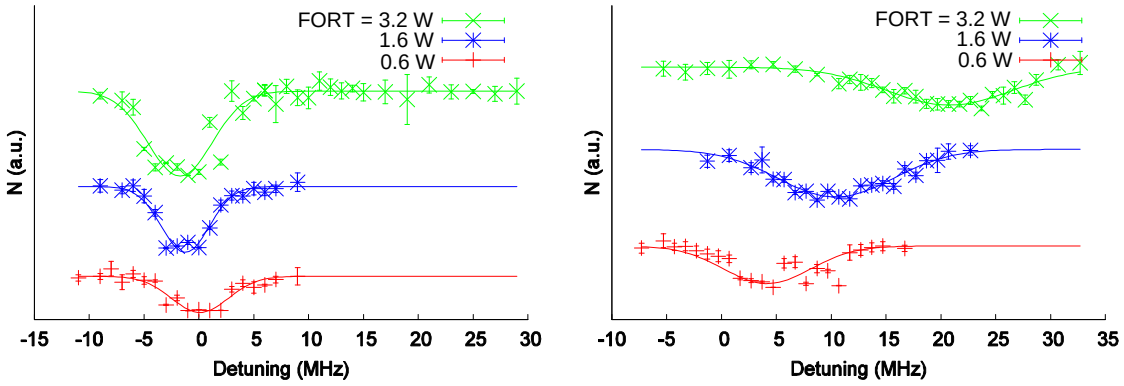

Figure 6.5: Measurement of the polarizability of the $^3D_2$ state. Atoms are excited to (Left) M=±1 (Right) M=±2 of the $^3D_2$ state. The resonance frequency shifts due to the different polarizabilities between the ground state and the $^3D_2$ (M=±1 and ±2) state.

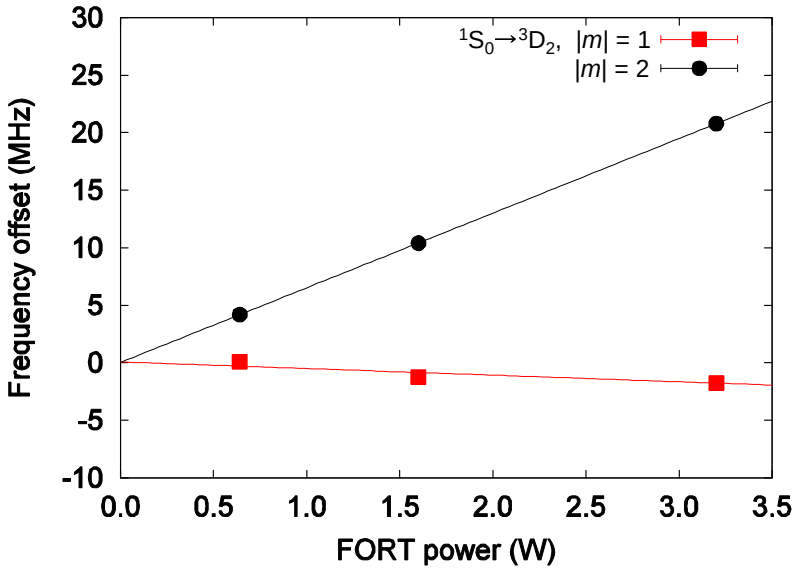

Figure 6.6: Shift of the resonance frequency in Fig.6.5 are summarized. Resonance frequency are plot as a function of the FORT powers. Solid lines are linear fits to data whose slopes describe the difference of polarizabilities.

6.1.3 Magnetic field compensation

Multichannel collisions in a magnetic field

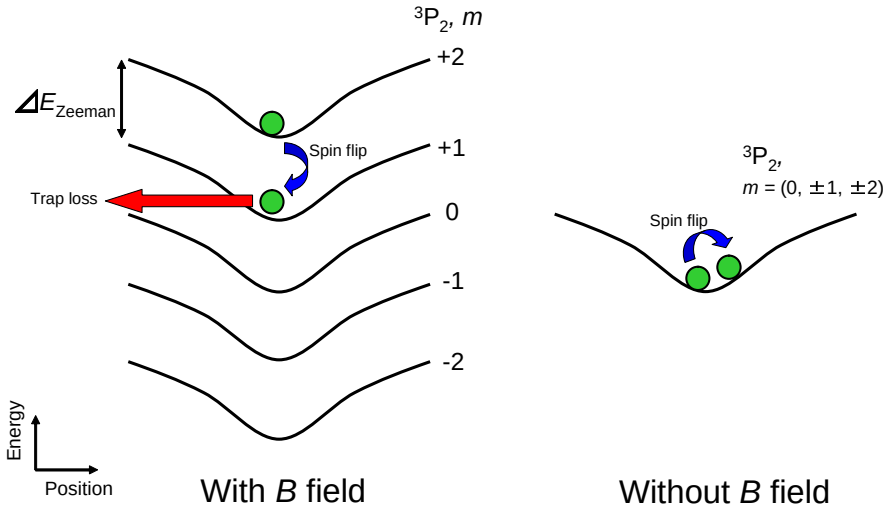

Figure 6.7: (Left): Multichannel collisions in a magnetic field could lead to a trap loss in a FORT. Atoms can obtain the kinetic energy corresponding to the Zeeman splitting via multichannel collisions. (Right): Such trap loss process can be suppressed in zero magnetic field.

In a FORT which can trap atoms in all magnetic sublevels, we can keep trapping of the $^3P_2$ atoms even if multichannel collisions occur (Fig. 6.7(Right)). However, if a large magnetic field exists in a trap region, the multichannel collision could lead to a trap loss. This is because atoms may obtain large kinetic energy corresponding to a Zeeman splitting $\Delta E_{\mathrm{Zeeman}}$ between two potentials for two different spin states. If this kinetic energy is larger than the trap depth, atoms could escape from the trap as shown in Fig. 6.7(Left). We, then, first measured the residual magnetic field at the trap region and canceled it by additional coils.

Experiment

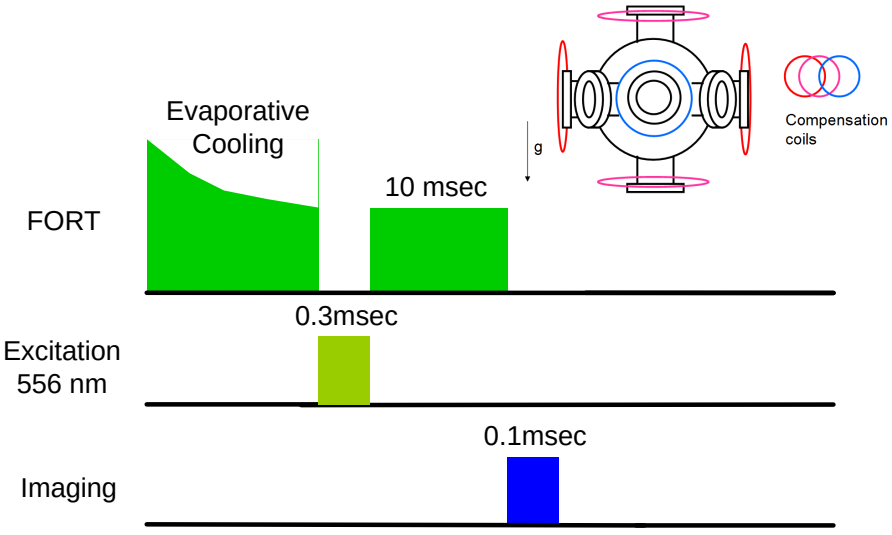

Figure 6.8: Measurement of the residual magnetic field. Zeeman splittings of the $^3P_1$ state were used. In order to remove the light shift, we turned off the FORT laser during the excitation.

To measure the magnetic field at the trap region, the Zeeman splitting of the $^1S_0 \leftrightarrow {}^3P_1$ transition ($g = 1.49$, 2.08 MHz/G) was used. The experimental procedure is schematically shown in Fig. 6.8. After evaporative cooling, we irradiated an excitation laser pulse (556 nm). To remove the light shift, the FORT laser was turned off during the excitation. After the excitation, 10 ms was required to open the mechanical shutter for an imaging system.

Figure 6.9 is the observed spectrum before canceling the residual magnetic field. The Zeeman splitting of abut 2 MHz was detected, which corresponds to the magnetic field of 0.9 G. Then, by adjusting currents of correction coils for x, y, z axes, we cancelled the residual magnetic field step by step as shown in Fig. 6.10. As a result, the residual magnetic field has been removed below 0.03 G which corresponds to a trap depth of 3 μK. Since the measurement of trap loss of atoms discussed later was carried out in a trap of 193 μK, we regard the trap loss due to the multichannel collisions should be suppressed.

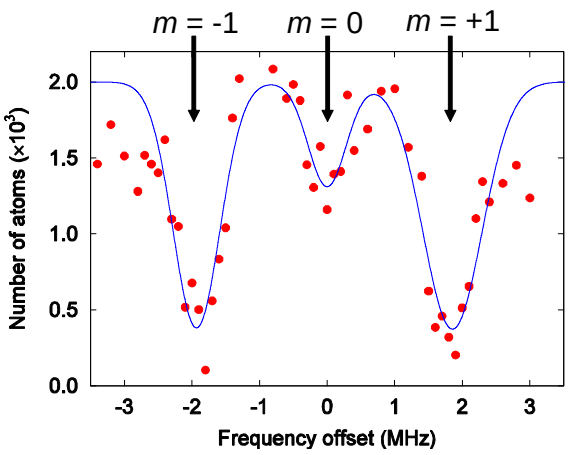

Figure 6.9: Zeeman splitting of the $^3P_1$ state due to the residual magnetic field of 0.9 G. The number of atoms in the ground state is plotted as a function of the frequency offset of the excitation laser (556 nm).

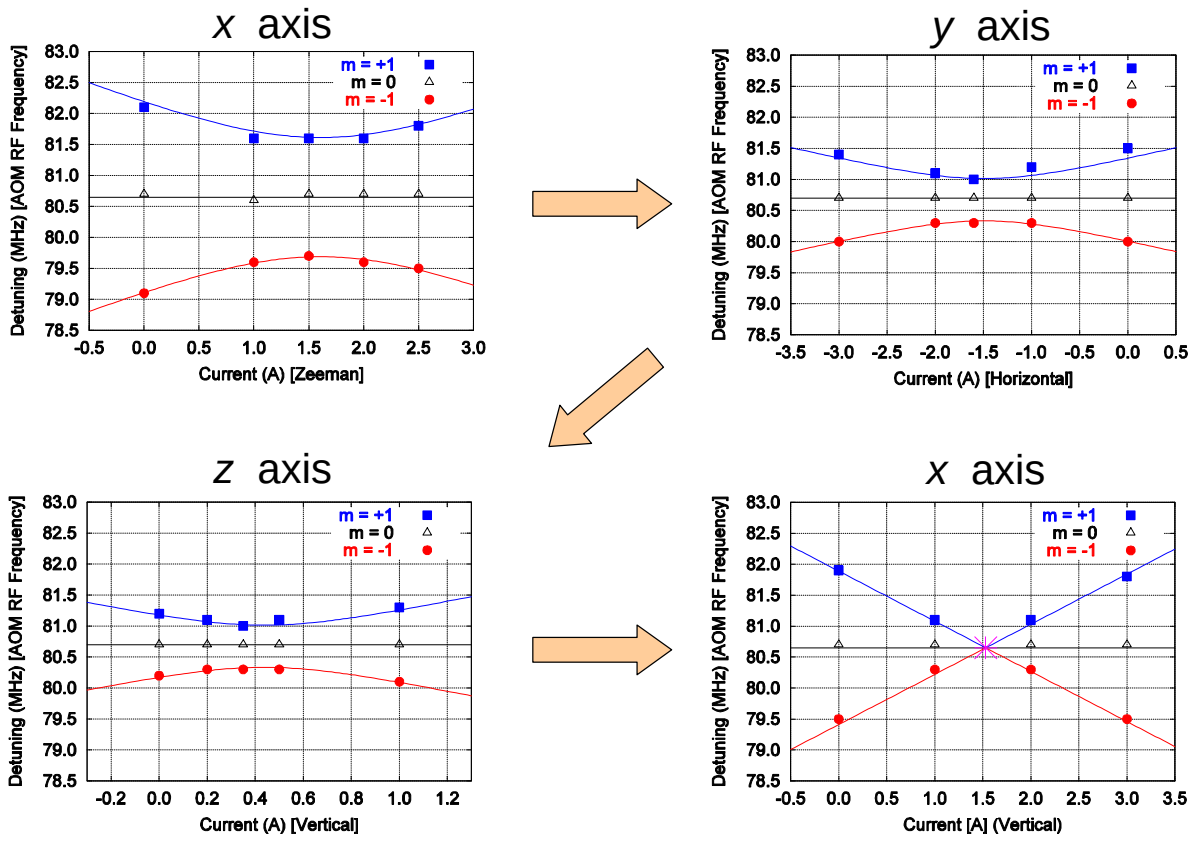

Figure 6.10: Residual magnetic field was compensated step by step by using compensation coils for x, y, z axes. Positions of the resonance frequency are plotted as a function of current of compensation coils.

6.1.4 Optical trapping of atoms in all magnetic sublevels of the $^3P_2$ state in a FORT

To begin with, we had to know whether or not we can trap the Yb[$^3P_2$] atoms in a FORT at 532 nm. We confirmed that atoms in all magnetic sublevels of the $^3P_2$ state can be optically trapped in a FORT at 532 nm. W e compared the number of atoms in a FORT before and after the excitation of 1 ms to detect the untrapped state.

Due to the selection rule of the E2 transition, we can selectively excite atoms to the $^3D_2(m = \pm 2) \rightarrow {}^3P_2(m = \pm 1$ and $\pm 2)$ and $^3D_2(m = \pm 1) \rightarrow {}^3P_2(m = 0, \pm 1$,and $\pm 2)$ by changing the polarization of the excitation laser (see also Fig. 6.2). We compared the number of atoms in these two cases. First, atoms were excited to the $^3D_2(m = \pm 2)$ state. As shown in Fig. 6.11(Left), we have not observed any trap loss after the excitation. This means that the $^3P_2(m = \pm 1$ and $\pm 2)$ states are trap states in the FORT at 532 nm. Similarly, by exciting atoms in the $^3D_2(m = \pm 1)$ state, we confirmed that $^3P_2(m = 0)$ state is also trap state (Fig. 6.11(Right)). Hence, we concluded that all magnetic sublevels of the $^3P_2$ state are trap states. As discussed later, we also see that this result is consistent with the direct measurement of the polarizability of the $^3P_2$ state using the $^1S_0 \leftrightarrow {}^3P_2$ direct transition.

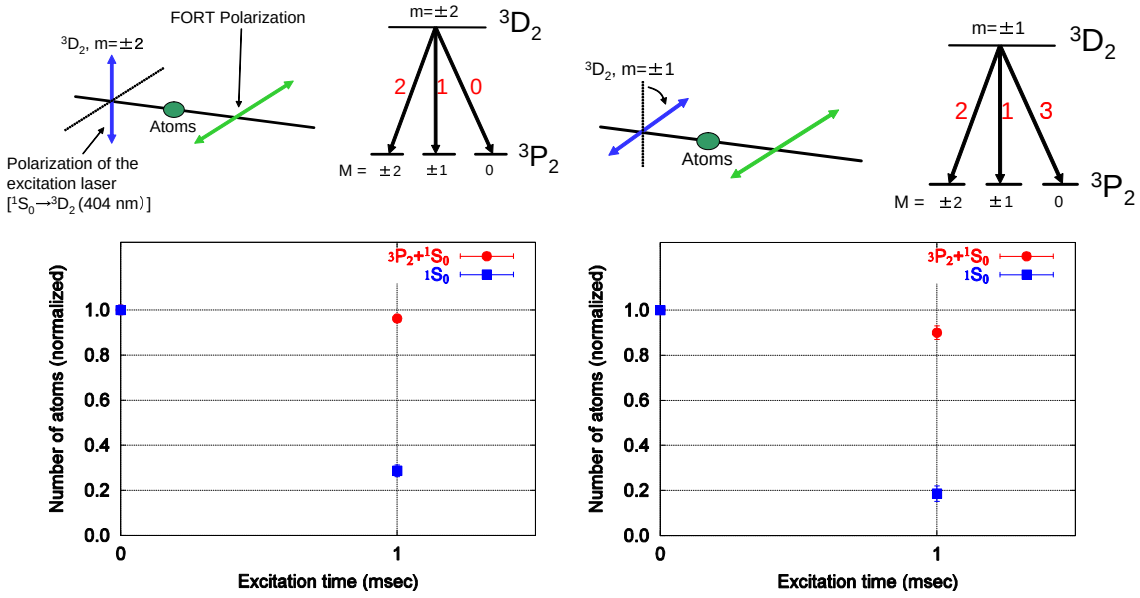

Figure 6.11: The number of atoms in a FORT (532 nm) before and after the excitation of atoms to the $^3P_2$ state are compared to detect the untrapped state. The number of atoms in the ground state (blue square) and both the $^1S_0$ and $^3P_2$ state (red circle) are shown. No significant trap loss was observed, which indicates that all levels are the trap state.

6.1.5 Trap frequency

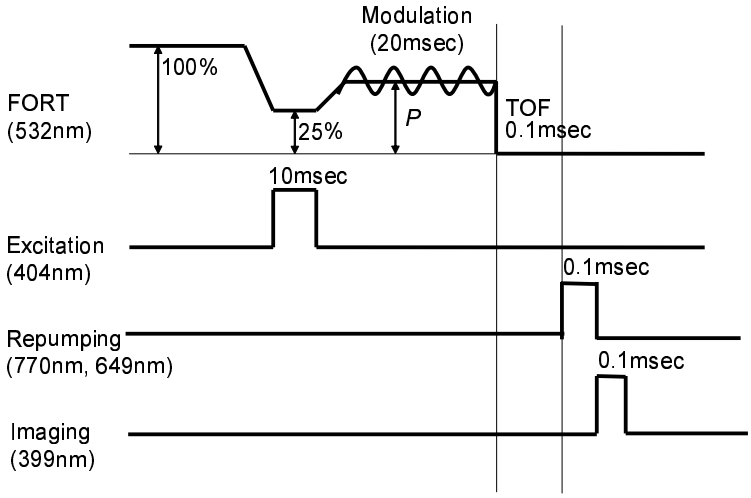

Figure 6.12: Time sequency of measurement of the trap frequency of the FORT for the $^3P_2$ atoms

In the previous experiment, we confirmed that all magnetic sublevels of the $^3P_2$ states are trap states. Then, we next measured the trap depth.

In order to determine the trap depth of a FORT, parametric resonance is commonly used. We regard a FORT potential as a harmonic potential. The atomic motion in a harmonic trap can be described by

$$\ddot{x}(t) = -\omega_0^2 x(t), \tag{6.15}$$

where $x(t)$ is the position and ω_0 is the characteristic frequency of a trap. Let us shake the trap with the frequency ω_e, that is,

$$\ddot{x}(t) = -\omega_0^2(1 + h\cos(\omega_e t))x(t) \tag{6.16}$$

where h is the modulation amplitude. This is known as a Mathieu differential equation. When the shaking frequency ω_e satisfies

$$\omega_e = \frac{2\omega_0}{n}, \tag{6.17}$$

where n is a natural number, this system is known to become unstable due to the resonance behavior. In such a case, atoms in a trap are strongly shaken and heated, which results in the trap loss. We are able to determine the trap frequency via (6.17).

The trap frequency for the radial direction ω_r in a FORT is given by

$$\omega_r = \sqrt{\frac{4U_0}{mw_0^2}}, \tag{6.18}$$

where m is the atomic mass and w_0 is the beam waist. The trap depth U_0 is proportional to the FORT laser power P (see (4.85)). In other words, from the (6.18), the trap frequency ω_r^2 is proportional to the laser power $P(\propto U_0)$. Thus, we can experimentally realize (6.16) by modulating the FORT power P by the AOM at frequency ω_e.

The experimental time sequence is shown in Fig. 6.12. After exciting atoms to all of the magnetic sublevels of the $^3P_2$ state in a FORT, the FORT power P was modulated by an AOM. The resonance frequencies were detected both as increasing atomic temperature (i.e., distribution width) and the number of atoms in a trap.

Experimental results

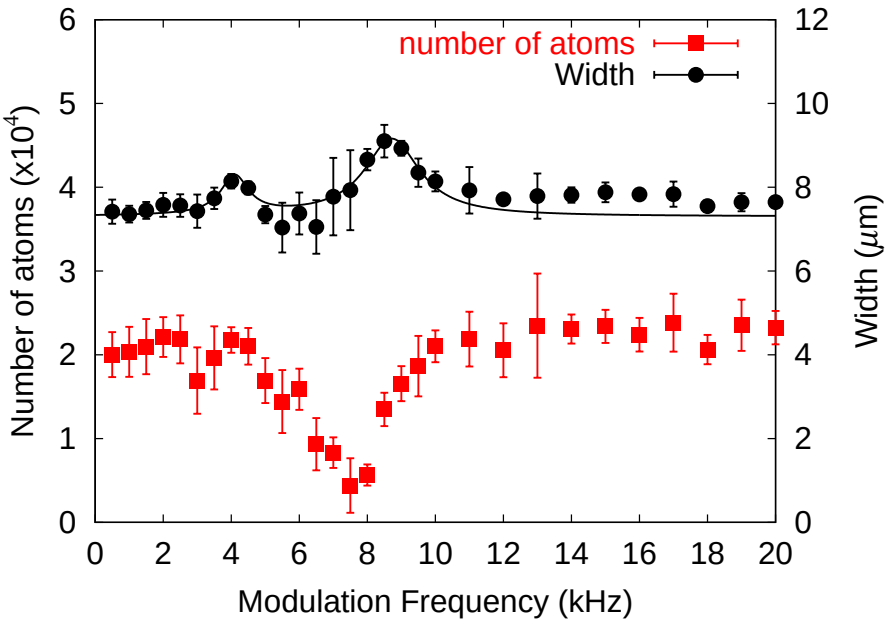

Figure 6.13: Parametric resonance. The number of atoms (red) and distribution width of the atomic cloud (black) are plotted as a function of modulation frequencies. Two resonance signals are clearly observed at 8.6 and 4.3 kHz.

Typical experimental results are shown in Fig. 6.13. The width of the atomic cloud which corresponds to the atomic temperature and the number of atoms are plotted as a function of modulation frequencies. Two resonance signals corresponding to $n = 1$ and 2 in (6.17) are clearly observed at 8.6 and 4.3 kHz, respectively, while the trap frequency of the $^1S_0$ state in this condition is 3.9 kHz. Note that to confirm the resonance observed at 8.6 kHz corresponds to $n = 1$ in (6.17), we took data up to 20 kHz ($> 2\times 8.6$ kHz). If it is $n = 2$, the other peak should appear around 17.2 kHz.

The resonance frequency is determined by fitting a Lorentzian function to the width of atomic clouds. Since all the magnetic sublevels of the $^3P_2$ state are populated in this measurement and in fact we experimentally confirmed that the atoms in every sublevel

are trapped, their trap frequencies can be thought to coincide with each other within the resolution of this measurement. This result is consistent with the measurement of polarizabilities of magnetic sublevels of the $^3P_2$ state using the ultranarrow $^1S_0 \leftrightarrow {}^3P_2$ transition in our different work, which indicates that the difference of the trap frequency between magnetic sublevels in this measurement is less than 1 kHz. Thus, in the following discussion, we consider that the trap depth of all magnetic sublevels of the $^3P_2$ state are same. With this information about the trap, we can also estimate a number density.

6.1.6 High density ultracold metastable atoms

Now we know the trap depth of our FORT. Thus, what we should aim next is a BEC in the metastable state.

We prepared ultracold and dense ground state Yb[$^1S_0$] atoms in a crossed FORT at a density of 2×10^{14} cm^{-1} and at a temperature of less than 0.7 μK. During excitation from the ground state to the $^3P_2$ state through the intermediate $^3D_2$ state, the atoms suffer from heating due to the spontaneous decay of the $^3D_2 \rightarrow {}^3P_1 \rightarrow {}^1S_0$ transitions. Nevertheless, we have successfully prepared Yb[$^3P_2$] atoms in density $n = 2 \times 10^{13}$cm^{-3}, temperature $T =$ 1.8 μK and PSD = 0.01. This is the highest density and lowest temperature ever achieved for the $^3P_2$ atoms.

In principle, PSD could be increased by performing further evaporative cooling of the Yb[$^3P_2$] atoms. We, however, found that it was not possible due to a large trap loss. As discussed in the next section, there is a large inelastic collisional process between Yb[$^3P_2$] atoms in a FORT which we identify as fine-structure changing collisions.

Cross dimensional relaxation measurement

Before proceeding to the next section, I discuss the elastic collision rate of Yb[$^3P_2$] atoms at this ultracold temperature (2 μK).

In general, since the trap loss is caused both by elastic and inelastic processes, it is difficult to separately measure one of them. Monroe *et al.* developed a technique to independently measure the elastic binary collision rate, which is called cross-dimensional relaxation measurement [72]. The basic idea is the following: First, we prepare atoms whose axial temperature is different from the radial one in a trap by some way. Then, we measure the thermalization time τ due to the elastic collisions between two dimensions in a trap. According to the Monte Carlo simulation, atoms collide 2.7 times to be thermalized [72], that is to say,

$$\bar{n}\beta_{\mathrm{el}}\tau = 2.7, \tag{6.19}$$

where $\bar{n}$ is the average density. $\beta_{\mathrm{el}} = \sigma_{\mathrm{el}}\bar{v}$ is the elastic collision rate constant, where σ_{el} is the elastic collision cross section and $\bar{v} = 4\sqrt{(k_{\mathrm{B}}T)/(\pi m)}$ is the mean relative velocity. Thus measuring the average density and the thermalization time, we can independently estimate the elastic collision rate β_{el}.

We first prepared atoms in the crossed FORT which were well thermalized and then heated the atomic cloud along the x direction by using the excitation of atoms to the $^3P_2$ state. We measured T_x and T_y as a function of holding time after the excitation. In Fig.

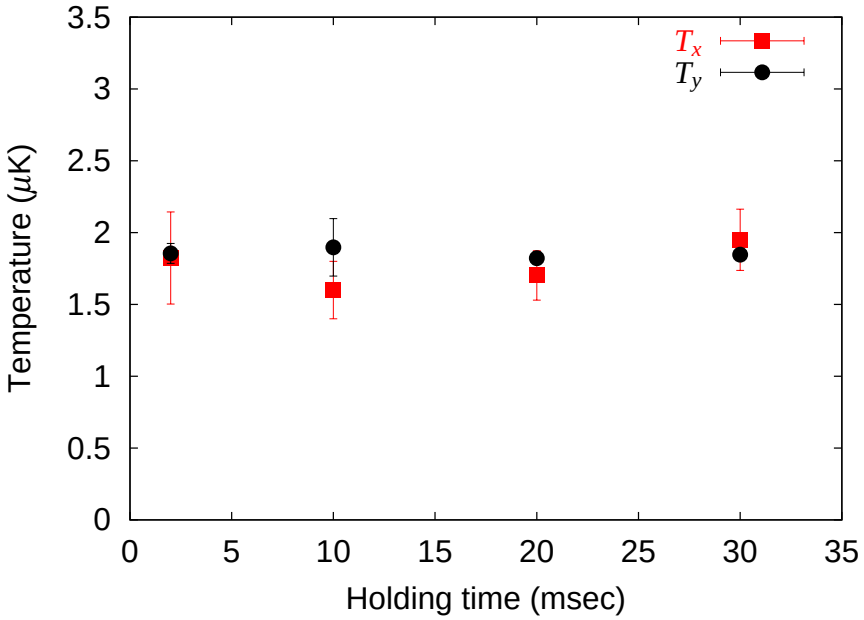

Figure 6.14: Cross dimensional relaxation measurement. Atoms are first heated to x direction by the excitation laser. We could not observe any difference between T_x and T_y 2 ms after the excitation (2 ms), which indicates that the system reaches thermal equilibrium within 4 ms at this ultracold temperature and high density.

6.14, T_x and T_y are shown as a function of time t after the excitation. Even 2 ms after the excitation of 2 ms, no significant difference between T_x and T_y was observed. Then we conclude that the system reaches the thermal equilibrium within 4 ms and thus the lower limit of the elastic collision rate is estimated to be 9×10^{-12} cm^{3}s^{-1} at the temperature of 2 μK. Assuming that the $\sigma_{\rm el}$ does not depend on T in the range of the present measurement, this result is consistent with the estimation discussed in the following section. Note that the relaxation due to the anharmonicity of the trap is measured not to be less than 50 ms in our different work [26].

6.2 Collisional properties between metastable atoms

As discussed in the previous section, further evaporative cooling of Yb[$^3P_2$] atoms in a FORT to reach a BEC turned out to be difficult because the trap loss is too large. Since atoms in all magnetic sublevels can be trapped in a FORT and then the trap loss due to multichannel collisions is suppressed, this indicates that there is another large inelastic loss process. In this section, details of the trap loss mechanism are discussed.

6.2.1 Two body collisions

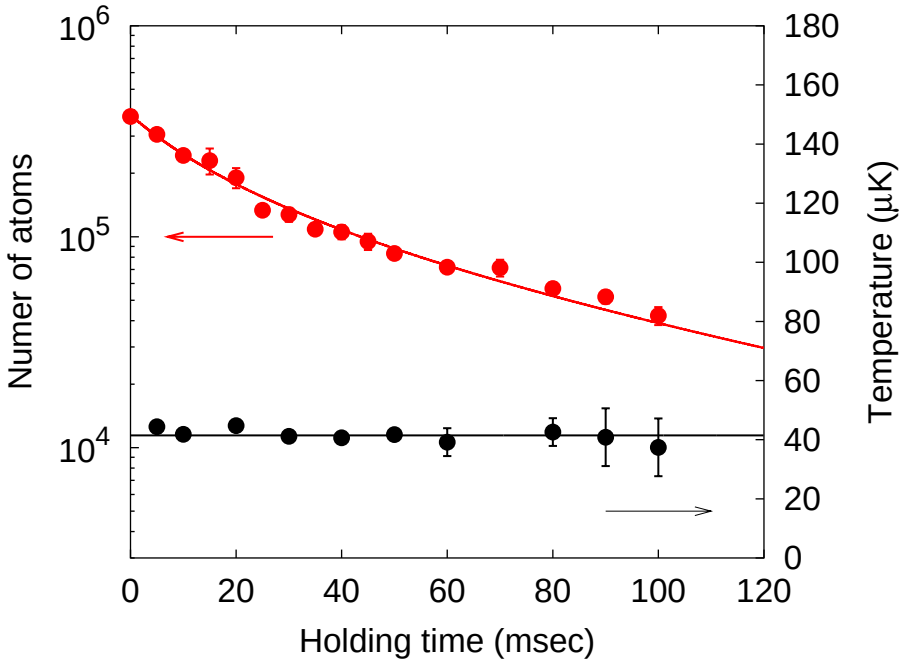

Figure 6.15: Measurement of the trap loss of $^3P_2$ atoms in a FORT. Non-exponential decay is caused by the trap loss due to two-body collisions. Constant temperature during this measurement indicates that the system reaches thermal equilibrium.

We measured the trap loss of the Yb[$^3P_2$] atoms from a single FORT. In Fig. 6.15, the number of the Yb[$^3P_2$] atoms in a FORT are plotted as a function of time after loading of atoms in every magnetic sublevels of the $^3P_2$ state. Note that the (presumably state independent) one-body trap loss lifetime due to background gas collisions is measured to be 15 s (Fig. 2.5) which is much longer than the observed trap lifetime. A significant feature is the non-exponential decay of atom number along the constant temperature of 41 μK. Our model for the trap loss which includes a combination of one-body loss and two-body loss is

$$\frac{\mathrm{d}N}{\mathrm{d}t} = -\Gamma N - \beta' N^2, \tag{6.20}$$

where N is the number of atoms, Γ is the one-body loss rate and β' is the measured two-body atom loss rate. The solid line in Fig. 6.15 is a fit of (6.20) to the trap loss data. β' is related to the density related (volume independent) two-body loss rate coefficient β by $\beta = \beta' V_{\rm eff}$, where $V_{\rm eff}$ is the effective volume of atoms given in the following discussion.

Effective volume

Here we consider the effective volume of atomic cloud in a FORT. Since a FORT potential is obtained by a focused Gaussian beam, the potential $U(r, z)$ is given by,

$$U(r,z) = -|U_0|\frac{w_0^2}{w^2(z)}\exp\left[-\frac{2r^2}{w^2(x)}\right], \tag{6.21}$$

where r and z are radial and axial coordinates and U_0 is the trap depth. Also,

$$w(z) = w_0^2\sqrt{1+\left(\frac{z}{z_{\rm R}}\right)^2}, \quad z_{\rm R} = \frac{\pi w_0^2}{\lambda}, \tag{6.22}$$

where w_0 is a beam waist, $z_{\rm R}$ is a Rayleigh length, and λ is the laser wavelength. Let the radius of the atomic cloud be $\rho(z)$. Then by considering the balance between the trap potential and the thermal energy of an atomic cloud, we have

$$-|U_0|\frac{w_0^2}{w^2(z)}\exp\left[-\frac{2\rho(z)^2}{w^2(x)}\right] = -|U_0| + k_{\rm B}T. \tag{6.23}$$

Thus, using the parameter η ($= U_0/(k_{\rm B}T)$) which is the ratio of the trap depth U_0 to the temperature T ($k_{\rm B}$ the Boltzmann constant), $\rho^2(z)$ is given by

$$\rho^2(z) = -\frac{w^2(z)}{2}\ln\left[\frac{w^2(z)}{w_0^2}\left(1-\frac{1}{\eta}\right)\right]. \tag{6.24}$$

Atoms can be trapped within the region in which $\rho^2(z) > 0$ is satisfied. Thus the edge of the atomic cloud along the axial direction $z_{\rm max}$ is given by

$$z_{\rm max} = z_{\rm R}\sqrt{\frac{1}{\eta-1}}. \tag{6.25}$$

Since the volume of the atomic cloud can be well approximated by a cylinder with the size of the FORT beam,

$$V_{\rm eff} = \pi\rho^2(0)(2z_{\rm max}) = \pi\omega_0^2 z_{\rm R}\ln\left(\frac{\eta}{\eta-1}\right)\sqrt{\frac{1}{\eta-1}}. \tag{6.26}$$

From the measured trap frequency, the trap depth is found to be $U_0/k_{\rm B}$ =193 μK for all magnetic sublevels. Since atomic temperature is 41 μK, we can determine $\eta = 4.7$. From the FORT parameters w_0=15 μm and $z_{\rm R}$= 1.3 mm, we can determined the density related two-body loss rate $\beta = 1.3(4)\times10^{-11}$ cm^3/sec. Note that β consists of both inelastic $\beta_{\rm in}$ and elastic $\beta_{\rm el}$ collision rates. By using a theoretical model for evaporative cooling, we will next separately estimated $\beta_{\rm in}$ and $\beta_{\rm el}$.

6.2.2 Elastic and inelastic collision rates under thermal equilibrium conditions

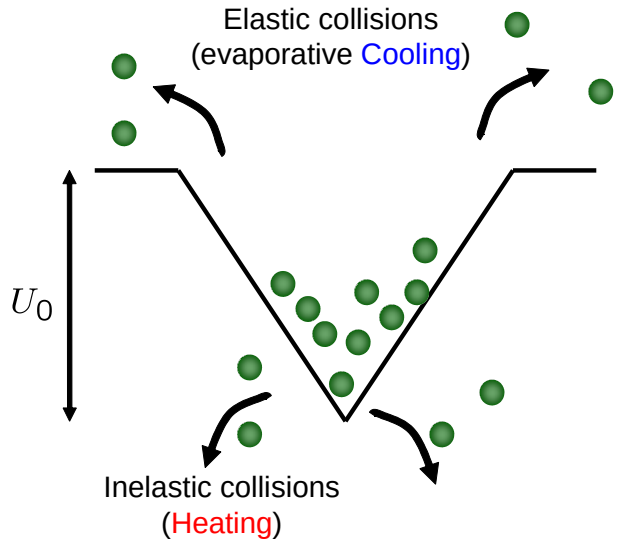

Figure 6.16: Loss of atoms in a trap is caused by the elastic and inelastic collisions. While elastic collisions lead to cooling of atoms (evaporative cooling), inelastic ones lead to heating. Finally, both effects equilibrate and system reaches the thermal equilibrium.

In addition to the non-exponential trap decay, the other important feature in Fig. 6.15 is the constant atomic temperature throughout the 120 ms holding time at $T = 41$ μK. In general, the trap loss due to two body collisions can be classified by elastic and inelastic processes. The elastic collisions lead to evaporative cooling and inelastic collisions lead to heating since not only hot atoms but also cold atoms can be escaped from the trap via inelastic collisions (Fig. 6.16). The observed constant temperature along with the large trap loss of atoms indicates that the system reaches thermal equilibrium. In other words, the cooling effect due to the elastic collisions equilibrates with the heating effect due to the inelastic collisions. Under the thermal equilibrium condition, the relation between the observed two-body decay rate β and the elastic $\beta_{\rm el}$ and inelastic $\beta_{\rm in}$ collision rate can be separately described. This model was first developed by deCarvalho and Doyle [73] and is briefly summarized here.

First, we assume that the density distribution is given by

$$n(\mathbf{r}) = n_0 \exp\left[-\frac{U(\mathbf{r})}{k_{\rm B}T}\right], \tag{6.27}$$

where n_0 is the peak density. This description is valid in case of the infinitely deep trap. If the trap depth is finite, (6.27) is still valid when $\eta > 4$ [73] which is satisfied in our case. This approximation is called "large-η approximation".

We next introduce the collisional effective volume. When a single inelastic scattering leads to loss of one atom in a trap, the inelastic collision rate $\dot{N}_{\rm in}$ is given by

$$\dot{N}_{\rm in} = -(n_0 \bar{v}_{\rm rel} \sigma_{\rm in})(\Lambda_{\rm eff} n_0) \tag{6.28}$$

where $\Lambda_{\rm eff}$ is the collisional effective volume, $\bar{v}_{\rm rel} = 4\sqrt{(k_{\rm B}T)/(\pi m)}$ is the mean relative velocity between atoms, $\sigma_{\rm in}$ is the inelastic scattering cross section. On the other hand, under thermal equilibrium conditions,

$$\dot{N} = V'_{\rm eff} \dot{n}_0, \tag{6.29}$$

where $V'_{\rm eff}$ is the effective volume defined by $N = n_0 V'_{\rm eff}$. By substituting (6.29) into (6.28), we have

$$\begin{aligned} (\dot{n}_0)_{\rm in} &= -\left(\frac{\Gamma_{\rm eff}}{V'_{\rm eff}} \bar{v}_{\rm rel} \sigma_{\rm in}\right) n_0^2 \\ &= -\beta_{\rm in} n_0^2 \end{aligned} \tag{6.30}$$

Similarly, by using f the probability of elastic collisions which result in trap loss of one atom,

$$\begin{aligned} \dot{n}_0 &= (\dot{n}_0)_{\rm in} + (\dot{n}_0)_{\rm el} \\ &= -(\beta_{\rm in} + f\beta_{\rm el}) n_0^2 \\ &= -\beta n_0^2 \end{aligned} \tag{6.31}$$

Using the ratio of elastic to inelastic scattering rate $\gamma \equiv \sigma_{\rm el}/\sigma_{\rm in}$,

$$\beta_{\rm in} = \frac{1}{f\gamma + 1}\beta, \quad \beta_{\rm el} = \frac{\gamma}{f\gamma + 1}\beta. \tag{6.32}$$

One of the significant conclusions in [73] is that f and γ in (6.32) depends only on η under thermal equilibrium conditions. We next calculate f and γ.

We assume that the trap is a linear elliptical shape whose long and short axes correspond to axial and radial direction of the FORT potential, respectively. Then the potential is given by

$$U(r,z) = U_0 \sqrt{\left(\frac{z}{R_z}\right)^2 + \left(\frac{r}{R_r}\right)^2}, \quad \left(\frac{z}{R_z}\right)^2 + \left(\frac{r}{R_r}\right)^2 \leq 1, \tag{6.33}$$

where R_z and R_r denote the axial and radial length of the trap, respectively. However, by using $\frac{z}{R_z} = \rho_z$ and $\frac{r}{R_r} = \rho_r$ and using the polar coordinate instead of the cylindrical coordinate, the potential (6.33) is equivalent to $U(r) = U_0 r$ $(0 \leq r \leq 1)$. We, then, can apply the discussion in [73] to our system.

The total energy of atoms E in the trap is given by

$$E = N E_{\rm ave}, \tag{6.34}$$

where N is the number of atoms in a trap and $E_{\rm ave}$ is the average energy of an atom in a trap. By differentiating (6.34) by t under thermal equilibrium conditions,

$$E_{\rm ave} = \frac{\dot{E}}{\dot{N}} = \frac{\dot{N}_{\rm eva}E_{\rm eva} + \dot{N}_{\rm ine}E_{\rm ine}}{\dot{N}_{\rm eva} + \dot{N}_{\rm ine}} = \frac{f\gamma E_{\rm eva} + E_{\rm ine}}{f\gamma + 1}, \tag{6.35}$$

where $\dot{E}_{\rm ave} = 0$ due to thermal equilibrium conditions and $\dot{N}_{\rm eva}/\dot{N}_{\rm ine} = f\gamma$. From (6.35), γ is written as

$$\gamma = \frac{E_{\rm ine} - E_{\rm ave}}{f(E_{\rm ave} - E_{\rm eva})}. \tag{6.36}$$

Under the large-η approximation, f, $E_{\rm ave}$, $E_{\rm eva}$ and $E_{\rm ine}$ are described by only η as given in [73] and shown in Fig. 6.17 for $\eta > 4$. For $\eta = 4.7$ in this experiment, $f = 0.099$ and $\gamma = 2.2$. As a result, the elastic and inelastic collision rate constant is given by

$$\begin{aligned} \beta_{\rm el} &= 2.3(6) \times 10^{-11} \quad {\rm cm^3 s^{-1}} \\ \beta_{\rm in} &= 1.0(3) \times 10^{-11} \quad {\rm cm^3 s^{-1}} \end{aligned} \tag{6.37}$$

for the temperature of 41 μK.

This inelastic collision rate constant is enormously large. Since the trap loss due to multichannel collisions was suppressed in a FORT, the trap loss observed in this measurement must be due to a different physical mechanism which we interpret as fine-structure changing collisions in this ultracold temperature regime.

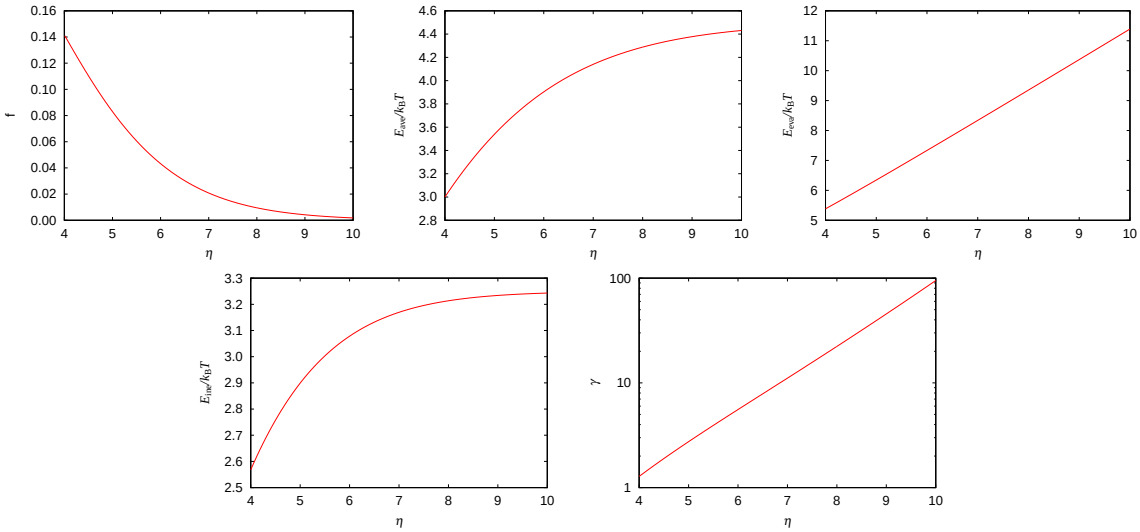

Figure 6.17: All of f, $E_{\rm ave}$, $E_{\rm eva}$, $E_{\rm ine}$ and γ are determined by only η.

6.2.3 Fine structure changing collisions

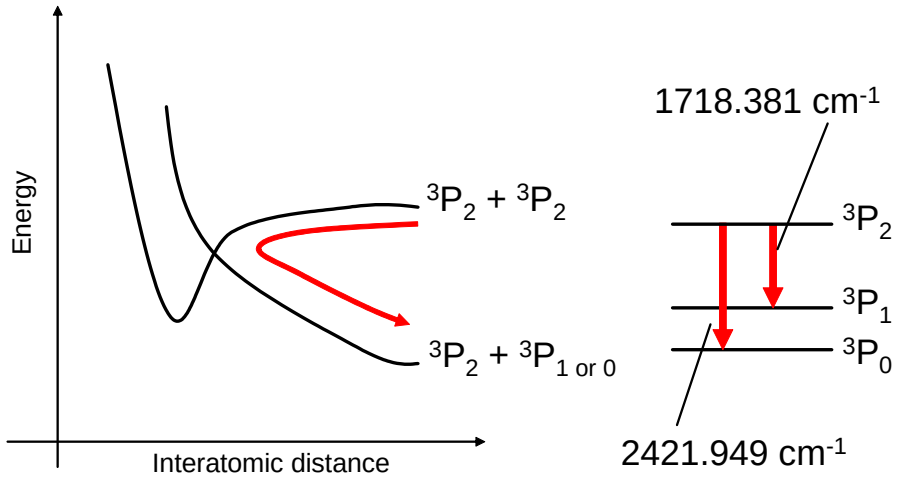

Figure 6.18: Fine structure changing collisions. If the potential curve of $^3P_2 - ^3P_2$ pairs intersect with that of $^3P_2 - ^3P_1$ or $^3P_2 - ^3P_0$ at some point, one of the colliding $^3P_2$ atoms can transit to other state of the fine structure ($^3P_1$ or $^3P_0$). In such case, the atom obtains the energy difference as its kinetic energy.

In Fig. 6.18, the mechanism of fine structure changing collisions are schematically shown. If the potential curve of the $^3P_2 - ^3P_2$ pairs intersect with that of the $^3P_2 - ^3P_1$ or $^3P_2 - ^3P_0$ curves at some point, one of the colliding $^3P_2$ atoms can transit to other state of the fine structure ($^3P_1$ or $^3P_0$) via collisions. In such a case, the atom obtains the energy difference as its kinetic energy. The energy difference between fine structure levels is much larger than the trap depth, such atoms immediately escape from the trap.

In our setup, atoms in every magnetic sublevel can be trapped in a FORT. Hence, the trap loss due to the multichannel collisions in the $^3P_2$ state which were essential obstacles in a magnetic trap is expected to be suppressed. Thus the existence of fine-structure changing collisions is strongly suggested. The previous theoretical works revealed details of fine-structure changing transitions in collisions of Mg[^3P_j], O[^3P_j], Sc[^2D_j], and Ti[^3F_j] atoms with closed-shell atoms at a high temperature. However, there has not been no theoretical work on the fine-structure changing collisions between atoms in the $^3P_2$ state at ultralow temperature achieved in the present work. While the recent experiment of magnetically trapped Ca atoms studied multichannel collisions between $^3P_2$ atoms and discussed the possibility of the fine-structure changing process [2], we believe that our work is the first definite experimental measurement of this process between $^3P_2$ atoms. For the further understanding of the observed large inelastic collision rate and possibilities of the fine structure changing collisions, a quantitative theory on collisional properties of $^3P_2$ atoms is highly desirable.

6.3 Effect of the black body radiation

For Strontium atoms in the metastable $^3P_2$ state, scattering rate of photons from the black-body radiation (BBR) at room temperature is large [17]. We investigate the effect of black body radiation on the metastable Yb atoms. This calculation was first done by Mizoguchi [74] in our group. The BBR effect is an important information in this study. Thus it is again briefly introduced here.

The stimulated transition rate $R_{\rm st}$ by BBR is given by

$$R_{\rm st} = B\rho(\omega), \tag{6.38}$$

where B is the Einstein B coefficient and $\rho(\omega)$ is the density of the photon energy of the blackbody which is well known the Planck formula,

$$\rho(\omega) = \frac{\hbar\omega^3}{\pi^2c^3}\frac{1}{e^{\frac{\hbar\omega}{k_{\rm B}T}}-1}. \tag{6.39}$$

On the other hand, the B coefficient is related to the A coefficient (spontaneous emission) by

$$B = \frac{\pi^2c^3}{\hbar\omega^3}A. \tag{6.40}$$

According to these three equations, we have

$$R_{\rm st} = \frac{A}{e^{\frac{\hbar\omega}{k_{\rm B}T}}-1}. \tag{6.41}$$

To calculate the spontaneous emission rate A, let us consider the Fermi's golden rule which gives the (spontaneous and stimulated) emission rate

$$W_{\rm em} = \frac{2\pi}{\hbar^2}|\langle b|H^+_{\rm int}|a\rangle|^2\delta(\omega_{\rm ba}-\omega_k), \tag{6.42}$$

where $|a\rangle$ and $|b\rangle$ are the initial and final state. In the real system, some modes $\mathrm{d}\omega$ are included in a range of frequencies $\mathrm{d}\omega_k$. Considering the number of modes per unit energy interval in a large cubic V,

$$\mathrm{d}N = \frac{V}{(2\pi)^3}k^2\mathrm{d}k\mathrm{d}\Omega_k, \tag{6.43}$$

where $\mathrm{d}\Omega_k = \sin\theta_k\mathrm{d}\theta_k\mathrm{d}\phi_k$. From the (6.42),

$$\begin{aligned}\mathrm{d}W_{\rm em} &= \frac{2\pi}{\hbar^2}|\langle b|H_{\rm int}|a\rangle|^2\frac{\mathrm{d}N}{\mathrm{d}\omega_k}\\ &= \frac{V\omega^2}{(2\pi)^2c^3\hbar^2}|\langle b|H_{\rm int}|a\rangle|^2\mathrm{d}\Omega_k.\end{aligned} \tag{6.44}$$

We consider only E1 and M1 transitions. By integrating the matrix element of E1 and M1 transitions given in section 4.2, we can find

$$\int|\langle b|H^+_{\int}|a\rangle_{\rm E1andM1}|^2\mathrm{d}\Omega_k = (n+1)\frac{\hbar\omega}{2V\epsilon_0}\frac{8}{3}\pi|\langle b|\mathbf{M}|a\rangle|^2, \tag{6.45}$$

where $\mathbf{M}$ denotes $e\mathbf{r}$ and $\boldsymbol{\mu}_L$ for E1 and M1 transitions, respectively. Since the term 1 within $(n+1)$ corresponds to the spontaneous emission (the other corresponds to stimulated emission), integrating (6.44) and using (6.45) lead to

$$A = \begin{pmatrix} J_b & 1 & 2 \\ -M_b & q & M'_a \end{pmatrix}^2 \frac{\omega^3}{3\pi\epsilon_0\hbar c^3} |\langle b||\mathbf{M}||a\rangle|^2. \tag{6.46}$$

Here we separate the dependence of the magnetic sublevels which is included in a Wigner-3j symbol. Finally, from (6.41) and (6.46), the photon scattering rate in BBR which does not include the information about the magnetic sublevels is

$$R_{\rm st} = \frac{1}{e^{\frac{\hbar\omega}{k_{\rm B}T}} - 1} \frac{\omega^3}{3\pi\epsilon_0\hbar c^3} |\langle b||\mathbf{M}||a\rangle|^2. \tag{6.47}$$

In Fig. 6.19, scattering rates of the $(6s6p)^3P_2 \rightarrow (6s6p)^3P_1$(M1), $(5d6s)^3D_x(x{=}1,2,3)$ (E1), $(6s7s)^3S_1$(E1) and $(5d6s)^1D_2$(E1) transitions are shown. We used theoretical values of reduced matrix elements given in [60]. Note that Fig. 6.19 does not include the information about the magnetic sublevels. If one wants to see it, one just has to multiply the square of a Wigner-3j symbol which is always less than 1. As you can see in Fig. 6.19, the photon scattering rate of the $(6s6p)^3P_2$ state in BBR at room temperature is less than 10^{-4} Hz (10000 s) which is much longer than the lifetime 15 s. As a result, we can conclude that the effect of the BBR radiation can be negligible in case of the metastable Yb[$^3P_2$].

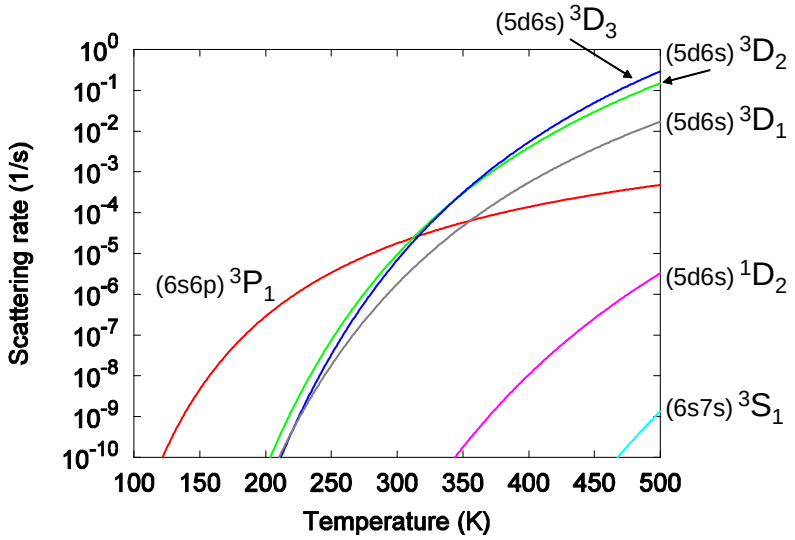

Figure 6.19: Photon scattering rate of the $^3P_2$ state in the BBR radiation field. Scattering rates from the $^3P_2$ state are shown as a function of temperature. At room temperature (300 K), BBR effects in the $^3P_2$ state are negligibly small ($< 10^{-4}$ Hz).

6.4 Optical trapping of Yb atoms in the $^3P_0$ state

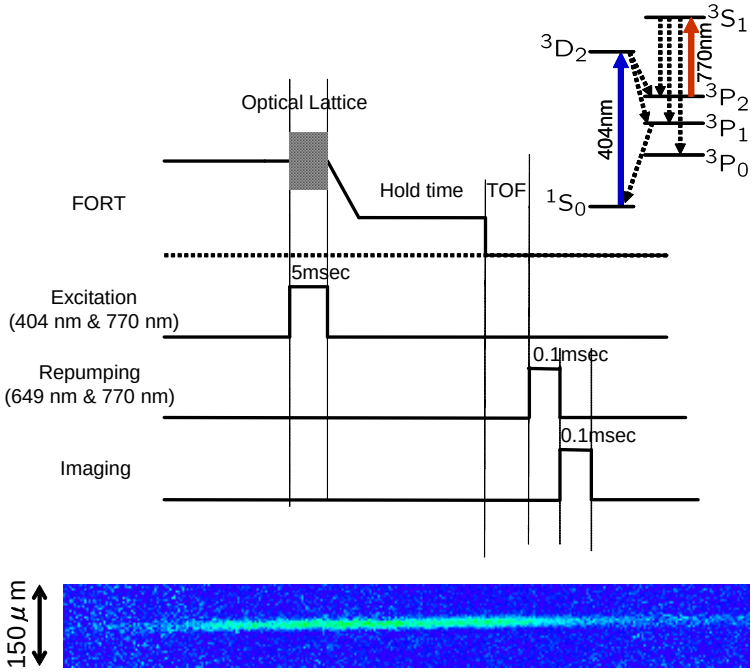

Figure 6.20: Trapping of Yb[$^3P_0$] atoms in a FORT. (Top) By irradiating the 770-nm laser in addition to 404-nm excitation laser during the excitation, the $^3P_0$ state becomes a dark state. To suppress the trap loss by excitation lasers, tight confinement in 1D optical lattice potentials was used. (Bottom) Absorption image of trapped Yb[$^3P_0$] atoms in a FORT.

We report optical trapping of Yb[$^3P_0$] atoms in a FORT at 532 nm. Recently, the $^3P_0$ state in two-electron atoms attract interests from the viewpoint of novel frequency standards and atomic clocks using the $^1S_0 \leftrightarrow ^3P_0$ "clock" transition. A collision shift is one of the main issues toward such applications. It is, then, important to investigate the collisional property between Yb[$^3P_0$] atoms. In this study, we have successfully trap Yb[$^3P_0$] atoms in a FORT and measured trap frequency by the parametric resonance technique.

Figure 6.20 shows experimental procedures. By irradiating the 770-nm laser ($^3P_2 \leftrightarrow ^3S_1$) in addition to the 404-nm laser, the $^3P_0$ state becomes a dark state. However, excitation cycles for atoms to be transferred to the $^3P_0$ state lead to heating and trap loss of atoms in a trap. To overcome this problem, we made use of the tight confinement of the (1D) optical lattice potentials during the excitation and successfully trap atoms in the $^3P_0$ state in a FORT (see Fig. 6.20).

In addition, we measured the trap frequency by the parametric resonance technique. Observed resonances are shown in Fig. 6.21. Although the number of atoms is small, we could observe resonance signals and confirm the dependence on a FORT power. The

estimated trap potentials are 130 μK for parameters $P = 6$ W, $w_0 = 15$ μm and $\lambda = 532$ nm.

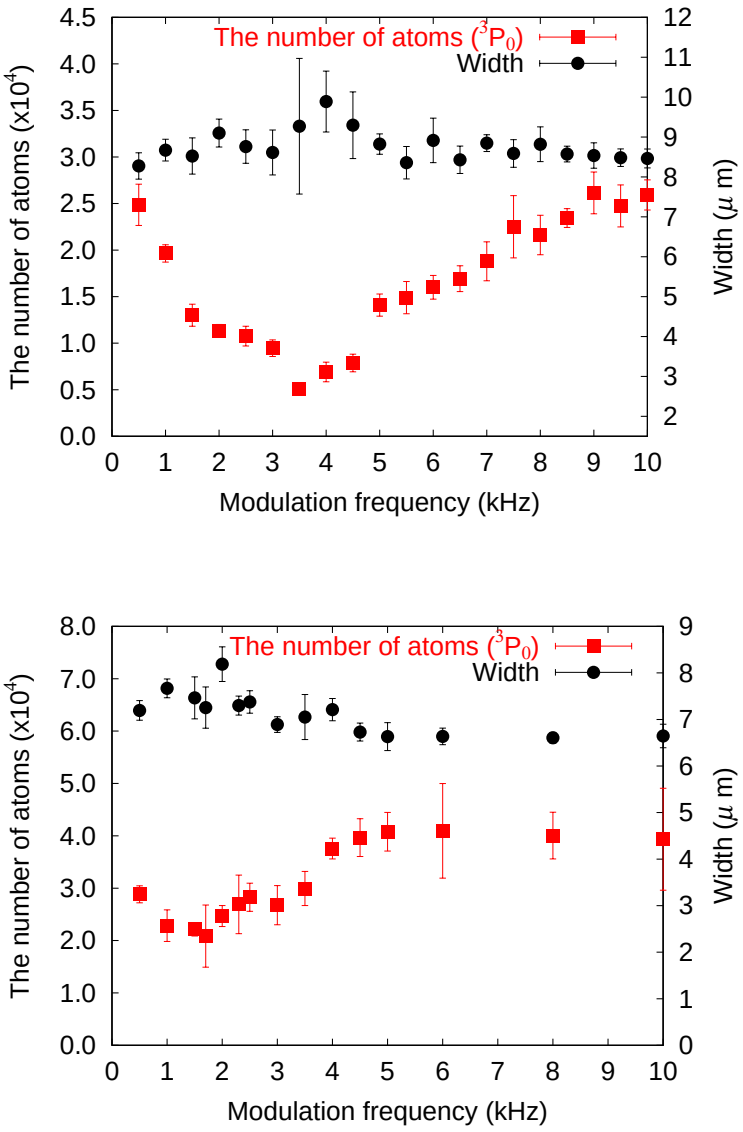

Figure 6.21: Measurement of the trap frequencies of Yb[$^3P_0$] atoms in a FORT by the parametric resonance technique. Shift of the resonance signal for two different FORT power (Top: 6.4 W, Bottom: 1.6 W) was observed.

Chapter 7

Observation and application of the ultranarrow $^1S_0 - ^3P_2$ transition

We have successfully observed the ultranarrow magnetic quadrupole $^1S_0 \leftrightarrow {}^3P_2$ transition in Yb bosonic (^{174}Yb) and fermionic (^{171}Yb, ^{173}Yb) isotopes using the developed laser system at 507 nm in Chapter 3.

Due to its ultranarrow linewidth, this transition had never been observed before this study. In this chapter, we first describe the experiment to estimate the resonance frequency using an optical frequency comb. Using this transition, high-resolution spectroscopy of ultracold atoms and a BEC has been demonstrated. We have selectively excited atoms to all of the magnetic sublevels of the $^3P_2$ state. Also, polarizabilities of all magnetic sublevels of the $^3P_2$ state were precisely measured. We also demonstrated the magnetic resonance imaging (MRI) experiment in which atoms in a trap were addressed by using a magnetic field gradient. Details about the spectroscopy of a BEC will be presented in the next Chapter. Basic properties of the $^1S_0 \leftrightarrow {}^3P_2$ transition are summarized in Table 7.1 and 7.2.

Table 7.1: Magnetic moment of the $(6s6p)^3P_2$ state in isotopes. F is the total angular momentum and μ_B is a Bohr magneton.

	Bosons	^{171}Yb		^{173}Yb				
F	2	3/2	5/2	1/2	3/2	5/2	7/2	9/2
μ/μ_B	3	2.7	3	−1	0.3	1.3	2.2	3

Table 7.2: Important parameters of the magnetic quadrupole ${}^1S_0 \leftrightarrow {}^3P_2$ transition in Yb [60, 75].

		${}^1S_0 \leftrightarrow {}^3P_2$		
		Boson	Fermion	Unit
Wavelength	λ	507.35		nm
Lifetime	τ	15	6.3 (^{171}Yb)	s
			7.2 (^{173}Yb)	s
Natural linewidth	$\frac{\Gamma}{2\pi} = \frac{1}{2\pi\tau}$	10.6	25 (^{171}Yb)	mHz
			22 (^{173}Yb)	mHz
Saturation intensity	$I_{\mathrm{sat}} = \frac{\pi hc}{3\lambda^3\tau}$	1.1	2.5 (^{171}Yb)	$\times 10^{-8}$mW/cm^2
			2.2 (^{173}Yb)	$\times 10^{-8}$mW/cm^2
Recoil frequency		4.4		kHz
Doppler broadening (FWHM)	$\delta\nu_{\mathrm{D}}^{\mathrm{FWHM}}$	$32.0 \times \sqrt{T[\mu\mathrm{K}]}$		kHz

7.1 Estimation of the resonance frequency

Since no one had ever observed the ${}^1S_0 \leftrightarrow {}^3P_2$ transition before our experiment, we did not know the resonance frequency. It is rather difficult to find an ultranarrow resonance without any information about its resonance frequency. Thus we first roughly estimated the resonance frequency $f_{\rm est}$ of the ${}^1S_0 \leftrightarrow {}^3P_2$ transition (507 nm).

7.1.1 Basic idea

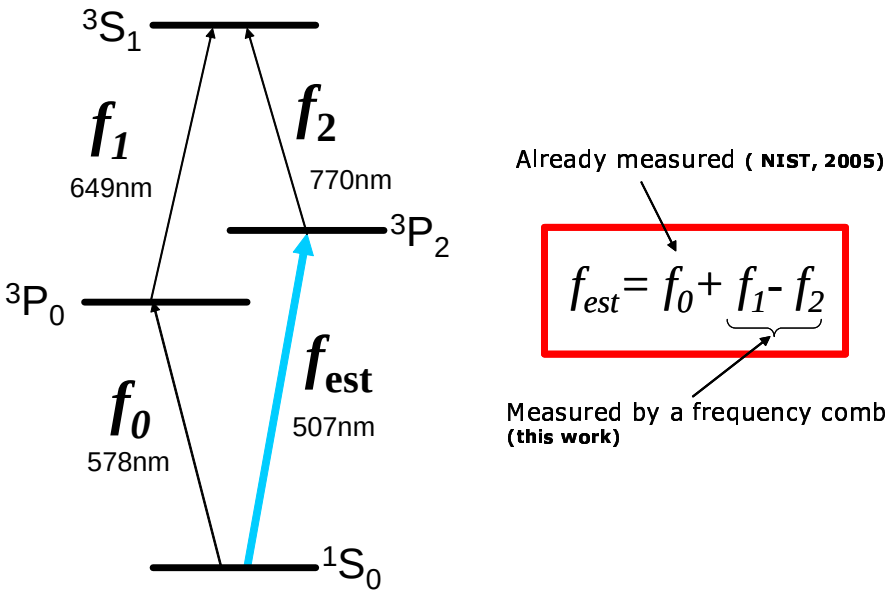

Figure 7.1: The desired resonance frequency $f_{\rm est}$ can be estimated from three known frequencies. f_0 was measured in [34] and f_1 and f_2 were measured in this work.

As shown in Fig. 7.1, combining three resonances of $f_0({}^1S_0 \leftrightarrow {}^3P_0$, 578 nm), $f_1({}^3P_0 \leftrightarrow {}^3S_1$, 649 nm), and $f_2({}^3P_2 \leftrightarrow {}^3S_1$, 770 nm), we can calculate $f_{\rm est}$ by

$$f_{\rm est} = f_0 + f_1 - f_2. \tag{7.1}$$

The absolute frequency f_0 of the so-called "clock" transition (${}^1S_0 \leftrightarrow {}^3P_0$) in fermion isotopes ^{171}Yb and ^{173}Yb was measured by the NIST group [34]. In order to calculate the desired frequency $f_{\rm est}$, we then measured frequencies of the $f_1({}^3P_0 \leftrightarrow {}^3S_1$, E1, 649 nm) and $f_2({}^3P_2 \leftrightarrow {}^3S_1$, E1, 770 nm) transitions for fermionic isotopes by an optical frequency comb.

For bosonic isotopes, although the absolute frequency of the clock transition f_0 had not been presented anywhere at the moment, we can estimate $f_{\rm est}$ by using a fact that the isotope shift of all ${}^3P$ states are similar to each other in Yb. To see this, let us consider the isotope shift between ^{174}Yb (boson) and ^{171}Yb (fermion) as an example (Fig. 7.3). As shown in Fig. 7.2, isotope shifts of the ${}^3P_x \leftrightarrow {}^3S_1$ (x=0,1,2) transitions are almost same

with each other within a several hundred MHz. By considering the isotope shift of the ${}^3P_2 \leftrightarrow {}^3S_1$ and ${}^3P_1 \leftrightarrow {}^3S_1$ transitions between ^{171}Yb and ^{174}Yb shown in Fig. 7.3, we can derive following relations.

$$\begin{aligned} \Delta_4 + \Delta_3 &\simeq \Delta_4 + \Delta_2 \\ \therefore \Delta_3 &\simeq \Delta_2, \end{aligned} \tag{7.2}$$

where Δ_2, Δ_3, and Δ_4 are isotope shifts of the ${}^3P_1$, ${}^3P_2$ and ${}^3S_1$ states, respectively. The resonance frequency of the ${}^1S_0 \leftrightarrow {}^3P_2$ transition in boson isotopes (^{174}Yb in this example) can be estimated by

$$\begin{aligned} {}^{171}f_{\rm est} - {}^{174}f_{\rm est} &= \Delta_1 + \Delta_3 \\ &\simeq \Delta_1 + \Delta_2 \quad (\because (7.2)) \\ &= {}^{171}f_3 - {}^{174}f_3 \end{aligned}$$

$$\therefore \quad {}^{174}f_{\rm est} = {}^{171}f_{\rm est} - ({}^{171}f_3 - {}^{174}f_3). \tag{7.3}$$

where ${}^{171}f_3 - {}^{174}f_3$, the isotope shift of the ${}^1S_0 \leftrightarrow {}^3P_1$ transition between ^{171}Yb and ^{174}Yb was already measured in [42].

Isotope shifts of ${}^3P_x \rightarrow {}^3S_1$ transition

Yb	${}^3P_0$ (649 nm)	${}^3P_1$ (680 nm)	${}^3P_2$ (770 nm)
170	-524(21)		-543.0(15)
171	-345(25)		-326.3(20)
172	0	0	0
173	185(38)		196.0(5)
174	413(20)		425.3(3)
176	805(17)	801	851.0(6)

(MHz)

Isotope shifts in Mg (MHz)

	${}^3P_0$-${}^3S_1$	${}^3P_1$-${}^3S_1$	${}^3P_2$-${}^3S_1$
^{25}Mg-^{24}Mg	-210(36)	-201(21)	-204(7)
^{26}Mg-^{24}Mg	-396(6)	-390(5)	-390(7)

Figure 7.2: (Top) Isotope shifts of the ${}^3P_x \leftrightarrow {}^3S_1$ (x=0,1,2) transitions in Yb are almost same with each other within several tens of megahertz [76, 77, 78]. This characteristic may be common in two-electron atoms. (Bottom) For example, isotope shifts in Mg atoms coincide with each other within a several megahertz [79].

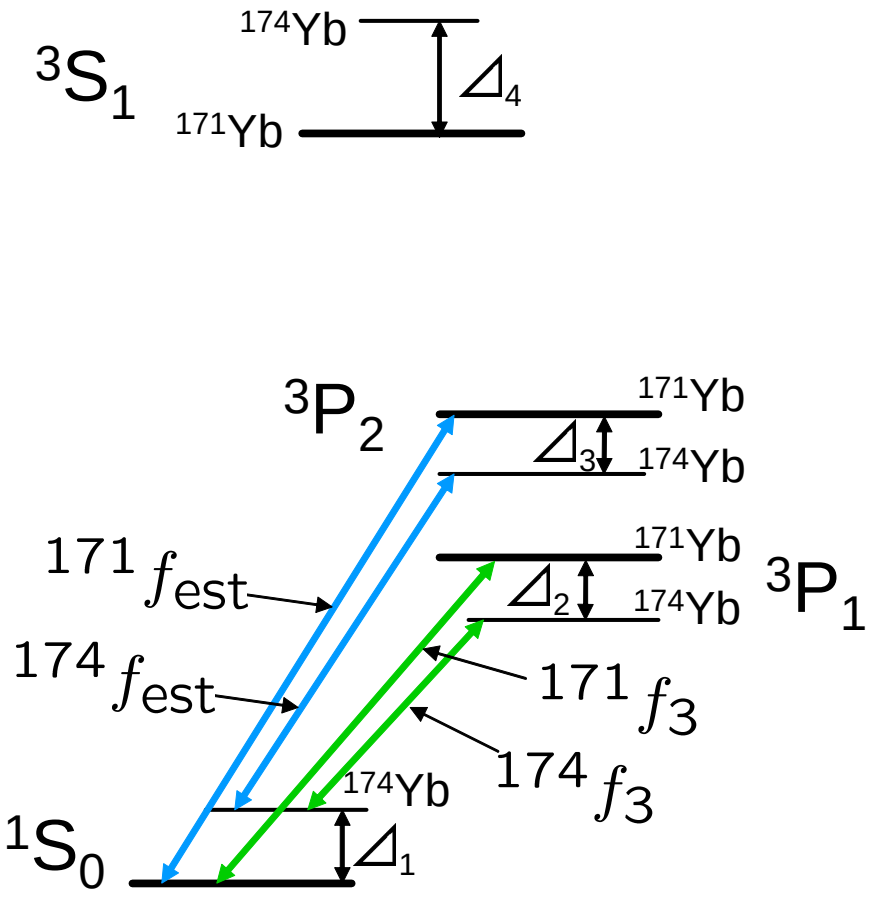

Figure 7.3: Similar isotope shifts ($\Delta_2 \simeq \Delta_3$) between ${}^3P_x$ (x=0,1,2) states enable us to estimate the resonance frequency ${}^{174}f_{\rm est}$(unknown) from ${}^{171}f_{\rm est}$(known) and already measured isotope shifts ${}^{171}f_3 - {}^{174}f_3$ of the ${}^1S_0 \leftrightarrow {}^3P_1$ transition by ${}^{174}f_{\rm est} = {}^{171}f_{\rm est} - ({}^{171}f_3 - {}^{174}f_3)$.

7.1.2 Frequency measurement of the $^3P_2 - ^3S_1$ (770 nm) and $^3P_0 - ^3S_1$ (649 nm) transitions by an optical frequency comb

Since both the $^3P_2 - ^3S_1$ (770 nm) and $^3P_0 - ^3S_1$ (649 nm) transitions are strong electric-dipole (E1) transition with natural linewidth of 12 MHz, spectroscopy of these transitions are relatively easy. To this end, we have to first make population in the metastable $^3P_0$ and $^3P_2$ states. We use an opto-galvano cell (Hamamatsu Photonics, L2783) where Yb atoms are emitted by an electric discharge in Neon buffer gas of about 10 Torr. Because the electric discharge is a rather violent process, some Yb atoms are populated in the $^3P_2$ and $^3P_0$ state in the interaction region.

We performed saturation spectroscopy of metastable atoms as schematically shown in Fig. 7.4. The pump laser was chopped (3 kHz) by a mechanical chopper to get rid of the background level and the signal was obtained by a lock-in amplifier. Resonance frequency was measured by an optical frequency comb (FC8003, Menlo Systems GmbH). The frequency comb is generated by a femtosecond Ti:sapphire laser (Gigajet 20, GigaOptics GmbH) with a repetition rate of 824 MHz. Femtosecond pulses are injected into a highly nonlinear photonic crystal fiber which expands the comb range to an octave spanning. Then, the carrier-envelope offset frequency is derived from a beat frequency in the self-referenced interferometer. Both the repetition rate and the carrier-envelope offset frequency are locked to the commercially available Rb frequency standard (PRS10, Stanford Research Systems). Laser frequency is measured as an RF beat signal between the measured laser and the nearest frequency comb. Details about the frequency comb will be presented in Chapter 9.

Because the accuracy of the measurement of tens of megahertz was good enough for the present purpose, we measured frequency of the beat signal not by a frequency counter but by a spectrum analyzer. We tuned the laser frequency at the top of resonance signals obtained in saturation spectroscopy, left it there and measured the frequency of the RF beat signal.

Observed spectra are shown in Fig.7.5 ($^3P_0 - ^3S_1$, 649 nm) and Fig.7.6 ($^3P_2 - ^3S_1$, 770 nm). All resonance signals were identified by reference to the isotope shift and hyperfine splitting previously measured in [77, 78]. Solid lines in Fig.7.5 and 7.6 are fits to data by summation of corresponding Lorentzian functions, which well agree with observed spectra.

For fermions (^{171}Yb and ^{173}Yb), hyperfine splittings can be described by [80]

$$\nu = \nu_0 + A\frac{K}{2} + B\frac{3K(K+1) - 4I(I+1)J(J+1)}{8I(2I-1)J(2J-1)} \tag{7.4}$$

where ν is the resonance frequency, ν_0 is the unperturbed frequency (resonance frequency when hyperfine interaction doesn't exist), A and B are hyperfine constants, J is the electric angular moment, I is the nuclear spin , $F = I + J$ and $K = F(F+1) - I(I+1) - J(J+1)$. Hyperfine constants A, B and ν_0 relative to that in ^{174}Yb are shown in the bottom of Fig. 7.5 and 7.6 for the relevant transitions.

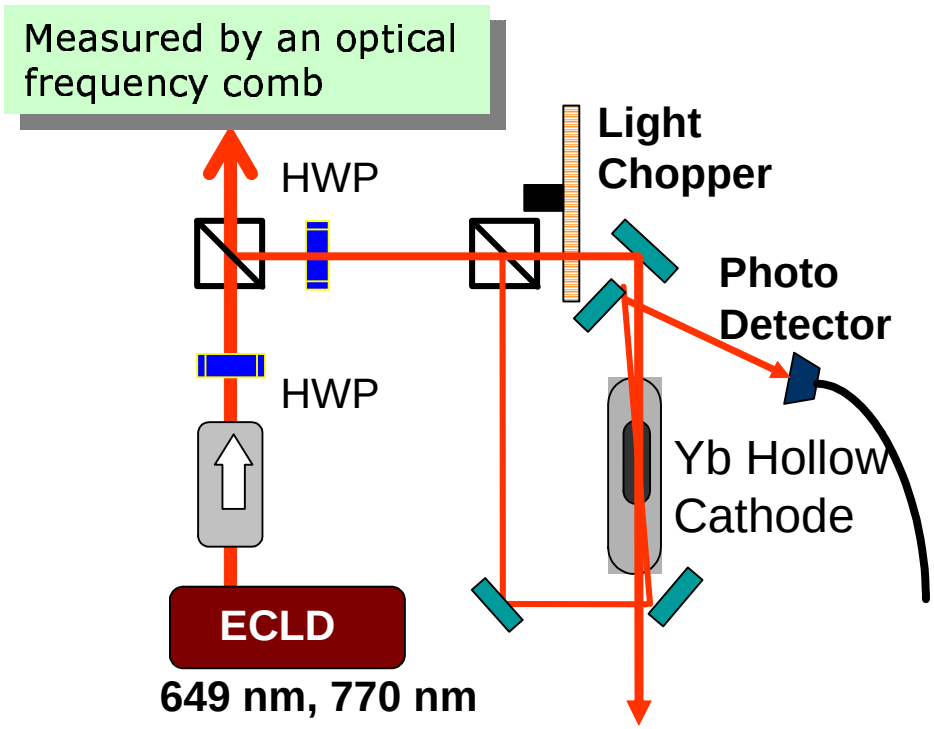

Figure 7.4: Saturation spectroscopy. A pump beam was chopped (3 kHz) for the purpose of removing the background and the resonance signal was obtained by the lock-in amplifier. After tuning the laser frequency at the top of the resonance, the laser frequency was measured by an optical frequency comb.

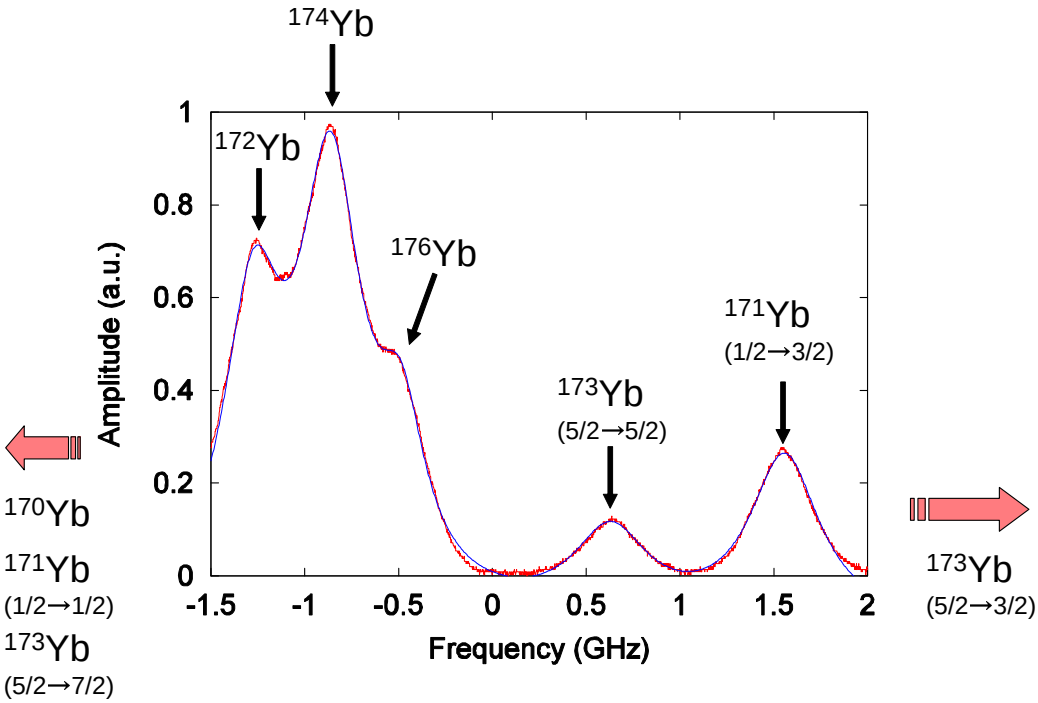

	Isotope shift
170	-937(41)
171	-758(45)
172	-413(20)
173	-228(58)
174	0
176	392(37)

(MHz)

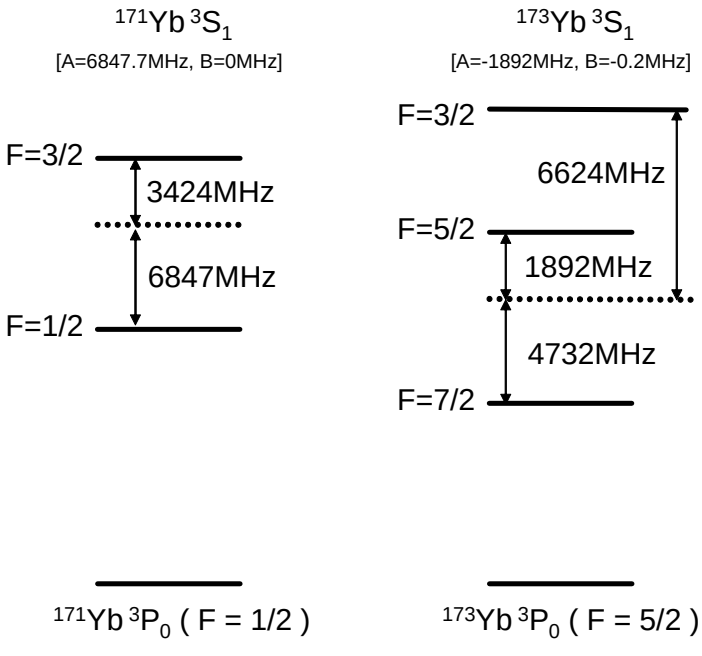

Figure 7.5: Spectra of the ${}^3P_0 \leftrightarrow {}^3S_1$ transition (649 nm) obtained by the saturation spectroscopy using discharged Yb atoms. The solid line is a fit to data by a summation of Lorentzian functions whose peak positions are identified by the results of the frequency measurement and previously measured isotope shifts shown below [77, 78]. Dotted line in the level diagram indicates "center" frequency listed in the table by the side.

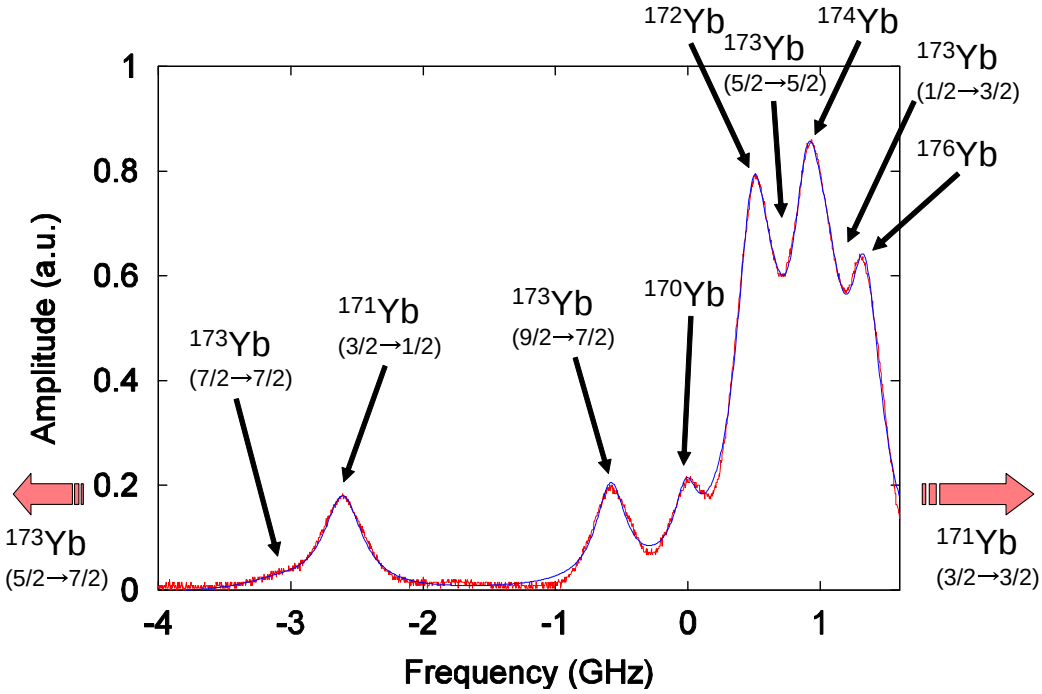

	Isotope Shift
170	-968.3(18)
171	-751.6(23)
172	-425.3(3)
173	-229.3(8)
174	0
176	425.7(3)

(MHz)

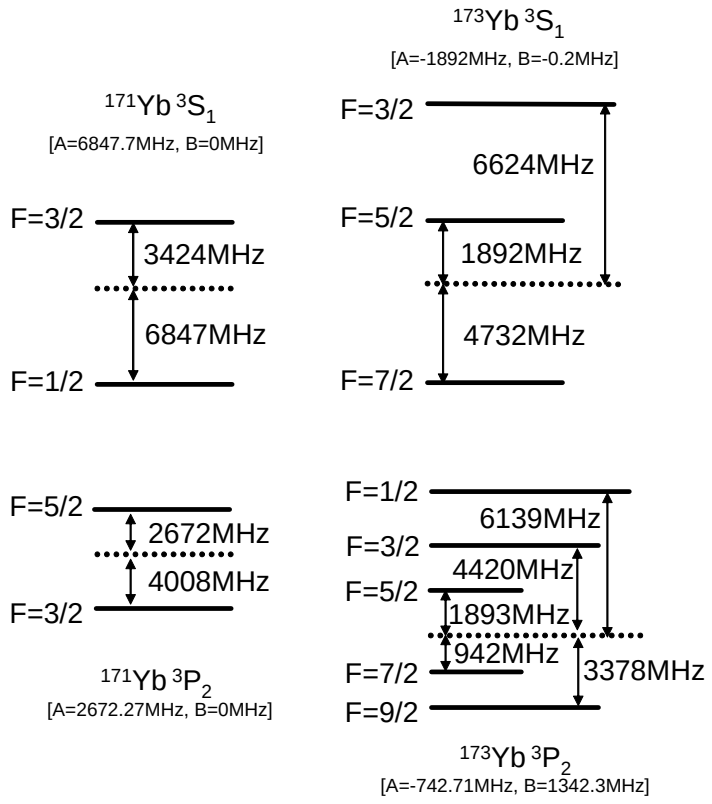

Figure 7.6: Spectra of the ${}^3P_0 \leftrightarrow {}^3S_1$ transition (770 nm) [78].

7.1.3 Results

Results of the estimation are shown in Fig. 7.7. The resonance frequency of the ${}^1S_0 \leftrightarrow {}^3P_0$ transition in bosonic isotopes and f_1 in ^{170}Yb could not be measured in this experiment. Then they were derived by assuming same isotope shifts with that of the ${}^1S_0 \leftrightarrow {}^3P_1$ transition.

Major problem of this estimation is the large pressure shift due to buffer gas (Neon) in an opto-galvano cell. Pressure broadening and shift of the ${}^3P_0 \leftrightarrow {}^3S_1$ transition was measured in [81](${}^3P_0 \leftrightarrow {}^3S_1$ (649 nm) in Neon: $2.5(\pm 0.3) \times 10^{-9}\mathrm{s}^{-1}\mathrm{cm}^3$ (broadening) and $-0.5(\pm 0.1) \times 10^{-9}\mathrm{s}^{-1}\mathrm{cm}^3$ (shift))[1]. However, experiment for the ${}^3P_2 \leftrightarrow {}^3S_1$ transition has not been reported. We assumed same values for the ${}^3P_2 \leftrightarrow {}^3S_1$ transition. This may lead to a large error in this estimation. We, however, regarded that the resonance frequency must be located within a hundred megahertz around these estimated values. In fact, we have successfully found the resonance.

	f_0 (578nm)	f_1 (649nm)	f_2 (770nm)	f_{est}(507nm)
170	518296.2954(14)	461867.918(37)	389259.442(33)	590904.860(50)
171	518295.8366	461868.091(35)	389259.690(23)	590904.326(42)
172	518295.0089(20)	461868.425(33)	389259.973(24)	590903.550(41)
173	518294.5768	461868.620(49)	389260.220(24)	590903.066(55)
174	518294.0215(19)	461868.855(37)	389260.412(24)	590902.554(44)
176	518293.6238(24)	461869.272(37)	389260.849(23)	590902.138(44)

(GHz)

Figure 7.7: Estimation of the resonance frequency of the ${}^1S_0 \leftrightarrow {}^3P_2$ transition. f_0 for ^{171}Yb and ^{173}Yb were measured in [34].

[1] These value was measured to the buffer gas number density.

7.2 Observation of the ultranarrow $^1S_0 - {}^3P_2$ transition

Based on the information of the resonance frequency estimated in the previous section, we found the resonances. The $^1S_0 \leftrightarrow {}^3P_2$ transition is the M2 transition. The Rabi frequency Ω can be described by [82]

$$\Omega\ [\mathrm{kHz}] = 2\pi \times \begin{cases} 0.204\sqrt{I\ [\mathrm{W/cm^2}]} \\ \\ 2.280\sqrt{I\ [\mathrm{W/cm^2}]} \end{cases}, \tag{7.5}$$

where I is the intensity of the excitation laser. In this experiment, the maximum intensity of the excitation laser at atoms is 40 W/cm^2. If we make use of the theoretical transition strength given in [60, 75], (7.5) indicates the Rabi frequencies $\sim 2\pi\times$ 1 kHz for bosonic isotopes and $\sim 2\pi\times$ 10 kHz for fermionic isotopes.

We first used fermionic isotope ^{173}Yb in a compressed MOT to find the resonance due to its relatively large transition strength caused by the hyperfine mixing effect [75] which is further described in the following discussion. In addition, we artificially broaden the spectrum [83, 34] to find the resonance as easy as possible. First, we used relatively "hot" (several hundred microkelvin) atoms in order to utilize a Doppler broadening. For example, 230 kHz can be expected for 50 μK. Second, we rapidly switched on and off the MOT laser during the excitation in order to utilize a broadening due to the ac Stark effect induced by the MOT laser. Third, the broadening due to the Zeeman effect induced by the MOT magnetic field gradient ($\sim$ 14 G/cm) was also used. With the help of these, we have succeeded in observing the resonances. Fig. 7.8 shows the number of atoms in the MOT until we found the resonance. The MOT loading time was reduced to 1 $\sim$ 3 s to search the resonance as fast as possible. Frequency of the excitation laser was scanned at 200 kHz (507 nm) intervals and irradiated to atoms for 300 ms. The resonance can be detected as the decrease of the number of atoms in a MOT. This is because the MOT does not work for metastable $^3P_2$ atoms and the lifetime of the metastable $^3P_2$ state is 15 s which is long enough for atoms to fall from the MOT region by gravity. In this study, the transitions we found are the $^1S_0$ (F=5/2) $\leftrightarrow$ $^3P_2$ (F=5/2) transition in ^{173}Yb, the $^1S_0$ (F=1/2) $\leftrightarrow$ $^3P_2$ (F=5/2) transition in ^{171}Yb, and $^1S_0 \leftrightarrow {}^3P_2$ transition in ^{174}Yb.

7.2.1 Fermions: ^{173}Yb [$^1S_0(F{=}5/2) \leftrightarrow {}^3P_2(F{=}5/2)$] and ^{171}Yb [$^1S_0(F{=}1/2) \leftrightarrow {}^3P_2(F{=}5/2)$]

Hyperfine mixing effect - induced E1 transition

The linewidth of the $^1S_0 \leftrightarrow {}^3P_2$ transition in Yb fermionic isotopes is expected to be slightly broader than that of bosonic isotopes due to the hyperfine mixing (HFM) effect. The HFM effect is caused by the interaction H_{HFI} between a nuclear spin I and a total electric angular momentum J. Regarding H_{HFI} as a first order perturbation, the mixed $^3P_2'$ state is described as

$$\left|{}^3P_2', F, m_F\right\rangle = \sum_{\alpha} \frac{\langle {}^3P_2, F, m_F | H_{\mathrm{HFM}} | \alpha \rangle}{E(\alpha) - E({}^3P_2)} \left|\alpha\right\rangle, \tag{7.6}$$

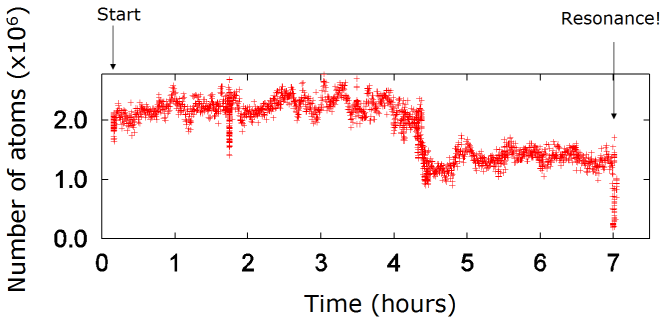

Figure 7.8: Road to the resonance. The number of atoms in the MOT is plotted as a function of time. Frequency of the excitation laser was scanned at 200 kHz (507 nm) intervals. After 4.2 hours, the number decreases because we made the MOT loading time shorter in order to accelerate the sequence. Finally, seven hours later, early in the morning (at 3:50 am on Sunday, March 4th, 2007), we found the resonance.

where α is all possible states. The matrix element of the E1 transition between the mixed $^3P_2'$ state and the $^1S_0$ ground state is

$$\langle {}^3P_2', F, m_F | r_q^{(1)} | {}^1S_0, F', m_{F'} \rangle = \sum_\alpha \frac{\langle {}^3P_2, F, m_F | H_{\rm HFI} | \alpha \rangle}{E(\alpha) - E({}^3P_2)} \langle \alpha | r_q^{(1)} | {}^1S_0, F', m_{F'} \rangle. \qquad (7.7)$$

Since α includes some states which are connected to the ground state via the E1 transition (e.g. $(6s6p)^3P_1$), this matrix element does not vanish in some cases. This means that, if atoms have a nuclear spin, the $^1S_0 \leftrightarrow {}^3P_2$ transition can occur through the E1 transition in addition to the M2 transition.

As for Yb atoms, fermionic isotopes ^{173}Yb and ^{171}Yb have nuclear spin 5/2 and 1/2, respectively, but all bosonic isotopes do not have a nuclear spin (see Table 2.1). As a result, we can expect the HFM effect only for fermionic isotopes. Note that the selection rules of the E1 transition induced by the hyperfine mixing is same as that of the E1 transition. For example, the $^1S_0(F{=}5/2) \leftrightarrow {}^3P_2(F{=}5/2)$ transition via HFM-E1 is allowed, but the $^1S_0(F{=}5/2) \leftrightarrow {}^3P_2(F{=}1/2)$ transition is not since $\Delta F = 2 > 1$ which is not allowed in the E1 transition (see Fig. 7.9).

To exploit the spectral broadening induced by the HFM effect in fermionic isotopes[2], we chose the $^1S_0(F{=}5/2) \leftrightarrow {}^3P_2(F{=}5/2)$ transition in ^{173}Yb as a first target. Fig. 7.10 shows the observed spectrum whose spectral width is broadened to ~ 1 MHz due to several effects mentioned above. Using this transition, we next carried out the spectroscopy of ultracold fermionic isotopes which were cooled by evaporative cooling. The residual magnetic field split the $^3P_2(F{=}5/2)$ state split into six Zeeman sublevels, one of which

[2]In order to find other two resonances($^1S_0(F{=}5/2) \leftrightarrow {}^3P_2(F{=}3/2)$, $^1S_0(F{=}5/2) \leftrightarrow {}^3P_2(F{=}7/2)$), we had to use two AOMs to compensate the frequency interval between the atomic resonance and the ULE resonance. The $^1S_0(F{=}5/2) \leftrightarrow {}^3P_2(F = 5/2)$ required only one AOM, which was technically much easier than others.

is shown in Fig. 7.11. The Zeeman splitting of the ground state $^1S_0(F{=}1/2)$ is about three orders of magnitude less than that of the $^3P_2$ state because the nuclear spin is much smaller than the electric spin. Then the Zeeman splittings of the $^3P_2$ state were observed.

After finding the resonance in ^{173}Yb, we could find the resonance in the other fermionic isotope ^{171}Yb with relative ease. The reason is that the frequency interval (isotope shift) between them can be estimated with the accuracy of ∼1 MHz by using Eq. (7.3) and the information in [34], Fig. 7.5 and Fig. 7.6. We tried to find the $^1S_0(F{=}1/2) \leftrightarrow {}^3P_2(F{=}5/2)$ transition in which the HFM effect does not contribute (see Fig.7.9). The observed spectrum is shown in Fig. 7.11.

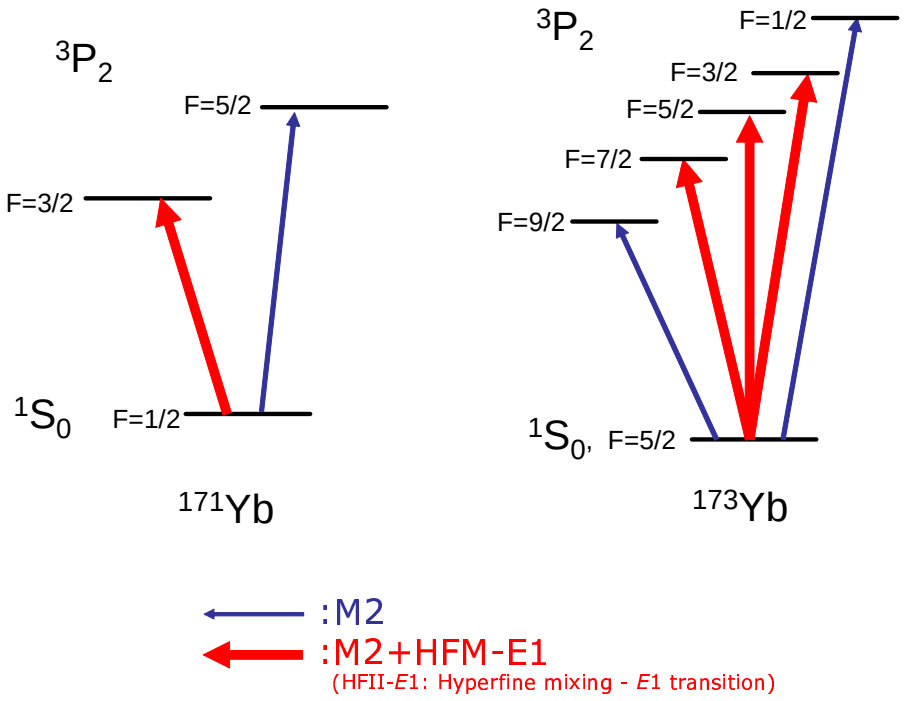

Figure 7.9: Hyperfine mixing can occur between levels which satisfy the selection rule of the E1 transition. Possible transitions via the HFM-E1 transition are described by thick lines. Other transitions are possible only through the M2 transition.

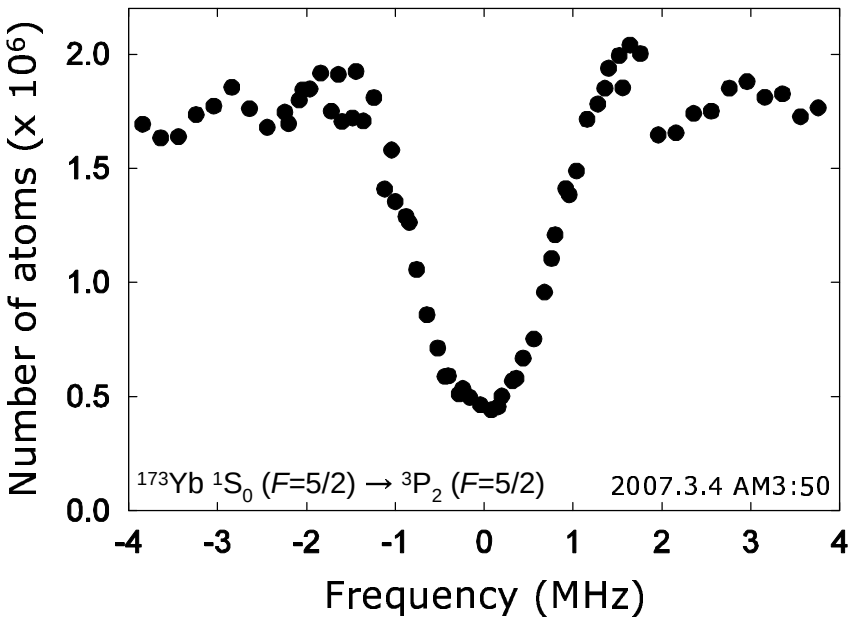

Figure 7.10: The first spectrum of the $^1S_0(F{=}5/2) \leftrightarrow {}^3P_2(F{=}5/2)$ transition in fermion isotope ^{173}Yb. The spectral width was artificially broadened in this measurement.

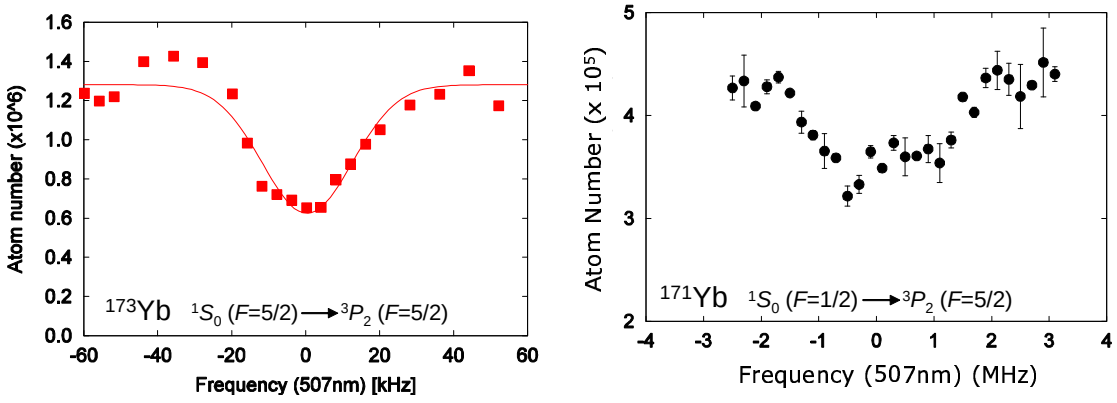

Figure 7.11: (Left): Spectrum in ultracold ^{173}Yb. The residual magnetic field split the $^3P_2(F{=}5/2)$ state into six Zeeman sublevels. One of them is shown here. (Right): The $^1S_0(F{=}1/2) \leftrightarrow {}^3P_2(F{=}5/2)$ resonance in ^{171}Yb. The HFM effect does not work in this transition.

7.2.2 Boson: ^{174}Yb

Finding the $^1S_0 \leftrightarrow ^3P_2$ transition in bosonic isotopes is crucially important. First, it enables the coherent excitation of a BEC in the ground state to the metastable $^3P_2$ state. Furthermore, we have the ultranarrow magnetic-insensitive $^1S_0(m{=}0) \leftrightarrow ^3P_2(m{=}0)$ transition in bosonic isotopes. This kind of transition is well known as a "clock" transition. In fact, an atomic clock using this transition has been proposed in [3].

Since our group has realized a BEC of ^{174}Yb in the previous work [24], we searched the resonance in ^{174}Yb among five stable bosonic isotopes of Yb. By irradiating the excitation laser to atoms in a compressed MOT for 3 s, we have successfully found the resonance which is shown in Fig.7.12. In the following sections and chapters, experiments using the $^1S_0 \leftrightarrow ^3P_2$ transition in ^{174}Yb will be presented in detail.

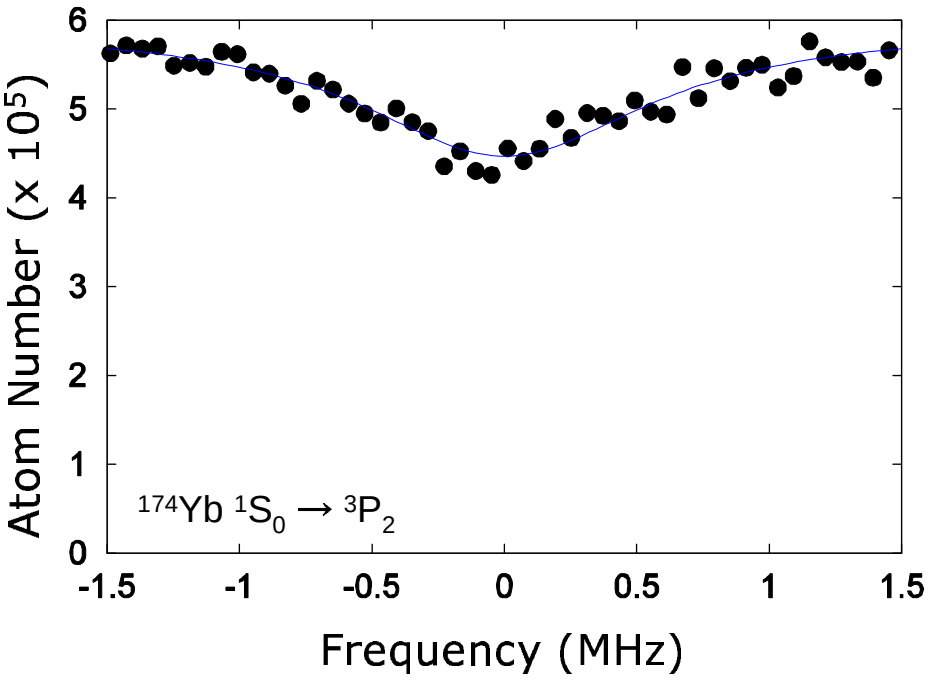

Figure 7.12: The $^1S_0 \leftrightarrow ^3P_2$ transition in ^{174}Yb. Atoms in a compressed MOT were used. Spectrum was artificially broadened to make it easier for us to find the resonance, which results in $\sim$1 MHz spectral width.

7.3 Selective excitation to all magnetic sublevels of the $^3P_2$ state in ^{174}Yb

The $^3P_2$ state in a bosonic isotope ^{174}Yb has five magnetic sublevels corresponding to m = 0, ±1 and ±2. If we consider the high-resolution spectroscopy using this transition, the selective excitation of atoms to the arbitrary magnetic sublevel of the $^3P_2$ state is inevitable. For example, in order to measure the absolute frequency of the clock transition, we need to observe well separated $^1S_0 \leftrightarrow {}^3P_2(m{=}0)$ transition. When we measure the polarizability of each magnetic states, each magnetic sublevels must be well distinguished. Hence we have demonstrated the selective excitation of atoms to any magnetic sublevels.

The experimental procedure and configuration of lasers and the magnetic field are shown in Fig. 7.13. Atoms are cooled by evaporative cooling in a crossed FORT and excited in the FORT. Atomic temperature is about 1 μK. As an external magnetic field, we used the residual magnetic field at the crossed FORT region.

Fig. 7.14 shows the obtained spectra. Fig. 7.14(a) is the spectrum obtained by roughly scanning the frequency of the excitation laser, in which five components are included with the interval of ∼1.5 MHz corresponding to the residual magnetic field of 0.7 G. The relative signal strength of each components depends on the selection rule of the M2 transition. As already discussed in 4.2, the selection rule depends on the polarization of the excitation laser, the FORT polarization, and the external magnetic field. Fig. 7.14(b)−(f) are detailed spectra of each magnetic sublevels. The spectral width are almost consistent with the Doppler width.

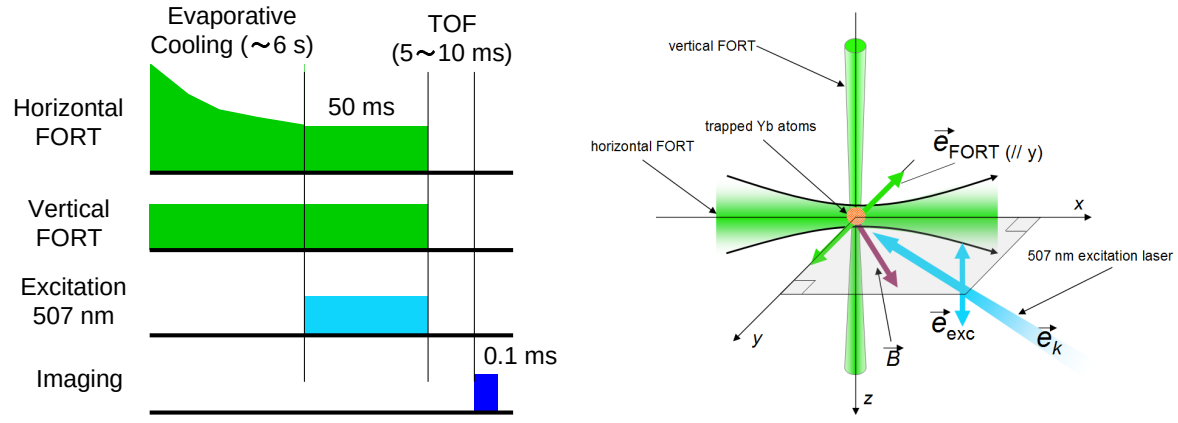

Figure 7.13: (Left): Time sequence of the experiment and (Right): configuration of lasers and the magnetic field.

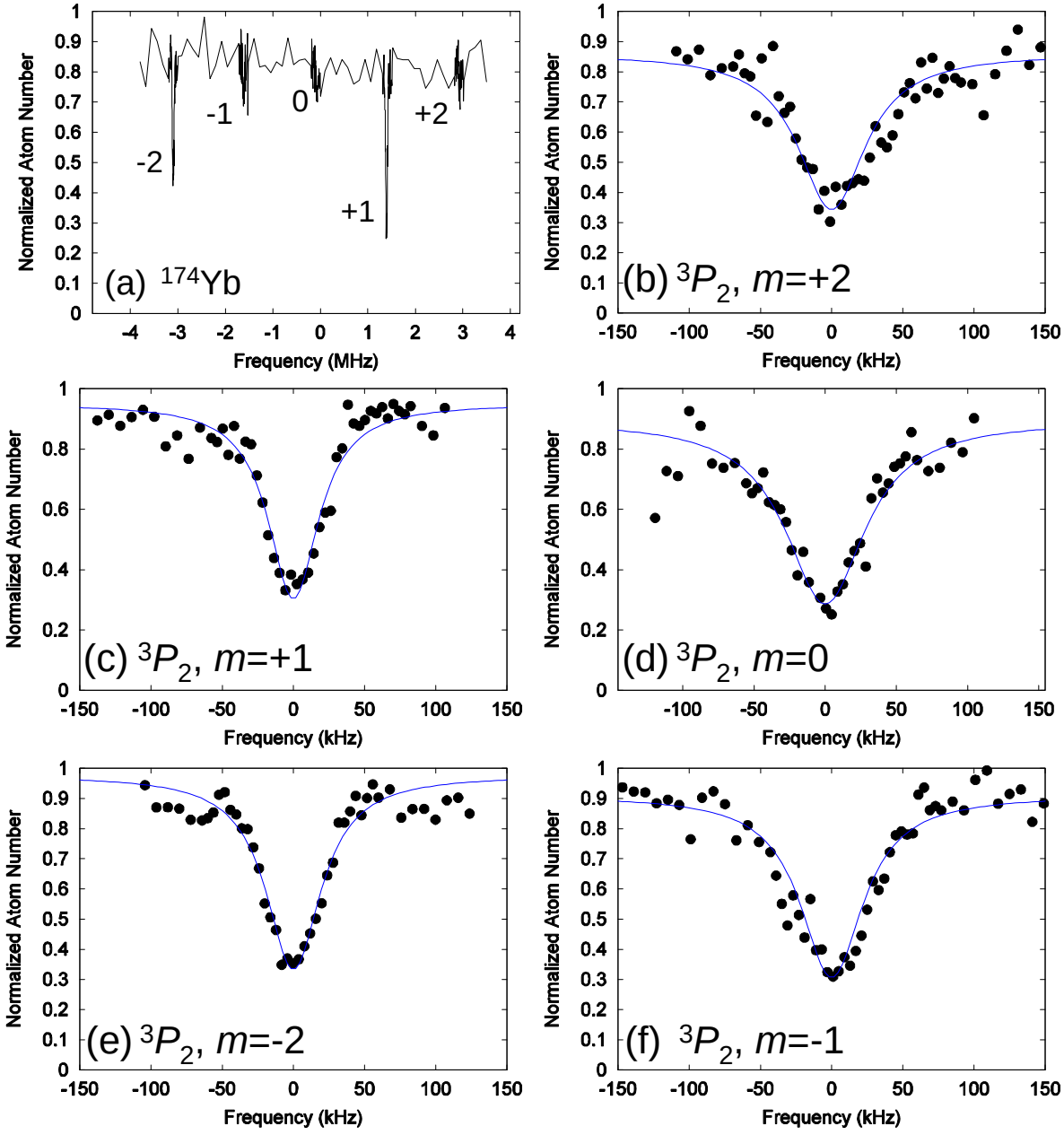

Figure 7.14: Selective excitation to five magnetic sublevels of the $^3P_2$ state in ^{174}Yb. (a): The spectrum obtained by roughly scanning the frequency of the excitation laser. The red solid line is a fit by five Gaussian functions with experimental parameters such as the polarization of the excitation laser, the FORT polarization, and the external magnetic field. (b)−(f): Detailed spectra of each magnetic sublevels.

7.4 Measurement and control of ac polarizabilities

The ac polarizability is the important information when we use a FORT since it determines the trap depth of the FORT. In general, the polarizabilities of the ground state and the excited state are different, except for the case of the magic wavelength. Thus the resonance frequency of atoms in a FORT depends on the FORT power. Usually, in order to measure the ac polarizability, parametric resonance technique was used as we previously did in section 6.1.5. However, thanks to the ultranarrow linewidth of the ${}^1S_0 \leftrightarrow {}^3P_2$ transition, we can obtain much precise information than that obtained from the parametric resonance experiment. In a FORT, the resonance frequency ν can be described as

$$\nu = \nu_0 - \frac{I}{4}(\alpha_{\mathrm{P},m} - \alpha_{\mathrm{S}}), \tag{7.8}$$

where ν_0 is the transition frequency between unperturbed atomic states, I is the FORT intensity, $\alpha_{\mathrm{P},m}$ and α_{S} are the polarizabilities of magnetic sublevel m of the ${}^3P_2$ state and the ${}^1S_0$ ground state, respectively. We measured the dependence of the frequency shift of the resonance of each magnetic sublevels ($|m| = 0,\ 1,\ 2$) on a FORT power. Since the ac polarizability of the ground state α_{S} can be precisely estimated, we can derive the polarizability of the ${}^3P_2$ state. Time sequence of the experiment and configuration of lasers are shown in Fig. 7.15. In this experiment, the magnetic field was aligned almost parallel to the polarization of the horizontal FORT.

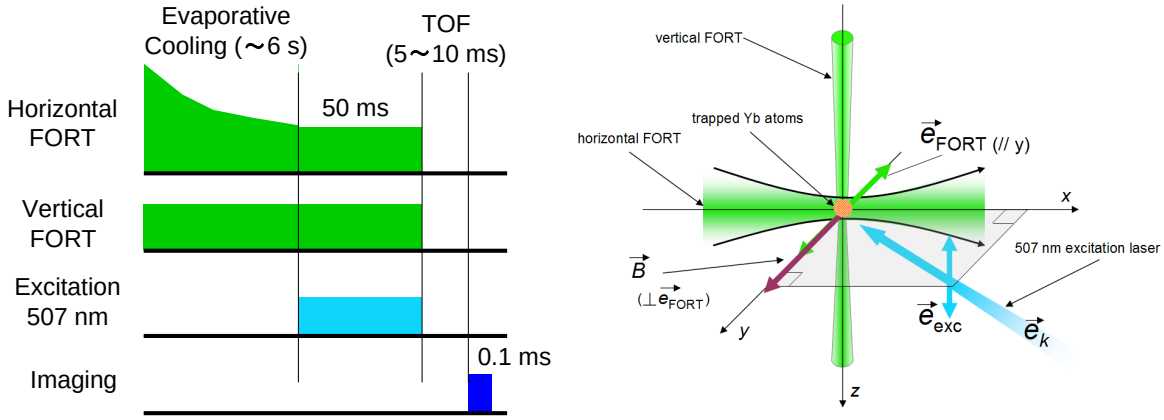

Figure 7.15: (Left): Time sequence of the experiment and (Right): configuration of lasers and the magnetic field.

Temperature shift

When we determine the center frequency of each spectrum, we have to consider the temperature shift as discussed in section 5.2. To do so, we have to know the value of $\Omega_{\mathrm{g,ex}}$ which can be determined by the polarizability. In the present case, we already know the rough value of the polarizability of the $^3P_2$ state from the parametric resonance experiment as shown in section 6.1.5. Thus, we first assumed the polarizability of the $^3P_2$ state and fit the data to derive the temperature shift in which the free parameter is the polarizability α_1, the center frequency and the signal strength. After compensating the temperature shift, we could estimate the polarizability. In this experiment, all of the derived polarizability were well agreed with the fitted polarizability.

In the Fig. 7.16, three spectra corresponding to the $^1S_0 \leftrightarrow {}^3P_2(|m|{=}2)$ transition for three different FORT powers are shown as an example. The solid lines are the fit of data by the (5.21). In order to measure the temperature of atoms, the TOF technique was used. The arrows on the horizontal axis describe the unperturbed resonance frequency of the spectrum shown with the same color. The center frequencies ν_0 estimated by this fitting are plotted as a function of the FORT powers in Fig. 7.17 with data corresponding to $|m| = 0$ and 1. Using the known value of the polarizability of the ground state α_{S}, the polarizabilities of all of the magnetic sublevels of the $^3P_2$ state are determined which are listed in Table 7.4. In addition, from these observations, we can conclude that atoms in all the magnetic substates of the $^3P_2$ state can be optically trapped by a FORT at 532 nm, which is consistent with the result of the parametric resonance and also important for future studies of the $^3P_2$ atoms.

Table 7.3: Polarizability of the $^3P_2$ state (**B** is almost parallel to the $\mathbf{e}_{\mathrm{FORT}}$).

	$\lvert m\rvert$=0	$\lvert m\rvert$=1	$\lvert m\rvert$=2	Unit
$\alpha_{\mathrm{P},m}$	41.8±0.3	40.6±0.3	38.3±0.1	mHz(mW/cm^2)$^{-1}$

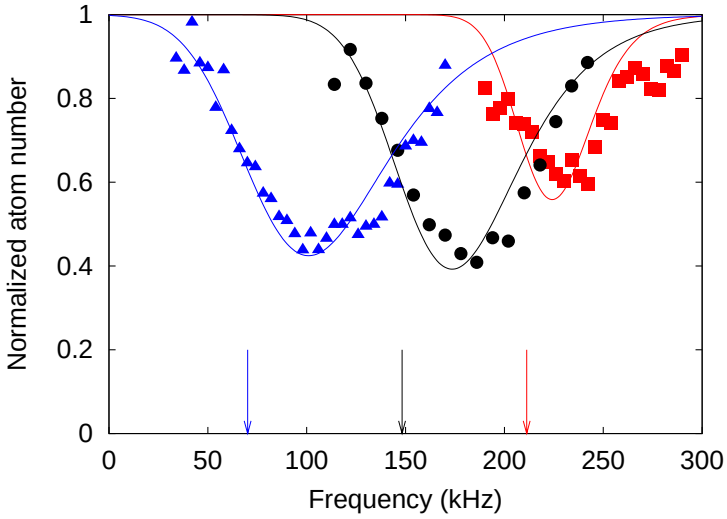

Figure 7.16: Due to the temperature shift (see 5.2), the observed resonance frequency is slightly shifted from the true resonance frequency. In this figure, three spectra corresponding to three different FORT powers 56, 146, and 250 mW are shown. Solid lines are the fit of (5.12) to the data. Each arrow indicates the position of the true resonance frequency for spectra in the same color.

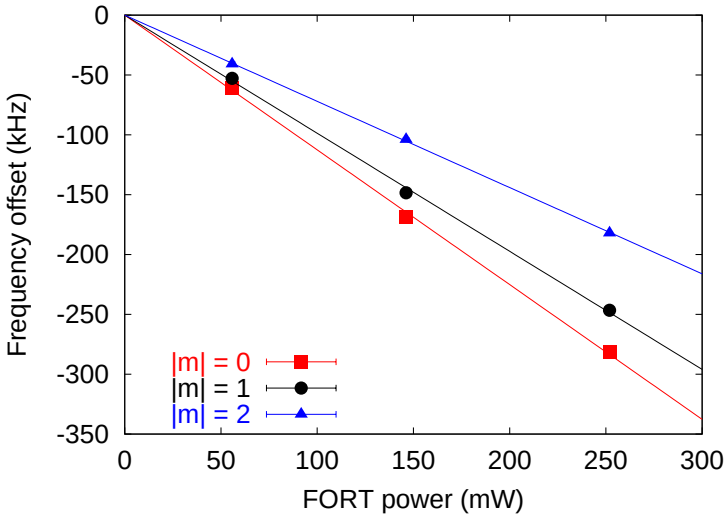

Figure 7.17: Measurement of the polarizability of every magnetic sublevel of the $^3P_2$ state. The resonance frequencies determined by considering the temperature shift are plotted as a function of FORT powers. Solid lines are the linear fit to the data based on (7.8).

7.4.1 Control of the polarizability

Five magnetic substates of Yb[$^3P_2$] in a FORT can be mixed with each other by the external magnetic field. As a result, their eigenvalues depend both on the FORT polarization and on the direction of the external magnetic field. One of the significant phenomena is that, even if $m = 0$, the energy level (light shift) can be shifted by the external magnetic field in a FORT. This technique was previously utilized as an ac Stark shift cancellation method using the $^3P_1$ state in Sr [84].

We performed the same measurement as that in the previous section by rotating the external magnetic field. As an example, Fig. 7.18 shows how the magnetic field "insensitive" resonance ($^1S_0 \leftrightarrow {}^3P_2$, $m = 0$) can be easily shifted just by rotating the external magnetic field. We also measured the polarizability of the $^3P_2(m{=}0)$ state in case of $\mathbf{B} \parallel \mathbf{e}_{\mathrm{FORT}}$ and $\mathbf{B} \perp \mathbf{e}_{\mathrm{FORT}}$ as schematically shown in Fig. 7.19(Top). Fig. 7.19(Bottom) shows the frequency shift of the resonance for two cases. Here, one can see the clear controllability of the polarizability of the $^3P_2(m{=}0)$ state. In particular, we should mention to our successful realization of making the polarizability of the $^3P_2(m{=}0)$ state almost same as that of the ground state. This would enable us to perform ultrahigh-resolution spectroscopy of atoms in an optical lattice [8].

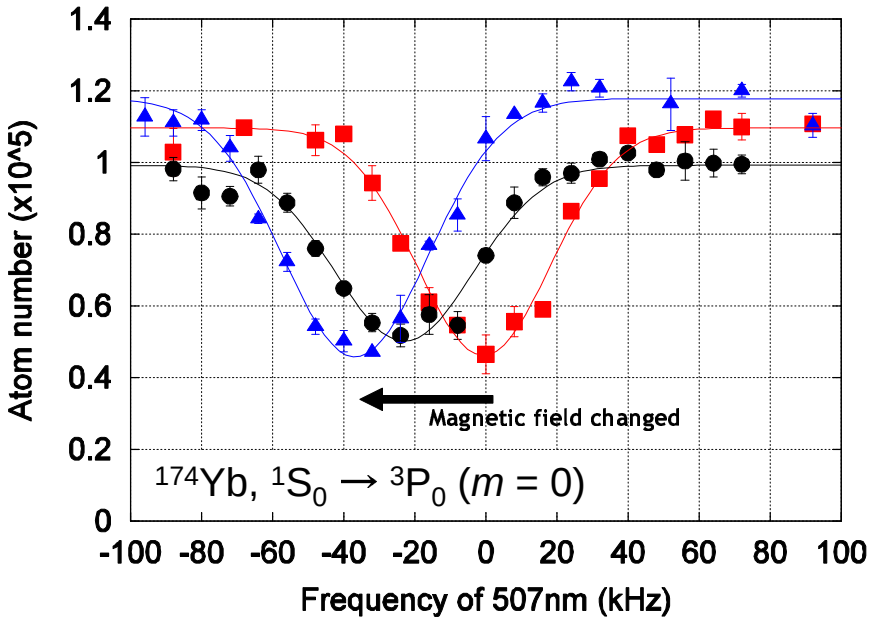

Figure 7.18: The resonance frequency of the magnetic field insensitive $^1S_0 \leftrightarrow {}^3P_2(m{=}0)$ transition can be changed in a FORT just by rotating the external magnetic field. This results from the mixing of eigenstates of atoms in a FORT which is induced by the external magnetic field.

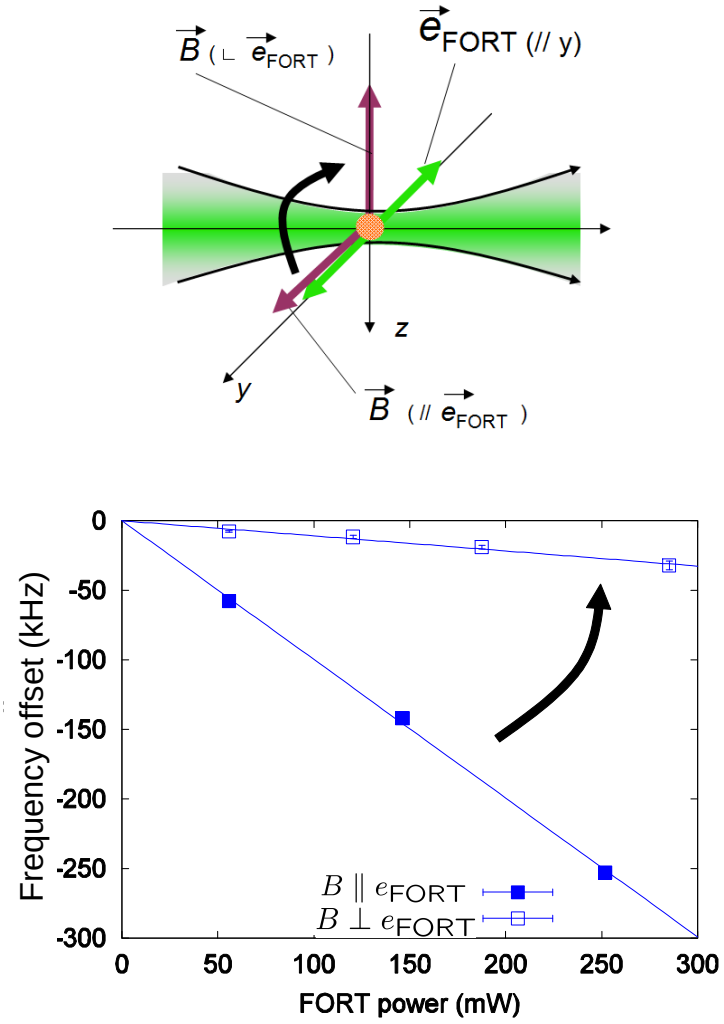

Figure 7.19: Change of the polarizability of the ${}^3P_2(m{=}0)$ state. (Top) Configuration of lasers and the external magnetic field are schematically shown. (Bottom) Polarizability is clearly changed by rotating the external magnetic field. In particular, when $\mathbf{B}$ is almost perpendicular to $\mathbf{e}_{\mathrm{FORT}}$, the situation is similar to the magic wavelength situation where the ac Stark shifts are almost the same for the ${}^1S_0$ and ${}^3P_2(m=0)$ states.

7.5 Magnetic resonance imaging of ultracold atoms

Magnetic resonance imaging (MRI) is well known as the technique to visualize the human body mainly for the medical purpose. Such MRI system usually uses the magnetic resonance of a hydrogen nuclear spin in a body, that is to say, the nuclear magnetic resonance (NMR). In addition, by applying the magnetic gradient, the information about the position of the NMR signal can be obtained.

In atomic physics, the MRI technique has also been developed mainly in the experiment using alkali metals. In such experiments, a microwave pulse induces the transition between two different hyperfine spin states in atoms which are addressed in a magnetic field gradient. Sodium atoms in a magnetic trap was first investigate by using the MRI technique [85]. One of the recent important experiments is the imaging of the Mott insulator shells. By using the spin changing collisions, the MRI technique have enabled the observation of the shell structure of the Mott insulator [86]. More recently, spatially resolved microwave spectroscopy of a trapped Fermi gas with resonant interactions has been demonstrated [87].

In this work, we developed the basic technique of the MRI. The basic idea is that atoms in the ${}^3P_2(m{=}+2)$ state in a magnetic gradient can be energetically distinguished by the ultranarrow ${}^1S_0 \leftrightarrow {}^3P_2(m{=}+2)$ transition. In general, the transition linewidth is too large to distinguish atoms in a realistic magnetic field gradient. In other words, the size of the atomic cloud is too small to be addressed with the realistic magnetic gradient. To the contrary, since the natural linewidth of the ${}^1S_0 \leftrightarrow {}^3P_2$ transition is extremely narrow, we can distinguish atoms in a small region such as a FORT.

For example, let us imagine that the typical magnetic field gradient generated by the MOT coils of 10 G/cm is applied to the atomic cloud. The Zeeman shift of the ${}^3P_2(m{=}+2)$ state is 4 GHz/m in such a magnetic field gradient. The most narrowest laser linewidth ever achieved reaches below 1 Hz [88], then we assume that we can use the excitation laser whose linewidth is 1 Hz. Then, in principle, the spectral resolution can be expected to be 0.25 nm. In other words, we can energetically distinguish two atoms which are separated to 0.25 nm. Furthermore, so far, this resolution is limited only by the technical reason (laser linewidth). The natural linewidth of the ${}^1S_0 \leftrightarrow {}^3P_2$ transition is about 10 mHz which is smaller than the above estimation by a factor of two. In addition, the magnetic field gradient which is much larger than 10 G/cm is easily obtained. Hence, the extremely high spatial resolution can be expected even with the present experimental technique in this field.

The basic principle of this experiment is schematically shown in Fig. 7.20. When the flat magnetic field is applied to the atomic cloud, the Zeeman shift induced in the ${}^3P_2(m{=}+2)$ state is same for all atoms in a cloud. Thus, the spectral width is mainly determined by the Doppler width. On the other hand, when the magnetic gradient is applied, the Zeeman shift induced to the atoms depends on the position, which leads to the broadening of the spectrum of the ${}^1S_0 \leftrightarrow {}^3P_2(m{=}+2)$ transition in addition to the Doppler width.

We have used the ultracold atoms whose temperature is 0.5 μK. After evaporative cooling, we have applied the magnetic gradient by turning on the MOT coil. Fig. 7.20

shows the obtained spectra before and after applying the magnetic field gradient. We can clearly observe the spectral broadening due to the MRI effect. We should also note that the resonance signal became drastically weak as the magnetic gradient increased. This is reasonable because the number of atoms which are resonant with the excitation laser at a certain frequency decreases due to the position dependent Zeeman shift. Thus, ideally, we should have used the same excitation time for two cases and detected how the position dependent excitation in atomic cloud occurred in order to demonstrate the MRI. Unfortunately, the resolution of our present imaging system is not high enough for such a purpose. Instead, we made the excitation time longer to obtain the same signal strength for both conditions. In this measurement, the excitation time is much longer than the trap frequency. Thus, atoms passed over the resonant region for many times and were excited. The larger the magnetic gradient became, the narrower the resonant region became. Then, atoms had to pass over for many times to be excited, which resulted in the longer excitation time.

In Fig. 7.20, spectra taken before and after turning on the MOT coils are compared. Since we could not know where atoms were in the magnetic field gradient, it is not possible to quantitatively analyze these spectra. Nevertheless, spectral broadening induced by the magnetic gradient has been clearly observed.

This technique of spatial addressing has great potential for future experiments, such as addressing of the individual site of the optical lattice potentials which must be a key technique for the quantum computation experiment [82, 13] and the construction of the quantum simulator [45].

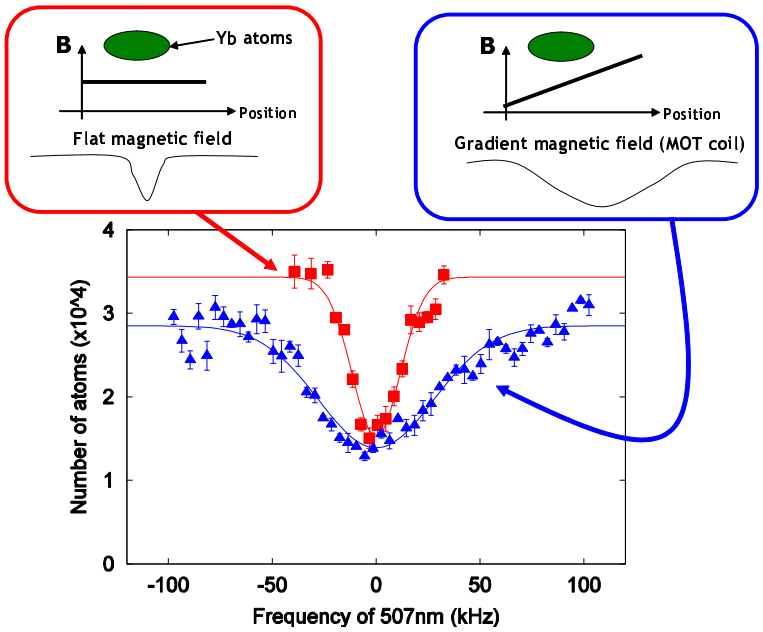

Figure 7.20: Demonstration of the magnetic resonance imaging. The magnetic field gradient applied to atoms leads to spectral broadening of the magnetic field sensitive ultranarrow ${}^1S_0 \leftrightarrow {}^3P_2 (m = +2)$ transition.

Chapter 8

High-resolution spectroscopy of a BEC

One of the significant properties of a BEC is its large mean field energy. The mean field energy U_0 results from the interatomic interaction energy. At low energies where only the s-wave scattering occurs, U_0 of a BEC is described by

$$U_0^{\mathrm{BEC}} = \frac{4\pi\hbar^2}{m} na, \tag{8.1}$$

where m is the atomic mass, n is the number density and a is the s-wave scattering length. Thus, the large number density n of a BEC results in its large mean field energy.

Previously the large mean field energy of a BEC was, for example, used to identify a hydrogen BEC [89]. The BEC phase transition has been usually confirmed by the sudden appearance of a dense central core inside a thermal cloud. However, that was not easy with the hydrogen BEC since taking absorption images to see the spatial distribution of hydrogen atoms was difficult due to technical reasons. Then, the large mean field shift of the resonance frequency in a two-photon transition was used to identify a hydrogen BEC.

In experiments with alkali metals, the mean field energy has also played an important role. For example, the collision shift in the clock transition $|F,0\rangle \leftrightarrow |F+1,0\rangle$ in sodium atoms was accurately measured by using the large mean field energy of a BEC [90]. One of the recent remarkable applications of the mean field energy is the direct observation of the Mott insulator shell structure [91]. In 3D optical lattice potentials, it was predicted that the system should separate into Mott insulator shells with different occupation numbers for sufficiently strong interatomic interactions. By using RF spectroscopy, Campbell *et al.* detected the shift of the resonance frequency of the clock transition due to the layered structure of the Mott shells with occupancies from $n = 1$ to $n = 5$. Since the mean field energy is proportional to the number density (see (8.1)), the discrete frequency shift corresponding to the number of atoms in each site was successfully observed.

It is true that all of these experiments are excellent, but there also exist some limitations. First, the resolution of RF spectroscopy to detect the mean field energy in alkali metals is currently limited by the finite interaction time broadening. Atoms in two different states feel different mean field energies because of the difference of the scattering

length between a_{11} and a_{12} where a_{xy} is the scattering length between atoms in the states x and y. This difference leads to the mean field shift $\Delta\nu^{\mathrm{BEC}}$ described by

$$\Delta\nu^{\mathrm{BEC}} = \frac{2\hbar}{m} n(a_{12} - a_{11}). \tag{8.2}$$

In case of alkali metals, $a_{12} - a_{11}$ is small. For sodium atoms as an example, $a_{12} - a_{11} = (3.15 - 2.71) = 0.44$ nm which results in the frequency shift of $\Delta\nu = 250$ Hz for the number density of $n = 1{\times}10^{14}$ cm^{-3}. The interaction time broadening is more than 500 Hz. Thus in order to achieve the higher resolution, we have to use longer excitation RF pulses which is so far difficult due to, for example, the short trap lifetime of atoms in such a system [90]. Second, addressing atoms by using position-dependent Zeeman shift in a stronger magnetic field gradient to pursue the higher spatial resolution [86] may affect alkali metals in the ground state. This is because the total angular momentum F is no longer the good quantum number under the strong magnetic field (Paschen-Back effect).

The ultranarrow $^1S_0{\leftrightarrow}^3P_2$ transition[1] in Yb has great possibilities to overcome such obstacles. First, according to the result of this work, the mean field shift of this transition in Yb is much larger than that of alkali metals as described in Table 8.1. The mean field shift of the $^1S_0{\leftrightarrow}^3P_2$ transition is larger than others by an order of one. In this work, this large mean field shift enabled us to successfully observe not only the frequency shift but also the distortion of the lineshape due to the mean field energy of a BEC which has never been observed in alkaline metals. Second, the ground state of Yb is spinless. Hence any strong magnetic field gradient for spatial addressing of Yb atoms by using the Zeeman shift of the $^3P_2$ state does not affect atoms in the ground state at all.

It is sure that Yb has two ultranarrow optical transitions, i.e., not only the $^1S_0{\leftrightarrow}^3P_2$ transition but also the $^1S_0{\leftrightarrow}^3P_0$ "clock" transition. However, the $^1S_0{\leftrightarrow}^3P_2$ transition has advantages in some points. In bosonic isotopes of Yb, the $^1S_0{\leftrightarrow}^3P_0$ transition is strictly forbidden. While a novel technique to realize it in bosonic isotopes by using a strong magnetic field has been recently invented, the transition strength is still very weak [33, 35]. Thus, considering spectroscopy of a BEC, the much stronger (but narrow enough for high resolution)$^1S_0{\leftrightarrow}^3P_2$ transition is desirable. In addition, since the $^1S_0{\leftrightarrow}^3P_0$ transition is the magnetic insensitive transition, addressing of atoms by the magnetic field gradient is impossible, while the $^3P_2$ state has four magnetic field sensitive sublevels: $^3P_2(m = \pm1$ and $\pm2)$.

In this study, we have demonstrated the detection of a mean field energy of a BEC by using the ultranarrow $^1S_0{\leftrightarrow}^3P_2$ optical transition in Yb. We have observed not only the large mean field shift due to a BEC, but also the change of the lineshape which reflected the density distribution of a BEC in a trap. Finally, we have successfully determined a_{12} from the observed spectrum. In the following, we will first introduce a mean field energy of a BEC. Then, the spectral lineshape expected in spectroscopy of a BEC in a trap will be discussed. After presenting the experimental method, we will show the experimental results and discuss the observed spectrum in detail.

[1]The natural linewidth of 10 mHz corresponds to the energy resolution of 0.5 pK ($= 5 \times 10^{-13}$K) which is the extremely high-resolution.

Table 8.1: Frequency shift by the mean field energy of a BEC for the number density of $n = 1\times10^{14}\mathrm{cm}^{-3}$.

	a_{12} (nm)	a_{11} (nm)	$\Delta\nu^{\mathrm{BEC}}$(Hz)	Ref.
^{23}Na	3.15	2.71	241	[90]
^{87}Rb	5.19	5.32	−19	[91]
^{174}Yb	−33	5.53	−2792	[30] and this work.

8.1 Mean field energy

Pseudo potential

When two neutral atoms come so close to each other that atoms can see atomic nucleus, the interatomic interaction is repulsive. Otherwise, atoms must collapse and cannot stably exist. The length scale of this repulsive core is, in general, less than 1 nm. On the other hand, there is the attractive interaction known as van der Waals force between neutral atoms. The reach of the van der Waals force is about 10 nm. As a result, the net force between neutral atoms is sum of the repulsive force by a hard-sphere and the attractive force by the van der Waals force. Whether the net force becomes repulsive or attractive depends on atomic species[2]. In dilute neutral atomic gasses, the average interatomic length is 100 nm. Thus, the effect of the complicated realistic interatomic potential within 10 nm can be described only by a phase shift δ_l of the scattering wave function before and after the scattering. This can be seen in the radial part of the scattering wave function $R_{kl}(r)$ in the $r \to \infty$ limit:

$$R_{kl}(r) \simeq \frac{1}{kr}\sin(kr + \delta_l - \frac{\pi}{2}l). \tag{8.3}$$

In particular, when the only s-wave scattering can occur at low energies, the s-wave phase shift is given by

$$\delta_0 = -ka, \tag{8.4}$$

where $k = |\mathbf{k}|$ is the wavenumber vector of the scattering wave and a is the scattering length. According to the (8.3), δ_0 shifts the origin of $R_{kl}(r)$ by a. Thus, the scattering wavefunction $\psi(\mathbf{r})$ for the s-wave scattering in the center-of-mass coordinate satisfies the Schrödinger equation

$$(\nabla^2 + k^2)\psi(\mathbf{r}) = 0 \quad (r > a) \tag{8.5}$$

$$\psi(\mathbf{r}) = 0 \quad (r \le a). \tag{8.6}$$

This indicates that when we consider the s-wave scattering, we can regard the interatomic potential as a hard-sphere potential with radius a.

[2]In case of ^{174}Yb, it is repulsive.

In general, it is difficult to solve (8.5) due to the boundary condition (8.6). However, Huang and Yang [92] proved that, for s-wave scattering, (8.5) and (8.6) are equivalent to the equation

$$(\nabla^2 + k^2)\psi(\mathbf{r}) = 4\pi \frac{\tan(ka)}{k} \delta(\mathbf{r}) \frac{\partial}{\partial r}(r\psi(\mathbf{r})). \tag{8.7}$$

At low energies,

$$\frac{\tan(ka)}{k} = a + \frac{1}{2}(ka)^2 \frac{2}{3} a + \cdots.$$

When we consider the s-wave scattering, the effect of the terms a^3 (p-wave) and higher can be neglected. As a result, (8.7) becomes

$$\begin{aligned} -\frac{\hbar^2 \boldsymbol{\nabla}}{m}\psi(\mathbf{r}) + U(r)\psi(\mathbf{r}) &= E\psi(\mathbf{r}) \\ U(r) &= \frac{4\pi a \hbar^2}{m} \delta(\mathbf{r}) \frac{\partial}{\partial r} r. \end{aligned} \tag{8.8}$$

Thus the interatomic interaction potential at low energies (s-wave scattering) is given by (8.8) which is known as a pseudo potential.

Thomas-Fermi approximation

Using the pseudo potential, the Hamiltonian H for N atoms in a trap $V_{\text{ext}}(\mathbf{r})$ at low energies is given by

$$H = -\sum_{i=1}^{N} \left\{ \frac{\hbar^2}{2m} \nabla^2 + V_{\text{ext}}(\mathbf{r}_i) \right\} + \frac{4\pi a \hbar^2}{m} \sum_{i<j} \delta(\mathbf{r}_i - \mathbf{r}_j) \frac{\partial}{\partial r_{ij}} r_{ij}. \tag{8.9}$$

In a BEC, all atoms occupy the same one-particle wavefunction $\phi(\mathbf{r})$. Thus we can introduce $\psi(\mathbf{r})$ as a wavefunction of a condensate which is defined by

$$\psi(\mathbf{r}) = \sqrt{N}\phi(\mathbf{r}). \tag{8.10}$$

Then, the density of a condensate $n(\mathbf{r})$ can be described by

$$n(\mathbf{r}) = |\psi(\mathbf{r})|^2. \tag{8.11}$$

Now we can present the energy E of the system and the total atom number N as follows[3].

$$\begin{aligned} E(\psi) &= \int \left[\frac{\hbar^2}{2m} |\boldsymbol{\nabla}|^2 + V_{\text{ext}}(\mathbf{r})|\psi(\mathbf{r})|^2 + \frac{1}{2} \frac{4\pi a \hbar^2}{m} |\psi(\mathbf{r})|^4 \right] \mathrm{d}\mathbf{r} \\ N &= \int |\psi(\mathbf{r})|^2 \mathrm{d}\mathbf{r}. \end{aligned} \tag{8.13}$$

[3]Here, we use the fact that $\psi(\mathbf{r})$ doesn't diverge at $\mathbf{r} = 0$. In such a case, the pseudo potential becomes

$$U(\mathbf{r}) = \frac{4\pi a \hbar^2}{m} \delta(\mathbf{r}). \tag{8.12}$$

This is because

$$U(\mathbf{r})\psi(\mathbf{r}) = \frac{4\pi a \hbar^2}{m} \delta(\mathbf{r}) \frac{\partial}{\partial r}(r\psi(\mathbf{r}))$$

Minimizing the energy E with the binding condition (8.13) by the method of Lagrange multipliers gives us the time-independent Gross-Pitaevskii equation:

$$\left[-\frac{\hbar^2}{2m}\nabla^2 + V_{\rm ext}(\mathbf{r}) + \frac{4\pi a\hbar^2}{m}|\psi(\mathbf{r})|^2\right]\psi(\mathbf{r}) = \mu\psi(\mathbf{r}) \tag{8.14}$$

where μ is the chemical potential. Here the third term in the left-hand side is called mean field energy.

When we treat a BEC with a large number of atoms, the mean field energy is much larger than the kinetic energy. Then the kinetic energy term can be safely neglected. This is known as Thomas-Fermi approximation. In this approximation, the Gross-Pitaevskii equation becomes

$$\left\{V_{\rm ext}(\mathbf{r}) + \frac{4\pi a\hbar^2}{m}|\psi(\mathbf{r})|^2\right\} = \mu\psi(\mathbf{r}), \tag{8.15}$$

and then the density distribution is given

$$n(\mathbf{r}) = |\psi(\mathbf{r})|^2 = \begin{cases} \left(\dfrac{4\pi\hbar^2 a}{m}\right)^{-1}(\mu - V_{\rm ext}(\mathbf{r})) & (\mu > V_{\rm ext}(\mathbf{r})) \\ \\ 0 & (\mu \le V_{\rm ext}(\mathbf{r})) \end{cases} \tag{8.16}$$

This implied that the density distribution of a BEC in a trap is the inverse of the trap shape.

Line shape of the excitation spectrum of BEC in a trap

Let us consider the excitation of atoms in a BEC in a trap. We assume that the excitation is so weak that the excited atoms interact only with the atoms in the ground state. Thus, the interaction between atoms in the excited state is neglected.

According to the (8.14), the effective potentials $V^{\rm eff}$ for a BEC in the ground state $|g\rangle$ and an atom in a excited state $|e\rangle$ in a trap are

$$\begin{aligned} V^{\rm eff}_{|g\rangle}(\mathbf{r}) &= V_{\rm ext}(\mathbf{r}) + \frac{4\pi\hbar^2 a_{gg}}{m}n(\mathbf{r}) = \mu \\ V^{\rm eff}_{|e\rangle}(\mathbf{r}) &= V_{\rm ext}(\mathbf{r}) + \frac{4\pi\hbar^2 a_{ge}}{m}n(\mathbf{r}), \end{aligned} \tag{8.17}$$

where a_{12} denotes the scattering length between atoms in the state $|1\rangle$ and $|2\rangle$. In Fig.8.1, these effective potentials are schematically shown in case of $a_{ge} < 0$.

$$\begin{aligned} &= \frac{4\pi a\hbar^2}{m}\left(\delta(\mathbf{r})\psi(\mathbf{r}) + \delta(\mathbf{r})r\frac{\partial\psi(\mathbf{r})}{\partial r}\right) \\ &= \frac{4\pi a\hbar^2}{m}\delta(\mathbf{r})\psi(\mathbf{r}). \end{aligned}$$

The lineshape of the excitation spectrum of a BEC in a trap can be derived by calculating the transition probability from the flat potential $V^{\rm eff}_{|g\rangle}(\mathbf{r}) = \mu$ to individual vibrational levels in $V^{\rm eff}_{|e\rangle}(\mathbf{r})$. The resulting lineshape is given by [93]

$$I(\nu) = \frac{15h(\nu-\nu_0)}{4n_0\Delta U}\sqrt{1-\frac{h(\nu-\nu_0)}{n_0\Delta U}}, \quad \Delta U = \frac{4\pi\hbar^2}{m}(a_{ge}-a_{gg}), \tag{8.18}$$

where ν_0 is the unperturbed resonance frequency (including the recoil shift in our experiment), n_0 is the peak number density. The lineshape Eq. (8.18) is schematically shown in Fig. 8.1(Right). Reflecting a mean field energy, the spectrum is drastically shifted to the red side from the original position in case of $a_{ge} < 0$. If $a_{ge} > 0$, it is shifted to the blue side. The asymmetry of the lineshape reflects the anomalous density distribution of a BEC in a trap.

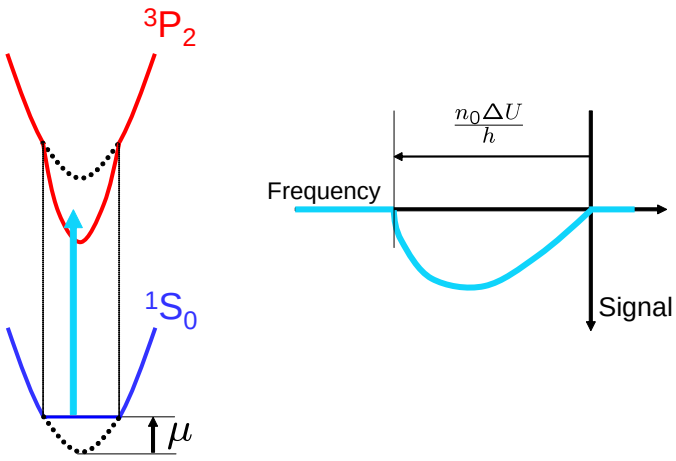

Figure 8.1: (Left): Effective potentials for a BEC in a harmonic trap are schematically shown both for the $^1S_0$ state and the $^3P_2$ state in case of $a_{12} < 0$. Reflecting the density distribution of atoms in a trap, the effective potentials are modified as described in Eq. (8.17). (Right): Excitation spectrum (Eq. (8.18)) between these two effective potentials is shown. Due to the mean field energy, the resonance frequency shifts and the lineshape becomes distorted.

8.2 BEC in a harmonic trap

In Fig. 8.2, the time sequence and configurations of lasers and the magnetic field are schematically shown. After evaporative cooling for 6 s, atomic temperature reaches 1.2, 0.5, 0.3 μK and a BEC in this measurement. This is done by reducing the final FORT powers depending on the desired atomic temperature. Then the excitation laser is irradiated for 50 ms. The intensity of the excitation laser is less than $I = 100$ mW/cm^2. We

use the magnetic-field-insensitive ${}^1S_0 \leftrightarrow {}^3P_2(m=0)$ transition for spectroscopy. After the TOF time t, the absorption images are taken.

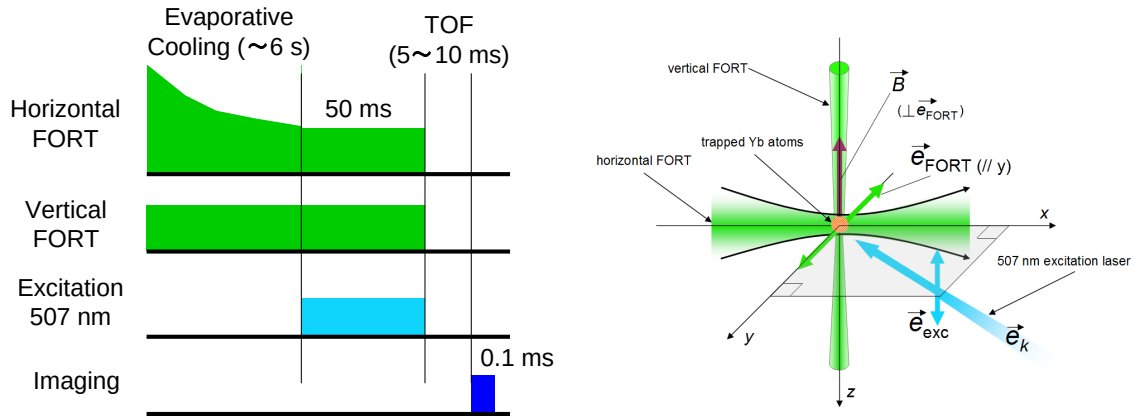

Figure 8.2: (Left): Time sequence for spectroscopy of a BEC. (Right): Configuration of the polarization of the FORT, the magnetic field, and the incident direction of the excitation laser in this measurement are schematically shown.

The magnetic field is applied to almost vertical to the polarization of the horizontal FORT beam. Using thermal atoms, the light shift in this configuration was measured in advance as shown in Fig. 8.3. The temperature shifts have been already compensated (removed) by using the (5.12). As a result, the ratio of the trap depth between the ${}^3P_2(m=0)$ and ${}^1S_0$ states is determined to be $U_{{}^3P_2(m=0)}/U_{{}^1S_0} = 1.02 \pm 0.01$ which is very close to the magic wavelength condition.

Figure 8.4 (Top) shows the observed spectra for thermal atoms at three different temperatures and a BEC. In this figure, only the frequency drift of the excitation laser due to the instability of the ULE cavity was compensated. Such drift was estimated from the difference of resonance frequencies in two data taken at two different times under the same conditions ($\Delta\nu_{\rm LS}$ in Table 8.2). We assumed that the frequency of the excitation laser linearly drifted during this measurement. Solid lines in spectra of thermal atoms (T=1.2, 0.5, and 0.3 μK) are fit of (5.21). All spectra are equally shifted by the recoil shift.

A significant feature in Fig. 8.4(Top) is the large shift of the resonance frequency after the BEC transition. This is clearly caused by sudden increase of the atomic density due to the BEC transition. Also, the spectral lineshape is distorted, which reflects the characteristic density distribution of a mean-field limited BEC in a harmonic trap. All these features can be well described by (8.18) (solid line in the BEC spectrum). The scattering length a_{11} has been accurately measured to be 5.53 nm via photoassociation spectroscopy in our laboratory [30]. Thus, the free parameter in (8.18) is only a_{12}. By fitting (8.18) to the observed spectrum, we could estimate that $a_{12} = -33(\pm 10)$ nm.

Using a_{12} determined in this study, we now can estimate the collision shift $\Delta\nu_{\rm col}$ for

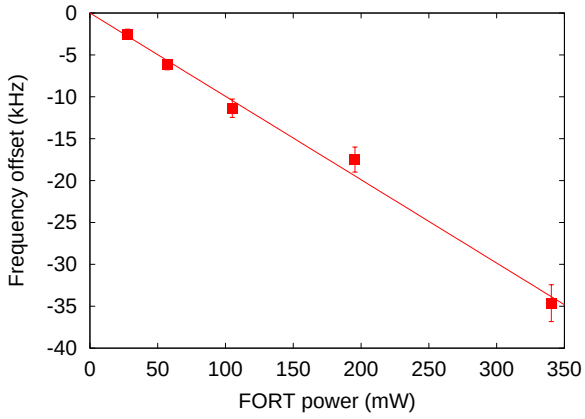

Figure 8.3: Measurement of the light shift in the configuration of Fig. 8.2 (Right). Temperature shifts in these data have been already removed.

thermal atoms[4] which is listed in Table 8.2. In addition, the position of atoms in a trap slightly shifts from the focal point of the FORT laser due to the gravity. This also leads to the shift of the resonance frequency estimated as $\Delta\nu_{\rm gr}$ in Table 8.2. After compensated all frequency shifts[5] mentioned above except for the mean field shift in a BEC spectrum, we again compare the BEC spectrum with those of thermal atoms as shown in Fig. 8.4 (Bottom). Here, one can clearly see the frequency shift caused by the mean field energy of a BEC. As predicted in (8.18), the upper edge of the BEC spectrum coincides with the unperturbed (no collision shift) resonance frequency.

In conclusion of this section, we have successfully detected the mean field energy of a BEC by using an ultranarrow ${}^1S_0 \leftrightarrow {}^3P_2$ transition in Yb. From the fitting of the lineshape, we can also determine the s-wave scattering length between atoms in the ${}^1S_0$ state and the ${}^3P_2$ state. Now the mean field shift corresponds one-to-one with the number density n in (8.18). Also, the s-wave scattering length $a_{12} = -33$ nm is very large, compared to that of alkali metals (see Table 8.1). Furthermore, by performing the spectroscopy in a magnetic field gradient, it is possible to address atoms by the position-dependent Zeeman shift. As a result, it is well within our ability to obtain the high resolution density profile of atomic clouds at any point in a trap by using the ${}^1S_0 \leftrightarrow {}^3P_2$ transition in Yb. Such a technique must be a powerful tool in the studies of, for example, the phase separation in the mixture of two (or more) degenerate gasses and the density structure of condensates in 1D, 2D and 3D optical lattice potentials.

[4]Note that the collision shift is twice of the Eq. (8.2). In general, the collision shift is given by

$$\Delta\nu_{\rm col} = g_2(0)\frac{2\hbar}{m}n(a_{12} - a_{11}), \tag{8.19}$$

where $g_2(0)$ is the equal point value of the second order correlation function. $g_2(0) = 2 - (n_{\rm BEC}/n)^2$ for a uniform Bose gas in thermal equilibrium [94, 95].

[5]The broadening due to the finite size of the condensate which implies a distribution of momenta [96] is estimated to be about 10 Hz in our case. Hence, it is neglected.

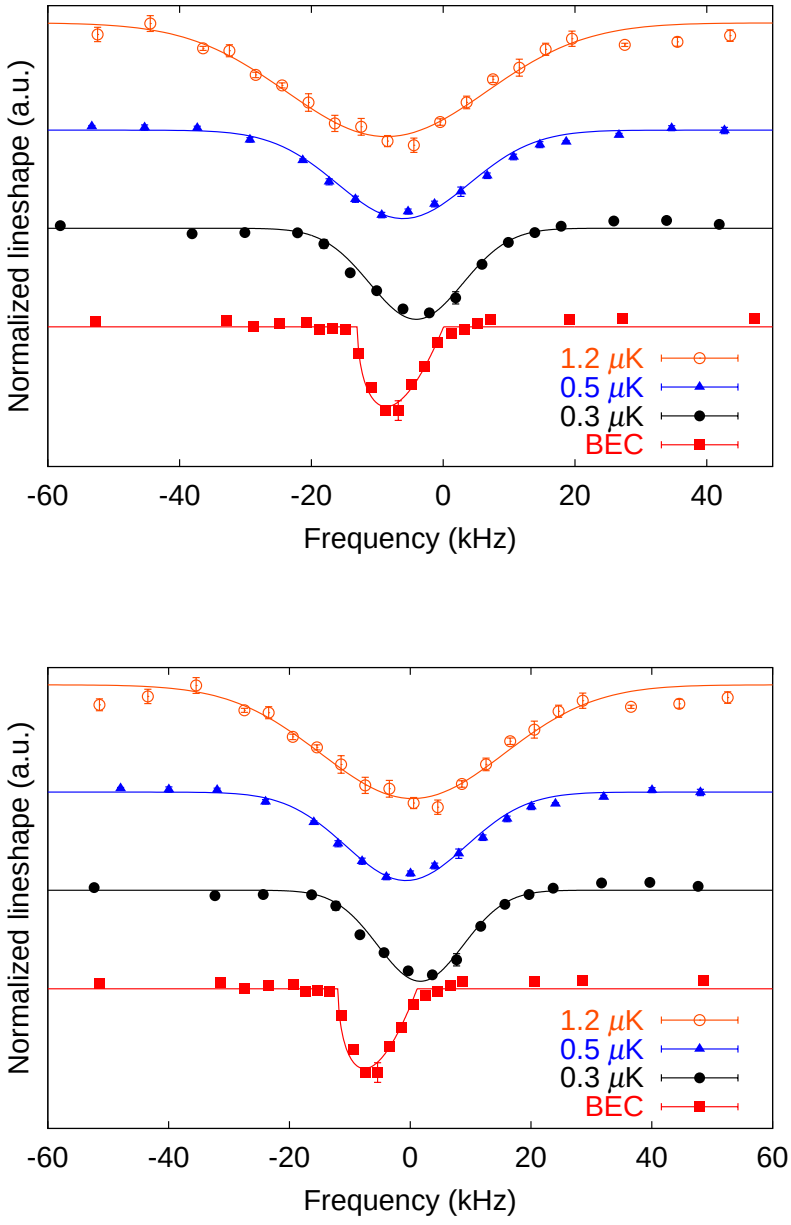

Figure 8.4: Spectroscopy of ultracold ^{174}Yb atoms and a BEC in a FORT by using the $^1S_0 \leftrightarrow {}^3P_2(m{=}0)$ transition. Solid lines in spectra of thermal atoms are fit of the lineshape of (5.21) to the data. The solid line in the BEC data is a fit of (8.18) to the spectrum. (Top): Only the ULE drift of the excitation laser was compensated. (Bottom): All frequency shifts (see Table 8.2) except for the mean field shift in a BEC spectrum are compensated. Here one can clearly see the mean field shift of a BEC.

Table 8.2: Experimental parameters for data in Fig. 8.4. T: atomic temperature, $\bar{\omega}$: the geometrical average of the trap frequency, n: number density, $\Delta\nu_{\rm col}$: collision shift, $\Delta\nu_{\rm LD}$: light shift, and $\Delta\nu_{\rm gr}$: frequency shift by the gravity.

$T(\mu\mathrm{K})$	N	$\bar{\omega}/2\pi$ (Hz)	$n(\mathrm{cm}^{-3})$	$\Delta\nu_{\rm col}$ (kHz)	$\Delta\nu_{\rm LS}$ (kHz)	$\Delta\nu_{\rm gr}$ (kHz)
1.2	1.2×10^5	610	5.6×10^{13}	-3.1	-5.9	0.0
0.5	5.9×10^4	420	4.4×10^{13}	-2.5	-2.9	0.1
0.3	4.1×10^4	370	6.8×10^{13}	-3.8	-2.0	0.1
BEC	2.9×10^4	140	4.8×10^{14}	-12.8	-1.4	0.2

8.3 BEC in 1D optical lattice potential

Using optical lattice potentials, we can tightly confine atoms in a small region within the length scale of the optical wavelength. When such atoms are excited by the laser along the confinement axis, the laser field felt by atoms is phase modulated by the oscillation frequency. As a result, sidebands appear in the excitation spectrum. This kind of tight confinement is known as the Lamb-Dicke confinement which is characterized by the Lamb-Dicke parameter [97]

$$\delta = k_{507}\sqrt{\frac{\hbar}{2m\Omega_{\rm g}}} = \sqrt{\frac{E_{\rm R}^{507}}{\hbar\Omega_{\rm g}}}, \tag{8.20}$$

where k_{507} and $E_{\rm R}^{507}(= 0.21\mu\mathrm{K}$ for 507 nm) are the wavenumber and the recoil energy of the excitation laser. $\Omega_{\rm g}$ denotes the trap frequency of the ground state. Thus, the smaller δ means the tighter confinement.

A significant feature of the Lamb-Dicke confinement is that the carrier component doesn't suffer from the Doppler effect, which enables the Doppler free spectroscopy. Thus spectroscopy of thermal atoms and a BEC in optical lattice potentials enables us to precisely measure the mean field shift and broadening of the spectrum without suffering from the Doppler broadening. In addition, since the tight confinement of lattice potentials increase the number density at each site, the effect of the mean field energy become larger than that in usual harmonic traps.

In Fig. 8.5, the time sequence of the experiment and configurations of lasers and the magnetic field are schematically shown. After evaporative cooling to make a BEC, 1D optical lattice potential was ramped up to $9.6E_{\rm R}$ for 100 ms. Since we observed the interference pattern between BEC arrays, we regard that a BEC was adiabatically loaded into optical lattice potentials. Then the excitation laser was irradiated for 50 ms along with the optical lattice laser. By turning off all lasers and letting atoms freely expand in the TOF time t, we took absorption images.

The observed spectrum is shown in Fig. 8.7. First, we can clearly identify two peaks. These peaks correspond to the $|^1S_0, 0\rangle \rightarrow |^3P_2, 0\rangle$ and $|^1S_0, 0\rangle \rightarrow |^3P_2, 1\rangle$ transitions, where $|a, n\rangle$ denotes the state of atoms in the electric state a and the nth vibrational levels of the trap. In this measurement, the Lamb-Dicke parameter is ($\delta =$) 0.4. Assuming that

the trap depth of the ${}^1S_0$ state is same as that of the ${}^3P_2$ state, the ratio of the transition strength between the $|{}^1S_0, 0\rangle \to |{}^3P_2, 0\rangle$ and $|{}^1S_0, 0\rangle \to |{}^3P_2, 1\rangle$ transitions is given by [97]

$$P_{00} : P_{01} = 1 : \delta^2 = 1 : 0.16, \tag{8.21}$$

which is consistent with the observed signal strengths.

To analyze the width of the observed spectrum, we need to know the density distribution of condensates in each site. To this end, based on the discussions in [98], we assume that the wave function of a BEC in 1D optical lattice potentials is given by

$$\Phi_0(\mathbf{r}) = \sum_{k=0,\pm1,\cdots,k_{\rm M}} f_k(y)\Phi_k(\mathbf{r}_\perp), \tag{8.22}$$

where k labels each site and $2k_{\rm M}+1$ is the number of lattice sites. $f_k(y)$ and $\Phi(\mathbf{r}_\perp)$ are the wave function along the axial (confinement, y-axis) direction and the radial direction (xz-plane), respectively. Here we assume the Gaussian function $f_k(y) = e^{-(y-kd)^2/2\sigma^2}$ where d is the lattice interval and σ characterizes the width of the condensates along the confinement direction in each well. σ is given by $\sigma = d/(\pi s^{1/4})$ with $s = ((\hbar\omega_y)/(2E_{\rm R}^{532}))^2$, ω_y the trap frequency along the confinement direction and $E_{\rm R}^{532}$ the recoil energy of the FORT laser ($E_{\rm R}^{532} = 0.194$ μK for 532 nm). We assume that the confinement along the axial direction is so strong that σ is not affected by interaction energies in each site.

On the other hand, the radial direction should be treated by the Thomas-Fermi approximation. Hence the wave function of the kth site in the radial direction is give by

$$|\Phi_k(x,z)|^2 = \frac{m}{2\sqrt{2}\pi\hbar^2 a}\mu_k\left(1 - \frac{r_\perp^2}{(R_\perp)_k^2}\right), \tag{8.23}$$

where μ_k and $(R_\perp)_k = \sqrt{2\mu_k/m\omega_{(\perp)}^2}$ are the chemical potential and the Thomas-Fermi radius of the kth condensate, respectively. Here, m is the atomic mass, a is the s-wave scattering length, $r_\perp = \sqrt{x^2+z^2}$ and $\omega_{(\perp)}$ is the radial trap frequency of the envelope harmonic potential. μ_k satisfies

$$\mu_k = \frac{1}{2}m\omega_{(y)}^2 d^2(k_{\rm M}^2 - k^2), \tag{8.24}$$

where $\omega_{(y)}$ denotes the axial trap frequency of the harmonic potential (not the lattice trap frequency). From the normalization condition $N = \sum N_k$, the $k_{\rm M}$ is give by

$$k_{\rm M} = \sqrt{\frac{2\hbar\bar{\omega}}{m\omega_{(y)}^2 d^2}}\left(\frac{15}{8\sqrt{\pi}}N\frac{a}{a_{\rm ho}}\frac{d}{\sigma}\right)^{1/5}. \tag{8.25}$$

Here, $\bar{\omega} = (\omega_{(y)}\omega_{(\perp)}^2)^{1/3}$ is the geometrical average of the trap frequency of the harmonic trap, $a_{\rm ho} = \sqrt{\hbar/m\bar{\omega}}$ is the oscillator length. The number of atoms in each site is give by

$$N_k = \frac{15}{16}\frac{N}{k_{\rm M}}\left(1 - \frac{k^2}{k_{\rm M}^2}\right)^2. \tag{8.26}$$

In this work, the parameters are the followings: $\omega_{(y)} = 2\pi \times 140$ Hz, $\omega_{(\perp)} = 2\pi \times 99$ Hz, $d = 266$ nm, $N = 5{\times}10^4$, $a = 5.53$ nm [30], $a/a_{\rm ho} = 7.3{\times}10^{-3}$, $s = 9.6$ and $\sigma/d = 0.18$. As a result, $k_{\rm M} = 13$ and the chemical potential μ_k in each site is shown in Fig. 8.6(Top). In this figure, we compare the chemical potential at each site with $\hbar\omega_\perp$ and $\hbar\omega_{(y)}$. In Fig. 8.6(Top-Left), $\hbar\omega_{(y)} \gg \mu_k$ for every site. Thus we can justify the approximation that we can determine the Gaussian width by neglecting the two-body interaction at each site. Similarly, $\hbar\omega_\perp < \mu_k$ for all k justifies the application of the Thomas-Fermi approximation.

Using the Eq. (8.23), the atomic peak density ($\mathbf{r} = 0$) at each site could be determined as shown in Fig. 8.6(Bottom). Now we can calculate the spectral shape considering that the observed spectrum is summation of lineshapes Eq. (8.18) in each lattice site whose atomic density is given by Fig. 8.6(Bottom). Since we determined the a_{12} from the BEC spectroscopy in the previous section, there are no free parameters. The result of this calculation is shown in Fig. 8.7 as a solid line which well agrees with the observed spectrum.

As a result, we can conclude that we have succeeded in spectroscopically observing the on-site interaction at each site of the 1D optical lattice potentials by using an ultranarrow ${}^1S_0 \leftrightarrow {}^3P_2$ transition in Yb. Since in the experiments using the optical lattice potentials, the hopping energy and the on-site interaction energy are the important parameters. The technique developed in this work enables us to precisely measure the on-site interaction energies in such experiments. Also, the density distribution of mixtures of condensates in optical lattice potentials can be precisely observed. Moreover, by additionally using the MRI technique, we can observe the density distribution of any lattice site you want to see.

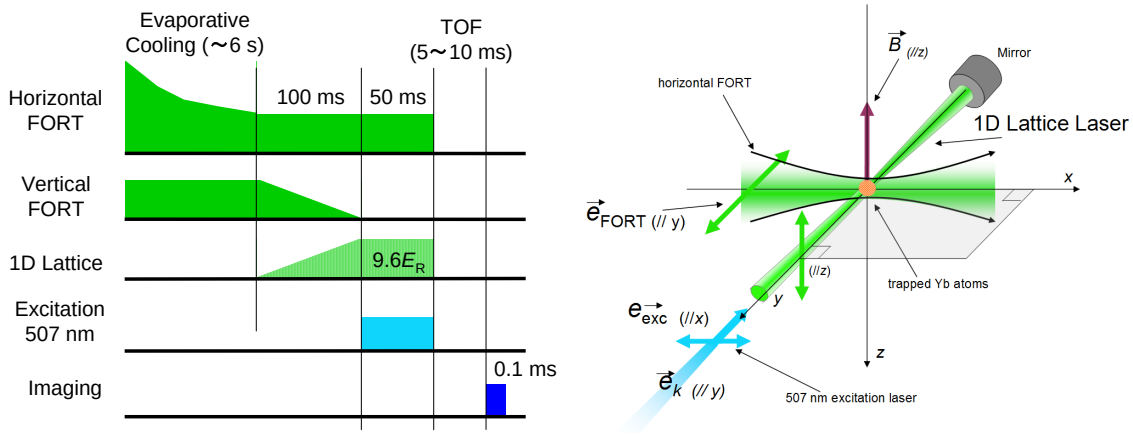

Figure 8.5: (Left) Time sequence and (Right) configurations of lasers and the magnetic field for 1D optical lattice experiment are shown.

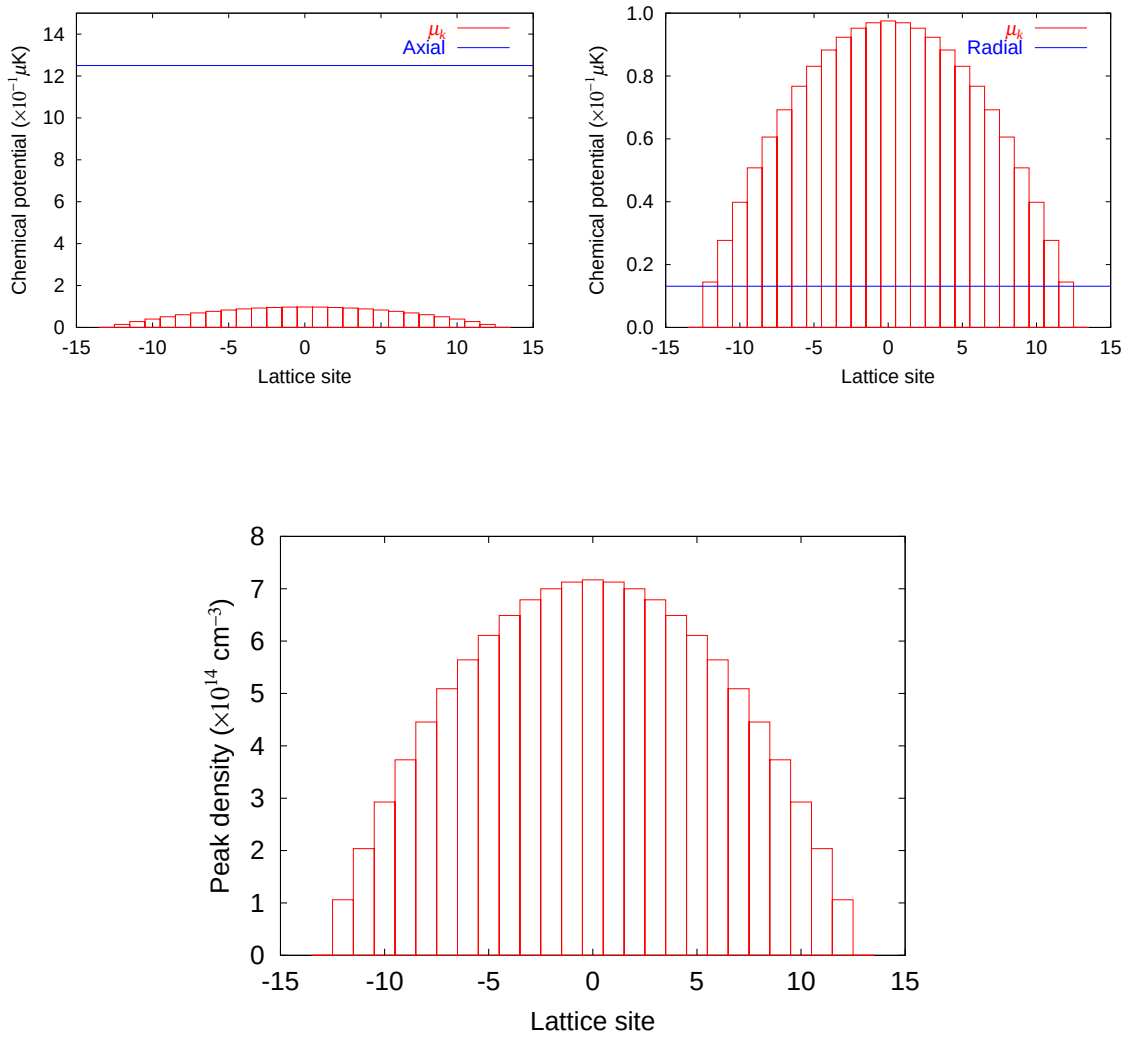

Figure 8.6: (Top): Chemical potentials of condensates in each site are compared to the energy of motion along the axial axis (Left) and the radial axis (Right). (Bottom): Calculated atomic density at each site are shown.

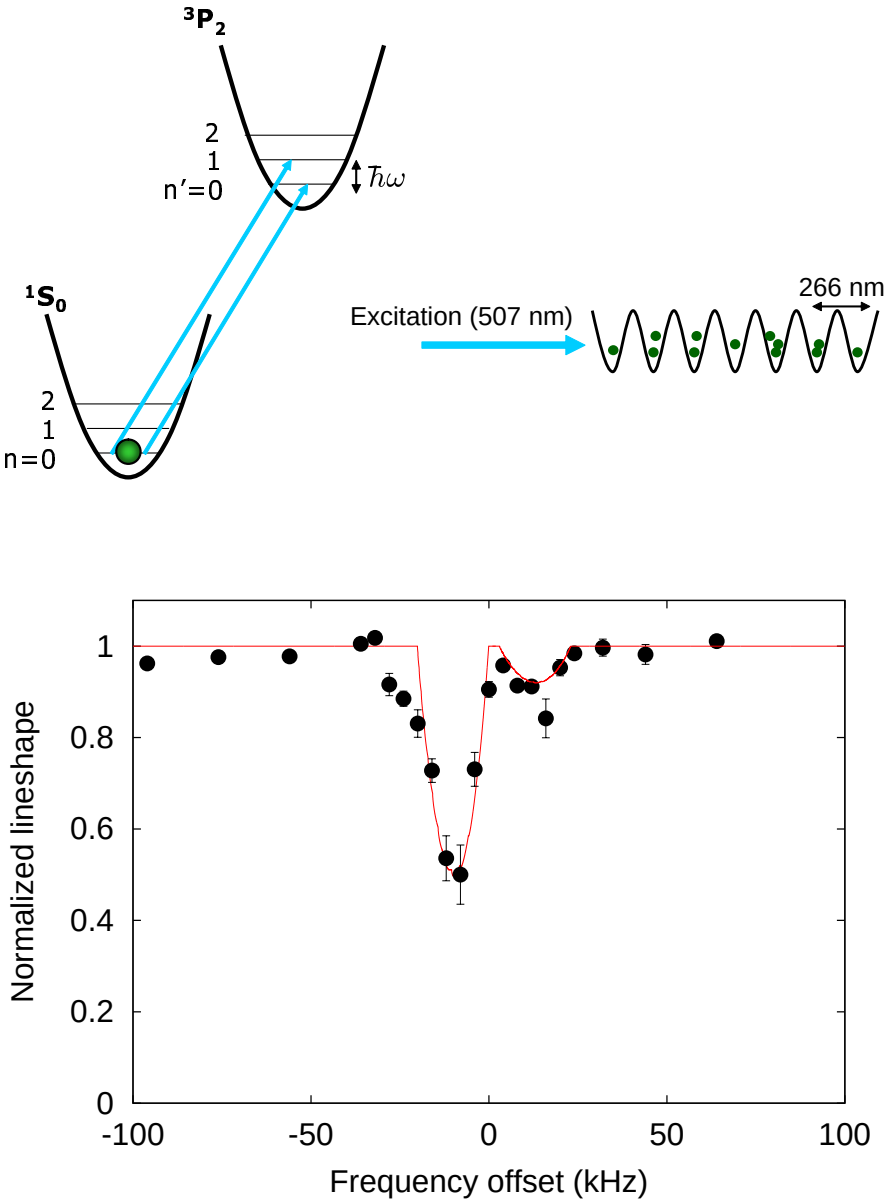

Figure 8.7: (Top): Experimental situation in spectroscopy of a BEC in 1D optical lattice potentials is schematically shown. The tight confinement of lattice potentials leads to the increase of the separation between vibrational levels of a trap. (Bottom): Observed spectrum. In addition to the carrier spectrum corresponding to the $|^1S_0, 0\rangle \rightarrow |^3P_2, 0\rangle$ transition, the heating sideband $|^1S_0, 0\rangle \rightarrow |^3P_2, 1\rangle$ was also successfully observed. The solid line is the calculated spectrum assuming the mean field broadening by "mini" BECs in each lattice site.

Chapter 9

Frequency measurement of the clock transition in ^{174}Yb

The $^1S_0 \leftrightarrow {}^3P_2(m=0)$ transition is ultranarrow and insensitive to a magnetic field. It have been one of the candidates of the frequency standards using the optical transition [3]. We measured the frequency of the clock transition by using an optical frequency comb. In this chapter, we first introduce some basics of a frequency comb. Then the frequency measurement of the clock transition will be presented.

Frequency is one of the most accurately measured physical quantities [99]. Since the optical frequency $f \sim 10^6$ GHz is much larger than the present electronic frequency counters, it is impossible to directly measure the optical frequency. Hence, techniques to convert an optical frequency to the radio frequency where we can use accurate frequency counters have been developed for a long time such as harmonic frequency chains [100], interval bisection [101] techniques and so on. However, the breakthrough is a frequency comb technique invented by Udem *et al.* in 1999 [102].

Frequency comb is based on the mode locked femtosecond laser pulses. In the femtosecond laser cavity with cavity length L, a pulse is circulating with the round trip time $T = v_\mathrm{g}/L$ (for the bow-tie cavity) where v_g is the group velocity of pulses. As a result, the output pulses are generated with the repetition rate $f_\mathrm{rep} = 1/(2\pi T)$ (~ 1 GHz). The group velocity v_g which is the velocity of the pulse envelope is, in general, different from the phase velocity v_p which is the velocity of the carrier wave. The phase of a carrier wave in each pulse, then, shifts by $\Delta\phi$ from neighbor pulses.

In a frequency domain, femtosecond pulse trains are equally spaced frequency combs. The interval between each comb is given by f_rep. The phase shift $\Delta\phi$ appears as so called carrier envelope frequency offset f_CEO ($< f_\mathrm{rep}$). Thus the frequency of the nth comb f is given by

$$f = nf_\mathrm{rep} + f_\mathrm{CEO}. \tag{9.1}$$

Let us consider the beat signal (f_beat) between the frequency comb and an external laser f_laser. Considering a beat signal from the nearest n_0th comb, the frequency of the external laser can be written as

$$f = f_\mathrm{CEO} + n_0 f_\mathrm{rep} + f_\mathrm{beat}. \tag{9.2}$$

Since f locates somewhere between two frequency combs, f_{beat} is always smaller than f_{rep}. Thus, all frequencies f_{CEO}, f_{rep} and f_{beat} are in a radio frequency region and can be accurately measured by frequency counters. Also, it is possible to determine the integer n_0 ($\sim 10^6$) by using a common wavemeter. As a result, the absolute frequency f of the external laser can be accurately measured by (9.2).

When we use the frequency comb, we first have to stabilize (determine) f_{rep} and f_{CEO} in (9.2). To this end, using the 10 MHz frequency standard based on a Coordinated Universal Time (UTC) is desirable.

9.1 FC 8003 – Menlo Systems GmbH

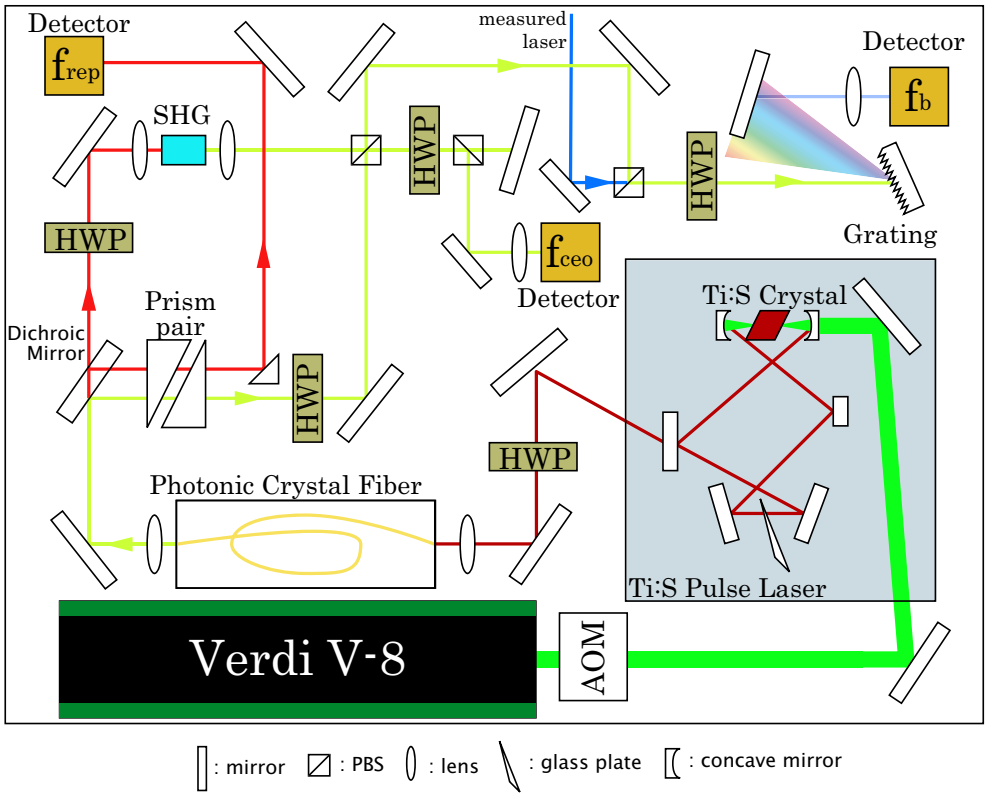

Figure 9.1: Schematics of the frequency comb system (FC 8003, Menlo Systems GmbH) used in this study.

Figure 9.1 shows the optical frequency comb system[1] used in this work (FC 8003, Menlo Systems (GmbH)). A femtosecond cavity is designed to make f_{rep} lie around 825 MHz. A photonic crystal fiber [103, 104] enables the octave spanning of the comb region which is necessary to detect the f_{CEO}. The following optics are designed to detect and stabilize the f_{rep} and f_{CEO} which is explained below.

We note that in stead of the frequency standard based on a UTC which is required to stabilize f_{rep} and f_{CEO}, we used the Rb frequency standard (PRS10, Stanford Research Systems) which will be referred as "Rb clock" in this thesis. To estimate the accuracy of the Rb clock, we compared the Rb clock signal with the UTC(NICT) after the measurement.

9.1.1 f_{rep}

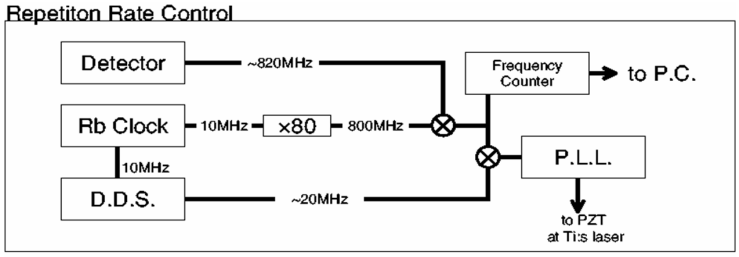

Figure 9.2: Block diagram of the RF system to stabilize f_{rep} to the Rb clock.

Detection

f_{rep} usually lies between a few 10 MHz and a few GHz. Thus it can be determined by directly measuring the pulse interval with a fast photodiode.

Stabilization

To stabilized the f_{rep} to the Rb clock, the RF system described in Fig. 9.2 is used. A double-balanced mixer mixes the f_{rep} and Rb clock signal and converts the f_{rep} ($\sim$ 820 MHz) down to $\sim$ 20 MHz. Next, it is additionally mixed with the DDS (Direct Digital Synthesizer) signal. By using a PLL (Phase-Locked Loop), the error signal can be obtained to lock the downconverted signal to the DDS signal. Since $f_{\mathrm{rep}} = L/(2\pi v_g)$, the feedback signal is applied to the PZT attached to one of mirrors in a femtosecond laser cavity[2].

[1] This frequency comb belongs to NICT, Tokyo. We moved the system from Tokyo to Kyoto before the measurement.

[2] The original PZT driver installed in FC 8003 was very noisy. We replaced it by the PTZ driver M-2647 (MESS-TEK, Japan).

In the frequency measurement, f_{rep} was adjusted by the DDS frequency by several Hz in order to place the beat frequency between the comb and the measured laser at the appropriate RF frequency for the frequency counter (20 $\sim$ 30 MHz in this system).

9.1.2 f_{CEO}

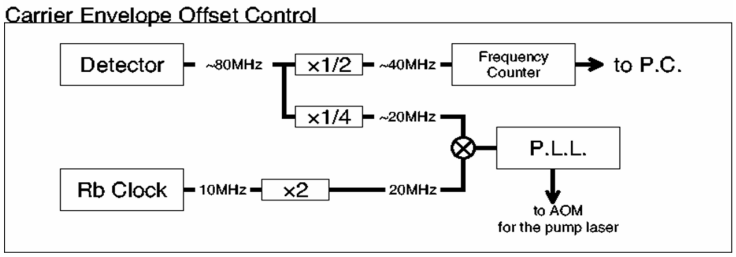

Figure 9.3: Block diagram of the RF system to stabilize f_{CEO} to the Rb clock.

Detection

Since f_{CEO} is caused by the phase difference in each pulse, we require the interferometer. Thanks to the photonic crystal fiber, the comb contains an optical octave. Let us consider the beat signal between the second harmonics of the nth comb f_{n} and the $2n$th comb $f_{2\mathrm{n}}$ which can be written as

$$\begin{aligned} 2 \times f_{\mathrm{n}} &= 2nf_{\mathrm{rep}} + 2f_{\mathrm{CEO}} \\ f_{2\mathrm{n}} &= 2nf_{\mathrm{rep}} + f_{\mathrm{CEO}}. \end{aligned} \tag{9.3}$$

Thus $2 \times f_{\mathrm{n}} - f_{2\mathrm{n}} = f_{\mathrm{CEO}}$. The second harmonic of a comb is obtained by a BBO crystal and interfered with the original comb laser. A beat signal is detected by a fast photodiode. The prism pair in Fig. 9.1 is used to adjust the time delay of one arm of the interferometer.

Stabilization

Figure 9.3 shows the RF system to lock the f_{CEO} to the Rb clock. f_{CEO} is always stabilized at 80 MHz by locking it to Rb clock signal (10 MHz $\times$ 8). An error signal obtained by a PLL is feedbacked to the RF power used to adjust the pump power of the femtosecond laser [105].

9.1.3 Position of f_{rep} and f_{CEO}

When we use a frequency comb, four kinds of positions of each frequency are possible as shown in Fig. 9.4. To determine whether the measured frequency f is upper side

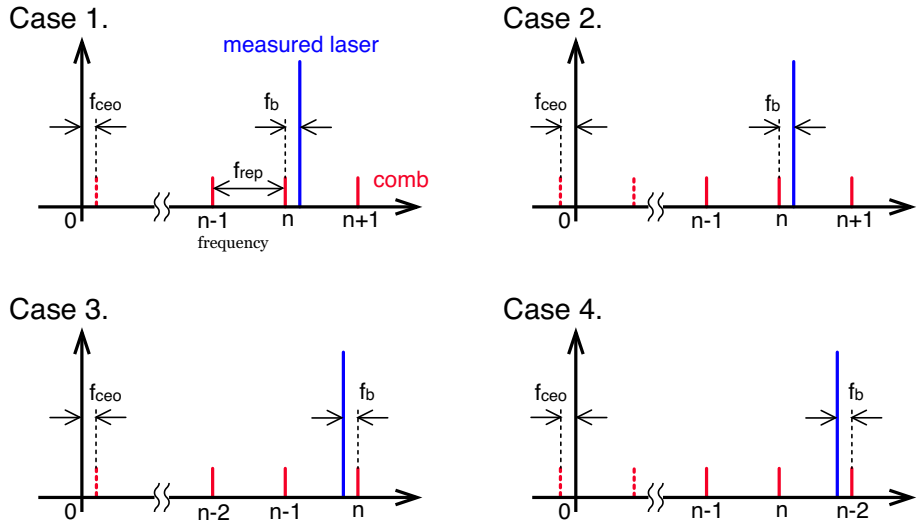

Figure 9.4: Four kinds of positional relationship of f, f_{rep}, and f_{CEO} are possible.

or lower side of the comb, we change the DDS frequency by a few Hz. If f is upper side of the comb (Case 1 and 2 in Fig. 9.4), the beat frequency f_{beat} becomes small by increasing the f_{rep} and vise versa. Similarly, as for the f_{CEO}, if it is +80 MHz (Case 3 and 4 in Fig. 9.4), the beat frequency f_{beat} becomes small as f_{CEO} increases by changing the RF power applied to the AOM. In order to determine the number of comb n in (9.2), we use the wavemeter WA-1500 (Burleigh/EXFO). Further information about the comb measurement is described in [106].

9.2 Experiment and analysis

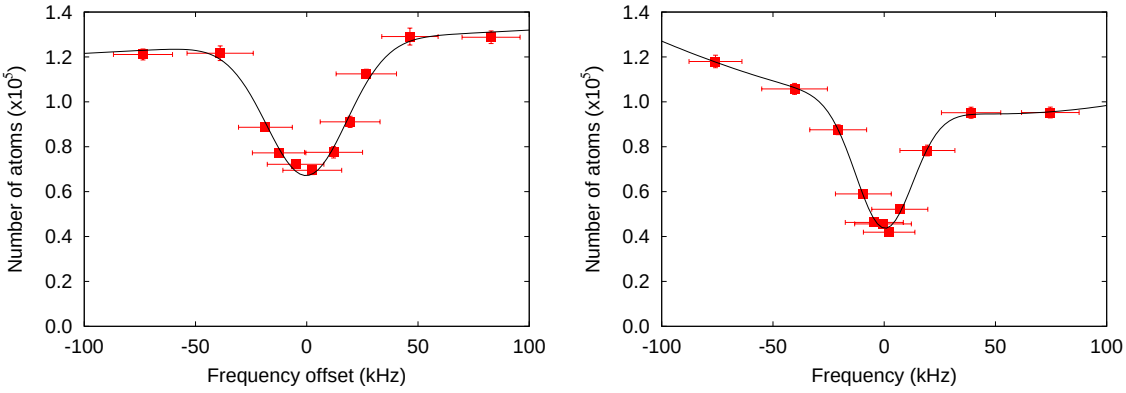

Figure 9.5: Typical spectra of the ${}^1S_0 \leftrightarrow {}^3P_2(m{=}0)$ transition.

We excite atoms in a FORT whose wavelength is not a magic wavelength. Thus, the

transition frequency suffers from the light shift depending on a FORT power. To remove such effects, we measured the transition frequency at three different FORT powers and extrapolated the unperturbed resonance frequency at zero FORT power. Note that the weak magnetic field was applied to separate the clock transition from other magnetic sensitive transitions. Also, one of the FORT lasers of the crossed FORT configuration was turned off just before the excitation to eliminate the additional light shift.

Figure 9.5 shows typical spectra of the clock transition. The number of atoms in the ground state is plotted as a function of the frequency offset of the excitation laser (507 nm). The spectral width is determined almost by the Doppler width. The atomic temperature is about 1 μK in this measurement. We chose 11 frequencies around the resonance and measured the laser frequency by a comb for 100 s at each frequency. Since our typical experimental procedure (loading, cooling and excitation of atoms) takes 10 s, more than 10 CCD images were taken in order to measure the number of atoms.

The center frequency is determined as follows. We first fit the summation of the sine function and the Gaussian function to the data. In some data, we found the slight shift of the background level due to the instability of the initial number of trapped atoms. As shown in Fig. 9.5, such a shift can be well described by the sine function. This may be caused by the sine-shape frequency shift of the MOT laser for a long term which is stabilized to the ULE cavity.

In order to carry out the weighted fitting of data, we convert the error in the x axis σ_x (frequency) to that in y axis σ_y by taking [107]

$$\sigma_y(\text{equiv}) = \sqrt{\sigma_y^2 + \left(\frac{\mathrm{d}f(x)}{\mathrm{d}x}\sigma_x\right)^2}, \tag{9.4}$$

where $f(x)$ is a fitting function. Then, we used the weighted least-square fit. Here, note that we have to consider the temperature shift, that is to say, we use not the Gaussian function but the (5.21). However, the ratio of the trap depth of the ground state to that of the excited state in m_{ex} is required which is not known before the fitting. Then we regards m_{ex} as one of the fitting parameters. Since we could separately estimate the m_{ex} from the fitting results, we evaluated the consistency between these two values and estimated m_{ex}.

We also compensated the collision shift by (5.26) and the recoil shift by (5.11). Using the scattering length between atoms in the ground state and the $^3P_2$ state a_{12} obtained by the BEC spectroscopy (see section 8.2), the collision shift is estimated to be 2$\sim$3 kHz in the present case. In addition, when the trap depth is shallow, we have to consider the effects of the gravity (= 0.2 μK/μm) while it was relatively small (about 1 kHz) in this measurement.

Finally, considering all of these frequency shifts, the unperturbed frequency is determined by the linear weighted least-square fit as shown in Fig. 9.6. The transition frequency is determined to be

$$590\ 902\ 342\ 562 \pm 3 \pm 60\ \text{kHz}. \tag{9.5}$$

Here The first error results from the statistical uncertainties originating from fitting of the data to find a resonance frequency, linear fitting of the observed resonance frequencies,

and the frequency counting. The second error is associated with uncertainties of the Rb frequency standard (10 MHz) used for the optical frequency comb which is estimated below.

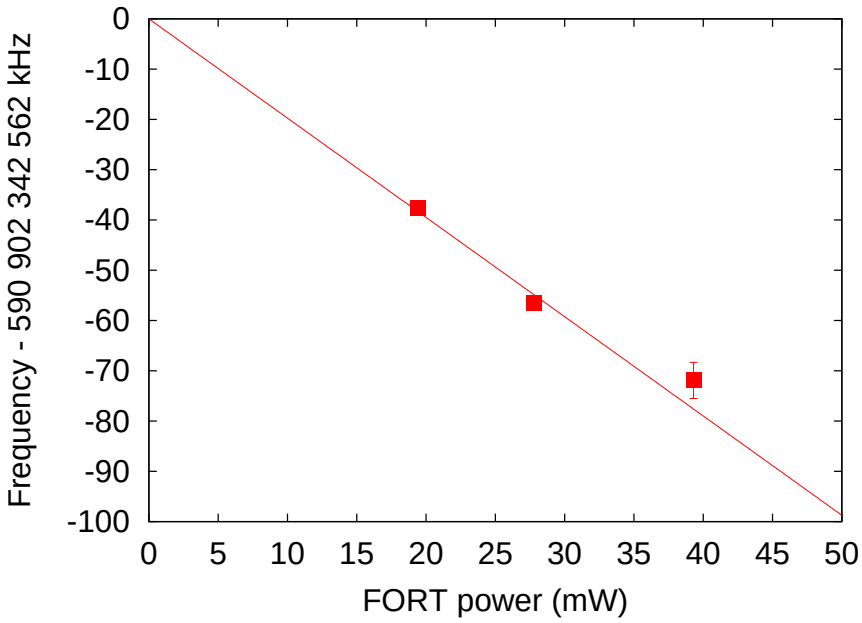

Figure 9.6: Resonance frequencies are shown as a function of the FORT power. Each resonance frequency was measured by an optical frequency comb.

9.2.1 Rb clock

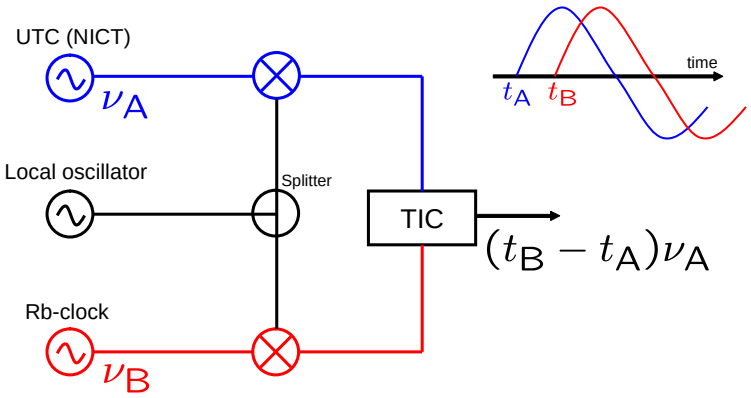

Figure 9.7: Block diagram of the DMTD system.

In order to evaluate the measured frequency, we estimated the accuracy of the Rb clock (PRS10, Stanford Research Systems). To this end, we compared the Rb clock with the

UTC(NICT) by a DMTD (Dual Mixer Time Difference) system. The mechanism of the DMTD system is schematically shown in Fig. 9.7. It has two inputs and one output. The reference signal, UTC(NICT)-10 MHz, is put into the input A. The measured signal, the Rb-clock, is put into the input B. Then, the DMTD system outputs the phase difference $\Delta\phi = (t_{\rm B} - t_{\rm A})\nu_{\rm A}$ where $t_{\rm B} - t_{\rm A}$ is the time interval between the input A and B. By observing $\Delta\phi$ for a long time and if $\Delta\phi$ is

1. constant, $\nu_{\rm A} = \nu_{\rm B}$
2. decreasing, $\nu_{\rm A} < \nu_{\rm B}$
3. increasing, $\nu_{\rm A} > \nu_{\rm B}$.

Thus, we can determine whether the Rb clock frequency is larger or smaller than the UTC(NICT). Qualitatively, the difference can be described by

$$\Delta t = \left(\frac{1}{\nu_{\rm A}} - \frac{1}{\nu_{\rm B}}\right) \times \nu_0 \times T, \tag{9.6}$$

where $\nu_0 = 10$ MHz, T is the total measurement time and Δt is the change of $(t_{\rm A} - t_{\rm B})$ during T. Since $\nu_{\rm A} \sim \nu_{\rm B} \sim \nu_0$, this equation can be written as

$$\Delta\nu = \left(\frac{\Delta t}{T}\right) \nu_0, \tag{9.7}$$

where $\Delta\nu = \nu_{\rm A} - \nu_{\rm B}$. For example, let us consider the case where the $\Delta\phi$ decreases from 0.7 to 0.4 during the measurement time $T = 8{\times}10^4$ s (about one day). Then, since $\Delta t = (0.7 - 0.4) \times 10^{-7} = 3 \times 10^{-8}$ s, we can state that the measured frequency is larger than the UTC(NICT) by 4 μHz. In general, the result is described by $\Delta\nu/\nu_0$ as a function of measurement time.

Figure 9.8 shows the stability of Rb clock when we change the magnetic field and temperature around it. Based on this measurement, we evaluate all possible environmental errors (temperature, magnetic field) and estimated the error of 60 kHz.

Finally, in Fig. 9.9, we show the Allan deviation between Rb clock and UTC(NICT) signal. The stability is limited by the stability of Rb clock ($\sim 10^{-12}$ at 100 s). In order to improve the accuracy of the frequency measurement, we should link the Rb clock to the GPS signal for a long term frequency stability and may use the hydrogen maser for the short term frequency stability.

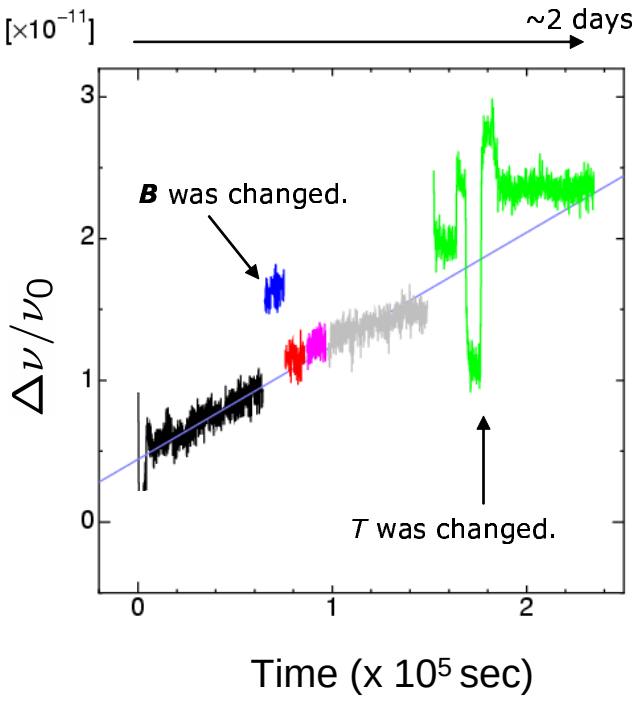

Figure 9.8: Frequency instability of Rb clock against the change of the external magnetic field and temperature. Rb clock was compared to the UTC(NICT) signal by the DMTD system. Magnetic field up to 1 G was applied and the temperature was changed from 15 to 35 °C.

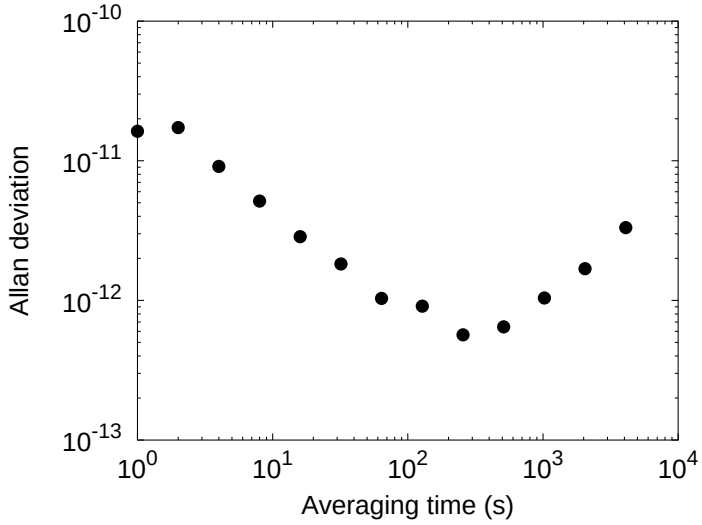

Figure 9.9: Allan deviation between Rb clock and UTC(NICT). The stability is limited by the stability of Rb clock ($\sim 10^{12}$ at 100 s).

Chapter 10

Summary and outlook

10.1 Summary

Optical trapping of $^3P_2$ atoms and their unique collisional properties

We investigated the unique collisional properties of $^3P_2$ atoms. In previous studies, evaporative cooling of $^3P_2$ atoms in a magnetic trap was unsuccessful due to the large trap loss caused by multichannel collisions in a magnetic trap. Therefore, we decided to trap $^3P_2$ atoms in an optical trap (FORT), which can trap $^3P_2$ atoms in every magnetic sublevel with the same strength. We can expect that, although multichannel collisions can still occur, they will not lead to the trap loss.

To this end, a new technique to prepare ultracold and dense $^3P_2$ atoms in a FORT was developed in this study. We first prepared pre-cooled $^1S_0$ atoms in a FORT and then optically excited such atoms to the $^3P_2$ state. By this new method, we achieved a number density of 2×10^{13} cm^{-3} at a temperature of 2 μK with a phase space density (PSD) of 0.01. Our newly achieved number density is larger than that in a previous study by an order of three [1].

While a trap loss due to the multichannel collisions must be suppressed in our FORT, we still observed large trap loss due to two-body inelastic collisions. Thus, we deduce the existence of a different inelastic collisional process, which we interpret as fine-structure changing collisions in this ultracold temperature regime. The previous theoretical studies revealed details of fine-structure changing transitions in collisions of Mg[^3P_j], O[^3P_j], Sc[^2D_j], and Ti[^3F_j] atoms with closed-shell atoms at a high temperature. However, there has not been any theoretical study on the fine-structure changing collisions between atoms in the $^3P_2$ state at ultralow temperatures achieved in the present study. While a recent experiment on magnetically trapped Ca atoms studied multichannel collisions between $^3P_2$ atoms and discussed the possibility of the fine-structure changing process [2], we believe that our study is the first definite experimental measurement of this process between $^3P_2$ atoms. For further understanding of the observed large inelastic collision rate and possibilities of the fine structure changing collisions, a quantitative theory on the collisional properties of $^3P_2$ atoms is highly desirable.

High-resolution spectroscopy of ultracold atoms and BECs using the ultranarrow $^1S_0 \leftrightarrow {}^3P_2$ transition

The other important achievement in this study is the successful observation of the ultranarrow magnetic quadrupole $^1S_0 \leftrightarrow {}^3P_2$ transition (507 nm) in Yb bosonic (^{174}Yb) and fermionic (^{171}Yb, ^{173}Yb) isotopes.

Previously, studies on ultranarrow transitions in two-electron atoms have aimed entirely at ultraprecise frequency standards. In contrast, this study showed how powerful the ultranarrow transition is as a tool for the spectroscopy of ultracold atoms and BECs.

We first developed a 507-nm ultranarrow-linewidth laser system. In order to observe the ultranarrow transition, the laser linewidth was reduced to less than 1 kHz by tightly locking it to a high-finesse optical cavity. This transition had never been observed prior to this study. Hence, we estimated the transition frequency using an optical frequency comb. The developed laser system and the estimated transition frequency enabled us to observe the $^1S_0 \leftrightarrow {}^3P_2$ transition for the first time.

High-resolution spectroscopy of a BEC was thus demonstrated. We successfully detected the mean field shift of a BEC using this ultranarrow optical transition. We observed not only the large mean field shift in a BEC, but also the change in the lineshape, which reflects the density distribution of a BEC in a trap. As a result, a_{12} (the scattering length between atoms in the $^1S_0$ state and the $^3P_2$ state) was successfully determined from the observed spectrum. Furthermore, we performed spectroscopy of condensates in 1D optical lattice potentials and observed the mean field shift due to the on-site interaction at each site. Since, in the experiments using optical lattice potentials, the hopping energy and the on-site interaction energy are important parameters, the technique developed in this study enabled us to measure the on-site interaction energies with high precision in such experiments.

Furthermore, the polarizabilities of all the magnetic sublevels of the $^3P_2$ state were determined with high precision. Using an optical frequency comb, we also measured the frequency of the magnetic-field-insensitive $^1S_0 \leftrightarrow {}^3P_2$ ($m = 0$) transition in ^{174}Yb, which is one of the candidates for next-generation atomic frequency standards [3].

10.2 Outlook

The $^3P_2$ state and the ultranarrow transition between the $^1S_0$ and the $^3P_2$ states have great potential for future studies in atomic physics.

As observed in this study, it is true that a large inelastic collision rate leads to a short trap lifetime of $^3P_2$ atoms even in a FORT. However, to overcome the trap loss due to inelastic collisions, we can use 3D optical lattice potentials or ultracold fermions, which do not collide with each other at ultracold temperatures. In particular, as for metastable $^3P_2$ bosons in 3D optical lattice potentials, the number of atoms finally becomes 1 or 0 per site due to strong two-body inelastic collisions. In such a situation, since no collision shift occurs, it is an ideal system for an atomic clock or for precise measurement.

Using the magnetically sensitive $^1S_0 \leftrightarrow {}^3P_2 (m = \pm 1, \pm 2)$ transitions in a magnetic field gradient, we can address atoms with ultrahigh spatial resolutions. In addition, considering

the large scattering length a_{12} of Yb, we can probe the density distribution of atoms at any point in a trap with higher precision, compared to experiments using alkaline metal atoms. Thus, for example, we may be able to probe the density distribution of a phase-separated mixture of different kinds of condensates. It will also be possible to measure the on-site interaction energy at any site of optical lattice potentials. Since, in experiments using optical lattice potentials, the hopping energy and the on-site interaction energy are important parameters, such a technique must therefore be a powerful tool in experimental studies of Bose-Hubbard models using optical lattice potentials.

Quantum computing using the dipole-dipole interaction of $^3P_2$ atoms between neighboring sites in optical lattice potentials has been proposed [82, 13]. Now, this is experimentally well within our capability [106]. Using the $^1S_0 \leftrightarrow {}^3P_2$ transition, we can initialize, manipulate, and read any qubit (atom) in optical lattice potentials.

The technique of controlling the polarizability of the $^3P_2$ state by an external magnetic field, as demonstrated in section 7.4.1, also has great potential. We may be able to realize Stark shift cancellation by only rotating the magnetic field. It may also be possible to realize a situation where Stark shift cancellation is satisfied both for the $^3P_0$ state and the $^3P_2$ state simultaneously. This could be done by adjusting the external magnetic field at the magic wavelength of the $^3P_0$ state. Such a situation must be an ideal system to compare two atomic clocks under the same circumstances or to test the time-varying fine structure constant α, [108] because no systematic errors exist in such a system.

In ion trap experiments, cooling of an ion by using an ultranarrow transition with a combination of quenching processes is a key technique [14]. In the case of neutral atoms, sideband cooling using the ultranarrow $^1S_0 \leftrightarrow {}^3P_2$ transition seems to be impossible due to the different trap shape between the states used for cooling and quenching. However, we may be able to use a repumping laser, which can immediately quench the $^3P_2$ atoms to the ground state (see Chapter 6). If the repumping time is considerably shorter than the trap frequency, it may be possible to make the heating effect negligibly small, thus allowing the sideband cooling mechanism to work. In addition, Reichenbach and Deutsch have recently proposed a novel sideband cooling technique using the $^1S_0 \leftrightarrow {}^3P_0$ clock transition and hyperfine states in a ^{171}Yb fermionic isotope [15]. Such a technique may be applied to the $^1S_0 \leftrightarrow {}^3P_2$ transition.

As for the frequency measurement demonstrated in Chapter 9, we need to further improve the accuracy. First, the Rb clock should be linked to a GPS signal for a long-term stability. To improve the short-term stability, the Rb clock may be replaced by, for example, a hydrogen maser system. Precise measurement of the absolute transition frequencies of hyperfine states of the $^3P_2$ state in fermionic isotopes in the kilohertz range will enable us to probe the nuclear magnetic octupole moments [109].

Furthermore, according to [115], the spectral width of I_2 molecules becomes narrowest around 507 nm ($\sim$ 40 kHz [HWHM]). Thus, the 507-nm laser source developed in this study has great potential as a new portable frequency standard using the narrow iodine spectra around 507 nm. We demonstrated the spectroscopy of I_2 molecules (Appendix C).

Appendix A

Calculation of the magic wavelength of the $^3P_2$ state

For future experiment, we estimated the magic wavelength of the $^3P_2$ state. The calculation seems not to be reliable in the visible region because we have to include effects of a lot of upper states. Here, we show the result above 900 nm where such effects may be small. The calculation was completely same as that in section 4.3. The matrix elements between the $(6s6p)^3P_2$ state and the following states are considered [60]: $(5d6s)^3D_1, (5d6s)^3D_2, (5d6s)^3D_3, (5d6s)^1D_2, (6s7s)^3S_1$. The linearly polarized FORT and zero magnetic field are assumed. In Fig. A.1, the calculation results are shown. The magic wavelength is estimated to be 965 nm for the $^3P_2(|m| = 1)$ state and 1030 nm for the $^3P_2(|m| = 0)$ state. In this region, there is no magic wavelength for the $^3P_2(|m| = 2)$ state.

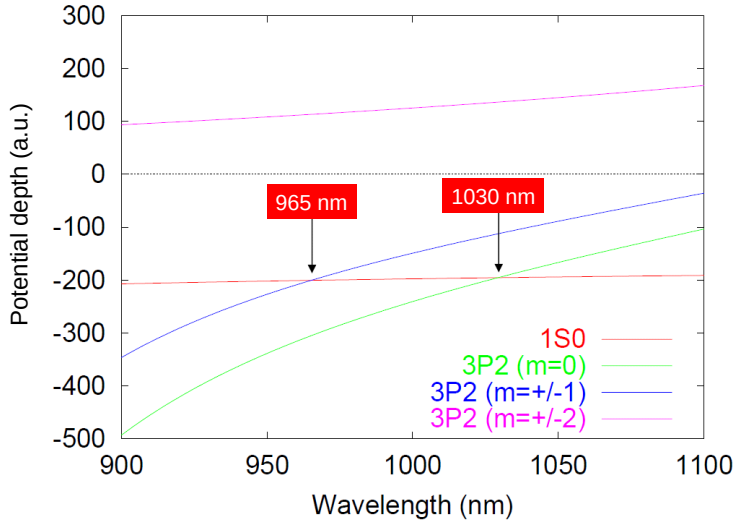

Figure A.1: Estimation of the magic wavelength of the $^3P_2$ state for linearly polarized FORT and zero magnetic field.

Appendix B

Basic theories on an SHG ring cavity

The MOT beam at 556 nm is obtained by a dye laser in our laboratory. In order to use a dye laser, we (students) have to work very hard; we must change dye and clean up the cavity almost every week, use Ar ion laser and so on. Thus, the new laser source at 556 nm which is stable and maintenance-free is strongly desired.

The double wavelength of the MOT beam is 1111.3 nm. This wavelength is close to the wavelength 1.3 μm which is known as zero-dispersion wavelength of the optical fiber. Recently the 1.3 μm laser is widely used in the field of optical broadband communications. Thus, many stable commercial lasers around 1 μm are now available.

We use a commercial fiber laser (Koheras or Keopsys) at 1111.3 nm. Its linewidth is below 100 kHz. In addition, we find that a nonlinear crystal LBO can convert 1111.3 nm to 555.6 nm efficiently by the proper ring cavity. We can obtain more than 400 mW green laser and its frequency locking scurvies for more than ten hours.

B.1 Theory of an SHG technique

B.1.1 Wave equation for a nonlinear medium

Let us consider a certain medium in which both averaged charge density and current density are zero. If the medium is illuminated by a laser beam, atoms and molecules inside the medium are polarized. Let the density of these induced electric dipoles be $\mathbf{P}(\mathbf{r})$. The electrostatic potential at $\mathbf{r}$ generated by $\mathbf{P}(\mathbf{r})$ can be written as

$$\phi(\mathbf{r}) = \frac{1}{4\pi\epsilon_0}\int_V \mathbf{P}(\mathbf{r}')\cdot\nabla\Big(\frac{1}{|\mathbf{r}-\mathbf{r}'|}\Big)\mathrm{d}V', \tag{B.1}$$

where V' is the volume of considered system. By using

$$\nabla'\Big(\frac{\mathbf{P}(\mathbf{x}')}{|\mathbf{r}-\mathbf{r}'|}\Big) = \frac{\nabla'\cdot\mathbf{P}(\mathbf{r}')}{|\mathbf{r}-\mathbf{r}'|} + \mathbf{P}(\mathbf{r}')\cdot\nabla'\Big(\frac{1}{|\mathbf{r}-\mathbf{r}'|}\Big) \tag{B.2}$$

and Gauss's divergence theorem

$$\oint_S \mathbf{A}(\mathbf{r})\cdot\mathbf{n}(\mathbf{r})\mathrm{d}S = \int_V \nabla\cdot\mathbf{A}(\mathbf{r})\mathrm{d}V \tag{B.3}$$

where $\mathbf{n}(\mathbf{r})$ is the normal vector at $\mathbf{r}$ on S, we can transform (B.1) into

$$\phi(\mathbf{r}) = -\frac{1}{4\pi\epsilon_0}\int_V \frac{\nabla' \cdot \mathbf{P}(\mathbf{r}')}{|\mathbf{r}-\mathbf{r}'|}\mathrm{d}V' + \frac{1}{4\pi\epsilon_0}\int_S \frac{-\mathbf{P}(\mathbf{r}')\cdot\mathbf{n}'}{|\mathbf{r}-\mathbf{r}'|}\mathrm{d}S'. \tag{B.4}$$

On the other hand, if we assume that, instead of $\mathbf{P}(\mathbf{r})$, some charges are distributed inside V and on the surface S and their distributions are given by $\rho_d(\mathbf{r})$ in V and $w_d(\mathbf{r})$ on S, the potential can be described as

$$\phi(\mathbf{r}) = \frac{1}{4\pi\epsilon_0}\int_V \frac{\rho_d(\mathbf{r}')}{|\mathbf{x}-\mathbf{x}'|}\mathrm{d}V' + \frac{1}{4\pi\epsilon_0}\int_S \nabla' \frac{w_d(\mathbf{r}')}{|\mathbf{r}-\mathbf{r}'|}\mathrm{d}S'. \tag{B.5}$$

Comparing (B.4) to (B.5), we have

$$\rho_d(\mathbf{r}) = -\nabla \cdot \mathbf{P}(\mathbf{r}). \tag{B.6}$$

This equation shows that we can regard induced electric dipoles $\mathbf{P}(\mathbf{r})$ as the charge distribution $\rho_d(\mathbf{r})$. From the Maxwell equation ($\nabla \cdot (\epsilon_0\mathbf{E}) = \rho$), we have

$$\begin{aligned} \nabla \cdot (\epsilon_0\mathbf{E}) &= \rho_d & \text{(B.7)}\\ &= -\nabla \cdot \mathbf{P}. & \text{(B.8)}\\ \therefore \quad \nabla \cdot (\epsilon_0\mathbf{E} + \mathbf{P}) &= 0, & \text{(B.9)} \end{aligned}$$

where $\mathbf{D} \equiv \epsilon_0\mathbf{E} + \mathbf{P}$ is called dielectric flux density .

In general, $\mathbf{P}$ is proportional to $\mathbf{E}$. However, in some mediums like nonlinear crystals we are considering, the nonlinear components of $\mathbf{P}$ plays an important role. In that case, $\mathbf{P}$ can be divided into a linear part $\mathbf{P}^{\mathrm{L}}$ and nonlinear parts $\mathbf{P}^{\mathrm{NL}}$, that is to say,

$$\begin{aligned} \mathbf{P} &= \mathbf{P}^{\mathrm{L}} + \mathbf{P}^{\mathrm{NL}} & \text{(B.10)}\\ &= \epsilon_0\chi^{(1)} \cdot \mathbf{E} + \epsilon_0\chi^{(2)} \colon \mathbf{EE} + \cdots, & \text{(B.11)} \end{aligned}$$

where $\chi^{(1)}$ is a linear electric susceptibility and $\chi^{(k)} (k \geq 2)$ are nonlinear electric susceptibilities. The electric susceptibility $\chi^{(k)}$ is generally a tensor of rank $k+1$.

Here we are interested in the second term ($\epsilon_0\chi^{(2)} \colon \mathbf{EE}$) in (B.11) because this term generates the second harmonic light. ":" means applying two vectors $\mathbf{E}$ and $\mathbf{E}$ to the tensor of rank 3 ($\chi^{(2)}$). Thus $\chi^{(2)} \colon \mathbf{EE}$ is a vector. If we represent $\chi^{(2)} \colon \mathbf{EE}$ by using their components, it is written as

$$(\chi^{(2)} \colon \mathbf{EE})_i = \chi^{(2)}_{ijk} E_j E_k \tag{B.12}$$

where subscripts are contracted. Hence the Maxwell equations in a medium are given by

$$\begin{aligned} \nabla \cdot \mathbf{D} &= 0 & \text{(B.13)}\\ \nabla \times \mathbf{E} &= -\frac{\partial \mathbf{B}}{\partial t} & \text{(B.14)}\\ \nabla \cdot \mathbf{B} &= 0 & \text{(B.15)}\\ \nabla \times \mathbf{H} &= \frac{\partial \mathbf{D}}{\partial t} & \text{(B.16)} \end{aligned}$$

We neglect the current density in (B.16) because we assumed that the current density is 0. Since

$$\nabla \times (\nabla \times \mathbf{E}) = \nabla(\nabla \cdot \mathbf{E}) - \triangle \mathbf{E} = - \triangle \mathbf{E} \tag{B.17}$$

$$\nabla \times \Big(- \frac{\partial \mathbf{B}}{\partial t} \Big) = -\mu_0 \frac{\partial}{\partial t}(\nabla \times \mathbf{H}) = -\mu_0 \frac{\partial^2 \mathbf{D}}{\partial t^2}, \ (\because (B.16)) \tag{B.18}$$

by taking the rotation of (B.14) and using $\mathbf{D} = \epsilon_0 \mathbf{E} + \mathbf{P}$, we have

$$\triangle \mathbf{E} = \epsilon \mu_0 \frac{\partial^2 \mathbf{E}}{\partial t^2} + \mu_0 \frac{\partial^2 \mathbf{P}^{\mathrm{NL}}}{\partial t^2}, \tag{B.19}$$

where $\epsilon = \epsilon_0(1 + \chi^{(1)})$. This is the basic wave equation for a medium which includes nonlinear polarization $\mathbf{P}^{\mathrm{NL}}$.

If a nonlinear crystal is illuminated by the electric field $\mathbf{E}_{\mathrm{in}}$, the nonlinear polarization $\mathbf{P}^{\mathrm{NL}}$ is induced in the crystal because $\mathbf{P}^{\mathrm{NL}} = \epsilon_0 \chi^{(2)} \vdots \mathbf{E}_{\mathrm{in}} \mathbf{E}_{\mathrm{in}}$. The physical meaning of (B.19) is that if $\mathbf{P}^{\mathrm{NL}}$ exists in the crystal, a certain electric field $\mathbf{E}_{\mathrm{out}}$ defined by (B.19) can exist and this electric field $\mathbf{E}_{\mathrm{out}}$ is the second harmonics we want to generate.

B.1.2 Phase matching condition

In the following discussion, details of the calculations of (B.19) are shown. Let us assume that the incident electric field to a crystal is

$$\mathbf{E}_{\mathrm{in}}(\mathbf{r}, t) = \mathbf{E}^0_{\mathrm{in}} e^{i(\mathbf{k} \cdot \mathbf{r} - \omega t)}. \tag{B.20}$$

We assume that $\mathbf{E}^0_{\mathrm{in}}$ doesn't depend on $\mathbf{r}$ because if we compare $\mathbf{E}_{\mathrm{in}}$ to the generated electric field, we always use strong $\mathbf{E}_{\mathrm{in}}$ for nonlinear crystals. Because $\mathbf{P}^{\mathrm{NL}} = \epsilon_0 \chi^{(2)} \vdots \mathbf{E}_{\mathrm{in}} \mathbf{E}_{\mathrm{in}}$, $\mathbf{P}^{\mathrm{NL}}$ can be written as

$$\mathbf{P}^{\mathrm{NL}} = \epsilon_0 (\chi^{(2)} \vdots \mathbf{E}^0_{\mathrm{in}} \mathbf{E}^0_{\mathrm{in}}) e^{i(2\mathbf{k} \cdot \mathbf{r} - 2\omega t)}. \tag{B.21}$$

In order to examine how the second harmonics will be generated and grow up in the nonlinear crystal by $\mathbf{P}^{\mathrm{NL}}$, let us assume that the expected output electric field $\mathbf{E}_{\mathrm{out}}$ is given by

$$\mathbf{E}_{\mathrm{out}}(\mathbf{r}, t) = \mathbf{E}^0_{\mathrm{out}}(\mathbf{r}) e^{i(\mathbf{k}' \cdot \mathbf{r} - 2\omega t)}, \tag{B.22}$$

Notice that $\mathbf{k}'$ does not necessarily correspond with $2\mathbf{k}$ because of the difference of their indices of refraction in the crystal. For simplicity, we assume that the polarization of $\mathbf{E}_{\mathrm{out}}$ is parallel to x-axis. z-axis is parallel to $\mathbf{k}$. In this case, $\mathbf{E}_{\mathrm{out}}$ and $\mathbf{P}^{\mathrm{NL}}$ are simplified to

$$E^{\mathrm{out}}_x(z, t) = E^{0,\mathrm{out}}_x(z) e^{i(k'z - 2\omega t)} \tag{B.23}$$

$$P^{\mathrm{NL}}_x(z, t) = \epsilon_0 (\chi^{(2)}_{xjk} E^{0,\mathrm{in}}_j E^{0,\mathrm{in}}_k) e^{i(2kz - 2\omega t)} \tag{B.24}$$

Substituting (B.23) and (B.24) for (B.19) gives us

$$\frac{\mathrm{d}^2 E_x^{0,\mathrm{out}}}{\mathrm{d}z^2}(z) + 2ik'\frac{\mathrm{d}E_x^{0,\mathrm{out}}}{\mathrm{d}z}(z) - k'^2 E_x^{0,\mathrm{out}}(z) = -4\epsilon\mu_0\omega^2 E_x^{0,\mathrm{out}}(z) \\ -4\epsilon_0\mu_0\omega^2(\chi^{(2)}_{xjk}E_j^{0,\mathrm{in}}E_k^{0,\mathrm{in}})e^{i(2k-k')z} \quad \text{(B.25)}$$

If $P_x^{\mathrm{NL}}(z,t)$ does not exist, the amplitude of $E_x^{\mathrm{out}}(z,t)$ must be constant everywhere. In other words, by imposing the condition that if $P_x^{\mathrm{NL}}(z,t) \equiv 0$ then $E_x^{\mathrm{out}}(z,t) = E_x^{0,\mathrm{out}}(0)e^{-2i\omega t}$, we have

$$k^2 = 4\epsilon\mu_0\omega^2. \quad \text{(B.26)}$$

In addition, we assume that $E_x^{0,\mathrm{out}}$ does not change within the length of $\sim \lambda$(wavelength), that is to say,

$$\left|\frac{\mathrm{d}^2 E_x^{0,\mathrm{out}}}{\mathrm{d}z^2}(z)\right| \ll \left|k\frac{\mathrm{d}E_x^{0,\mathrm{out}}}{\mathrm{d}z}(z)\right|. \quad \text{(B.27)}$$

From (B.26) and (B.27), (B.25) can be transformed to

$$\frac{\mathrm{d}E_x^{0,\mathrm{out}}}{\mathrm{d}z}(z) = i\frac{2\mu_0\omega^2}{k}\epsilon_0(\chi^{(2)}_{xjk}E_j^{0,\mathrm{in}}E_k^{0,\mathrm{in}})e^{i\Delta kz} \quad \text{(B.28)}$$

$$\equiv i\frac{2\mu_0\omega^2}{k}p_0 e^{i\Delta kz}, \quad \text{(B.29)}$$

where $p_0 = \epsilon_0(\chi^{(2)}_{xjk}E_j^{0,\mathrm{in}}E_k^{0,\mathrm{in}})$ and $\Delta k = 2k - k'$. This equation can be easily integrated. Let the length of the crystal L,

$$E_x^{0,\mathrm{out}}(L) = \int_0^L \frac{\mathrm{d}E_x^{0,\mathrm{out}}}{\mathrm{d}z'}(z')\mathrm{d}z' \quad \text{(B.30)}$$

$$= \frac{2\mu_0\omega^2 p_0}{k}\frac{e^{i\Delta kL-1}}{\Delta k} \quad \text{(B.31)}$$

$$= -\frac{2\mu_0\omega^2 p_0}{k}\Big(\frac{\sin(\Delta kL/2)}{\Delta kL/2}\Big)Le^{i\Delta kL/2} \quad \text{(B.32)}$$

$$\therefore \quad |E_x^{0,\mathrm{out}}(L)| = \frac{2\mu_0\omega^2 p_0 L}{k}\left|\frac{\sin(\Delta kL/2)}{\Delta kL/2}\right| \quad \text{(B.33)}$$

Note that the relation between incident power P_{in} and generated power P_{out} is described as

$$P_{\mathrm{out}} \propto P_{\mathrm{in}}^2 \quad \text{(B.34)}$$

because p_0 includes square of $|E_x^{0,\mathrm{in}}|$.

In Fig.B.1, $|E_x^{0,\mathrm{out}}(L)|^2$ are shown as a function of $(\Delta kL)/2$. The condition to obtain the maximum second harmonics power is

$$\frac{\Delta k}{2}L = \frac{2k-k'}{2}L = 0 \quad \text{(B.35)}$$

$$\therefore \quad 2k - k' = 0 \quad \text{(B.36)}$$

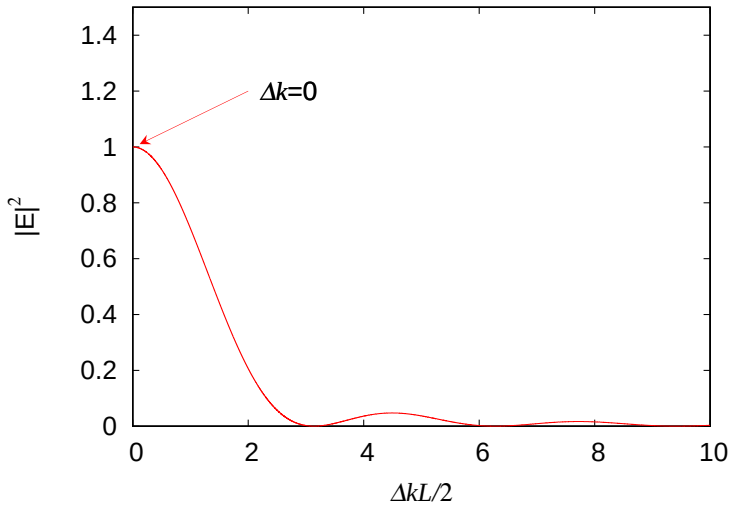

Figure B.1: Phase matching condition is satisfied at Δk=0. The vertical axis is normalized by $(2\mu_0\omega^2 p_0 L)/k$.

where k' and k are the wave vectors of the induced polarization and the output electric field respectively. This condition is called "Phase matching condition". k' and k can be described by the index of refraction $n(\omega)$,

$$k' = n(2\omega)\frac{2\omega}{c} \tag{B.37}$$

$$k = n(\omega)\frac{\omega}{c}. \tag{B.38}$$

Thus the phase matching condition can be given as

$$\frac{2\omega}{c}\{n(2\omega) - n(\omega)\} = 0 \tag{B.39}$$

$$\therefore \quad n(2\omega) = n(\omega), \tag{B.40}$$

which means that the nonlinear crystals for SHG have to be the same refraction index for both ω and 2ω. For the purpose of this, birefringent crystals are used. The specific characteristic of a birefringent crystal is that the crystal has two different refraction indices for each orthogonal polarization.

As an example, we will consider an uniaxial crystal which has one optic axis (so called c-axis). In an uniaxial crystal, the beam whose polarization is orthogonal to the c-axis is called "ordinary beam" and the beam whose polarization is parallel to the c-axis is called "extraordinary beam". Let the refraction indices for ordinary and extraordinary beams $n_o(\theta,\omega)$ and $n_e(\theta,\omega)$ respectively, where θ is the angle between c-axis and wave vector. The nonlinear crystals can be classified by the magnitude relation of $n_e(\theta,\omega)$ and $n_o(\theta,\omega)$. If $n_e(\theta,\omega) > n_o(\theta,\omega)$, the crystal is called a "positive uniaxial crystal". On the

other hand, if $n_o(\theta, \omega) > n_e(\theta, \omega)$, it is called a "negative uniaxial crystal". For a positive uniaxial crystal, if one chooses proper θ,

$$n_o(2\omega_1) = n_e(\omega_1) \tag{B.41}$$

is satisfied. In this case, the input beam should be the extraordinary beam and the output beam should be the ordinary beam, which is described as (e, e, o). This configuration is called "Type I phase matching". The configuration (e, o, e) or (e, o, o) is called "Type II phase matching".

B.1.3 CPM and NCPM

Since both n_e and n_o depend on θ, we have to tune the angle of a crystal so that the phase matching condition is satisfied. This method is called "Critical phase matching"(CPM). It is true that we can generate the second harmonics by CPM, but CPM has one defect. If $\theta \neq 90°$, the direction of the Poynting vector $\mathbf{S}$ does not correspond to the direction of the wave vector $\mathbf{k}$ for the extraordinary beam in the crystal. Thus the ordinary and the extraordinary beams separate as they propagate in the crystal, which leads to the loss of the conversion efficiency. This effect is called "walk off effect".

To overcome the walk off effect, "Non-critically phase matching"(NCPM) is used. The birefringence strongly depends on temperature in some crystals. Hence, the phase matching condition can be satisfied at $\theta = 90°$ by tuning a crystal temperature. Since no walk off effect exists at $\theta = 90°$, high conversion efficiency can be realized.

For the purpose of just generating SH, CPM is good enough if one can find a proper crystal. However, if one needs high power second harmonics, NCPM is desirable although additional temperature control system is required.

B.1.4 Conversion efficiency

In general, we use a CW Gaussian beam to generate a second harmonic. In this case, Eckardt *et al.* [110] showed that the conversion efficiency η_{CW} is given by

$$\eta_{\mathrm{CW}} = \frac{P_{\mathrm{out}}(2\omega)}{P_{\mathrm{in}}^2(\omega)} = \frac{2\omega^2 d_{\mathrm{eff}}^2 L k}{\pi \epsilon_0 c^3 n^3}\, h(B, \xi) \tag{B.42}$$

$$= 16\pi^2 \frac{d_{\mathrm{eff}}^2 L}{\epsilon_0 c n^2 \lambda_0^3} h(B, \xi) \qquad \text{(for Guassian beam)} \tag{B.43}$$

where $P_{\mathrm{in}}(\omega)$ and $P_{\mathrm{out}}(2\omega)$ are the powers of the incident fundamental(after surface losses) and the output second harmonic(before surface losses), c is the speed of light, ω is the angular frequency of incident fundamental, d_{eff} is an effective nonlinear coefficient, L is a crystal length, and k is the magnitude of the fundamental wave vector of incident fundamental inside the crystal. In the last equation, $k = 2\pi n/\lambda_0$ and $\omega = 2\pi c/\lambda_0$ where λ_0 is the wavelength of the fundamental incident are used. $h(B, \xi)$ is a function known as the Boyd and Kleinman focusing factor first introduced in [111]. Here, B and ξ are called

the walk-off parameter and the focusing parameter, respectively and defined as

$$B = \rho\frac{\sqrt{Lk}}{2} \tag{B.44}$$

$$\xi = \frac{L}{kw_0^2} = \frac{\lambda_0 L}{2\pi n w_0^2}, \tag{B.45}$$

where ρ is the birefringent walk off angle, w_0 is the $1/e$ amplitude radius at the beam waist. Also, if $\xi \ll 1$(weak focusing condition) and $\sqrt{\pi}w_0/\rho > L$ (birefringent walk off aperture length > crystal length), by assuming the perfect phase matching, $h(B,\xi)$ can be approximated as

$$h(B,\xi) \simeq \xi(1 - \frac{t^2}{12} + \frac{t^4}{120} - \frac{t^6}{1344} + \cdots) \tag{B.46}$$

where $t = 2B\sqrt{2\xi}$. According to [111], it is proved that $h(B,\xi)$ takes its maximum value at ξ=2.84 and B=0. In NCPM case, B=0 is always satisfied. Then we should design the cavity to make ξ close to 2.84.

B.1.5 LBO

Considering that generated 556 nm light by SHG technique will be used for MOT, the output power is expected to be 200∼300 mW at least. Therefore, NCPM is suitable for our experiment because it does not suffer from the loss of efficiency caused by the walk-off effect. We chose an LBO crystal because it can generate 555.6 nm light from 1111 nm light by Type-I NCPM according to [112] and also has a high damage threshold. Details about the light source of 111 1nm will be discussed in the next section.

Lithium triborate(LiB_3O_5, LBO) is a very popular and widely used nonlinear crystal. LBO is a negative biaxial crystal. According to the catalogue of CRYSTECH Inc., an LBO crystal has the following specific characteristics.

- Broad transparency range from 160 nm to 2600 nm
- Relatively large effective SHG coefficient (about three times that of KDP)
- High damage threshold (18.9 GW/cm^2 at 1053 nm)
- Type-I and Type-II Non-Critical Phase Matching (NCPM) over a wide wavelength range

We bought two LBO crystals (3×3×7 mm and 3×3×10 mm) from KASTON Inc.(China). Both sides of crystals are Anti-Reflection coated for 1111nm and 555.6nm light. The damage threshold of the AR coat is 300∼400 MW/cm^2 and reflectivity R of the AR coat is $R < 0.2$ % at 532 nm light.

B.2 Design of the Ring Cavity

The easiest method to generate the second harmonics is to put a nonlinear crystal at the focal point of the fundamental light. It is true that the second harmonics will be produced by this method. However it may be very weak due to small conversion efficiency. Thus, in general, the optical cavity is used to accumulate the power of fundamental light and we put a nonlinear crystal into the cavity. A Fabry-Pérot resonator and a ring type resonator is generally used as an optical cavity. For the purpose of generating second harmonics, a ring type resonator is commonly used. The reason is that the fundamental light propagates in one direction in the ring type resonator and the generated second harmonics in nonlinear crystal also travel in the same direction. On the contrary, the fundamental travels back and forth between two mirrors in a Fabry-Pérot resonator. As a result of this, the second harmonics are generated in both opposite directions. In order to use generated second harmonics as much as possible, this is not convenient[1]. We, then, decided to use a ring cavity.

In order to design a ring cavity for the SHG, the following two procedures are required. First, we have to find best parameters related to reflectivities of cavity mirrors which make ξ close to 2.84. ξ is determined by the Rayleigh length z_R of the fundamental laser at the nonlinear crystal. For the calculation of z_R, ABCD matrices are used [113]. Next, by considering the loss rate on the surfaces of mirrors and crystals, the "impedance matching condition" is examined. By using all these parameters, we can estimate the SHG conversion efficiency η_{SHG} and then predict the theoretically expected SHG power.

B.2.1 ABCD matrices

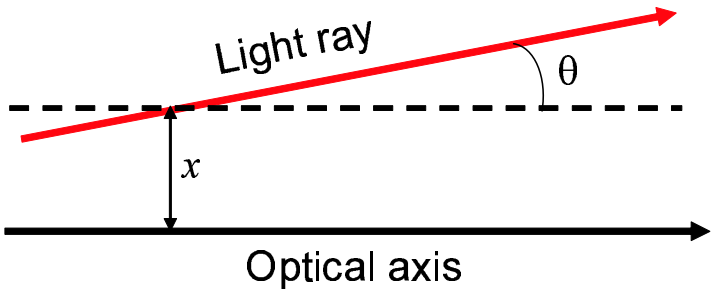

Figure B.2: Definition of the ray vector.

In order to design the optical system, ABCD matrices are often used [113, 114]. In this method, every optical element is described by a 2×2 matrix and assembles of such optics can be represented just by multiplying ABCD matrices of each elements. The most powerful point of this method is that the change of a Gaussian beam can be traced by

[1]There exists some methods to efficiently pick up the second harmonics generated in a Fabry-Pérot cavity by using their polarization.

using a famous ABCD law. Hence, when we design the optical cavity, this method is often used to calculate the beam waist, the total cavity length for the stable cavity operation and so on.

There exist two kinds of ABCD matrices. This makes the situation a little complicated. The difference is the treatment of the refractive index. In the following discussion, these two methods will be used parallel. One will be introduced as Kogelnik [113] and the other is Yariv [114]. As shown in Fig.B.2, a light ray can be defined by

$$\begin{pmatrix} x \\ n\theta \end{pmatrix} \quad \text{[Kogelnik]}, \qquad \begin{pmatrix} x \\ \theta \end{pmatrix} \quad \text{[Yariv]}, \tag{B.47}$$

where x is the position, θ is the angle and n is the refractive index of the medium. This vector is called a "ray vector". When this light ray propagates through some optics, ray vector changes. ABCD matrices describe the relationship between the input ray vector and the output one.

$$\begin{pmatrix} x_{\text{out}} \\ n_{\text{out}}\theta_{\text{out}} \end{pmatrix} = \begin{pmatrix} A & B \\ C & D \end{pmatrix} \begin{pmatrix} x_{\text{in}} \\ n_{\text{in}}\theta_{\text{in}} \end{pmatrix} \quad \text{[Kogelnik]} \tag{B.48}$$

$$\begin{pmatrix} x_{\text{out}} \\ \theta_{\text{out}} \end{pmatrix} = \begin{pmatrix} A & B \\ C & D \end{pmatrix} \begin{pmatrix} x_{\text{in}} \\ \theta_{\text{in}} \end{pmatrix} \quad \text{[Yariv]}, \tag{B.49}$$

B.2.2 Examples of ABCD matrices

ABCD matrices are already known for many optical components we usually use. In this section, I will introduce some ABCD matrices required for our subsequent calculations.

· Propagation d in n medium

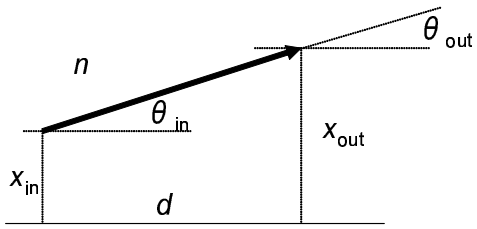

Figure B.3: Propagation d in n medium

From Fig.B.3 , the next relation must be satisfied.

$$\theta_{\rm out} = \theta_{\rm in}, \qquad x_{\rm out} = x_{\rm in} + d\theta_{\rm in} \tag{B.50}$$

Then the ABCD matrix becomes

$$\begin{pmatrix} x_{\rm out} \\ n\theta_{\rm out} \end{pmatrix} = \begin{pmatrix} 1 & d/n \\ 0 & 1 \end{pmatrix} \begin{pmatrix} x_{\rm in} \\ n\theta_{\rm in} \end{pmatrix} \quad \text{[Kogelnik]} \tag{B.51}$$

$$\begin{pmatrix} x_{\rm out} \\ \theta_{\rm out} \end{pmatrix} = \begin{pmatrix} 1 & d \\ 0 & 1 \end{pmatrix} \begin{pmatrix} x_{\rm in} \\ \theta_{\rm in} \end{pmatrix}. \quad \text{[Yariv]}$$

· Entering from n_1 medium to n_2 medium

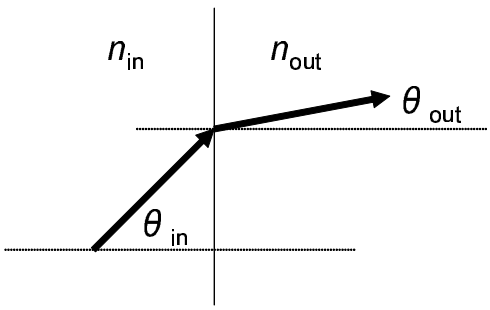

Figure B.4: Entering from n_1 medium to n_2 medium

According to the Snell's law,

$$n_{\rm in}\theta_{\rm in} = n_{\rm out}\theta_{\rm out}, \qquad x_{\rm out} = x_{\rm in}. \tag{B.52}$$

Then,

$$\begin{aligned} \begin{pmatrix} x_{\rm out} \\ n_{\rm out}\theta_{\rm out} \end{pmatrix} &= \begin{pmatrix} 1 & 0 \\ 0 & 1 \end{pmatrix} \begin{pmatrix} x_{\rm in} \\ n_{\rm in}\theta_{\rm in} \end{pmatrix} \quad \text{[Kogelnik]} \\ \begin{pmatrix} x_{\rm out} \\ \theta_{\rm out} \end{pmatrix} &= \begin{pmatrix} 1 & 0 \\ 0 & n_{\rm in}/n_{\rm out} \end{pmatrix} \begin{pmatrix} x_{\rm in} \\ \theta_{\rm in} \end{pmatrix}. \quad \text{[Yariv]} \end{aligned} \tag{B.53}$$

· Reflection by curved mirror whose curvature is R

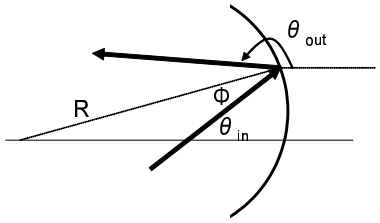

Figure B.5: Reflection by curved mirror whose curvature is R

From Fig.B.5,

$$\begin{aligned} \tan\theta_{\rm out} &= \tan(\pi + \theta_{\rm in} - 2\phi) = \tan(-\theta_{\rm in} + 2\phi) \\ \therefore \quad \theta_{\rm out} &= -\theta_{\rm in} + 2\phi \end{aligned} \tag{B.54}$$

$$\theta_{\rm in} - \phi = \frac{x_{\rm in}}{R}. \tag{B.55}$$

By substituting (B.55) to (B.54),

$$\theta_{\rm out} = \theta_{\rm in} - \frac{2}{R}x_{\rm in} \tag{B.56}$$

$$x_{\rm out} = x_{\rm in}. \tag{B.57}$$

Then the ABCD matrix is derives as follows.

$$\begin{aligned} \begin{pmatrix} x_{\rm out} \\ n\theta_{\rm out} \end{pmatrix} &= \begin{pmatrix} 1 & 0 \\ -2n/R & 1 \end{pmatrix} \begin{pmatrix} x_{\rm in} \\ n\theta_{\rm in} \end{pmatrix} \quad \text{[Kogelnik]} \\ \begin{pmatrix} x_{\rm out} \\ \theta_{\rm out} \end{pmatrix} &= \begin{pmatrix} 1 & 0 \\ -2/R & 1 \end{pmatrix} \begin{pmatrix} x_{\rm in} \\ \theta_{\rm in} \end{pmatrix}. \quad \text{[Yariv]} \end{aligned} \tag{B.58}$$

B.2.3 ABCD law

There exists a famous and very useful law between ABCD matrices and q-factor of Gaussian beam. This is know as the "ABCD law". Note that because of the difference of the definition of the base for ABCD matrices in Kogelnik and Yariv representation, the ABCD law is also different.

Generally, we can consider the ABCD matrix as a black box. However the next two equations are always valid.

$$\begin{cases} x_{\text{out}} = Ax_{\text{in}} + Bn_{\text{in}}\theta_{\text{in}} \\ n_{\text{out}}\theta_{\text{out}} = Cx_{\text{in}} + Dn_{\text{in}}\theta_{\text{in}} \qquad \text{[Kogelnik]} \end{cases} \tag{B.59}$$

$$\begin{cases} x_{\text{out}} = Ax_{\text{in}} + B\theta_{\text{in}} \\ \theta_{\text{out}} = Cx_{\text{in}} + D\theta_{\text{in}} \qquad \text{[Yariv]} \end{cases}$$

Let us introduce the optical ray R which is the vector whose direction is perpendicular to the wave front. By assuming small θ, we can obtain the next equation.

$$\begin{aligned} R_{\text{out}} = \frac{x_{\text{out}}}{\theta_{\text{out}}} &= \frac{Ax_{\text{in}} + Bn_{\text{in}}\theta_{\text{in}}}{\left(\frac{1}{n_{\text{out}}}\right)(Cx_{\text{in}} + Dn_{\text{in}}\theta_{\text{in}})} \\ &= \frac{n_{\text{out}}(AR_{\text{in}} + Bn_{\text{in}})}{CR_{\text{in}} + Dn_{\text{in}}} \quad \text{[Kogelnik]} \end{aligned} \tag{B.60}$$

$$\begin{aligned} R_{\text{out}} = \frac{x_{\text{out}}}{\theta_{\text{out}}} &= \frac{Ax_{\text{in}} + B\theta_{\text{in}}}{Cx_{\text{in}} + D\theta_{\text{in}}} \\ &= \frac{AR_{\text{in}} + B}{CR_{\text{in}} + D} \quad \text{[Yariv]} \end{aligned}$$

As you can easily confirm, R and q-value for Gaussian beam are converted by optical elements in a same manner. For example, both satisfy the lens equation, and so on. This means that, we can replace R by q included in above equations.

$$\begin{aligned} \left(\frac{q_{\text{out}}}{n_{\text{out}}}\right) &= \frac{A\left(\frac{q_{\text{in}}}{n_{\text{in}}}\right) + B}{C\left(\frac{q_{\text{in}}}{n_{\text{in}}}\right) + D} \quad \text{[Kogelnik]} \\ q_{\text{out}} &= \frac{Aq_{\text{in}} + B}{Cq_{\text{in}} + D} \quad \text{[Yariv]} \end{aligned} \tag{B.61}$$

This is the "ABCD law".

Kogelnik's ABCD matrices satisfy one more useful relation[2]. If we consider the opposite propagation with same optical path described by same ABCD matrices, next two equations must be satisfied.

$$\begin{pmatrix} x_{\rm out} \\ n\theta_{\rm out} \end{pmatrix} = \begin{pmatrix} A & B \\ C & D \end{pmatrix} \begin{pmatrix} x_{\rm in} \\ n\theta_{\rm in} \end{pmatrix} \qquad \text{[from left to right]}$$

$$\begin{pmatrix} x_{\rm in} \\ -n\theta_{\rm in} \end{pmatrix} = \begin{pmatrix} A & B \\ C & D \end{pmatrix} \begin{pmatrix} x_{\rm out} \\ -n\theta_{\rm out} \end{pmatrix} \qquad \text{[from right to left]}$$

This can be possible only for Kogelnik' base. If we use Yariv's base, the second equation is not always satisfied. We can easily see this difference by considering the light which enters medium n_2 from n_1.

Applying the inverse matrix to the second equation and comparing two equations with each other, we get

$$A = D, \qquad AD - BC = 1. \tag{B.62}$$

Let me repeat that this is not always valid for Yariv's base.

According to the definition of q-factor of Gaussian beam,

$$\frac{1}{q} = \frac{1}{r} - i\frac{\lambda}{\pi w^2}. \qquad (q-\text{factor}) \tag{B.63}$$

where r is the curvature and w is a spot size.

Let us consider designing the optical cavity by using ABCD matrices. In the stable optical cavity, a certain ray from some point surely return to the same point with same q-factor. This means that, $q_{\rm out} = q_{\rm in}$ in (B.61). Therefore by constructing the total ABCD matrix and solving the quadratic equation, you have complex number q described by ABCD. According to (B.63), you can estimate the beam curvature from real part of q, and the imaginary part can be used to calculate the beam waist.

[2]Yariv's ABCD matrices also sometimes satisfy the same relation, but not always. Kogelnik's ABCD matrices always satisfy this relation.

B.2.4 Ring cavity

Let us consider a ring cavity as an example. With the aid of ABCD matrices introduced in the previous sections, the total ABCD matrix for the ring cavity of Fig. B.6 can be described as[3]

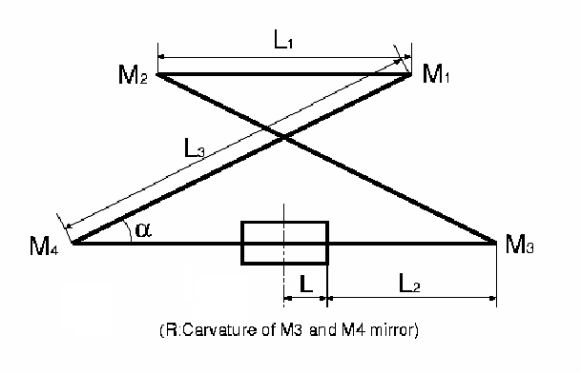

Figure B.6: The ring cavity for SHG. L is the half length of a nonlinear crystal.

$$\begin{pmatrix} 1 & L \\ 0 & 1 \end{pmatrix}\begin{pmatrix} 1 & 0 \\ 0 & 1/n \end{pmatrix}\begin{pmatrix} 1 & L_2 \\ 0 & 1 \end{pmatrix}\begin{pmatrix} 1 & 0 \\ -2/R & 1 \end{pmatrix}\begin{pmatrix} 1 & L_1+2L_3\cos\alpha \\ 0 & 1 \end{pmatrix} \times\begin{pmatrix} 1 & 0 \\ -2/R & 1 \end{pmatrix}\begin{pmatrix} 1 & L_2 \\ 0 & 1 \end{pmatrix}\begin{pmatrix} 1 & 0 \\ 0 & n \end{pmatrix}\begin{pmatrix} 1 & L \\ 0 & 1 \end{pmatrix} \quad \text{[Yariv]} \tag{B.64}$$

where R is the curvature of M4 and M3 and n is the refractive index of an LBO crystal. Note that the direction of the fundamental light is perpendicular to the surface of a nonlinear crystal and that next equation must be satisfied from the geometrical restriction.

$$L_1 = 2L_3\cos\alpha - 2(L + L_2). \tag{B.65}$$

One of the possible designs is shown in Fig. B.7 with some parameters. Calculating the conversion efficiency η_{SHG} by using these parameters, (B.43) and parameters in Table. B.1 gives us

$$\eta_{\mathrm{SHG}} = 1.4 \times 10^{-4}. \quad [\mathrm{W}^{-1}] \tag{B.66}$$

B.2.5 Enhancement factor

In [110], Eckardt *et al.* showed that the ratio of the fundamental power incident on the ring cavity P_1 and the fundamental power reflected from the cavity P_{r} is written as

$$\frac{P_{\mathrm{r}}}{P_1} = \frac{(\sqrt{r_1} - \sqrt{r_m})^2}{(1 - \sqrt{r_1 r_m})^2}, \tag{B.67}$$

[3]Starting point is the center of the SHG crystal.

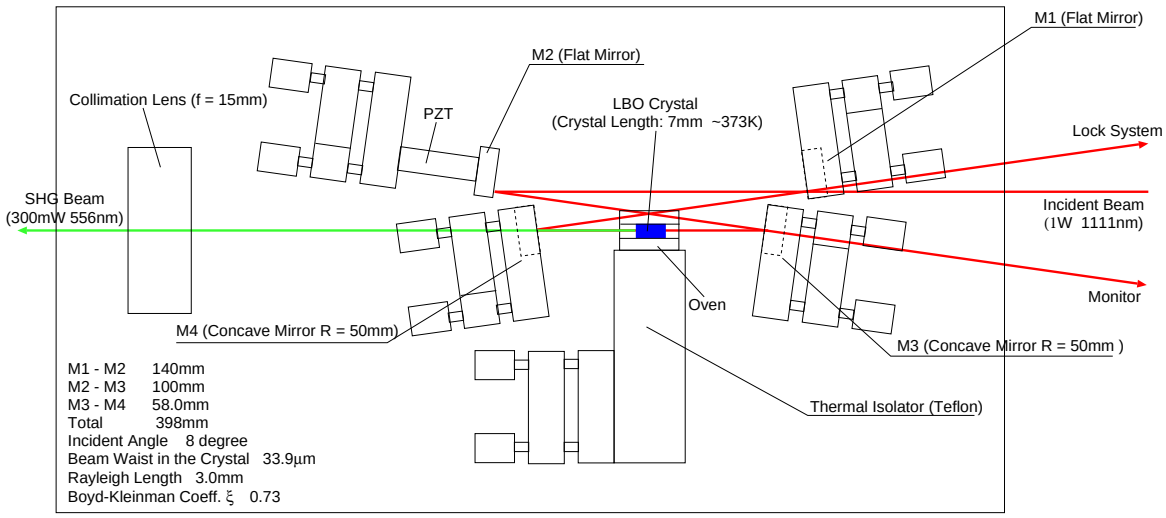

[Mirror Coating] (λ_1 =1111nm λ_2 = 556nm)

	Left Side	Right Side
M1	R = 99.7% @ λ_1	AR @ λ_1
M2	N/A	100% @ λ_1
M3	R = 100% @ λ_1	AR @ λ_1
M4	AR @ λ_2	R = 100% @ λ_1 & AR @ λ_2 (Dichroic Mirror)

Figure B.7: One of the possible designs. The calculated output power is 300∼400mW.

where r_1 is the power reflection coefficient of the cavity mirror M1 (see Fig.B.7), r_m is called a cavity reflectance parameter and defined as

$$r_m = T t_{\rm SG} r_2, \tag{B.68}$$

where $t_{\rm SG}(=(1-\eta_{\rm SHG}P_c))$ is the crystal transmission. P_c is the circulating fundamental power just inside the first mirror M1. r_2 is the power reflection coefficient of the ring cavity mirrors M2, M3 and M4. T is the single-pass power transmission coefficient which does not include P_c and r_2.

From (B.67) and (B.68), we can achieve $P_{\rm r}$=0 by choosing proper r_1 which satisfies $r_1 = r_m$. This condition is called "impedance matching condition". When this condition is satisfied, the maximum P_c is achieved. Therefore we have to carefully choose the reflectivity of M1.

To determine P_c for given P_1, we can use the next equation given in [110].

$$\frac{P_c}{P_1} = \frac{1-r_1}{(1-\sqrt{r_1 r_m})^2}. \tag{B.69}$$

Since r_m is a function of P_c, we can calculate P_c as a function of r_1.

B.2.6 Numerical computations for 1111.3→556 nm, and 798→399 nm system

Now we can estimate the expected SHG power of designed system. For the purpose of numerical calculations, we use (B.43). In TableB.1, required parameters are listed. I also calculated the theoretically expected values for the LAS system. LAS is used in our laboratory to convert 798 nm to 399 nm.

Table B.1: Parameters for SHG systems in our laboratory(1111.3 nm→555.6 nm and 798 nm→399 nm). λ_0 and P_0 are the wavelength and incident power of fundamental light, n is the refractive index for the fundamental light, L_{crystal} is the crystal length, z_{R} and w_0 are the Rayleigh length and the beam waist of the fundamental light at the crystal, d_{eff} is the effective nonlinear coefficient, h is the Boyd-Kleinman coefficient, and η_{SHG} is the SHG conversion efficiency.

	Fiber laser	LAS
λ_0 (nm)	1111.3	798
P_0(W)	1	1
n	1.56	1.61
$L_{\text{crystal}} = 2L$ (mm)	7	12
z_{R}(mm)	3.0	10.5
w_0 (μm)	33.9	51.6
d_{eff} (pm/V)	1.24	0.75
$h(B, \xi)$	0.73	0.36
$\eta_{\text{SHG}}(\times 10^{-4}\text{W}^{-1})$	1.4	1.1

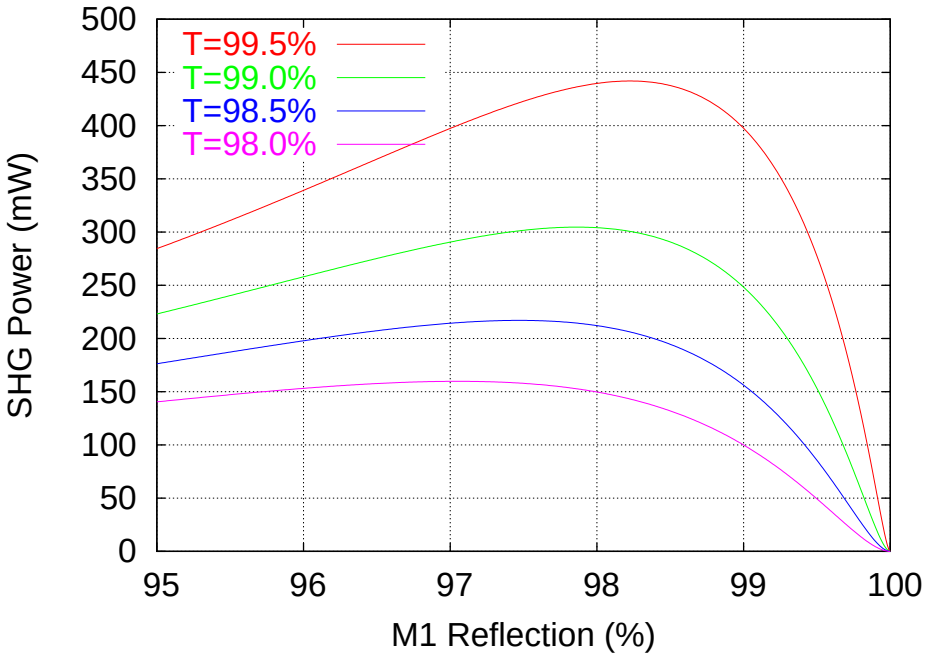

Figure B.8: Theoretically expected SHG power for 1111.3→556nm SHG system[NCPM, Type-I]. P_0=1W, w_0 = 33.9μm, L_{crystal}(Crystal length)=7mm.

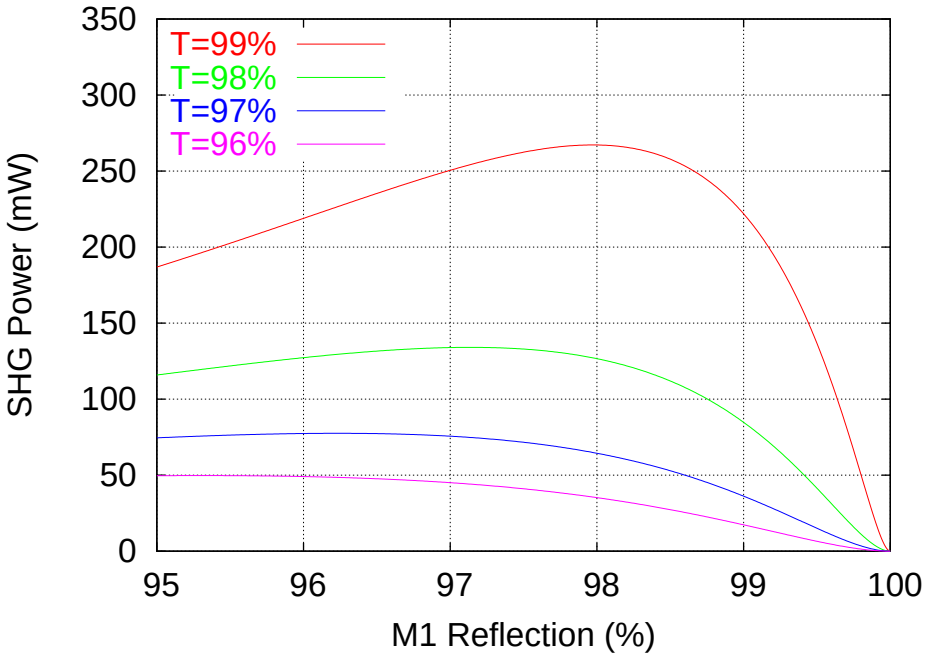

Figure B.9: Theoretically expected SHG power for 798→399nm SHG system[CPM, Type-I]. P_0=1W, w_0 = 51.6μm, L_{crystal}(Crystal length)=12mm.

Appendix C

Iodine spectroscopy at 507 nm

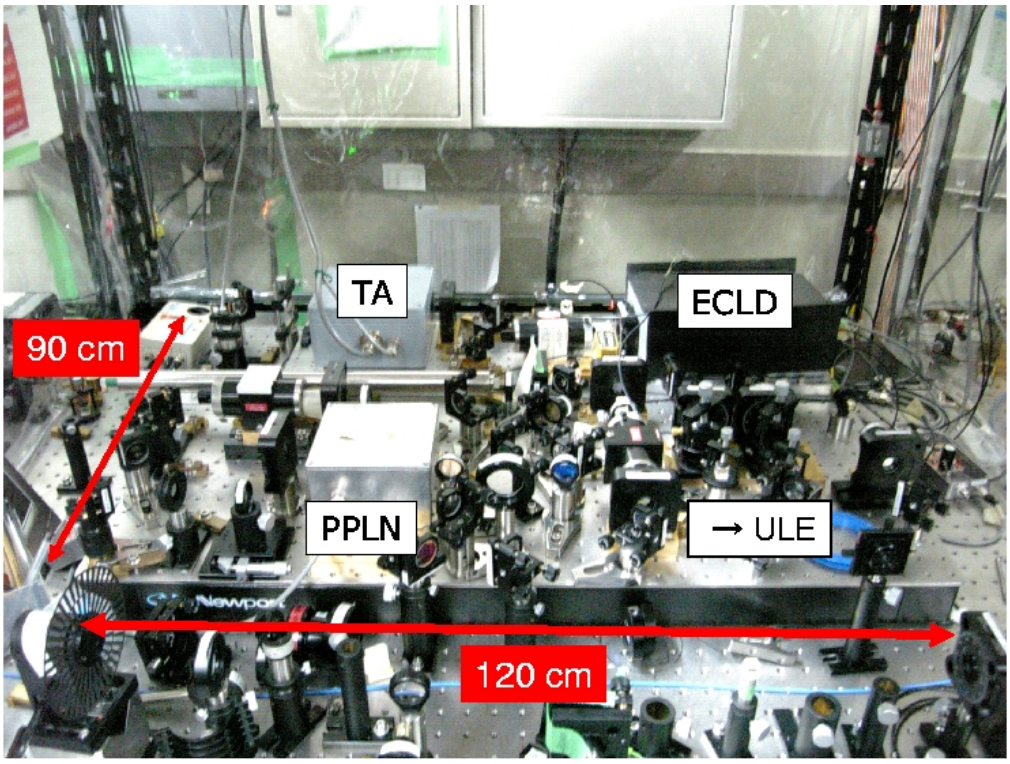

Figure C.1: Ultranarrow "compact" laser system at 507 nm developed in this study. All components are installed on an optical table of 90×120 cm.

According to the [115], the spectral width of iodine molecules becomes narrowest around 507 nm. Thus, our compact laser system (see Fig. C.1) has possibility of a future high performance transportable frequency reference. We therefore demonstrate spectroscopy of iodine molecules using the developed laser system.

We first performed absorption spectroscopy of iodine molecules. Observed spectra over 50 GHz are shown in Fig. C.2 . The amplitude is normalized so that distortions

of the signal due to power fluctuations are removed. The numbers labeled to some of the spectra in Fig. C.2(Bottom) correspond to those in [116]. In addition, the detailed spectrum of one of the lines in No. 1388 resonance in Fig. C.2(Bottom) was obtained via saturation spectroscopy as shown in Fig. C.3. The spectrum in Fig. C.3 is broadened by saturation broadening and residual Doppler broadening due to the slight misalignment between the pump and probe lasers in saturation spectroscopy. Further development of the system toward high-resolution spectroscopy of iodine molecules using, for example, the modulation transfer technique [117, 118] is now in progress.

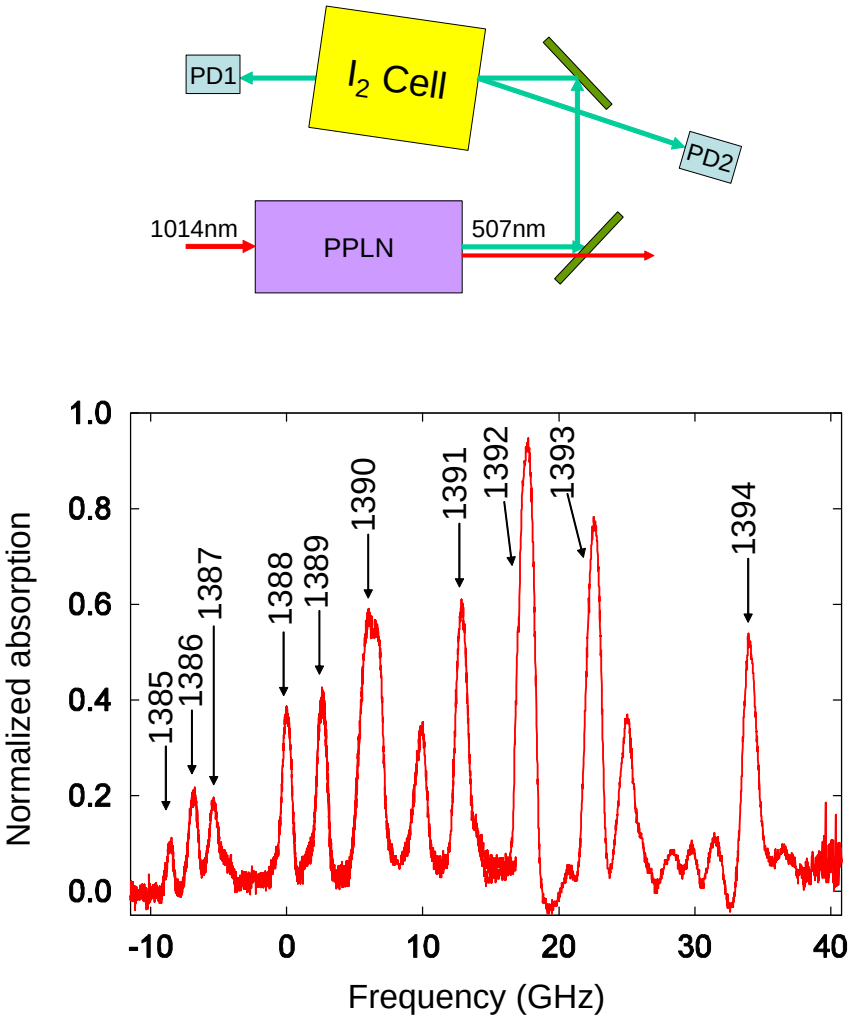

Figure C.2: Absorption spectroscopy of iodine molecules over the 50 GHz around 507 nm. Some of resonances are identified to those in [116] and labeled with the corresponding numbers.

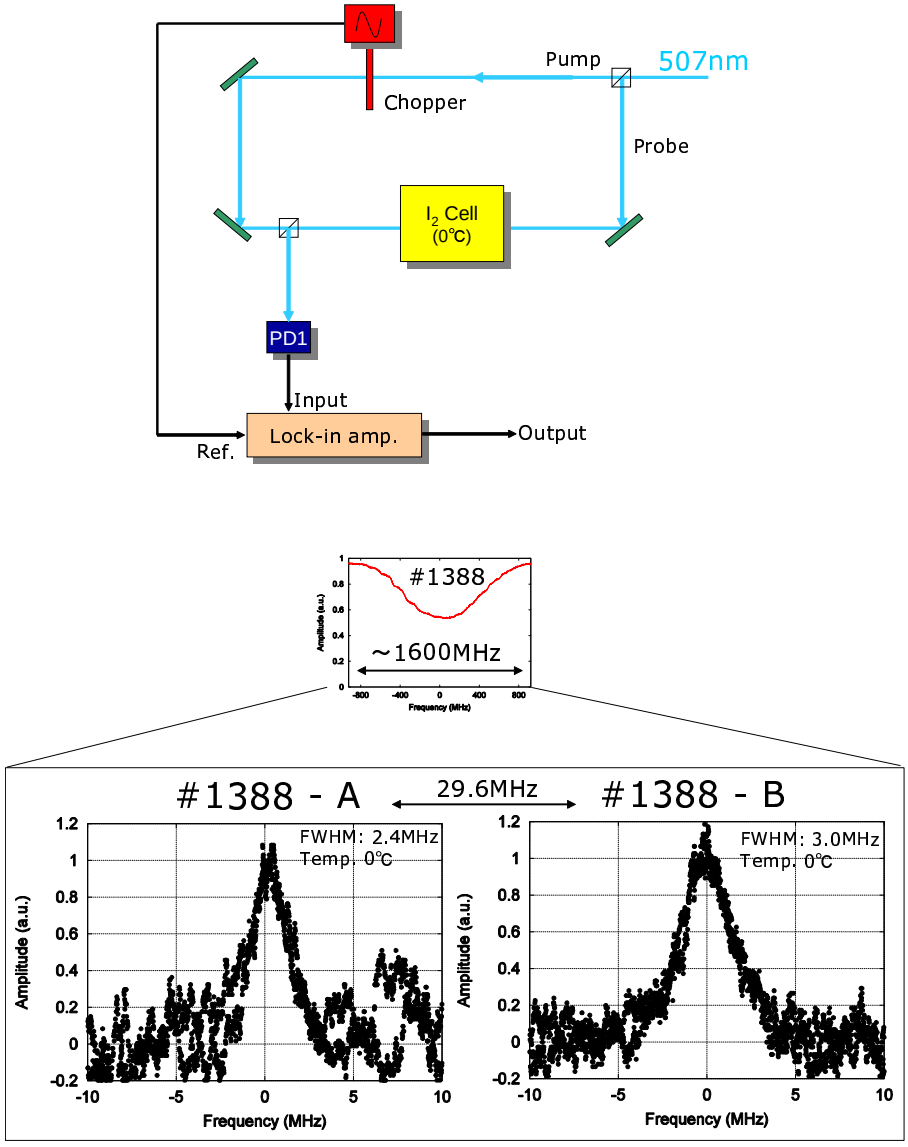

Figure C.3: Detailed spectra of one of the lines in No.1388 resonance in Fig. C.2 taken by saturation spectroscopy.

Appendix D

Spherical harmonics and vector spherical harmonics

Some spherical harmonics and vector spherical harmonics used in this work are listed below [1].

(D.2)

Spherical harmonics $r^L Y_{L,M}(\theta,\phi)$

$$Y_{0,0}(\theta,\phi) = \sqrt{\frac{1}{4\pi}}$$

$$rY_{1,0}(\theta,\phi) = \sqrt{\frac{3}{4\pi}} r_0^{(1)}, \qquad rY_{1,\pm1}(\theta,\phi) = \sqrt{\frac{3}{4\pi}} r_{\pm1}^{(1)}$$

$$r^2 Y_{2,0}(\theta,\phi) = \sqrt{\frac{5}{4\pi}} \frac{3}{2} \left((r_0^{(1)})^2 - \frac{r^2}{3} \right)$$

$$r^2 Y_{2,\pm1}(\theta,\phi) = \sqrt{\frac{5}{4\pi}} \sqrt{3}\; r_0^{(1)} r_{\pm1}^{(1)}, \qquad r^2 Y_{2,\pm2}(\theta,\phi) = \sqrt{\frac{5}{4\pi}} \sqrt{\frac{3}{2}} \left(r_{\pm1}^{(1)} \right)^2$$

$$r^3 Y_{3,0} = \sqrt{\frac{7}{4\pi}} \frac{1}{2} r_0^{(1)} (5(r_0^{(1)})^2 - 3r^2)$$

$$r^3 Y_{3,\pm1} = \sqrt{\frac{7}{4\pi}} \sqrt{\frac{3}{8}} r_{\pm}^{(1)} (5(r_0^{(1)})^2 - r^2), \qquad r^3 Y_{3,\pm2} = \sqrt{\frac{7}{4\pi}} \sqrt{\frac{15}{2}} r_0^{(1)} (r_{\pm}^{(1)})^2$$

$$r^3 Y_{3,\pm3} = \sqrt{\frac{7}{4\pi}} \sqrt{\frac{5}{2}} (r_{\pm}^{(1)})^3$$

[1] First rank irreducible tensor $r_q^{(1)} (q = -1, 0, +1)$ are given by

$$r_{\pm1}^{(1)} = \mp \frac{1}{\sqrt{2}} (x \pm iy), \qquad r_0^{(1)} = z. \tag{D.1}$$

Vector spherical harmonics $\mathbf{Y}_{L,J,M}(\theta,\phi)$

$$\mathbf{Y}_{0,1,0} = \sqrt{\frac{1}{3}}(Y_{1,-1}\hat{\mathbf{e}}_{+1} - Y_{1,0}\hat{\mathbf{e}}_0 + Y_{1,1}\hat{\mathbf{e}}_{-1})$$

$$\mathbf{Y}_{1,0,\pm1} = Y_{0,0}\hat{\mathbf{e}}_{\pm1}, \quad \mathbf{Y}_{1,0,0} = Y_{0,0}\hat{\mathbf{e}}_0$$

$$\mathbf{Y}_{1,1,\pm1} = \pm\sqrt{\frac{1}{2}}(Y_{1,\pm1}\hat{\mathbf{e}}_0 - Y_{1,0}\hat{\mathbf{e}}_{\pm1}) \quad \mathbf{Y}_{1,1,0} = \sqrt{\frac{1}{2}}(Y_{1,1}\hat{\mathbf{e}}_{-1} - Y_{1,-1}\hat{\mathbf{e}}_{+1})$$

$$\mathbf{Y}_{1,2,\pm1} = \sqrt{\frac{1}{10}}(Y_{2,0}\hat{\mathbf{e}}_{\pm1} - \sqrt{3}Y_{2,\pm1}\hat{\mathbf{e}}_0 + \sqrt{6}Y_{2,\pm2}\hat{\mathbf{e}}_{\mp1})$$
$$\mathbf{Y}_{1,2,0} = \sqrt{\frac{1}{10}}(\sqrt{3}Y_{2,-1}\hat{\mathbf{e}}_{+1} - 2Y_{2,0}\hat{\mathbf{e}}_0 + \sqrt{3}Y_{2,1}\hat{\mathbf{e}}_{-1})$$

$$\mathbf{Y}_{2,1,\pm2} = Y_{1,\pm1}\hat{\mathbf{e}}_{\pm1}, \quad \mathbf{Y}_{2,1,\pm1} = \sqrt{\frac{1}{2}}(Y_{1,0}\hat{\mathbf{e}}_{\pm1} + Y_{1,\pm1}\hat{\mathbf{e}}_0)$$
$$\mathbf{Y}_{2,1,0} = \sqrt{\frac{1}{6}}(Y_{1,-1}\hat{\mathbf{e}}_{+1} + 2Y_{1,0}\hat{\mathbf{e}}_0 + Y_{1,1}\hat{\mathbf{e}}_{-1})$$

$$\mathbf{Y}_{2,2,\pm2} = \pm\sqrt{\frac{1}{3}}(\sqrt{2}Y_{2,\pm2}\hat{\mathbf{e}}_0 - Y_{2,\pm1}\hat{\mathbf{e}}_{\pm1})$$
$$\mathbf{Y}_{2,2,\pm1} = \mp\sqrt{\frac{1}{6}}(\sqrt{3}Y_{2,0}\hat{\mathbf{e}}_{\pm1} - Y_{2,\pm1}\hat{\mathbf{e}}_0 - \sqrt{2}Y_{2,\pm2}\hat{\mathbf{e}}_{\mp1})$$
$$\mathbf{Y}_{2,2,0} = \sqrt{\frac{1}{2}}(Y_{2,1}\hat{\mathbf{e}}_{-1} - Y_{2,-1}\hat{\mathbf{e}}_{+1})$$

$$\mathbf{Y}_{2,3,0} = \sqrt{\frac{1}{7}}(\sqrt{2}Y_{3,1}\hat{\mathbf{e}}_{-1} - \sqrt{3}Y_{3,0}\hat{\mathbf{e}}_0 + \sqrt{2}Y_{3,-1}\hat{\mathbf{e}}_{+1})$$
$$\mathbf{Y}_{2,3,\pm1} = \sqrt{\frac{1}{21}}(\sqrt{3}Y_{3,0}\hat{\mathbf{e}}_{\pm1} - \sqrt{8}Y_{3,\pm1}\hat{\mathbf{e}}_0 + \sqrt{10}Y_{3,\pm2}\hat{\mathbf{e}}_{\mp1})$$
$$\mathbf{Y}_{2,3,\pm2} = \sqrt{\frac{1}{21}}(Y_{3,\pm1}\hat{\mathbf{e}}_{\pm1} - \sqrt{5}Y_{3,\pm2}\hat{\mathbf{e}}_0 + \sqrt{5}Y_{3,\pm3}\hat{\mathbf{e}}_{\mp1})$$

Bibliography

[1] D. P. Hansen, J. R. Mohr, and A. Hemmerich,
"Magnetic trapping of metastable calcium atoms",
Phys. Rev. A **67**, 021401 (2003).

[2] Dirk Hansen and Andreas Hemmerich,
"Observation of Multichannel Collisions of Cold Metastable Calcium Atoms",
Phys. Rev. Lett. **96**, 073003 (2006).

[3] J. L. Hall, M. Zhu, and P. Buch
"Prospects for using laser-prepared atomic fountains for optical frequency standards applications"
J. Opt. Soc. Am. B **6**, 2194 (1989).

[4] M. H. Anderson, J. R. Ensher, M. R. Matthews, C. E. Wieman, and E. A. Cornell,
"Observation of Bose-Einstein Condensation in a Dilute Atomic Vapor",
Science **269**, 198 (1995).

[5] K. B. Davis, M. -O. Mewes, M. R. Andrews, N. J. van Druten, D. S. Durfee, D. M. Kurn, and W. Ketterle,
"Bose-Einstein Condensation in a Gas of Sodium Atoms"
Phys. Rev. Lett. **75**, 3969 (1995).

[6] C. C. Bradley, C. A. Sackett, J. J. Tollett, and R. G. Hulet,
"Evidence of Bose-Einstein Condensation in an Atomic Gas with Attractive Interactions",
Phys. Rev. Lett. **75**, 1687 (1995).

[7] Y. Takasu, K. Honda, K. Komori, T. Kuwamoto, M. Kumakura, Y. Takahashi, and T. Yabuzaki,
"High-Density Trapping of Cold Ytterbium Atoms by an Optical Dipole Force",
Phys. Rev. Lett. **90**, 023003 (2003).

[8] Masao Takamoto, Feng-Lei Hong, Ryoichi Higashi and Hidetoshi Katori,
"An optical lattice clock",
Nature(London) **435**, 321 (2005).

[9] Andrei Derevianko, Sergey G.Porsev, Svetlana Kotochigova, Eite Tiesinga, and Paul S.Julienne,
"Ultracold Collision Properties of Metastable Alkaline-Earth Atoms",
Phys. Rev. Lett. **90**, 063002 (2003).

[10] Robin Santra and Chris H.Greene
"Tensorial analysis of the long-range interaction between metastable alkaline-earth-metal atoms"
Phys. Rev. A **67**, 062713 (2003).

[11] Viatcheslav Kokoouline, Robin Santra, and Chris H.Greene,
"Multichannel Cold Collisions between Metastable Sr Atoms",
Phys. Rev. Lett. **90**, 253201 (2003).

[12] K.Góral, L.Santos, and M.Lewenstein
"Quantum Phases of Dipolar Bosons in Optical Lattices"
Phys. Rev. Lett. **88**, 170406 (2002).

[13] Andrei Derevianko and Caleb C.Cannon
"Quantum computing with magnetically interacting atoms"
Phys. Rev. A **70**, 062319 (2004).

[14] F.Diedrich, J.C.Bergquist, Wayne M.Itano, and D.J.Wineland,
"Laser Cooling to the Zero-Point Energy of Motion",
Phys. Rev. Lett. **62**, 403 (1989).

[15] I. Reichenbach and I. H. Deutsch,
"Sideband Cooling while Preserving Coherences in the Nuclear Spin State in Group-II-like Atoms",
Phys. Rev. Lett. **99**, 123001 (2007).

[16] S.B.Nagel, C.E.Simien, S.Laha, P.Gupta, V.S.Ashoka, and T.C.Killian,
"Magnetic trapping of metastable $^3P_2$ atomic strontium",
Phys. Rev. A **67**, 011401 (2003).

[17] Masami Yasuda and Hidetoshi Katori,
"Lifetime Measurement of the $^3P_2$ Metastable State of Strontium Atoms",
Phys. Rev. Lett. **92**, 153004 (2004).

[18] Jan Grünert and Andreas Hemmerich,
"Sub-Doppler magneto-optical trap for calcium",
Phys. Rev. A **65**, 041401 (2002).

[19] B. Pouilly, T. Orlikowski, and M. H. Alexander,
"Fully ab initio dynamics of fine-structure-changing transitions in collisions of Mg($3s3p^3P$) with He",
J. Phys. B: At. Mol. Phys. **18**, 1953 (1985).

[20] V. Aquilanti, R. Candori, and F. Pirani,
"Molecular beam studies of weak interactions for open-shell systems: The ground and lowest excited states of rare gas oxides",
J. Chem. Phys. **89**, 6157 (1988).

[21] R. V. Krems and A. Dalgarno,
"Shape resonances and nonadiabatic dynamics in O(^3P_j)+He collisions at cold and ultracold temperatures",
Phys. Rev. A **66**, 012702 (2002).

[22] C. I. Hancox, S. C. Doret, M. T. Hummon, R. V. Krems, and J. M. Doyle,
"Suppression of Angular Momentum Transfer in Cold Collisions of Transition Metal Atoms in Ground States with Nonzero Orbital Angular Momentum",
Phys. Rev. Lett. **94**, 013201 (2005).

[23] R. V. Krems, J. Kłos, M. F. Rode, M. M. Szczęśniak, G. Chałasiński, and A. Dalgarno,
"Suppression of Angular Forces in Collisions of Non-S-State Transition Metal Atoms",
Phys. Rev. Lett. **94**, 013202 (2005).

[24] Yosuke Takasu, Kenichi Maki, Kaduki Komori, Tetsushi Takano, Kazuhito Honda, Mitsutaka Kumakura, Tsutomu Yabuzaki, and Yoshiro Takahashi,
"Spin-Singlet Bose-Einstein Condensation of Two-Electron Atoms",
Phys. Rev. Lett. **91**, 040404 (2003).

[25] T. Fukuhara, S. Sugawa, and Y. Takahashi,
"Bose-Einstein condensation of an ytterbium isotope",
Phys. Rev. A **76**, 051604R (2007).

[26] T. Fukuhara, Y. Takasu, M. Kumarkua, and Y. Takahashi,
"Degenerate Fermi Gases of Ytterbium",
Phys. Rev. Lett. **98**, 030401 (2007).

[27] T. Fukuhara, Y. Takasu, S. Sugawa and Y. Takahashi,
"Quantum Degenerate Fermi Gases of Ytterbium Atoms",
J. Low. Temp. Phys. **148** 441 (2007).

[28] Y. Takasu, K. Komori, K. Honda, M. Kumakura, T. Yabuzaki, and Y. Takahashi,
"Photoassociation Spectroscopy of Laser-Cooled Ytterbium Atoms",
Phys. Rev. Lett. **93**, 123202 (2004).

[29] S. Tojo, M. Kitagawa, K. Enomoto, Y. Kato, Y. Takasu, M. Kumakura, and Y. Takahashi,
"High-Resolution Photoassociation Spectroscopy of Ultracold Ytterbium Atoms by Using the Intercombination Transition",
Phys. Rev. Lett. **96**, 153201 (2006).

[30] K. Enomoto, M. Kitagawa, K. Kasa, S. Tojo, and Y. Takahashi,
"Determination of the s-Wave Scattering Length and the C_6 van der Waals Coefficient of ^{174}Yb via Photoassociation Spectroscopy",
Phys. Rev. Lett. **98**, 203201 (2007).

[31] M. Kitagawa, K. Enomoto, K. Kasa, Y. Takahashi, R. Ciuryło, P. Naidon, and P. S. Julienne,
"Two-color photoassociation spectroscopy of ytterbium atoms and the precise determinations of s-wave scattering lengths",
Phys. Rev. A **77**, 012719 (2008).

[32] Z. Barber,
"Ytterbium Optical lattice Clock",
PhD thesis, University of Colorado, 2007.

[33] A. V. Taichenachev, V. I. Yudin, C. W. Oates, C. W. Hoyt, Z. W. Barber, and L. Hollberg
"Magnetic Field-Induced Spectroscopy of Forbidden Optical Transitions with Application to Lattice-Based Optical Atomic Clocks"
Phys. Rev. Lett. **96**, 083001 (2006).

[34] C. W. Hoyt, Z. W. Barber, C. W. Oates, T. M. Fortier, S. A. Diddams, and L. Hollberg
"Observation and Absolute Frequency Measurements of the $^1S_0$-$^3P_0$ Optical Clock Transision in Neutral Ytterbium"
Phys. Rev. Lett. **95**, 083003 (2005).

[35] Z. W. Barber, C. W. Hoyt, C. W. Oates, L. Hollberg, A. V. Taichenachev, and V. I. Yudin
"Direct Excitation of the Forbidden Clock Transition in Neutral ^{174}Yb Atoms Confined to an Optical Lattice"
Phys. Rev. Lett. **96**, 083002 (2006).

[36] Y. Takahashi, K. Honda, N. Tanaka, K. Toyoda, K. Ishikawa, and T. Yabuzaki,
"Quantum nondemolition measurement of spin via the paramagnetic Faraday rotation",
Phys. Rev. A **60**, 4974 (1999).

[37] D. DeMille,
"Parity Nonconservation in the $6s^2 {}^1S_0 \rightarrow 6s5d\,{}^3D_1$ Transition in Atomic Ytterbium",
Phys. Rev. Lett. **74**, 4165 (1995).

[38] M. Fujimoto,
"永久電気双極子モーメント検出のための Yb 原子のレーザー冷却"(in Japanese),
Master thesis, Kyoto University, 1997.

[39] J. E. Sansonetti, W. C. Martin, and S. L. Young,
Handbook of Basic Atomic Spectroscopic Data,
NIST, 2005.
http://physics.nist.gov/Handbook

[40] *NIST Atomic Spectra Database*,
http://physics.nist.gov/PhysRefData/Elements/index.html

[41] D. Das, S. Barthwal, A. Banerjee, and V. Natarajan,
"Absolute frequency measurements in Yb with 0.08 ppb uncertainty: Isotope shifts and hyperfine structure in the 399-nm $^1S_0 \rightarrow {}^1P_1$ line",
Phys. Rev. A **72**, 032506 (2005).

[42] D. L. Clark, M. E. Cage, D. A. Lewis, and G. W. Greenlees,
"Optical isotopic shifts and hyperfine splittings for Yb",
Phys. Rev. A **20**, 239 (1979).

[43] K. Honda, Y. Takasu, T. Kuwamoto, M. Kumakura, Y. Takahashi, and T. Yabuzaki,
"Optical dipole force trapping of a fermion-boson mixture of ytterbium isotopes",
Phys. Rev. A **66**, 021401 (2002).

[44] T. Kuwamoto, K. Honda, Y. Takahashi, and T. Yabuzaki,
"Magneto-optical trapping of Yb atoms using an intercombination transition",
Phys. Rev. A **60**, R745 (1999).

[45] T. Fukuhara,
"量子シミュレーションに向けたイッテルビウム原子のフェルミ縮退の実現" (in Japanese),
Master thesis, Kyoto University, 2005.

[46] L. Ricci, M. Weidemüller, T. Esslinger, A. Hemmerich, C. Zimmermann, V. Vuletic, W. König and T. W. Hänsch,
"A compact grating-stabilized diode laser system for atomic physics",
Opt. Commun. **117** 541 (1995).

[47] B. Dahmani, L. Hollberg. and R. Drullinger,
"Frequency stabilization of semiconductor lasers by resonant optical feedback",
Opt. Lett. **12**, 876 (1987).

[48] K. Hayasaka,
"Frequency stabilization of an extended-cavity violet diode laser by resonant optical feedback",
Opt. Comm. **206**, 401 (2002).

[49] S. Uetake, K. Hayasaka, and M. Watanabe,
"Saturation Spectroscopy of Potassium for Frequency Stabilization of Violet Diode Lasers",
Jpn. J. Appl. Phys. **42**, L332 (2003).

[50] R. W. P. Drever, J. L. Hall, F. V. Kowalski, J. Hough, G. M. Ford, A. J. Munley, and H. Ward,
"Laser phase and frequency stabilization using an optical resonator",
Appl. Phys. B **31**, 97 (1983).

[51] M. Weissbluth,
Atoms and Molecules,
Academic Press, 1978.

[52] K. Sugiyama and A. Morinaga,
"Frequency Stabilization of a Dye Laser to a Reference Cavity with Sub-Hertz Relative Linewidth",
Jpn. J. Appl. Phys. **30**, L1811 (1991).

[53] M. Scheid, F. Markert, J. Walz, J. Wang, M. Kirchner, and T. W. Hänsch,
"750 mW continuous-wave solid-state deep ultraviolet laser source at the 253.7 nm transition in mercury",
Opt. Lett. **32**, 955 (2007).

[54] D. M. Harber and M. V. Romalis,
"Measurement of the scalar Stark shift of the $6^1S_0 \rightarrow 6^3P_1$ transition in Hg",
Phys. Rev. A **63**, 013402 (2000).

[55] H. Hachisu, K. Miyagishi, S.G. Porsev, A. Derevianko, V. D. Ovsiannikov, V. G. Pal'chikov, M. Takamoto, and H. Katori,
"Trapping of Neutral Mercury Atoms and Prospects for Optical Lattice Clocks",
arXiv:0711.4638v1.

[56] R. A. Nyman, G. Varoquaux, B. Villier, D. Sacchet, F. Moron, Y. Le Coq, A. Aspect, and P. Bouyer,
"Tapered-amplified antireflection-coated laser diodes for potassium and rubidium atomic-physics experiments",
Rev. Sci. Instrum. 77, 033105 (2006).

[57] K. Liu and M. Littman,
"Novel geometry for single-mode scanning of tunable lasers",
Opt. Lett. **6**, 117 (1981).

[58] V. V. Vassiliev, S. A. Zibrov, and V. L. Velichansky,
"Compact extended-cavity diode laser for atomic spectroscopy and metrology",
Rev. Sci. Instrum. 77, 013102 (2006).

[59] A. I. Akhiezer and V. B. Berestetskii,
Elements of Quantum Electrodynamics,
Oldbourne Press, 1956.

[60] S. G. Porsev, Y. G. Rakhlina, M. G. Kozlov,
"Electric-dipole amplitudes, lifetimes, and polarizabilities of the low-lying levels of atomic ytterbium",
Phys. Rev. A **60**, 2781 (1999).

[61] N. Kolachevsky, J. Alnis, S. D. Bergeson, and T. W. Hänsch,
"Compact solid-state laser source for $1S-2S$ spectroscopy in atomic hydrogen,
Phys. Rev. A **73**, 021801(R) (2006).

[62] J. Léonard, A. P. Mosk, M. Walhout, P. van der Straten, M. Leduc, and C. Cohen-Tannoudji,
"Analysis of photoassociation spectra for giant helium dimers",
Phys. Rev. A **69**, 032702 (2004).

[63] Gediminas Juzeliūnas and Marius Mašalas,
"Absorption by cold Fermi atoms in a harmonic trap",
Phys. Rev. A **63**, 061602(R) (2001).

[64] B. J. Verhaar, J. M. V. A. Koelman, H. T. C. Stoof, and O. J. Luiten,
"Hyperfine contribution to spin-exhange frequency shifts in the hydrogen maser",
Phys. Rev. A **35**, 3825 (1987).

[65] E. Tiesinga, B. J. Verhaar, H. T. C. Stoof, and D. van Bragt,
"Spin-exchange frequency shift in a cesium atomic fountain",
Phys. Rev. A **45**, R2671 (1992).

[66] M. Bijlsma, B. J. Verhaar and D. J. Heinzen,
"Role of collisions in the search for an electron electric-dipole moment",
Phys. Rev. A **49**, R4285 (1994).

[67] S. J. J. M. F. Kokkelmans, B. J. Verhaar, K. Gibble, and D. J. Heinzen,
"Predictions for laser-cooled Rb clocks",
Phys. Rev. A **56**, R4389 (1997).

[68] Thomas C. Killian, Dale G. Fried, Lorenz Willmann, David Landhuis, Stephen C. Moss, Thomas J. Greytak, and Daniel Kleppner,
"Cold COllision Frequency Shift of the $1S-2S$ Transition in Hydrogen",
Phys. Rev. Lett. **81**, 3807 (1998).

[69] Kurt Gibble and Steven Chu,
"Laser-Cooled Cs Frequency Standard and a Measurement of the Frequency SHift due to Ultracold Collisions",
Phys. Rev. Lett. **70**, 1771 (1993).

[70] Y. Sortais, S. Bize, C. Nicolas, A. Clairon, C. Salomon, and C. Williams,
"Cold Collision Frequency Shifts in a ^{87}Rb Atomic Fountain",
Phys. Rev. Lett. **85**, 3117 (2000).

[71] C. J. Bowers, D. Budker, E. D. Commins, D. DeMille, S. J. Freedman, A. -T. Nguyen, and S. -Q. Shang,
"Experimental investigation of excited-state lifetimes in atomic ytterbium",
Phys. Rev. A **53**, 3103 (1996).

[72] C. R. Monroe, E. A. Cornell, C. A. Sackett, C. J. Myatt, and C. E. Wieman, "Measurement of Cs-Cs elastic scattering at T=30 μK",
Phys. Rev. Lett. **70**, 414 (1993).

[73] R. deCarvalho and J. Doyle,
"Evaporative cooling at low trap depth",
Phys. Rev. A **70**, 053409 (2004).

[74] M. Mizoguchi,
"光トラップされた極低温イッテルビウム原子気体の準安定励起状態 $^3P_2$ への光励起"(in Japanese),
Master thesis, Kyoto University, 2004

[75] Sergey G.Porsev and Andrei Derevianko,
"Hyperfine quenching of the metastable $^3P_{0,2}$ states in divalent atoms",
Phys. Rev. A **69**, 042506 (2004).

[76] Glenn E. Miller and John S. Ross
"Isotope shifts in the arc spectra of dysprosium, erbium and ytterbium"
J. Opt. Soc. Am. **66**, 585 (1976).

[77] R. W. Berends and L. Maleki
"Hyperfine structure and isotope shifts of transitions in neutral and singly ionized ytterbium"
J. Opt. Soc. Am. B **9**, 332 (1992).

[78] Takashi Wakui, Wei-Guo-Jin, Kenji Hasegawa, Haruko Umematsu, Tatsuya Minowa and Hidetoshi Katsuragawa
"High-Resolution Diode-Laser Spectroscopy of the Rare-Earth Elements"
J.Phys.Soc.Jpn. **72**, 2219 (2003).

[79] Lars Hallstadius and Jørgen E.Hansen
"Experimental Determination of Isotope Shifts in Mg I"
Z. Physik A **285**, 365 (1978).

[80] E. Arimondo, M. Inguscio, and P. Violino
"Experimental Determinations of the hyperfine structure in the alkali atoms"
Rev. Mod. Phys. **49**, 31 (1977).

[81] D. F. Kimball, D. Clyde, D. Budker, D. Demille, S. J. Freedman, S. Rochester, J. E. Stalnaker, and M. Zolotorev
"Collisional perturbation of states in atomic ytterbium by helium and neon"
Phys. Rev. A **60**, 1103 (1999).

[82] K. Shibata,
"光格子中のYb原子を用いた量子計算機の提案" (in Japanese),
Master thesis, Kyoto University, 2007.

[83] Irène Courtillot, Audrey Quessada, Richard P.Kovacich, Anders Brusch, Dmitri Kolker, Jean-Jacques Zondy, Giovanni D.Rovera, and Pierre Lemonde,
"Clock transition for a future optical frequency standard with trapped atoms",
Phys. Rev. A **68**, 030501 (2003).

[84] Tetsuya Ido and Hidetoshi Katori,
"Recoil-Free Spectroscopy of Neutral Sr Atoms in the Lamb-Dicke Regime",
Phys. Rev. Lett. **91**, 053001 (2003).

[85] A. G. Martin, K. Helmerson, V. S. Bagnato, G. P. Lafyatis, and D. E. Pritchard,
"rf Spectroscopy of Trapped Neutral Atoms",
Phys. Rev. Lett. **61**, 2431 (1988).

[86] Simon Fölling, Arture Widera, Torben Müller, Fabrice Gerbier, and Immanuel Bloch,
"Formation of Spatial Shell Structure in the Superfluid to Mott Insulator Transition",
Phys. Rev. Lett. **97**, 060403 (2006).

[87] Y. Shin, C. H. Schunck, A. Schirotzek, and W. Ketterle,
"Tomographic RF Spectroscopy of a Trapped Fermi Gas at Unitarity",
Phys. Rev. Lett. **99**, 090403 (2007).

[88] B. C. Young, F. C. Cruz, W. M. Itano, and J. C. Bergquist,
"Visible Lasers with Subhertz Linewidths",
Phys. Rev. Lett. **82**, 3799 (1999).

[89] Dale G.Fried, Thomas C.Killian, Lorenz Willmann, David Landhuis, Stephen C.Moss, Daniel Kleppner, and Thomas J.Greytak,
"Bose-Einstein Condensation of Atomic Hydrogen",
Phys. Rev. Lett. **81**, 3811 (1998).

[90] A. Görlitz, T. L. Gustavson, A. E. Leanhardt, R. Löw, A. P. Chikkatur, S. Gupta, S. Inouye, D. E. Pritchard, and W. Ketterle,
"Sodium Bose-Einstein Condensates in the F=2 State in a Large-Volume Optical Trap",
Phys. Rev. Lett. **90**, 090401 (2003).

[91] Gretchen K. Campbell, Jongchul Mun, Micah Boyd, Patrick Medley, Aaron E. Leanhardt, Luis G. Marcassa, David E. Pritchard, Wolfgang Ketterle,
"Imaging the Mott Insulator Shells by Using Atomic Clock Shifts",
Science **313**, 649 (2006).

[92] K. Huang and C. N. Yang,
"Quantum-Mechanical Many-Body Problem with Hard-Sphere Interaction",
Phys. Rev. **105**, 767 (1957).

[93] T. C. Killian,
"$1S$-$2S$ spectrum of a hydrogen Bose-Einstein condensate",
Phys. Rev. A **61**, 033611 (2000).

[94] W. Ketterle and H.-J. Miesner,
"Coherence properties of Bose-Einstein condensates and atom lasers",
Phys. Rev. A **56**, 3291 (1997).

[95] M. ö. Oktel, T. C. Killian, D. Kleppner, and L. S. Levitov,
"Sum rule for the optical spectrum of a trapped gas",
Phys. Rev. A **65**, 033617 (2002).

[96] J. Stenger, S. Inouye, A. P. Chikkature, D. M. Stamper-Kurn, D. E. Pritchard, and W. Ketterle,
"Bragg Spectroscopy of a Bose-Einstein Condensate",
Phys. Rev. Lett. **82**, 4569 (1999).

[97] D. J. Wineland and W. M. Itano,
"Laser cooling of atoms",
Phys. Rev. A **20**, 1521 (1979).

[98] P. Pedri, L. Pitaevskii, S. Stringari, C. Fort, S. Burger, F. S. Cataliotti, P. Maddaloni, F. Minardi, and M. Inguscio,
"Expansion of a Coherent Array of Bose-Einstein Condensates",
Phys. Rev. Lett. **87**, 220401 (2001).

[99] S.A.Diddams, J.C.Bergquist, S.R.Jefferts, and C.W.Oates,
"Standards of Time and Frequency at the Outset of the 21st Century",
Science **306**, 1318 (2004).

[100] D. A. Jennings, K. M. Evenson, D. J. E. Knight,
"Optical frequency measurements",
Proc. IEEE **74**, 168 (1986).

[101] H. R. Telle, D. Meschede, T. W. Hänsch,
"Realization of a new concept for visible frequency division: phase locking of harmonic and sum frequencies",
Opt. Lett. **15**, 532 (1990).

[102] Th. Udem, J. Reichert, R. Holzwarth, and T. W. Hänsch,
"Absolute Optical Frequency Measurement of the Cesium D_1 Line with a Mode-Locked Laser",
Phys. Rev. Lett. **82**, 3568 (1999).

[103] J. K. Ranka, R. S. Windeler, A. J. Stentz,
"Visible continuum generation in air-silica microstructure optical fibers with anomalous dispersion at 800 nm",
Opt. Lett. **25**, 25 (2000).

[104] D. J. Jones, S. A. Diddams, J. K. Ranka, A. Stentz, R. S. Windeler, J. L. Hall, S. T. Cundiff,
"Carrier-Envelope Phase Control of Femtosecond Mode-Locked Lasers and Direct Optical Frequency Synthesis",
Science **288**, 635 (2000).

[105] S. T. Cundiff and Jun Ye,
"Femtosecond optical frequency combs",
Rev. Mod. Phys. 75, 325 (2003).

[106] S. Kato,
"超狭線幅光学遷移を用いた磁気共鳴イメージングへ向けて：遷移周波数の推定と特殊真空槽の開発"(in Japanese),
Master thesis, Kyoto University, 2008.

[107] J. R. Taylor,
An Introduction To Error Analysis,
University Science Books, 1997.

[108] E. J. Angstmann, V. A. Dzuba, and V. V. Flambaum,
"Relativistic effects in two valence-electron atoms and ions and the search for variation of the fine-structure constant",
Phys. Rev. A **70**, 014102 (2004).

[109] K. Beloy, A. Derevianko, W. R. Johnson,
"Hyperfine structure of the metastable $^3P_2$ state of alkaline earth atoms as an accurate probe of nuclear magnetic octupole moments",
arXiv:0709.2655

[110] R. C. Eckardt, H. Masuda, Y. X. Fan, and R. L. Byer,
"Absolute and relative nonlinear optical coefficients of KDP, KD*P, BaB_2O_4, $LiIO_3$, MgO:$LiNbO_3$, and KTP measured by phase-matched second harmonic generation",
IEEE J. Quantum Electron. **26**, 922 (1990).

[111] G. D. Boyd and D. A. Kleinman,
"Parametric interaction of focused Gaussian light beams,"
J. App. Phys. **39**, 3597 (1968).

[112] V. G. Dmitriev, G. G. Gurzadyan, D. N. Nikogosyan,
Handbook of Nonlinear Optical Crystals,
Springer, (1991).

[113] H. Kogelnik, T. Li,
"Laser beams and resonators",
Appl. Opt. **5**, 1550 (1966).

[114] A. Yariv,
Quantum Electronics,
3rd ed. New York, Wiley, (1989).

[115] W.-Y. Cheng, L. Chen, T. H. Yoon, J. L. Hall, and J. Ye,
"Sub-Doppler molecular-iodine transitions near the dissociation limit (523-498 nm)",
Opt. Lett. **27**, 571 (2002).

[116] S. Gerstenkorn and P. Luc,
Atlas du Spectre d'Absorption de la Molécule d'Iode entre 14800-20000 cm^{-1},
Editions du Centre National de la Research Scientique, Paris, (1978).

[117] G. Camy, C. J. Bordé, and M. Ducloy,
"Heterodyne saturation spectroscopy through frequency modulation of the saturating beam",
Opt. Commun. **41**, 325 (1982).

[118] J. H. Shirley,
"Modulation transfer processes in optical heterodyne saturation spectroscopy",
Opt. Lett. **7**, 537 (1982).